

ELECTROCHROMISM FOR LINEAR AND NONLINEAR NANOPLASMONIC  
AND DIELECTRIC NANOPHOTONIC DEVICES

by

ERIC HOPMANN

A thesis submitted in partial fulfillment of the requirements for the degree of

Doctor of Philosophy

in

Photonics and Plasmas

Department of Electrical and Computer Engineering  
University of Alberta

© Eric Hopmann, 2023

# Abstract

The electrochromic (EC) effect has attracted constant research efforts since it was first described in the early 19<sup>th</sup> century. Conventionally, EC oxides (e.g.,  $\text{WO}_3$ ,  $\text{MoO}_3$ ,  $\text{V}_2\text{O}_5$ , and  $\text{NiO}$ ) are employed to modulate light transmittance in smart windows, which allow for up to 80% optical transmission modulation in several seconds. Recently, research in EC materials, in particular the optical properties of EC oxides, has led to novel functionalities transcending beyond their typical applications in smart windows. In a typical EC device light transmittance control is realized upon reversible ion intercalation, wherein resulting in modifying the real and imaginary parts of the refractive index. Dynamically altering the dielectric properties of an EC material gives direct control over the properties of nanophotonic devices. Furthermore, merging nanoplasmonics and nanophotonics with EC materials provides an additional degree of freedom and a new avenue to active control. Such an intriguing platform offers novel functionalities, such as dynamic high optical transmission modulation, structural color generation, and metasurface tunability at a low power consumption.

This thesis investigates the possibilities of integrating electrochromic  $\text{WO}_3$  into nanophotonic and nanoplasmonic devices. First, long lifetime ionic conductors are evaluated for use in EC devices. Common ion conductors are liquids or polymers, as well as amorphous crystals, which contain ionic species such as  $\text{H}^+$  or  $\text{Li}^+$ . Here, a polymeric poly acrylamide ion conductor is modified via simple chemical methods to increase its lifetime. Further, solid-state  $\text{LiNbO}_3$  processing for ionic

conduction is investigated and tailored as potential solid-state ion source in nanofabricated devices. Second, these ion conductors are integrated in plasmonic, electrochromic (i.e., plasmochromic) color and optical transmission modulation devices, for full color plasmonic display applications and ultra-high optical transmission modulation. Last,  $\text{WO}_3$  is utilized in combination with a plasma-enhanced chemical vapor deposition (PECVD) Silicon Nitride waveguide platform to create novel functionalities, such as ultra-high transmission modulation sensor applications and dynamic phase tuning. Through the EC modulation layer, we create a novel nonlinear photonic structure with the ability to dynamically and reversibly tune the second harmonic wavelength generated in a  $\text{SiN}_x$  waveguide.

# Preface

This thesis is an original work by Eric Hopmann.

Portions of Chapter 1 contain unpublished work currently under review.

Portions of Chapter 3 have been published in:

- E. Hopmann and A. Y. Elezzabi, “Electrochemical Stability Enhancement of Electrochromic Tungsten Oxide by Self-Assembly of a Phosphonate Protection Layer,” *ACS Applied Materials & Interfaces*, vol. 12, pp. 1930–1936, 2020.
- E. Hopmann, H. Li, and A. Y. Elezzabi, “Rechargeable  $Zn^{2+}/Al^{3+}$  dual-ion electrochromic device with long life time utilizing dimethyl sulfoxide (DMSO)-nanocluster modified hydrogel electrolytes” *RSC Advances*, vol. 9, no. 64, 2019.

Portions of Chapter 4 have been published in:

- E. Hopmann and A. Y. Elezzabi, “Plasmochromic Nanocavity Dynamic Light Color Switching,” *Nano Letters*, vol. 20, no. 3, pp. 1876–1882, 2020
- E. Hopmann, B. N. Carnio, C. J. Firby, B. Y. Shahriar, and A. Y. Elezzabi, “Nanoscale All-Solid-State Plasmochromic Waveguide Nonresonant Modulator,” *Nano Letters*, vol. 21, no. 5, pp. 1955-1961, 2021

And parts of Chapter 5 have been published in:

- E. Hopmann, B. Y. Shahriar, and A. Y. Elezzabi, “On-chip high ion sensitivity electrochromic nanophotonic light modulator,” *Nanoscale*, vol. 14, no. 17, pp. 6526–6534, 2022.

Other parts of Chapter 5 contain unpublished work which are currently under review.

“The most dangerous worldviews are the worldviews of those who have never viewed the world.”

— Alexander von Humboldt

# Dedication

To my wife Ashlie without whom this PhD would not have been possible. To my son Elliot without whom this PhD would have probably been easier, but a million times less fulfilling.

To the ones I lost along this long way.

# Acknowledgments

First, I would like to thank my supervisor, Prof. Abdul Elezzabi for the enthusiasm for research he has instilled in me. He gave me the opportunity to come to Canada and pursue an incredibly exciting, yet a challenging PhD. Without his faith in me, his support and infinite wisdom, I would not be where I am today. Through his mentorship, I gained invaluable skills in research, communication, and teamwork.

I would also like to thank all the colleagues and lab-mates that have helped and inspired me along the way: Curtis Firby, Shawn Greig, Nir Katchinskiy and Brett Carnio who welcomed me into their midst as a PhD student and have shared so much knowledge with me. Further thanks to Basem Shahriar, Ryan Boehnke, Amir Badkoobehhezaveh, Wu Zhang, Weilon Chang, Aiden McDermott, Liam McRae and Dr. Haizeng Li, for advice, challenges and endless discussions. All of you have contributed to this PhD experience and I wholeheartedly wish all of you the success you deserve. Further thanks to Tom Jones for the helpful discussions about nanofabrication and how to deal with endless days without daylight.

Special thanks to the support staff at the NanoFAB, without who this work would not be finished in a million years. Your help with process development, short-term after hour access and patience with me were essential to my PhD. Specifically, I would like to thank Dr. Aaron Hryciw, Stephanie Bozic, Scott Munro, Gustavo de Oliveira Luiz, Aditi Ganji and Glenn Elaszuk for the training and guidance I have received along the way.

This PhD would not have been possible without the endless support I have received from my family. Björn, Mama, Oma, without your love and support I would have never found the courage to go on this adventure. Thanks to Joan and Dolors who make speaking one, two or four languages seem so easy. Special thanks to Sherryl Jackson whose determination to see the positive side of things has been a real inspiration. Thanks to all my friends who gave words of wisdom and encouragement along the way. Lastly, I extend my infinite appreciation to my wife Ashlie, who has helped in so many more ways than she will ever know. Your love, faith and dedication have helped me in hours of frustration and resignation and gave me extra energy when things worked out. Thanks for celebrating my successes with me. Special shout out to Elliot Jasper Hopmann, who has given me the spirit and energy to believe that anything is possible.

*The University of Alberta is located on Treaty 6 territory, the traditional lands of  
First Nations and Métis people.*

# Table of Contents

1. Introduction.....	1
1.1 EC Devices.....	3
1.2 EC Performance Metrics .....	6
1.2.1 Optical Contrast.....	7
1.2.2 Switching Times .....	7
1.2.3 Coloration Efficiency.....	8
1.2.4 Cycle Life.....	8
1.2.5 Charge Capacity.....	9
1.2.6 Electrochemical Reversibility.....	9
1.2.7 CIE Color Code.....	10
1.3 EC Energy Storage Devices.....	11
1.3.1 EC Supercapacitors.....	11
1.3.2 EC Batteries .....	13
1.4 Active Nanophotonic and Nanoplasmonic ECDs .....	14
1.4.1 EC Plasmonic Color Printing and Display Devices.....	14
1.4.2 Active EC Cavity Devices .....	25
1.4.3 Modulation Materials for Integrated Photonics .....	36
1.4.4 Summary.....	46
1.5 Objectives.....	47
1.6 Structure of the Thesis.....	48
2. Background.....	51
2.1 Electrochromism .....	51
2.1.1 Electrochromic Oxides.....	52
2.1.2 Ion Conductors and Electrolytes.....	56
2.1.3 Electrochemical Description and Analysis .....	62
2.2 Optical Fields and Electromagnetic Waves in Photonic Devices .....	66
2.2.1 Harmonic Oscillations in the Free Electron Gas.....	71
2.2.2 Bulk Plasmons .....	72
2.3 Nanoplasmonics .....	73
2.3.1 Helmholtz Equation for Propagating Waves .....	74
2.3.2 Surface Plasmon Polaritons .....	76
2.3.3 Localized Surface Plasmon Resonance.....	81
2.3.4 Plasmonic Loss .....	84
2.4 Nonlinear Optical Materials.....	87

2.4.1	Second Harmonic Generation.....	88
2.4.2	Second Order Nonlinearity in Silicon Nitride.....	89
3.	Materials for Electrochromic Devices .....	91
3.1	Deposition Methods for EC WO <sub>3</sub> .....	92
3.1.1	Morphological Comparison .....	93
3.1.2	Electrochemical Properties of EC Thin Films .....	97
3.2	Ion Conductors for ECDs .....	109
3.3	WO <sub>3</sub> – NiO supercapacitor.....	115
3.4	Hydrogel Based WO <sub>3</sub> Dual Ion EC Battery <sup>131</sup> .....	118
3.4.1	DMSO Modified PAM Hydrogel Electrolytes .....	118
3.4.2	Dual-Ion EC Battery .....	125
3.5	Stability Enhancement for Electrochromic Thin Films <sup>233</sup> .....	133
3.6	Summary .....	143
4.	Plasmonic-Electrochromic “Plasmochromic” Devices .....	144
4.1	Surface Plasmon Propagation.....	146
4.1.1	Plasmochromic Kretschmann Stack (PCK): Design and Simulation 147	
4.1.2	PCK Experimental Results.....	151
4.2	Nanoplasmonic Waveguide Nonresonant Modulator <sup>117</sup> .....	155
4.2.1	PCWG Design and FDTD Simulations .....	156
4.2.2	PCWG Fabrication.....	162
4.2.3	Photo-Electrochemical Analysis of PCWG .....	166
4.2.4	Discussion.....	173
4.3	Plasmochromic Nanocavity <sup>81</sup> .....	173
4.3.1	Plasmochromic Nanocavity Design and Simulations.....	175
4.3.2	PCNC Fabrication.....	179
4.3.3	Experimental Results .....	183
4.4	Summary and Discussion .....	194
5.	EC for Linear and Nonlinear Nanophotonic Applications .....	196
5.1	Experimental Setup .....	197
5.2	Ion Sensing in EC Waveguide <sup>281</sup> .....	199
5.2.1	SiN <sub>x</sub> waveguide (SNWG) Design and Simulations.....	200
5.2.2	SNWG Fabrication.....	206
5.2.3	Experimental Results .....	209
5.2.4	Discussion.....	218
5.3	Dynamic Nonlinear Photonic Waveguides .....	219

5.3.1	SHWG Device Design and Simulations .....	220
5.3.2	SHWG Fabrication.....	229
5.3.3	SHWG Experimental Results.....	237
5.3.4	Discussion.....	253
5.4	Summary .....	254
6.	Conclusion & Outlook .....	256
6.1	Future Directions.....	259
6.2	Outlook.....	260
	Thesis Publication List (as of Oct 25 <sup>th</sup> , 2022).....	262
	References .....	264
	Appendix A: Process Parameter .....	295
	Appendix B: Fabrication Process for Silicon Nitride EC Waveguides	
	297	

# List of Tables

Table 1: A list of transitions metals and their respective colors in their reduced and oxidized forms. ....	1
Table 2: Performance parameter for selected EC supercapacitors. ....	13
Table 3: EC batteries based on WO <sub>3</sub> and their performance metrics.....	14
Table 4: Comparison of selected active EC plasmonic modulation technologies. Values for peak wavelength, wavelength shift and switching times are extracted from figures and graphs as they were not indicated in the referenced articles.....	23
Table 5: Comparison of selected Fabry-Perot type cavity devices. Values for color range, FWHM and optical transmission modulation are extracted from figures and graphs from the cited references.....	36
Table 6: Regions of the electromagnetic spectrum.....	67
Table 7: Comparison of morphological properties of 250 nm thick WO <sub>3</sub> film deposited by different methods.....	97
Table 8: Summary of the optical, ionic, and EC properties of PAM hydrogel, PMMA gel and LiNbO <sub>3</sub> solid electrolytes.....	114
Table 9: Calculated Na <sup>+</sup> ion concentration based on calibration curve and resulting error.....	218

# List of Figures

- Fig. 1.1: Typical EC materials arranged according to the spectrum of their light interaction. .... 2
- Fig. 1.2: Schematic of an exemplary EC smart window based on ion intercalation. Here, the ion storage layer consists of an active material, such as zinc or aluminum or a complementary EC material.<sup>14</sup> ..... 5
- Fig. 1.3: Performance of active gold nanostructure arrays coated conductive polymers. (a) LSPR of PANI coated Au nanostructures in 1 air, 2 water, 3 PANI reduced and 4 PANI oxidized. (b) Plasmonic extinction and wavelength shift for PEDOT coated Au array as a function of applied voltage.<sup>54,56</sup> ..... 17
- Fig. 1.4: Sol-gel modified Ag nanoparticles with a WO<sub>3</sub> modulation layer. (a) SEM image of the colloidal silver particles. (b) Voltage-dependent extinction spectra for the modified Ag nanoparticle samples.<sup>57</sup> ..... 18
- Fig. 1.5: Dynamic gap plasmon color printing device. (a) Schematic of the EC plasmonic nanodevice consisting of Al nanostructures and a solid PEO electrolyte. (b) Reflectance spectra (left) and wavelength of minimum reflection (right) taken cyclic voltammetry, showing a continuous wavelength shift.[62] ..... 20
- Fig. 1.6: Plasmonic nanopixels based on a PANI modulation layer. (a) Schematic of the proposed device. An 80 nm Au nanoparticle is coated in a 20 nm thick PANI shell and placed on an Au mirror, creating a plasmonic "hot spot" between the Au components. (b) FDTD simulation of the electric field distribution and (c) absorption and scattering spectra determined through the numerical approach. (d) Dark-field images of the nanopixel during electrochemical redox cycling.<sup>33</sup> ..... 24
- Fig. 1.7: EC switching of a MIN resonant cavity. (a) Schematic of the active MIN cavity with an Au NHA and polypyrrole as the EC modulation material. (b) Optical light modulation induced through EC cycling of PP under a viewing angle between 0-14°.<sup>68</sup> ..... 26
- Fig. 1.8: WO<sub>3</sub> based resonant nanocavities for color generation. (a) Reflectance spectra for WO<sub>3</sub>/W nanocavities as a function of WO<sub>3</sub> layer thickness. (b) Dynamic reflectance of a 163 nm thick WO<sub>3</sub>/W cavity (in a 1 M LiClO<sub>4</sub> electrolyte) as a function of applied voltage.<sup>32</sup> ..... 28

Fig. 1.9: (a) Reflection mode EC color display devices. Reflectance spectra measured from film and substrate side exhibit asymmetric colors. (b) Mn <sub>2</sub> O <sub>3</sub> based EC battery with high color tunability. <sup>72,73</sup> .....	29
Fig. 1.10: EC cavity color devices developed by Lee <i>et al.</i> (a) Reflection type device with (b) corresponding reflectance spectra. (c) Transmission type device with (d) the corresponding spectra. <sup>75</sup> .....	30
Fig. 1.11: EC Bragg-Reflector type color displays. (a) Sputtering process showing sharp resonances in the reflectance spectra (left) and a schematic of the device (right). (b) Colloidal fabrication process based on alternating layers of NiO and WO <sub>3</sub> nanoparticles spin coated onto FTO substrates. Reflectance spectra during coloration and SEM image of device architecture. <sup>74,76</sup> .....	32
Fig. 1.12: (a) Schematic diagram of cavity operating in the F–P resonance mode. Inset: Reflection spectra of the proposed structure operating in the F–P resonance mode. (b) Same device operating in the Fano resonance mode. (c) Reflection spectra as a function of lithiation with resonance mode.....	33
Fig. 1.13: (a) Images of the large-scale color printing devices fabricated by Gugole <i>et al.</i> (b) Fabry-Perot type EC cavity with absorber for higher chromaticity. <sup>78,79</sup> .....	34
Fig. 1.14: (a) Microheater design with doped silicon profiles to create an electrical resistor in a half-etched 220 nm SOI waveguide. (b) SEM image of a fabricated 6 μm-long bowtie microheater on a 6 μm-long Sb <sub>2</sub> Se <sub>3</sub> . <sup>87</sup>	38
Fig. 1.15: Schematic of an on-chip MZI having a patterned monolayer WS <sub>2</sub> on both arms of the MZI. Optical transmittance of the MZI for the TE mode at different voltages. The top figure shows the optical mode profile for the TE mode where the arrows illustrating the field lines aligned along the plane of WS <sub>2</sub> monolayer. <sup>88</sup> .....	39
Fig. 1.16: Planar waveguide with EC modulation layer. (a) Schematic of the device including planar waveguide, buffer layer and EC cell. (b) Achievable modulation in reduced (labeled: red) and oxidized (labeled: green) state of Lu(PC) <sub>2</sub> .....	42
Fig. 1.17: (a) Schematic of synaptic transmission modulation via Ca <sup>2+</sup> ions and corresponding device design. (b) Voltage dependent optical transmission in the artificial synapse. <sup>29</sup> .....	43
Fig. 1.18: Wavelength-dependent effective indices of TE <sub>0,tele</sub> and TM <sub>2,vis</sub> at (a) 20°C, and (b) 70°C, with black arrows indicating phase matching; (c) simulated phase-matched pump wavelength λ <sub>PM</sub> as a function of temperature. ....	45

Fig. 2.1: Electrochromic transition metal oxides (TMO) showing both cathodic (blue) and anodic (red) coloration. Note that Vanadium and its oxides experience both coloration types <sup>115</sup> .....	52
Fig. 2.2: Optical transmittance of a 300 nm thick WO <sub>3</sub> film on ITO in its oxidized (blue) and reduced (red) state. <sup>50</sup> .....	54
Fig. 2.3: Schematic band structures for different types of electrochromic oxides. Shaded regions signify filled states and E denotes the energy. From Ref. <sup>118</sup> .....	55
Fig. 2.4: Cyclic voltammetry for electrochemical analysis. (a) Schematic of the CV measurement cell. (b) Typical CV curve with anodic and cathodic peak currents (I <sub>pc,pa</sub> ) and potentials (E <sub>pa,pc</sub> ) indicated. <sup>14</sup> .....	65
Fig. 2.5: Schematic of the propagating wave at the metal-dielectric interface.....	75
Fig. 2.6: SPP dispersion relation at an interface between a lossless metal and air (grey) and silica (black). The dashed lines indicate purely imaginary propagation constants between the bound and the radiative states. <sup>15578</sup>	
Fig. 2.7: Sketch of a homogeneous sphere placed into an electrostatic field. <sup>155</sup> ..	81
Fig. 2.8: (a) In an optical cavity with dimensions larger than half wavelength $\lambda/2n$ energy alternates between $u_E$ (left), and $u_H$ (right). (b) In a cavity with a characteristic size $< \lambda/2$ , $u_H$ is too small; hence, the cavity radiates energy out (purple arrows). (c) Free carriers lead to a current flow, J, and the energy alternates between $u_E$ and kinetic energy of carriers $u_K$ . The optical diffraction limit is overcome, but the motion of carriers is strongly damped at a rate $\gamma$ , and the SPP mode becomes lossy. <sup>162</sup> ....	86
Fig. 2.9: Second harmonic generation process. (a) Schematic of the SHG process. (b) Energy level description of SHG. ....	89
Fig. 3.1: Electrodeposition of WO <sub>3</sub> from peroxy tungstic solution. The deposition current density saturates and tends towards $J = 4 \text{ mA/cm}^2$ (red). Simultaneously, the deposition rate decreases for time beyond 60 s.	94
Fig. 3.2: SEM images of the surface of EC WO <sub>3</sub> deposited via (a) electrodeposition and (b) spray coating.....	95
Fig. 3.3: CV measurements of a 250 nm thick EC WO <sub>3</sub> film deposited on ITO via (a) electrodeposition and (b) reactive magnetron sputtering. The applied voltage is measured with respect to an Ag/AgCl reference electrode. Voltage sweep rates are varied from 100 mV/s to 1 mV/s as indicated.....	98

Fig. 3.4: CV measurements of 250 nm thick WO <sub>3</sub> films deposited via electrodeposition (ED) and sputtering (SP) compared. (a) CV curve for a voltage sweep rate of 10 mV/s. (b) Areal capacitance of the investigated films as a function of the sweep rate. ....	100
Fig. 3.5: CV measurement of a 250 nm thick NiO film deposited via reactive magnetron sputtering. ....	101
Fig. 3.6: Spectro-electrochemical analysis of 250 nm thick WO <sub>3</sub> films prepared via electrodeposition and sputtering. An alternating voltage of $V = \pm 1$ V is applied to the EC electrode and the current profile, as well as the optical transmission are measured. ....	102
Fig. 3.7: Spectro-electrochemical analysis of a 250 nm thick NiO film. ....	103
Fig. 3.8: EIS analysis of a 250 nm thick sputtered WO <sub>3</sub> sample on ITO in 100 mM LiClO <sub>4</sub> in PC. a) Nyquist plot of the real and imaginary part of the resistance as a function of applied voltage (vs. Ag/Ag <sup>+</sup> Cl <sup>-</sup> ). b) Bode plot of the phase angle over frequency. ....	104
Fig. 3.9: a) XPS spectrum of W4f region for a pristine sample indicating W <sup>6+</sup> and W <sup>5+</sup> contributions. b) Tauc plot of WO <sub>3</sub> as a function of lithiation. ....	106
Fig. 3.10: UPS spectrum of WO <sub>3</sub> thin film on W with its corresponding secondary electron energy cut-off value. The Fermi energy is determined to be 0 eV. ....	107
Fig. 3.11: Valence band edge spectrum for WO <sub>3</sub> . a) Valence band determination for WO <sub>3</sub> on W. b) Close-up of defect states close to E <sub>F</sub> . ....	108
Fig. 3.12: XPS analysis of the LiNbO <sub>3</sub> samples sputtered under the same conditions for (a) without the addition oxygen flow (b) with 1 sccm O <sub>2</sub> flow. ....	111
Fig. 3.13: CV measurements of supercapacitor type smart devices. (a) a WO <sub>3</sub> /NiO ECD having PMMA gel electrolyte, and (b) a WO <sub>3</sub> /NiO having a reactively sputtered Li <sup>+</sup> containing LiNbO <sub>3</sub> ion conductor. ....	116
Fig. 3.14: Spectro-electrochemical analysis of supercapacitor type smart window ECDs having (a) PMMA gel electrolyte and (b) LiNbO <sub>3</sub> solid ion conductor. ....	117
Fig. 3.15: Characterization of modified and unmodified PAM hydrogels. (a) FTIR spectra of a DMSO-modified and a DI hydrogel. The important absorption peaks are indicated. (b) EDX spectra of freeze-dried hydrogels with and without DMSO modification. Samples are soaked in 1 M ZnSO <sub>4</sub> prior to the drying process. ....	120

- Fig. 3.16: SEM image of freeze-dried hydrogels without (a) and with DMSO (b) modification. Scale bar: 2 $\mu$ m..... 121
- Fig. 3.17: Possible mechanisms of DMSO incorporation into PAM-hydrogel. (a) Water molecule mediated dipolar interactions. (b) Copolymerization of sulfone with acrylamide..... 122
- Fig. 3.18: Long-term retention measurements weight and ionic conductivity of PAM hydrogels. (a) Relative weight of unmodified and modified hydrogel samples over 30 days at 30% RH. (b) Ionic conductivity as a function of time of DI and DMSO:H<sub>2</sub>O hydrogel samples. The samples were soaked in ZnAl-electrolyte for 24h before the measurements were taken..... 124
- Fig. 3.19: Schematic of the proposed double layer device with Al<sup>3+</sup> intercalation at the WO<sub>3-x</sub> cathode and Zn/Zn<sup>2+</sup> redox reaction at the zinc anode. .. 126
- Fig. 3.20: Cyclic voltammetry of a hydrogel-based EC battery. (a) CV measurement of the EC dual-ion battery assembled with DMSO-modified hydrogel electrolyte between 0.4 V and 1.2 V vs Zn/Zn<sup>2+</sup> at different cycling speeds. (b) CV measurement of WO<sub>3</sub>-zinc EC battery at 0.5 mV/s sweep rate. The pink and light blue colored bars indicate the oxidation and the reduction regions..... 127
- Fig. 3.21: (a) First four charge-discharge profiles of dual-ion Zn<sup>2+</sup>/Al<sup>3+</sup> WO<sub>3</sub> battery under constant current of J = 10 mA/cm<sup>2</sup>. (b) Temperature dependence of charge-discharge capacity and CE of WO<sub>3</sub>-zinc battery having a DMSO-modified hydrogel electrolyte..... 129
- Fig. 3.22: (a) Rise and fall of colored-bleached cycling of electrochromic double layer device with DMSO-modified electrolyte between 0.1 V and 1.2 V. (b) Transmission spectra of single layer EC battery with DMSO-modified hydrogel electrolyte at  $\lambda = 632$  nm..... 133
- Fig. 3.23: (a) Schematic of the protection layer functionality where the grey layer represents the passivated metal oxide surface. DDPA molecules bind to the surface covalently by Lewis acid base reaction between surface hydroxide groups and the phosphonic acid head group. (b) Schematic of the resulting artificial SEI. DDPA forms a well-ordered monolayer on the WO<sub>3</sub> surface, resulting in a hydrophobic surface. Nonetheless, K<sup>+</sup> ions can freely pass the protection layer, while the integrity of the tungsten oxide is maintained, and possible etching products are blocked..... 137
- Fig. 3.24: Contact angle analysis of (a) cleaned ITO surface, (b) electrodeposited WO<sub>3</sub> thin film and (c) DDPA SAM modified WO<sub>3</sub> surface. DI water is used for the droplets..... 138

Fig. 3.25: XPS spectra of WO <sub>3</sub> sample with no SAM and with DDPA SAM modification. (a,d) and (b,e) show the oxygen 2s and tungsten 4f region of the sample with no SAM and with DDPA modification, respectively. (c) Full survey.....	139
Fig. 3.26: Electrochemical impedance spectra of a 40 nm thick WO <sub>3</sub> electrodes on ITO with and without DDPA SAM modifications. The frequency regions as indicated by arrows. Measurements are conducted in 1 M KCl aqueous electrolyte.....	140
Fig. 3.27: Electrochemical analysis of modified and unmodified WO <sub>3</sub> electrodes. (a) CV analysis of electrode with no SAM and (b) with DDPA SAM at 100 mV/s sweep rate in 1M KCl. (c) Current density as a function of time for cyclic voltammetry in 1M KCl for WO <sub>3</sub> electrodes with no SAM and with DDPA SAM. The inset depicts the same measurement in 1M LiCl. ....	142
Fig. 4.1: Schematic of the Kretschmann-type SPP measurement. (a) Schematic of measurement device with MIM EC structure with a thin Ta <sub>2</sub> O <sub>5</sub> ion conduction layer. Light is coupled through a prism and a nanopolished quartz substrate attached to the prism via index matching adhesive. (b) Calculated reflectance for a fully oxidized/reduced WO <sub>3</sub> film at $\lambda = 633$ nm excitation.....	147
Fig. 4.2: Refractive index (n) and extinction coefficient (k) for NiO under different intercalation levels for a 200 nm thick film.....	148
Fig. 4.3: FDTD simulation of the electric field distribution in a PCK device. (a) 633 nm laser light excitation coupling to the PCK at $t = 18$ fs after the start of simulation. (b) SPP propagation along the top Au surface at $t = 23$ fs after the start of simulation.....	150
Fig. 4.4: Calculations of the reflectance of a PCK as a function of excitation angle and WO <sub>3</sub> thickness. (a) Reflectance for $C = 0$ mC/cm <sup>2</sup> intercalated charge and (b) Reflectance for $C = 62.5$ mC/cm <sup>2</sup> intercalated charge. ....	151
Fig. 4.5: Experimental results for EC dependence of the PCK device. (a) SPP resonance measurements for EC cycling at +3V and -3V. (b) Fixed angle measurement light intensity as a function of the applied potential. (c) I-V curves of the PCK device. (d) Electrical resistance resulting from the I-V measurements. ....	154
Fig. 4.6: Schematic of the PCWG device operation. (a) Delithiated state: WO <sub>3</sub> is transmissive - On. (b) Lithiated State: WO <sub>3</sub> is absorbent - Off. (c) Overview of the device structure with light and ion diffusion paths indicated.....	157

- Fig. 4.7: The refractive index and the extinction coefficient of a 200 nm thick  $\text{WO}_3$  film on W at different intercalation levels of  $\text{Li}^+$  ions.  $\text{Li}^+$  ions are intercalated through a constant applied current in a 0.1 M  $\text{LiClO}_4$  electrolyte. Intercalated charge is the product of current over time. 158
- Fig. 4.8: (a) FDTD simulated plasmon transmittance at 1550 nm for PCWGs of width  $w = 2 \mu\text{m}$  and lengths  $L = 5 \mu\text{m}$  and  $10 \mu\text{m}$ . Shown also is the optical transmittance of a 50 nm thick  $\text{WO}_3$  film. (b) Comparison of simulated and measured transmittance of a 50 nm thick  $\text{WO}_3$  on ITO for different intercalation levels..... 159
- Fig. 4.9: FDTD simulations of the normalized magnitude of the E-field distribution in a  $2 \mu\text{m}$  wide PCWG captured at  $5 \mu\text{m}$  propagation length: (a) with fully oxidized  $\text{WO}_3$  and (b) after the  $\text{Li}^+$  ion intercalation..... 160
- Fig. 4.10: SEM images of the PCWG device at different stages of the fabrication process. (a) Etched trench after waveguide patterning. (b) Beam structure after DRIE etch. (c) Close-up of defined PCWG devices. 163
- Fig. 4.11: XRD spectra of: (a) reactively sputtered  $\text{WO}_3$  film on Si. (b) 100 nm thick sputter deposited  $\text{LiNbO}_3$  film on Si. The peaks indicated by (\*) are due the Si substrate. .... 164
- Fig. 4.12: SEM images of finished PCWG devices. (a) Overview of the fabricated PCWG (light propagation direction is indicated by the black arrow). (b) Close-up of MIM waveguide structure ( $\text{Li}^+$  ions diffusing path is indicated by the white arrow). .... 166
- Fig. 4.13: Photo-electrochemical analysis of PCWG devices. (a) Voltage dependent optical transmission of a  $0 \mu\text{m}$  long PCWG. (b) Comparison of loss per unit length of a  $10 \mu\text{m}$  and a  $20 \mu\text{m}$  long PCWGs. .... 167
- Fig. 4.14: Comparison of lithiation dependent optical transmission of a simulated and a measured  $10 \mu\text{m}$  long PCWG. Measured values for intercalated charge are determined as current over time..... 169
- Fig. 4.15: Switching dynamics of PCWG devices. (a) Comparison of time dependent optical transmission for PCWGs and planar EC at  $V = -2.5$  V. (b) Coloration dynamics and indicated switching times for  $10 \mu\text{m}$  long PCWG. (c) Switching times for  $20 \mu\text{m}$  long PCWG..... 171
- Fig. 4.16: Switching times of the PCWGs. (a) Time-dependent light transmission switching behavior under various  $\pm 2.5$  V duty cycles. (b) Transmittance modulation of the PCWG over 3000 s, or 200 cycles. .... 172
- Fig. 4.17: PCNC based on EC  $\text{WO}_3$  insulator layer able to modulate reflectance over broad spectral range. (a) Schematic of the plasmochromic device

based on an electrochromic  $\text{WO}_3$  layer and a gold resonator (not to scale). Lithium ions are contained in the 1 M  $\text{LiClO}_4$  electrolyte and represented as pink spheres (exaggerated in size). The top ITO film on glass serves as the counter electrode. (b) Close-up schematic of the Lithium ions (pink) diffusing through the gold nanohole channels into the tungsten (black) oxide (red) film. Depicted here is the cubic phase of  $\text{WO}_3$ . ..... 177

Fig. 4.18: FDTD simulations of PCNC. (a) Simulated reflectance spectra of a PCNC with a periodicity of 452 nm and a hole diameter of 224 nm with and without NHA. (b) Reflectance as a function of lithiation. The arrows indicate the location of the plasmon resonance wavelength absorption  $\lambda_p$ . ..... 179

Fig. 4.19: Polystyrene nanosphere synthesis results. (a) Average particle size as a function of amount of styrene added to the reaction. (b) Histogram of PS nanosphere size distribution for 8.5 ml styrene addition to the reaction..... 180

Fig. 4.20: FESEM images of PS nanospheres during lithography process. (a) PS nanospheres on Si substrate for size determination. (b) NHA showing defects due to the absence of the PDDA coating. (c,d) Nanoholes after Au sputtering..... 182

Fig. 4.21: Schematic of the experimental measurement cell used to investigate the PCNC device. The space between ITO and  $\text{WO}_3$  electrode is filled with 1 M  $\text{LiClO}_4$ . ..... 184

Fig. 4.22: Spectro-electrochemical characteristics of the PCNC. (a)  $100 \mu\text{m} \times 100 \mu\text{m}$  size raw images of the reflected color at various stages of the lithiation process. Images are taken with a CMOS camera. (b) Experimentally obtained reflectance at various stages of the lithiation. (c) FDTD simulated reflectance spectra multiplied by experimentally obtained source spectrum at various stages of the lithiation process. The dashed arrow is the same as that in (b). ..... 185

Fig. 4.23: Comparison of experiment and simulation. (a) Experimentally measured peak reflected wavelength and the reflected intensity as a function of increasing lithiation. (b) Peak wavelength and intensity for the FDTD simulated results. The simulated data follow the same experimental data shown in (a). ..... 186

Fig. 4.24: Comparison of measured (blue) and simulated (red) reflectance using the same light source for different lithiation states ( $0 - 8 \text{ mC/cm}^2$ ). To model a realistic light source, FDTD simulation reflectivities were normalized to the source spectrum to achieve absolute reflectivity (i.e., reflectance). The resulting reflectance was multiplied with the

- experimentally obtained source spectrum, yielding the corrected reflectance spectra plotted in red. .... 187
- Fig. 4.25: CV of a PCNC under a constant sweep rate of 100 mV/s in 1 M LiClO<sub>4</sub>. (a) 100 cycles of CV measurement plotted versus time to illustrate the high electrochemical stability of the device. After 100 cycles of voltage sweep, the PCNC shows 85% charge capacity retention. (b) Single CV measurement at 10 cycles of voltage sweep. The lithiation and delithiation processes show a high reversibility (7.9 mC/cm<sup>2</sup> intercalation vs. 7.2 mC/cm<sup>2</sup> extracted charge). .... 188
- Fig. 4.26: (a) Color modulation over time. The spectra are normalized to show the high reproducibility of spectral colors. (b) Time dependence of the color modulation process of the plasmochromic device by applying -3 V to 1 V potential. Full color modulation takes place in a duration of ~ 4 seconds..... 189
- Fig. 4.27: Absorbance spectrum of thin NHA sample on SiO<sub>2</sub> and WO<sub>3</sub> as well as the respective Voigt fit..... 190
- Fig. 4.28: PCNC reflectance at 0 mC/cm<sup>2</sup> intercalated charge with Voigt fits indicating the cavity mode and reflection from the NHA. .... 191
- Fig. 4.29: Comparison of PCNC with and without NHA. a) Experimental reflected spectra obtained for PCNC in delithiated state through white light measurement and b) difference in reflection spectra indicated as additional absorption due to NHA. .... 192
- Fig. 4.30: Simulated reflectance spectra for PCNCs with and without NHA. a) Reflectance for PCNC under 1.5 mC/cm<sup>2</sup> lithiation and b) 4.5 mC/cm<sup>2</sup> lithiation..... 194
- Fig. 5.1: Schematic illustration of the free-space coupling setup used to investigate the linear and nonlinear optical properties of EC SiN<sub>x</sub> based photonic waveguides. A Er<sup>3+</sup> doped fiber laser is coupled via a NA = 0.85 objective into the waveguide samples. Spectro- or photometer are used to analyze the transmitted signal..... 198
- Fig. 5.2: Schematic of the EC nanophotonic waveguide Na<sup>+</sup> ion sensor and light modulator. (a) A positively biased WO<sub>3</sub> layer drives Na<sup>+</sup> ions out of the EC material and renders it transparent. (b) A negatively biased WO<sub>3</sub> layer leads to an accumulation of Na<sup>+</sup> ions inside the EC material. The balancing charge (electrons) from the W electrode dope the WO<sub>3</sub> to a high charge carrier density of ~10<sup>21</sup> cm<sup>-3</sup>, resulting in a lossy EC optical modulation layer and low light transmission..... 202
- Fig. 5.3: Representation of FDTD simulation results of a 2 μm wide and a 0.75 μm high SiN<sub>x</sub> waveguide core. (a,b) E-field distribution in and around the

SiN<sub>x</sub> waveguide for different SiO<sub>2</sub> spacer thicknesses. Material thicknesses and geometries are indicated through the shaded areas.203

Fig. 5.4: (a) Calculated plasmonic loss resulting from optical mode coupling to the metallic contact for a SiO<sub>2</sub> spacer thickness of 150 nm. Optical loss becomes negligible for a distance greater than 2μm. (b) FDTD simulation of the modulated optical transmission at 1550 nm through the SiN<sub>x</sub> waveguide having various WO<sub>3</sub> lengths. .... 204

Fig. 5.5: Refractive index and extinction coefficient of PECVD SiN<sub>x</sub> before and after rapid thermal annealing (RTA) at 1100°C for 2 minutes (Repeated 5 times). .... 207

Fig. 5.6: Topological, morphological, and material properties of the EC photonic waveguide. (a) Cross-section SEM image of the SiN<sub>x</sub> waveguide having a SiO<sub>2</sub> cladding layer and conductive gold film. (b) Low magnification SEM image of the SiN<sub>x</sub> waveguide. The image depicts the underlying bright SiO<sub>2</sub> layer as well as the Si substrate. (c) High resolution image of the WO<sub>3</sub> surface. The WO<sub>3</sub> film consists of particulates having sizes ranging between 20 and 80 nm. .... 208

Fig. 5.7: Optical loss experienced in SNWGs of varying length. (a) without WO<sub>3</sub> layer and (b) with WO<sub>3</sub> layer on top of SiO<sub>2</sub> cladding. .... 210

Fig. 5.8: Spectro-electrochemical analysis of 200 μm long SNWG. (a) Optical transmittance for different Na<sup>+</sup> ion concentrations during CV. The voltage is cycled at v = 50 mV/s. (b) Current-voltage characteristics of SNWG (Same parameter as in (a)). .... 211

Fig. 5.9: Retention of achievable optical transmission modulation over 2000 On-Off cycles. The applied voltage is alternated between V = ±1.5 V, while the optical transmittance is measured accordingly. .... 212

Fig. 5.10: Optical transmittance as a function of time for: (a) intercalation of Na<sup>+</sup> ions at an applied voltage of V = -1.5 V and (b) deintercalation of Na<sup>+</sup> ions at an applied voltage of V = +1.5V. The indicated times correspond to the nearest dashed line's intercepts with the curves. 213

Fig. 5.11: Waveguide length dependent optical transmittance as a function of time. (a) Optical transmission for 50 μm, 100 μm and 200 μm long SNWG over time when a voltage of V = +1.5 V is applied. (b) Optical transmission for 50 μm, 100 μm and 200 μm long EC nanophotonic waveguide over time when a voltage of V = -1.5 V is applied. .... 214

Fig. 5.12: Na<sup>+</sup> ion sensor operation of SNWG. (a) Dynamic intercalation curve for the investigated EC photonic waveguide ion sensor device for an abrupt voltage onset of -1.5 V. (b) Optical transmission taken 10 s after voltage onset for different electrolyte concentrations. The dashed lines

indicate where data points are taken from. The blue curve corresponds to a empirical fit with four independent variables. ....	215
Fig. 5.13: Schematic of the SHWG. (a) An overview of the general device design and functionality. (b) Delithiation of the WO <sub>3</sub> layer leads to phase-matching at lower wavelengths. (c) Intercalation of Li <sup>+</sup> ions into WO <sub>3</sub> change the SH wavelength.....	221
Fig. 5.14: Effective refractive indices for FE TE <sub>00</sub> and SH TE <sub>03</sub> optical modes in a SHWG. (a) At 0 mC/cm <sup>2</sup> lithiation of WO <sub>3</sub> and a 200 nm thick SiO <sub>2</sub> layer and (b) at 15 mC/cm <sup>2</sup> lithiation.....	222
Fig. 5.15: Electric field distribution in SHWG structure with 200 nm thick spacer layer (facet: 850 nm x 1400 nm). (a) FE TE <sub>00</sub> mode showing strong overlap with WO <sub>3</sub> layer. (b) SH TE <sub>03</sub> mode strongly localized to SHWG core.....	224
Fig. 5.16: Coherence length of a SHWG device having a delithiated (0 mC/cm <sup>2</sup> ) and a fully lithiated (15 mC/cm <sup>2</sup> Li <sup>+</sup> ) EC WO <sub>3</sub> modulation layer. ....	225
Fig. 5.17: Spectra of source and SH signal for FDTD simulations. (a) FDTD source consisting of two 150 fs pulses and measured NIR spectrum. (b) FDTD simulated SH spectrum and analytical solution from source spectrum. ....	226
Fig. 5.18: FDTD simulation results for SHWG devices as a function of lithiation. (a) For a 250 μm long SHWG and (b) for a 1 mm long SHWG. ....	228
Fig. 5.19: FDTD simulation results for a 1 mm long SHWG as a function the intercalated charge for two spacer thicknesses. (a) SH wavelength at peak intensity during lithiation. (b) Peak intensity of the FE signal during lithiation.....	229
Fig. 5.20: Microscope images taken during fabrication process. (a) 100× magnification image of two patterned waveguide masks. (b) 10× magnification image of the bottom contact before deposition of the ECD. ....	230
Fig. 5.21: Etch rate of SiO <sub>2</sub> and PC43 as a function of the CHF <sub>3</sub> gas flow.....	231
Fig. 5.22: Microscope images taken during fabrication process. (a) 5× image after deposition of ECD. (b) 5× image of the final device after scoring..	232
Fig. 5.23: EDX analysis of SHWG after fabrication process. (a) FESEM image with indicated EDX line scan directions. (b) Vertical line scan indicating normalized Si, O, and N signal. (c) Horizontal elemental composition along line scan. Signals are normalized due to the strong Si signal. (d)	

False color FESEM image of SHWG facet containing the “scallops” produced by the DRIE step.....	236
Fig. 5.24: FESEM image of the ECD deposited on Si during the SHWG fabrication process with thicknesses for WO <sub>3</sub> , LiNbO <sub>3</sub> and NiO indicated. ....	237
Fig. 5.25: Schematic of the experiment conducted to measure dynamic harmonic generation. a) Side view of the sample with nonlinear SiN <sub>x</sub> core (NL) and electrically driven ECD. b) Top view with off-set contacts. Fundamental NIR mode is indicated as red arrow, SH signal is indicated as blue arrow.....	238
Fig. 5.26: SH power measured as a function of pump laser power (P <sub>p</sub> ) and waveguide length. (a) For C = 0 mC/cm <sup>2</sup> intercalated charge and (b) for C = 16 mC/cm <sup>2</sup> intercalated charge (i.e., lithiation).....	239
Fig. 5.27: (a) SHG conversion efficiency at C = 0 mC/cm <sup>2</sup> intercalated charge as a function of waveguide length. Note that the SH power is divided by the waveguide length to emphasize the maximum achievable conversion efficiency. (b) SH power over time for a l = 1 mm long SHWG.....	241
Fig. 5.28: SH spectra measured for SHWG having d = 350 nm spacer thickness and l = 1 mm length as a function of lithiation.....	242
Fig. 5.29: Normalized SH spectra for SHWG as a function of lithiation. (a) For l = 0.25 mm SHWG length and (b) for l = 0.5 mm SHWG length.....	243
Fig. 5.30: Influence of SHWG width on SH spectrum and power. (a) SH spectra of SHWGs having different widths. (b) SH power as a function of SHWG width. ....	245
Fig. 5.31: Experimental results for SH wavelength shift as a function of lithiation. (a) Experimentally measured SH wavelength shift in comparison to that from the FDTD simulation. (b) Current flow direction dependence of the induced SH wavelength shift. ....	247
Fig. 5.32: CV analysis of SHWG at v = 25 mV/s sweep rate. (a) SH wavelength at peak intensity, as well as transmitted FE optical intensity as a function of voltage. (b) The corresponding CV curve at a sweep rate of 25 mV/s. ....	249
Fig. 5.33: EC behavior of the SHWG over time. (a) SH wavelength at peak intensity depicted as a function of the CV cycles. (b) SH wavelength non-volatile bistability of SHWG after abruptly turning off the applied voltage and measuring the SH signal over time.....	250
Fig. 5.34: Switching dynamics of the SHWG transmission and SH wavelength. The applied voltage is alternated between V = - 2 V and V = 1 V. ....	251

Fig. 5.35: SHWG performance with 1 M LiClO<sub>4</sub> liquid electrolyte. SH wavelength (blue) and NIR FE transmittance as a function of the intercalated charge..... 253

# List of Fundamental Constants and Abbreviations

## Fundamental Constants

$\mu_0 = 4\pi \times 10^{-7} \text{ H/m}$	Permeability of Free Space
$\epsilon_0 = 8.854 \times 10^{-12} \text{ F/m}$	Permittivity of Free Space
$c = 3 \times 10^8 \text{ m/s}$	Speed of Light
$m_e = 9.1 \times 10^{-31} \text{ kg}$	Mass of an Electron
$q = -e = 1.602 \times 10^{-19} \text{ C}$	Elementary Charge
$R = 8.314 \text{ J/Kmol}$	Ideal Gas Constant
$N_A = 6.022 \times 10^{23} \text{ mol}^{-1}$	Avogadro Constant
$\hbar = 1.055 \times 10^{-34} \text{ Js}$	Reduced Planck Constant
$k_B = 1.38 \times 10^{-23} \text{ J/K}$	Boltzmann Constant
$F = 96\,485.3 \text{ As/mol}$	Faraday Constant

## Abbreviations and Symbols

1D	One Dimensional
2D	Two Dimensional
3D	Three Dimensional
$\alpha$	Absorption Coefficient
$\alpha_p$	Polarizability
AC	Areal Capacitance
$\beta$	Plasmon Wavevector
$\Gamma$	Electrochemical Reversibility Factor
$\gamma$	Damping Coefficient
C	Inserted Charge
$c_x$	Concentration of Species X
CE	Counter Electrode
$CE_{cc}$	Electrochromic Coloration Efficiency
CV	Cyclic Voltammetry
d	Diameter
$d_t$	Thickness

D	Diffusion Coefficient
$\epsilon$	Permittivity
$\epsilon_r$	Relative Permittivity
EC	Electrochromic
ECD	Electrochromic Device
$E_{O,R}$	Redoxpotential
f	Frequency
$f_0$	Resonance Frequency
FP	Fabry-Perot
k	Wavevector
$k_{ex}$	Extinction Coefficient
$k_{an,cath}$	Reaction rate
$k_0$	Wavevector in Vacuum
l	Length
LSP	Localized Surface Plasmon
$\lambda$	Wavelength in a Dielectric Medium
$\lambda_0$	Wavelength in Free Space
$\mu$	Permeability
$\mu_r$	Relative Permeability
$\dot{m}$	Mass Flow
n	Refractive Index
$n_{eff}$	Effective Refractive Index
$n_e$	Charge Density
N	Free Electron Density
NIR	Near Infrared
$\Phi$	Potential
Q	Charge
q	Elemental Charge
$\sigma$	Conductivity
$\varsigma$	Rate Constant
r	Radius
$\dot{r}$	Deposition Rate
SC	Specific Capacitance
SEI	Solid Electrolyte Interface
$\tau_{b,c}$	Bleaching or Coloration Time
$\tau_e$	Electron Recombination Time
$\Delta T$	Optical Transmission Modulation
T	Transmittance

$T_{\text{Ox,Red}}$	Transmission in the Oxidized or Reduced State
TMO	Transition Metal Oxide
UV	Ultraviolet
$v$	Voltage Sweep Rate
V	Voltage
$V_{\text{OC}}$	Open Circuit Voltage
Vis	Visible
$\omega$	Radian Frequency
$\omega_{\text{P}}$	Plasma Frequency
$\omega_{\text{SP}}$	Surface Plasmon Frequency
ZIB	Zinc Ion Battery

# Chapter 1

## Introduction

Electrochromism is a phenomenon that describes the distinct change in a material's optical properties upon insertion or removal of ions through the application of an electrical bias. The electrochromic (EC) effect changes the optical absorption characteristics of the material across the UV, visible and near-infrared (NIR) spectrum through oxidation or reduction of the respective material. Hence, color change can occur between two colored states or render a colorless, transparent material to become light absorbent.<sup>1-3</sup> According to the direction of the color change (i.e., oxidation or reduction), materials are classified as either anodic or cathodic EC materials, or in the case of two-colored states, as polyelectrochromic material.<sup>4,5</sup>

Table 1: A list of transition metals and their respective colors in their reduced and oxidized forms.

<b>Transition Metal</b>	<b>Oxidized color</b>	<b>Reduced color</b>
Vanadium	Brownish yellow	Pale blue
Tungsten	Pale yellow	Blue
Nickel	Brown/black	Colorless
Molybdenum	Colorless	Blue-black

Often, the EC effect has been utilized to control light transmission for smart window applications.<sup>6-8</sup> However, the large bandwidth of the EC effect allows applications in the NIR and mid infrared (MIR). Polymer-based EC materials, such as polyaniline (PANI) and poly(3,4-ethylenedioxythiophene) polystyrene sulfonate (PEDOT:PSS) can act as near UV light modulation materials,<sup>9</sup> while most EC oxides and polymers cover the visible part of the electromagnetic (EM) spectrum.<sup>10,11</sup> In the NIR and MIR applications, often, nanostructured EC oxides or highly conductive nanoparticles on indium tin oxide (ITO) are employed.<sup>12,13</sup>

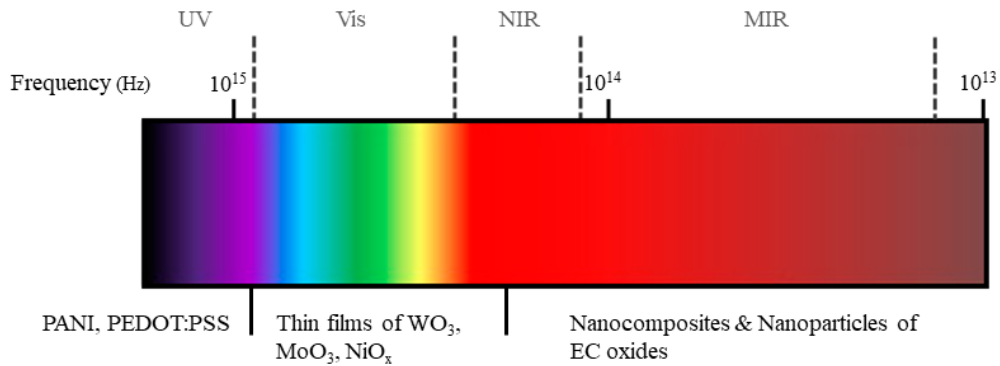


Fig. 1.1: Typical EC materials arranged according to the spectrum of their light interaction.

EC materials based on transition metal oxides (e.g.,  $\text{WO}_3$ ,  $\text{MoO}_3$ ,  $\text{NiO}$ ,  $\text{V}_2\text{O}_5$ ,  $\text{TiO}_2$ ,  $\text{Ta}_2\text{O}_5$ ...) display higher chemical and thermal stabilities, and hence, longer lifetimes than their organic counterparts. On the other hand, polymer-based EC materials exhibit higher color contrast and faster switching times. Due to their

compatibility with common nanofabrication standards, EC oxides are chosen for the devices investigated in this thesis.

In the following sections, an up-to-date review of the most important “conventional” EC devices (ECD) and their applications is provided. First, the metrics necessary to compare ECDs are introduced (Section 1.2). As EC supercapacitors and batteries have gained tremendous traction, EC energy storage devices are investigated and reviewed. Furthermore, a comprehensive analysis of nanophotonic and nanoplasmonic incorporation of the EC phenomena in nanoscale devices is laid out in Section 1.4. Finally, this introductory chapter introduces the thesis’ objectives and structure.

## 1.1 EC Devices

Discovered in the early 19<sup>th</sup> century, the EC effect and its associated color change in W bronzes and oxides through chemical means, was investigated and later proposed as a potential mechanism for “information displays”.<sup>10,14</sup> Today, a multitude of EC materials are finding a wide range of applications, such as light and heat management,<sup>1,13,15–21</sup> novel ion and gas sensors,<sup>22–28</sup> and even in photonic and plasmonic devices.<sup>13,29–36</sup> As the most prominent EC oxide, tungsten oxide ( $\text{WO}_3$ ) exhibits reversible change of its refractive index ( $\Delta n_{632\text{nm}} = 0.4$ ) and extinction coefficient ( $\Delta k_{\text{ex},632\text{nm}} = 0.55$ ) upon intercalation of  $\text{H}^+$ ,  $\text{Li}^+$ ,  $\text{Zn}^{2+}$ ,  $\text{Al}^{3+}$  and other multivalent ionic species. Similar changes of the refractive index and extinction can be found in PANI, NiO and other EC oxides, such as  $\text{MoO}_3$ ,  $\text{Mn}_2\text{O}_3$  and  $\text{TiO}_2$ . The conventional applications for the EC materials, which are light

transmission and heat modulation, have been appended by high-capacity energy storage. As such offering a new class of ECDs with dual functionality for smart windows, displays, and wearable electronics. On the other hand, the change in refractive index, that is inherent with the change in extinction for  $\text{WO}_3$ , bears the promise of integration in a new class of nanoscale, active photonic and plasmonic devices. On the fundamental level, direct control over the refractive index and the extinction coefficient of an EC material allow to change the properties of otherwise static devices, such as windows, photonic waveguides, and resonant cavities as well as plasmonic nanostructures.

The basic EC device (ECD) platform is an electrochemical cell consisting of two electrical contacts. When the ECD is employed as a smart window these contact electrodes are usually transparent conductive oxides (TCO); however, they can also be any metallic film that provides strong enough adhesion for the functional EC layers. In a conventional EC smart window, the cathodic EC layer is complimented by an anodic ion storage layer (which can be an EC material itself). The two functional electrodes are connected by an ion conductor (IC) or an electrolyte, which can either be in a liquid, or a polymer or a solid form. Notably, the EC material can be either a polymer or an oxide or a combination of both. The two key types of ECD operation involve light transmission/absorption modes, where both electrodes are transparent, or as a reflection mode, where the bottom electrode is comprised of a highly reflective metal film acting as a mirror. Since device performance is dependent on many of factors involving all the five individual layers of the ECD (Fig. 1.2), designing an efficient and a viable ECD

requires an iterative search process in finding the optimal combination of such material parameters.

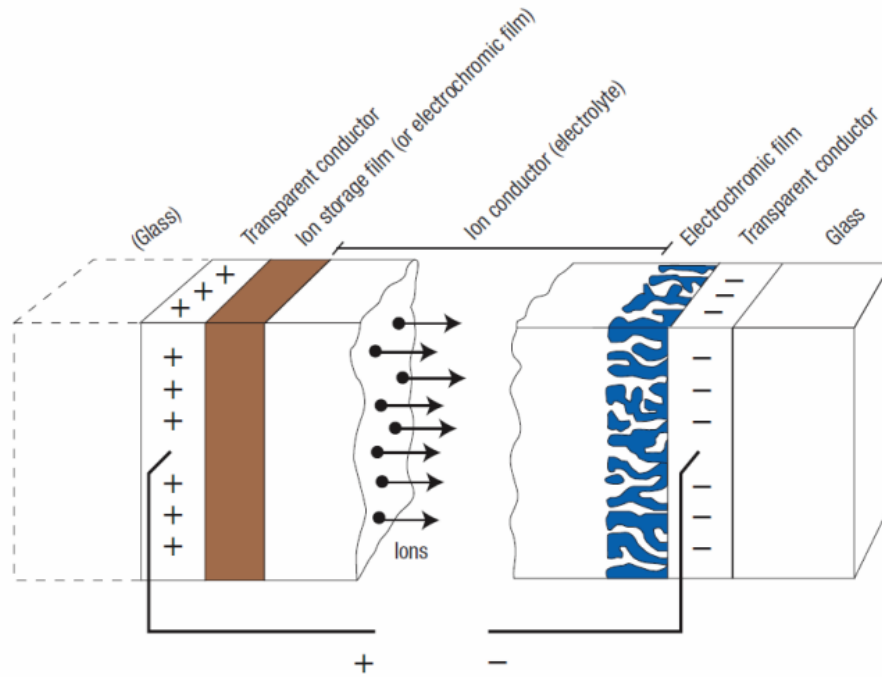


Fig. 1.2: Schematic of an exemplary EC smart window based on ion intercalation. Here, the ion storage layer consists of an active material, such as zinc or aluminum or a complementary EC material.<sup>14</sup>

Electrodes for ECDs must possess key properties. In a micro- and nanofabricated ECD, electrodes having high electrical conductivity are required to reduce the series resistance of the device, thus enhancing the electrical power consumption efficiency. Furthermore, the electrodes must adhere well to the EC material and exhibit high electrochemical stability to withstand irreversible processes occurring through reaction with the active components of the ECD. Typically, in EC smart windows, transparent conductors, such as indium doped tin

oxide (ITO), fluorine doped tin oxide (FTO) or aluminum doped zinc oxide (AZO), silver nanowire films and Graphene are employed as conductive films on transparent substrates, such as glass or plastics. These inorganic thin films provide both the strong adhesion and the high electrical conductivity necessary for effective device operation but nonetheless suffer from high rigidity. The brittle nature of the conductive oxides led to increased efforts in the use of more flexible conductive materials, such as organic compounds (e.g., PEDOT:PSS)<sup>37</sup> and metal grids (e.g., silver nanowires)<sup>38,39</sup>. Reflective ECDs and nanoscale architectures employ highly reflective (i.e., mirror-like) metal electrodes. While inherently highly conductive, noble metals, such as platinum (Pt) or gold (Au) do not provide sufficient adhesion for a transition metal oxide (TMO) material, so that adhesion promoters, such as tungsten (W) or chromium (Cr) are necessary. It is also crucial that the metallic electrodes must be electrochemically inert as to not oxidize during EC operation of the device. For this reason, aluminum (Al), titanium (Ti) and silver (Ag) are rarely used.

## 1.2 EC Performance Metrics

While the two most important metrics in an EC material or an ECD is its color change and contrast, there are several defining factors to quantify the operation characteristics of ECDs. Other performance parameters, such as the switching speed and electrical power utilization efficiency are important, but generally are less critical metrics. All of these performance metrics are by no means standardized but are rather comparison metrics inferred from the published literature in this field.

## 1.2.1 Optical Contrast

Typically, the optical contrast,  $\Delta T$  (%), of an EC material is defined as the percentage change in light transmission between oxidized and reduced state of the EC material, accordingly:

$$\Delta T (\%) = T_{\text{Ox}}(\%) - T_{\text{Red}}(\%) \quad (1.1)$$

For this purpose, the absolute change of light transmission is measured at either the wavelength of maximum absorbance or often at the specific wavelength of the HeNe laser (i.e.,  $\lambda = 632 \text{ nm}$ ).

However, advanced ECDs expressing ultra-high transmission modulation (i.e., ultrahigh optical contrast reaching several orders of magnitude), such as those discussed in this thesis, necessitate the use of the change of optical transmission in absolute units. The optical transmission modulation is defined as:

$$\Delta T = \frac{T_{\text{Ox}}}{T_{\text{Red}}} \quad (1.2)$$

## 1.2.2 Switching Times

The EC switching time is defined as the time it takes the ECD to switch the EC material from one redox state to another other. Since here are two distinct time scales (i.e., coloration time and bleaching time) involved in the EC light switching process, it is essential to define them independently. Here, the coloration time,  $\tau_c$ , is defined as the time it takes for the EC material to transition from the transparent to the absorbent state, while the bleaching time,  $\tau_b$ , describes the reverse process.

Most commonly, the switching time is calculated at the point at which the EC material achieves 90% of its full switching cycle. Other commonly used values are 75% or 95%.<sup>4,40</sup>

### 1.2.3 Coloration Efficiency

The coloration efficiency ( $CE_{ec}$ ) relates the optical contrast of an EC material to the intercalated charge per unit area:

$$CE_{ec} = \frac{\log(T_{Ox}/T_{Red})}{Q/A} \quad (1.3)$$

Where  $Q$ , is the intercalated charge in Coulomb and  $A$  is the area of the charge intercalation region in units of  $cm^2$ . The coloration efficiency is used as a measure of the charge efficiency of the EC coloration effect. Especially in applications such as smart windows, high  $CE_{ec}$  values are desirable since they infer a superior energy efficiency.

### 1.2.4 Cycle Life

For applications of EC materials in smart windows and photonic devices, EC material longevity is critical. The electrochemical stability is assessed by artificially aging the ECDs through repeated redox cycling. Irreversible effects, such as ion trapping, or material detachment can lead to degradation of the ECD over time. Notably, there is no benchmark aging time that is commonly used for device testing. Mostly, lifetimes for ECDs are reported in multiples of 1000 redox cycles.

### 1.2.5 Charge Capacity

Charge capacity measurements are dependent on the type of device under test. Since the stored charge is dependent on the applied voltage, in capacitor type ECDs, the charge capacity is given as the areal (AC) normalized to the EC electrode area or as a specific capacitance (SC) in Farad per weight of the EC material:

$$AC \left[ \text{mF}/\text{cm}^2 \right] \text{ or } SC [\text{F}/\text{g}] \quad (1.4)$$

Alternatively, for a battery type device, its performance on the other hand is related to the charge stored through application of a constant current and hence related to the amount of current in time (i.e. mAh). As such, the charge capacity is defined as:

$$AC \left[ \text{mAh}/\text{m}^2 \right] \text{ or } SC [\text{mAh}/\text{g}]. \quad (1.5)$$

### 1.2.6 Electrochemical Reversibility

Intercalation and deintercalation into an EC material occur through ionic current flows. The amount of the transferred charge; however, is not necessarily identical in both directions. An unbalanced redox process indicates irreversible intercalation of ionic species into the host material or detachment of the EC material into the electrolyte solution. As a measure of reversibility, the anodic and cathodic charge can be compared and related to each through:

$$\Gamma = \frac{Q_{\text{int}}}{Q_{\text{deint}}} \quad (1.6)$$

Here,  $Q_{\text{int}}$  and  $Q_{\text{deint}}$  are the transferred charge during intercalation and deintercalation processes, respectively. Both  $Q_{\text{int}}$  and  $Q_{\text{deint}}$  are obtained through cyclic voltammetry (CV) measurements by integrating over time the anodic and cathodic part of the CV curve.

### 1.2.7 CIE Color Code

A major driving force for the investigation of novel and advanced ECDs is the ability to create dynamic full-color displays with such a technology. Unfortunately, color is a rather difficult metric to compare, which is why the CIE color space is used to evaluate the modulation of EC color displays. The CIE color space relates values of X, Y, Z coordinates to the spectral sensitivity of human eye cone cells. The XYZ coordinates for the lightest light is called the color space's white point. The XYZ coordinates for the reddest possible red, greenest possible green and bluest possible blue are called the color space's red, green, and blue primaries. While the long (L), medium (M), and short (S) (i.e. L, M, S) are the three kinds of cone cells having the sensitivities in the short (S, 420 nm – 440 nm), middle (M, 530 nm – 540 nm) and long (L, 560 nm – 580 nm) wavelength range. Obviously, these curves present averages, since all eyes' sensitivity is different. Nonetheless, with the luminance Y, X a mix of L, M and S and Z representing solely short wavelengths, the CIE color space is represented as:

$$\begin{bmatrix} X \\ Y \\ Z \end{bmatrix} = \begin{bmatrix} 1.91020 & -1.11212 & 0.20191 \\ 0.37095 & 0.62905 & 0 \\ 0 & 0 & 1 \end{bmatrix} \begin{bmatrix} L \\ M \\ S \end{bmatrix} \quad (1.7)$$

## 1.3 EC Energy Storage Devices

Reversible ionic intercalation into a host material occurs through application of an external electrical bias, which leads to an ionic current flow in the ECD. Through intercalation of this current, electrical energy can be transformed and stored in the form of electrochemical potential, while simultaneously empowering chromatic changes in the involved materials. Hence, EC energy storage devices aim to combine high chromatic contrast or color change and exceptional charge capacity. Two types of EC energy storage devices are prevalent to date: supercapacitors and more recently batteries. Generally, supercapacitors exhibit higher power densities and faster charge/discharge while batteries provide the higher energy density. The fundamental difference between these two device designs is the type of counter electrode employed in each type of the device. While supercapacitors include an ion storage layer or EC counter electrode without an inherent standard potential, battery type devices include electrochemically active metal electrodes, such as zinc or aluminum.

### 1.3.1 EC Supercapacitors

The first EC supercapacitor device based on a NiO electrode, and a Ta<sub>2</sub>O<sub>5</sub> proton conduction layer was introduced by Deb *et al.* in 2005.<sup>41</sup> The device achieved a specific capacitance of 50 F/g with over 80% light transmission modulation at 632 nm wavelength. Nonetheless, the coloration efficiency of CE<sub>ec</sub> = 19 cm<sup>2</sup>/C was low and was owed to the parasitic currents. Since then, NiO electrodes prepared from sol-gel methods achieved higher specific capacitance up to 1386 F/g (i.e., in 1 M KOH electrolyte). The sol-gel prepared NiO nanoparticle

electrode achieves 63% light transmission modulation at 550 nm wavelength with  $CE_{cc} = 42.8 \text{ cm}^2/\text{C}$ . Coloration efficiency for NiO nanoflake based supercapacitors with a carbon cloth counter electrode exhibited  $CE_{cc} = 63.2 \text{ cm}^2/\text{C}$  with switching times  $\tau_c = 2.7 \text{ s}$  and  $\tau_b = 1.8 \text{ s}$  and an optical transmission modulation of 40%.<sup>42</sup>

$\text{WO}_3$  based supercapacitors have been reported to have an optical transmission modulation of  $\Delta T = 76\%$  and a high specific capacitance of  $SC = 639 \text{ F/g}$ . The  $\text{WO}_3$  nanoparticle film deposited on a FTO substrate achieved a coloration state in  $\tau_c = 3.1 \text{ s}$  and a bleaching state in  $\tau_b = 0.9 \text{ s}$ . Remarkably, such devices exhibit 95% charge capacity retention over 5000 switching cycles.<sup>43</sup> Combined with a stretchable Ag nanowire/PEDOT:PSS electrode, electrodeposited  $\text{WO}_3$  supercapacitors have achieved coloration efficiencies  $CE_{cc} = 124 \text{ cm}^2/\text{C}$  and an optical transmission modulation of  $\Delta T = 81.9\%$  at a wavelength  $\lambda = 632 \text{ nm}$ .<sup>44</sup> A flexible  $\text{WO}_3$  supercapacitor having a high areal charge capacity  $AC = 13.6 \text{ mF/cm}^2$  reached 90% optical transmission modulation in  $\tau_c = 1.7 \text{ s}$  and  $\tau_b = 1 \text{ s}$ , respectively.<sup>39</sup> Coloration efficiencies for  $\text{WO}_3$  supercapacitors of up to  $CE_{cc} = 140 \text{ cm}^2/\text{C}$  have been shown recently.<sup>45</sup> The specific device performance parameters are summarized in Table 2.

In addition to  $\text{WO}_3$  and NiO, several other EC materials, such as  $\text{V}_2\text{O}_5$ , PB or  $\text{MnO}_2$  are employed to either enhance the charge capacity or improve electrochemical stability.<sup>46,47</sup> Another approach to boost the charge capacity and coloration performance of  $\text{WO}_3$  based supercapacitors has been the doping with  $\text{MoO}_3$  colloids.<sup>48</sup>

Table 2: Performance parameter for selected EC supercapacitors.

Electrode	AC [mF/cm <sup>2</sup> ] or SC [F/g]	$\Delta T$ (%)	CE <sub>ec</sub> [cm <sup>2</sup> /C]	$\tau_c$ and $\tau_b$ [s]	Ref.
NiO	50/SC	80	19		49
NiO	74.8/AC	40	63.2	2.7, 1.8	42
WO <sub>3</sub>	639/SC	76	54.8	3.1, 0.9	43
WO <sub>3</sub>	221/SC	81.9	124	1.9, 2.8	44
WO <sub>3</sub>	13.6/AC	90	80.2	1.7, 1	39
WO <sub>3</sub>	23.4/AC	63	140	3.5, 4.9	45

### 1.3.2 EC Batteries

In batteries, WO<sub>3</sub> dominates as the EC material of choice due to its compatibility with several conventional ionic species in battery type devices, such as Zn<sup>2+</sup>, Al<sup>3+</sup> and Li<sup>+</sup>. EC batteries based on electrodeposited WO<sub>3</sub> with a Zn counter electrode have shown SC = 185.6 mAh/g specific capacity with V<sub>OC</sub> = 1.15 V open circuit voltage in a mixed Zn<sup>2+</sup>/Al<sup>3+</sup> electrolyte. The optical transmission modulation for such a device exceeded  $\Delta T = 88\%$  at  $\lambda = 652$  nm.<sup>50</sup> In a pure Al<sup>3+</sup> containing electrolyte, hydrothermally grown W<sub>18</sub>O<sub>49</sub> nanowires incorporated into an Al battery provide a V<sub>OC</sub> = 1.2 V and up to SC = 429 mAh/g charge capacity. The optical transmission modulation for this device was  $\Delta T = 50\%$  at  $\lambda = 652$  nm.<sup>51</sup> The significant battery parameters are summarized in Table 3. Notably, the introduced battery type ECDs all employ liquid, aqueous electrolytes, which hinders actual device integration.

Table 3: EC batteries based on WO<sub>3</sub> and their performance metrics

<b>Electrode</b>	<b>SC [mAh/g]</b>	<b><math>\Delta T</math> [%]</b>	<b>V<sub>oc</sub> [V]</b>	<b>Electrolyte</b>	<b>Ref.</b>
WO <sub>3</sub>	185.6/SC	88	1.15	Zn <sup>2+</sup> /Al <sup>3+</sup>	50
WO <sub>3</sub>	429/SC	50	1.2	Al <sup>3+</sup>	51

## 1.4 Active Nanophotonic and Nanoplasmonic ECDs

The change in dielectric properties of EC oxides and polymers is conventionally utilized in EC smart windows and other planar devices for heat and light modulation. When integrated in nanoscale devices, the EC effect can be enhanced through exploitation of plasmonic and photonic resonances as well as miniaturization effects. Such advanced ECDs have shown tremendous potential for color printing applications and ultra-high transmission modulation electrochemical photonic devices. In the following section, common phenomena that are employed in advanced ECDs are summarized.

### 1.4.1 EC Plasmonic Color Printing and Display Devices

Plasmonic devices and nanostructures have long been investigated for color printing and display applications.<sup>52,53</sup> However, the resonance wavelength of the excited plasmon is fixed by the dimensions of the plasmonic structure and the materials involved. The active control over the complex refractive index of WO<sub>3</sub> and other EC materials can change the dielectric environment of such plasmonic devices and structures to achieve a dynamic light modulation effect. For plasmonic

nanoparticles the localized surface plasmon resonance (LSPR) is directly dependent on the density of free surface electrons. Simplified through the Drude model, the free electron density  $N$  is related to the dielectric function,  $\epsilon(\omega)$ , as follows:

$$\epsilon(\omega) = \epsilon_{\infty} - \frac{\omega_p^2}{\omega^2 + i\gamma\omega} \quad (1.8)$$

Where  $\gamma$  is the damping constant of the electron oscillation,  $\epsilon_{\infty}$  the dielectric constant of the bulk material and  $\omega_p$  the plasma frequency, which is directly proportional to the free electron density  $N$ :

$$\omega_p = \left( \frac{Ne^2}{m^* \epsilon_0} \right)^{1/2} \quad (1.9)$$

Here,  $e$  is the elemental charge of an electron and  $m^*$  its effective mass and  $\epsilon_0$  is the dielectric permittivity of the vacuum. For a spherical plasmonic nanostructure, the static polarizability,  $\alpha_{\text{sph}}$ , can be formulated as:

$$\alpha_{\text{sph}} = 4\pi r^3 \frac{\epsilon(\omega) - \epsilon_{\text{med}}}{2\epsilon(\omega) + \epsilon_{\text{med}}} \quad (1.10)$$

Where  $r$  is the particle radius and  $\epsilon_{\text{med}}$  the permittivity of the surrounding medium. Resonance is achieved when the denominator tends towards zero. Hence, the properties and features of the LSPR can be directly influenced by its dielectric environment. Such a change can be induced through EC materials and exploited for dynamic color change of the LSPR in measurement and display applications.

The first mention of polymer coated plasmonic nanostructures for active plasmonic devices was reported in 2005 by Leroux *et al.*<sup>54</sup> Plasmonic nanodisk arrays having 150 nm diameter and 40 nm height in several different periodicities, were fabricated through electron beam lithography, with a plasmon resonance in air at  $\lambda_{\text{LSP}} = 597$  nm for  $\Delta_x = \Delta_y = 220$  nm grating period. When coated with polyaniline (PANI), the resonance shifts to  $\lambda_{\text{LSP}} = 633$  nm due to the increased dielectric permittivity of the environment (Fig. 1.3(a)). During redox cycling of the PANI coating, the resonance shifts to  $\lambda_{\text{LSP}} = 571$  nm in less than  $t < 10$  s. Furthermore, quenching of LSPR was observed for asymmetrical grating periods when the grid is excited with a polarization along the shorter dimension. Based on a similar Au nanoparticle array, Leroux *et al.* were able to show not only up to  $\Delta\lambda = 32$  nm wavelength shift via redox cycling of the PANI coating, but also a simultaneous increase in optical density of the device from  $\text{OD} = 0.08$  to  $\text{OD} = 0.34$ .<sup>55</sup> Such a multifunctional EC plasmonic device could serve as an optical switch for color and transmission modulation. In a similar approach based on lithography, Stockhausen *et al.* employed poly(3,4-ethylenedioxythiophene) (PEDOT) as the conductive polymer modulation layer.<sup>56</sup> Due to the higher change in dielectric properties of the real part of the permittivity at values below  $\epsilon' < 1$ , the change in resonance wavelength reaches up to  $\Delta\lambda = 180$  nm from approximately  $\lambda_{\text{LSP}} = 720$  nm to  $\lambda_{\text{LSP}} = 900$  nm (Fig. 1.3(b)). Notably, this study found that  $\Delta\lambda$  increases when  $\lambda_{\text{LSP}}$  goes to higher wavelengths.

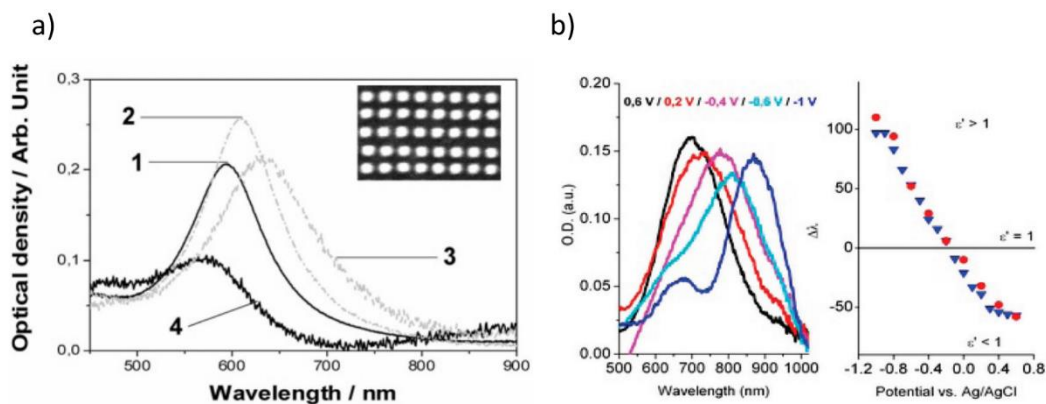


Fig. 1.3: Performance of active gold nanostructure arrays coated with conductive polymers. (a) LSPR of PANI coated Au nanostructures in 1 air, 2 water, 3 PANI reduced and 4 PANI oxidized. (b) Plasmonic extinction and wavelength shift for PEDOT coated Au array as a function of applied voltage.<sup>54,56</sup>

Wang *et al.* were the first to report  $\text{WO}_3$  sol-gel modified plasmonic Ag nanoparticle arrays exhibiting a strong shift in the wavelength of maximum extinction coefficient upon EC cycling of the electrochromic material.<sup>57</sup> The colloidal Ag nanoparticles, as well as the sol-gel modification process, promise ease of fabrication and higher scalability. Fig. 1.4(a) presents an SEM image of the investigated Ag nanoparticles having an average diameter of 100 nm. Correspondingly, a plasmonic extinction resonance at 431 nm is observed when a dip of EC material is casted on ITO.

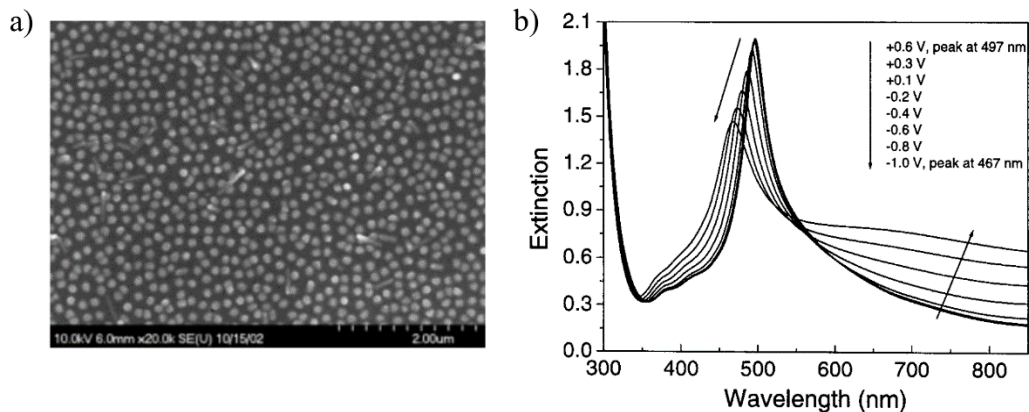


Fig. 1.4: Sol-gel modified Ag nanoparticles with a  $\text{WO}_3$  modulation layer. (a) SEM image of the colloidal silver particles. (b) Voltage-dependent extinction spectra for the modified Ag nanoparticle samples.<sup>57</sup>

As depicted in Fig. 1.4(b), when coated with the  $\text{WO}_3$  solution, the plasmonic resonance shifts to 498 nm wavelength. Cycling of the plasmonic nanoparticle array in 1 M  $\text{LiClO}_4$  in propylene carbonate (PC), leads to a decrease in the maximum extinction from  $k_{\text{ex}} = 1.95$  for the fully oxidized/bleached  $\text{WO}_3$  film to  $k_{\text{ex}} = 1.5$  for full reduction of the film. Simultaneously, the plasmonic resonance of the array shifts from 497 nm wavelength to 467 nm. Using polyaniline (PANI) coated Au nanorods having an average diameter,  $d = 52 \pm 3$  nm, and an average length,  $l = 111 \pm 6$  nm, Jiang *et al.* showed strong LSPR shifts through EC cycling. The coating of PANI shell on the individual Au nanorods was realized through surfactant-assisted chemical oxidative polymerization.<sup>58</sup> The polymerization process allows direct control over shell thickness and thus alters the EC properties of the plasmonic structure. The introduced nanorods exhibit wavelength shifts of  $\Delta\lambda = 100$  nm with resonance depth amplitude modulation of up to 10 dB. Finite

difference time domain (FDTD) simulations of the nanorod LSPR modulation suggest that wavelength modulation of up to  $\Delta\lambda = 130$  nm is feasible for such plasmonic nanorod array. Notably, such high dynamic light transmission modulation is achieved using PANI shell thickness  $d_t < 10$  nm. Here, switching speeds around  $\tau_{c,b} = 60$  s are realized. Such a colloidal Au nanorod technology further provides strong polarization dependence of the light scattered intensity.<sup>59</sup> Under the application of an alternating field at a frequency  $f = 1$  Hz, wavelength resonance switching occurs in less than 200 ms for PANI coated Au nanorods. Further investigation of the voltage-dependent behavior of Au nanorods in a custom measurement cell showed a shift in the resonance of PANI coated Au nanorods by  $\Delta\lambda = 11$  nm for an applied DC electric field of  $E = 10$  V/ $\mu$ m. A similar shift was observed for Barium Titanate (BTO) coatings, which indicates that nonlinear optical properties can be utilized in these kinds of devices as well. To overcome the limitations of Au nanorods and particles whose LSPR falls into the red and NIR spectral region, PANI coated Au nanocubes are employed.<sup>60</sup> These colloidal structures are grown in solution and can be spray coated onto different substrates. The PANI shell helps mitigate the detrimental effect of Au nanocube clustering and introduces a LSPR shift of up to  $\Delta\lambda = 30$  nm in the green spectral region.

While colloidal approaches to LSPR tuning show tremendous potential for sensor applications and potential control, the red and the NIR wavelength of nanorod and nanoparticle LSPRs necessitate more complex device design to cover the whole spectral region. Active EC light control over static, plasmonic devices has since been employed in various device architectures. Xu *et al.* employed the

EC polymer PolyProDot-Me<sub>2</sub> as a fast on-off switching layer for static plasmonic color arrays, achieving less than  $\tau_{c,b} = 25$  ms switching time for 80% light transmission modulation.<sup>61</sup> This application, however, makes solely the use of the change in extinction that is inherent during redox cycling of the material.

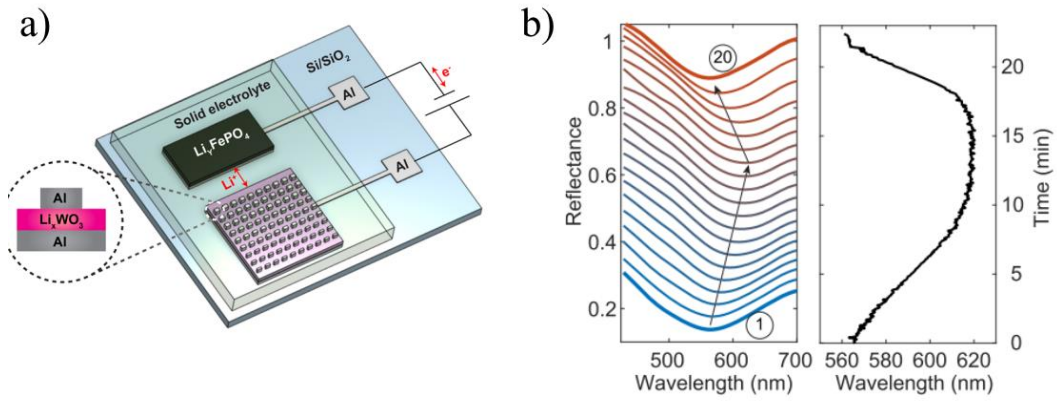


Fig. 1.5: Dynamic gap plasmon color printing device. (a) Schematic of the EC plasmonic nanodevice consisting of Al nanostructures and a solid PEO electrolyte. (b) Reflectance spectra (left) and wavelength of minimum reflection (right) taken cyclic voltammetry, showing a continuous wavelength shift.[62]

Li *et al.* introduced a plasmonic device consisting of a WO<sub>3</sub> modulation layer which allows for color switching and resonance modulation through EC cycling (Fig. 1.5 (a)).<sup>35</sup> The device incorporates Al electron beam lithography fabricated rectangular nano blocks having structure sizes ranging between 90 nm to 70 nm lengths and 50 nm to 30 nm widths with constant height of 30 nm. The solid polymer ion conductor consists of LiClO<sub>4</sub> dissolved in polyethylene oxide (PEO), while Li<sub>0.7</sub>FePO<sub>4</sub> acts as a source and sink for the Li<sup>+</sup> ions. The device exhibits a high dynamic wavelength shift range between  $\lambda_{\text{delith}} = 620$  nm and  $\lambda_{\text{lith}} =$

565 nm with up to  $r = 4.1$  nm/s modulation speed for the redshift and  $r = 1.8$  nm/s for the blue shift (Fig. 1.5(b)). Moreover, the rectangular design shape of the plasmonic scatterers leads to a strong dependence of the reflected spectrum on the polarization of the excitation source. Hence, for white light polarized along the long edge of the rectangle (i.e., along the length (L) side), the samples appear blueish in color, while they reflect an orange color when excited with a perpendicular light polarization. The EC nature of the modulation layer allows operation of this device between  $V = -2$  V for full lithiation and  $V = +1$  V for delithiation, as such creating a low working voltage window. Furthermore, once the external bias is turned off, the bistable nature of the EC effect allows the device to retain its state for tens of minutes.

In a colloidal approach to color printing with plasmonic nanostructures, Au nanoparticles are coated with EC PANI.<sup>33</sup> During oxidation of PANI, the plasmonic resonance of the 80 nm diameter Au nanoparticles on an Au mirror, shifts from the red color to yellowish green color (Fig. 1.6(a)). The high spectral bandwidth of the EC color change is owing its presence to the electromagnetic “hot spot” created between the plasmonic nanoparticle and the Au mirror surface. As shown in Fig. 1.6(b), the simulated field enhancement between the Au structures exceeds one order of magnitude. Simultaneously, FDTD simulations predict a shift of the reflectance spectra based on the scattering cross-section from  $\lambda_{\text{delith}} = 680$  nm to  $\lambda_{\text{lith}} = 590$  nm. Owing to the thin PANI shell, extinction losses are low. The experimentally captured dark-field images of the nanoplasmonic pixel device show a clear color change from red to green, with good homogeneity over an area of 1

$\mu\text{m}^2$  (Fig. 1.6(d)). Moreover, the plasmonic nanopixel device was shown to exhibit a video frequency (25 Hz) switching with electrochemical stability lasting for over 3 months. Along the same line, Lu *et al.* introduced PANI coated Au nanorods, where they extended the available colors for colloidal plasmonic displays into the blue spectral range, while at the same time achieving switching times as low as 5 ms.<sup>62</sup>

Zhang *et al.* introduced plasmonic resonance shifts in Au nanodisks fabricated through an anodic aluminum oxide (AAO) mask. This facile and scalable process leads to nanodisks exhibiting a plasmonic resonance at a wavelength of  $\lambda = 550$  nm.<sup>36</sup> After coating the nanodisk sample with PEDOT:PSS, the resonance shifts to  $\lambda_{\text{ox}} = 653$  nm in the oxidized state and  $\lambda_{\text{red}} = 718$  nm in the reduced state. Meanwhile, the reflectance reduces by only 5% from 53% to 48% during electrochemical cycling between  $\Delta V = \pm 1$  V. Furthermore, FDTD simulations show the shift in the plasmonic resonance caused by the oxidation of the PEDOT:PSS could accurately describe the wavelength shift and amplitude modulation of the LSPR. For a thin PEDOT:PSS layer of thickness of 27 nm, 95% color modulation could be achieved in less than  $t = 10$  s. A comparison of EC plasmonic resonance modulation approaches are presented in Table 4.

Table 4: Comparison of selected active EC plasmonic modulation technologies. Values for peak wavelength, wavelength shift and switching times are extracted from figures and graphs as they were not indicated in the referenced articles.

<b>Material</b>	<b>Approach</b>	<b>Wavelength (nm)</b>	<b>Wavelength Shift <math>\Delta\lambda</math> (nm)</b>	<b>Switching Time (s)</b>	<b>Ref.</b>
Au/PANI	Lithographic Disk Array	631	-62	< 10	54
Au/PEDOT	Lithographic Disk Array	720	+180	/	56
Ag/WO <sub>3</sub>	Colloidal Solution	498	-31	< 5 s	57
Au/PANI	Colloidal Nanorods	740	-100	< 240 s	58
Al/WO <sub>3</sub>	Lithographic Rectangle Array	620	-55	< 20 s	35
Au/PANI	Colloidal Spheres with a Mirror	680	-90	< 50 ms	33

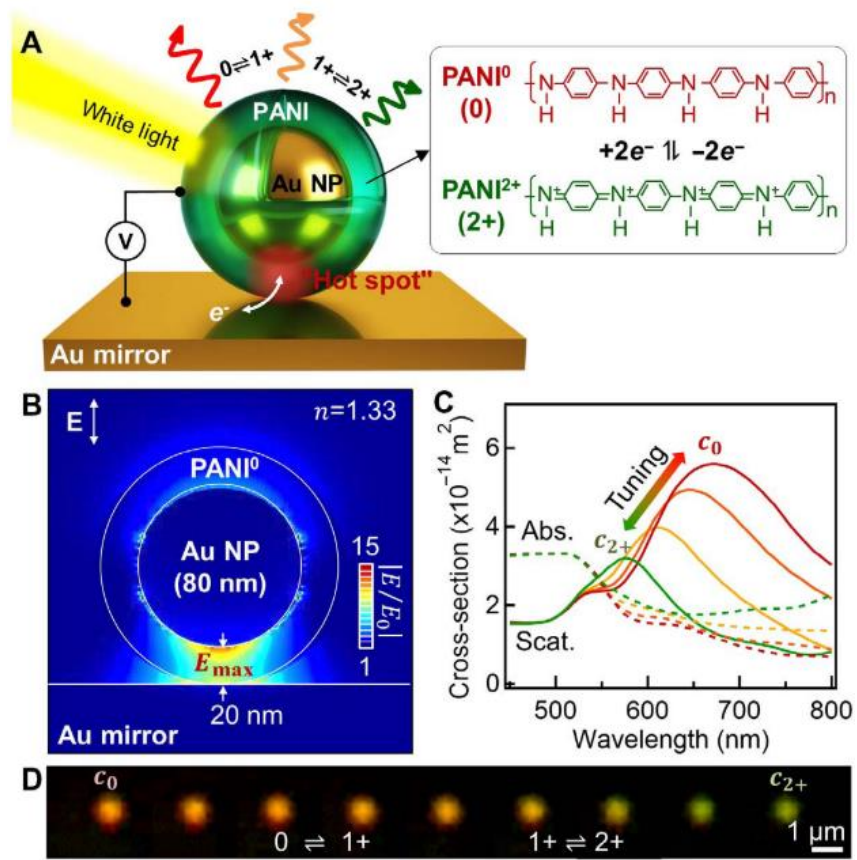


Fig. 1.6: Plasmonic nanopixels based on a PANI modulation layer. (a) Schematic of the proposed device. An 80 nm Au nanoparticle is coated in a 20 nm thick PANI shell and placed on an Au mirror, creating a plasmonic "hot spot" between the Au components. (b) FDTD simulation of the electric field distribution and (c) absorption and scattering spectra determined through the numerical approach. (d) Dark-field images of the nanopixel during electrochemical redox cycling.<sup>33</sup>

## 1.4.2 Active EC Cavity Devices

Fabry-Perot (F-P) resonators and nanocavities provide structural light colors based on the thickness and refractive index of the dielectric that fills the cavity. Under normal incidence, the resonance condition for a 2D thin film cavity of thickness  $t$  and a real refractive index of  $n_{\text{eff}}$ , is given by:

$$m \frac{\lambda}{n_{\text{eff}}} = 2d_t \quad (1.11)$$

Here,  $\lambda$  is the light wavelength, and  $m$  being an integer. In 2005, Kammler *et al.* were first to introduce the concept of utilizing EC materials in a cavity for active optics and photonics.<sup>63</sup> In this pioneering work, solid-state ECDs consisting of  $\text{WO}_3$  as the working electrode,  $\text{Ta}_2\text{O}_5$  as the ion conductor, and  $\text{NiO}$  as the ion storage layer are used in a Fabry-Perot 1D planar cavity to demonstrate light transmission wavelength modulation by  $\Delta\lambda = 2 \text{ nm}$ .<sup>64</sup> Surprisingly, this technology was not investigated further until 11 years later. Starting in 2016, static resonator reflections were used for EC modulated color imaging and printing. To create narrower resonance and higher chromaticity for cavity-based color printing devices, several works introduced a superstructure, consisting of a plasmonic nanohole array (NHA) as the top mirror of the cavity.<sup>65–67</sup> It was shown that the nanohole arrays create plasmonic resonances that spectrally overlap with the cavity reflection and therefore, act like spectral filters for the cavity.

To overcome the static nature of these metal-insulator-nanohole array (MIN) structures, Xiong *et al.* introduced several device design configurations utilizing

conjugated EC polymers for on-off switching. The reflection of the cavity is first determined through the thickness of a dielectric  $\text{Al}_2\text{O}_3$  layer placed between an Ag mirror and an Au NHA. The plasmonic NHA is then designed to achieve a spectral overlap by adjusting the period of the array.<sup>65</sup> Moreover, the plasmonic NHA exhibited insignificant change in the reflectivity for viewing angles between  $0^\circ$  and  $45^\circ$ . For EC based on-off switching, polypyrrole (PP) is first electropolymerized onto the Au NHA (Fig. 1.7(a)). The PP layer is then oxidized or reduced by applying a voltage between the NHA and a Pt counter electrode. In its oxidized state, PP is highly lossy, leading to the strong optical modulation over 25% in the blue region and up to 50% in the red spectral region (Fig. 1.7(b)). The highly chromatic blue, green and red color emitting cavities can be completely turned off.

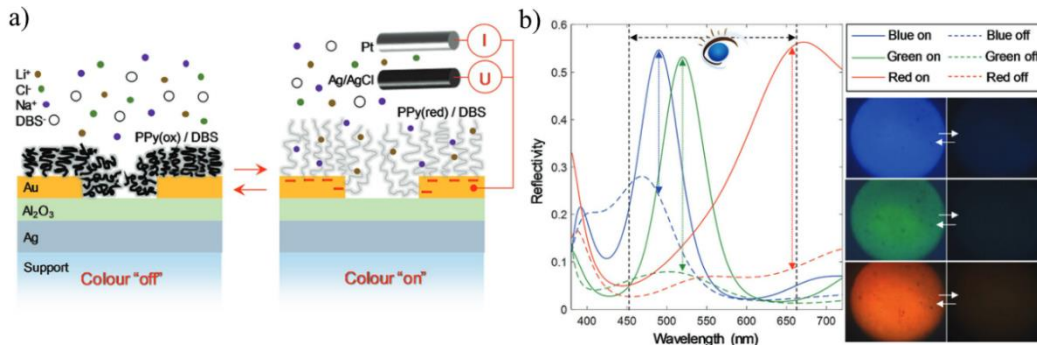


Fig. 1.7: EC switching of a MIN resonant cavity. (a) Schematic of the active MIN cavity with an Au NHA and polypyrrole as the EC modulation material. (b) Optical light modulation induced through EC cycling of PP under a viewing angle between  $0-14^\circ$ .<sup>68</sup>

Similarly, Xiong *et al.* reported on a MIN type resonant cavities consisting of a PEDOT:PSS switching layer integrated with a Cu plasmonic nanohole array. The

authors demonstrated a sub 1 s on-off switching times times.<sup>69</sup> A single switching operation of the cavity device required  $5.7 \text{ mJ/cm}^2$ , making the technology suitable for chromatic e-readers and plasmonic displays. In 2021 Gugole *et al.* published a comprehensive comparison of inorganic and organic switching materials for these kinds of static cavities.<sup>70</sup> Notably, their findings suggest that while organic EC switching materials, such as PEDOT:PSS and PProDOTMe<sub>2</sub> provide faster switching times ( $\tau_{c,b} < 1 \text{ s}$ ) and better electrochemical cycling stability ( $> 10^5$ ), other metrics, such as optical reflectance modulation and bistability drastically favor WO<sub>3</sub>. WO<sub>3</sub> based e-paper devices exhibit bistability over hours along with stability over 100s of electrochemical switching cycles. While both technologies have an advantage over conventional electrophoretic e-readers in terms of the achievable optical reflectance modulation and color range, they lack long term stability.

Following on the work introduced in this thesis (Section 4.3), several resonant cavity devices having an active dielectric were introduced. Wang *et al.* introduced WO<sub>3</sub> on W cavities for color tunable supercapacitor applications. Fig. 1.8(a) shows the reflectance spectra of selected WO<sub>3</sub> on W nanocavities as a function of the WO<sub>3</sub> thickness.<sup>32</sup> By increasing the thickness of the EC layer from 152 nm to 250 nm, all colors of the visible spectrum can be represented. Moreover, when redox cycling a 163 nm thick WO<sub>3</sub> on W Fabry-Perot resonator, the reflected color can be dynamically shifted from red to green as shown in Fig. 1.8(b). Employed as supercapacitors with two WO<sub>3</sub> based electrodes working in tandem, these cavity type color displays achieved high areal capacitance of up to  $AC = 23 \text{ mF/cm}^2$ ,

resulting in an energy density of  $1.13 \times 10^{-3}$  mWh/cm<sup>2</sup> for a charge current density of 0.05 mA/cm<sup>2</sup>. Simultaneously, the coloration efficiency reaches values as high as  $CE_{cc} = 149$  cm<sup>2</sup>/C.<sup>71</sup> The supercapacitor architecture retained over 92% of its capacitance when cycled 3000 times, thus, offering the possibility for color tunable EC energy storage devices.

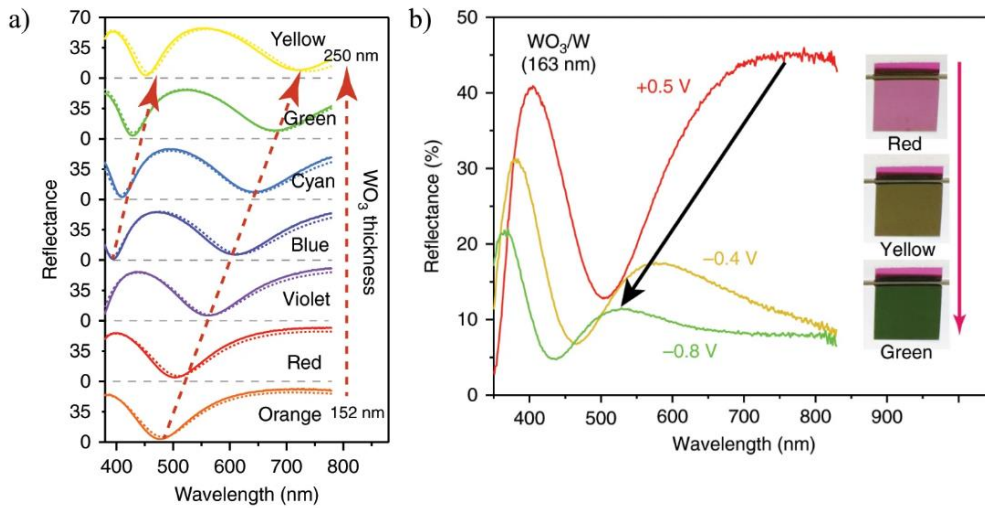


Fig. 1.8: WO<sub>3</sub> based resonant nanocavities for color generation. (a) Reflectance spectra for WO<sub>3</sub>/W nanocavities as a function of WO<sub>3</sub> layer thickness. (b) Dynamic reflectance of a 163 nm thick WO<sub>3</sub>/W cavity (in a 1 M LiClO<sub>4</sub> electrolyte) as a function of applied voltage.<sup>32</sup>

Chen *et al.* reported that thin ( $d_t = 4$  nm – 8 nm) metallic reflectors, such as W, Cu, Ag or Ti led to a significant difference in the reflectance from the backside of the device as compared to the film side (Fig. 1.9(a)). The devices consist of ITO on PET transparent electrodes with a PMMA gel electrolyte containing LiClO<sub>4</sub>. A thin layer of metal is deposited onto the EC electrode before deposition of 200 nm to 250 nm of WO<sub>3</sub>. This butterfly-like reflection asymmetry is strongly dependent on the material used for the thin metallic layer (e.g., W, Cu, Ag or Ti), since higher

refractive indices lead to a stronger phase shift between front and backside reflection. Similar to the work of Wang *et al.* the initial color of the device can be adjusted by the thickness of the  $\text{WO}_3$  and the ITO layers.<sup>32</sup>

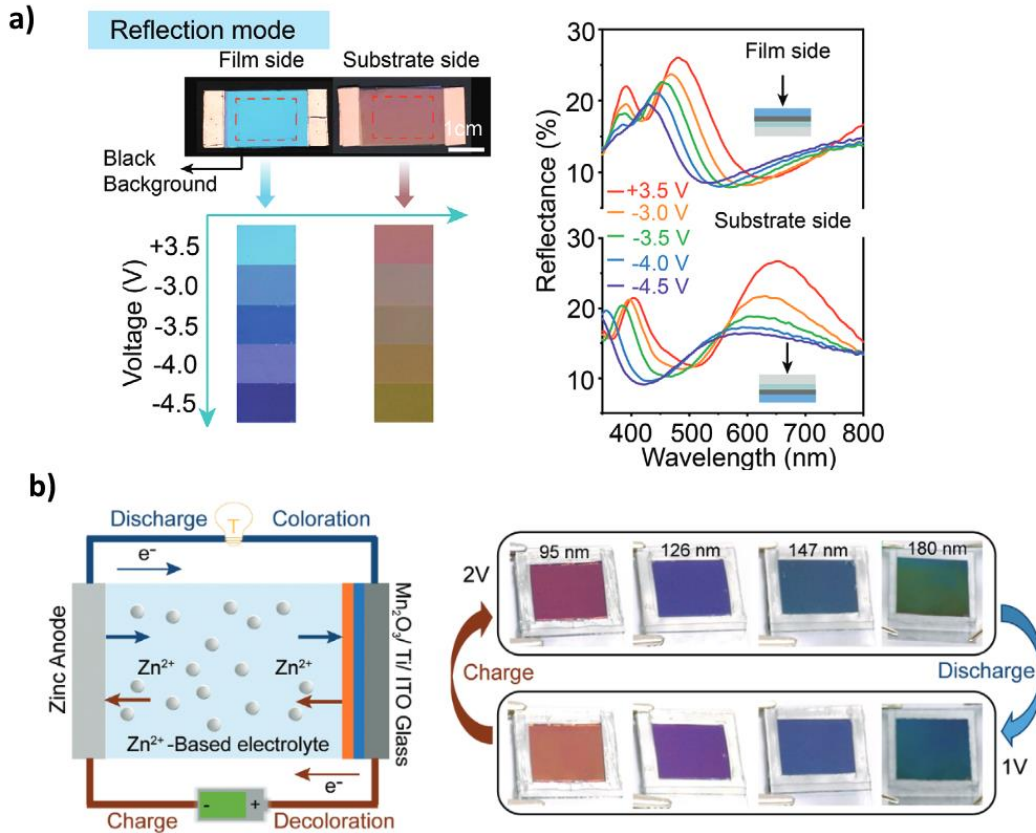


Fig. 1.9: (a) Reflection mode EC color display devices. Reflectance spectra measured from film and substrate side exhibit asymmetric colors. (b)  $\text{Mn}_2\text{O}_3$  based EC battery with high color tunability.<sup>72,73</sup>

Zhao *et al.* presented multiple approaches for colorful EC reflective type displays based on Fabry-Perot cavities.<sup>73,74</sup> In addition to the conventional cavity material  $\text{WO}_3$ ,  $\text{Mn}_2\text{O}_3$  has been shown to exhibit superior EC properties when employed in a battery type color device. Here,  $\text{Mn}_2\text{O}_3$  is deposited onto Ti and used

as the counter electrode in a zinc ion battery (ZIB) platform. Through the Fabry-Perot cavity style architecture, the poor EC performance of manganese oxide is overcome, and several distinct colors can be displayed in a charge-discharge cycle (Fig. 1.9(b)). Furthermore, the EC ZIB was shown to offer a high specific capacity of 283 mAh/g at 0.2 A/g current density with 64% charge capacity retention over 800 cycles. Ultimately, it was demonstrated here that through careful device design and material choice, rather weak EC effects in certain oxides can be enhanced through metasurfaces and cavities.

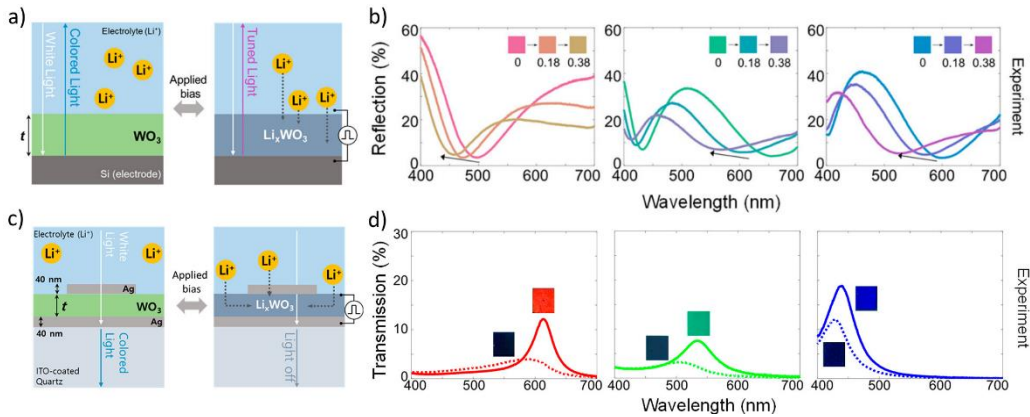


Fig. 1.10: EC cavity color devices developed by Lee *et al.* (a) Reflection type device with (b) corresponding reflectance spectra. (c) Transmission type device with (d) the corresponding spectra.<sup>75</sup>

Lee *et al.* presented two distinct device architectures for EC cavity color displays. Their reflective device, shown in Fig. 1.10(a) achieved up to  $\Delta\lambda = 107$  nm color shift throughout the visible spectrum as depicted in Fig 1.10(b).<sup>75</sup> The wavelength range of the device is set by the WO<sub>3</sub> layer thickness. However, a novel approach for transmission type devices is shown in Fig. 1.10(c), where plasmonic

Ag structures on top of a WO<sub>3</sub> cavity are used to create narrowband colors through light transmission. The presented device achieved mainly static colors with a maximum shift  $\Delta\lambda = 30$  nm, but present significant transmission modulation of 78%.

To increase the chromaticity of reflection type ECD displays, different approaches incorporating multilayer architectures have been introduced. By employing alternating multilayers of W/WO<sub>3</sub>, the initial full width at half maximum (FWHM) from the Bragg-reflector can be reduced to 60 nm, leading to higher chromaticity and a 40% wider color gamut (Fig. 1.11(a)).<sup>74</sup> However, the FWHM widens during coloration. This also is accompanied by a small change in color since only the top layer of the device can be actively color cycled. Hence, reflective electrodes with ion permeability are necessary to allow for redox cycling of the whole device. Another type of Bragg-reflector ECD was realized by Redel *et al.* who employed colloidal solutions of NiO and WO<sub>3</sub> nanoparticles to spin-coat alternating stacks of the EC films (Fig. 1.11(b)).<sup>76</sup> Layer thicknesses are very consistent throughout four device layers, leading to a distinct change in the reflectance spectrum when Li<sup>+</sup> ions are driven into the Bragg-reflector. However, this device only achieved 25 nm total color shift, mainly owing to the arising defects and inhomogeneities from to the colloidal the fabrication process and that the bottom layers experiencing less ion intercalation.

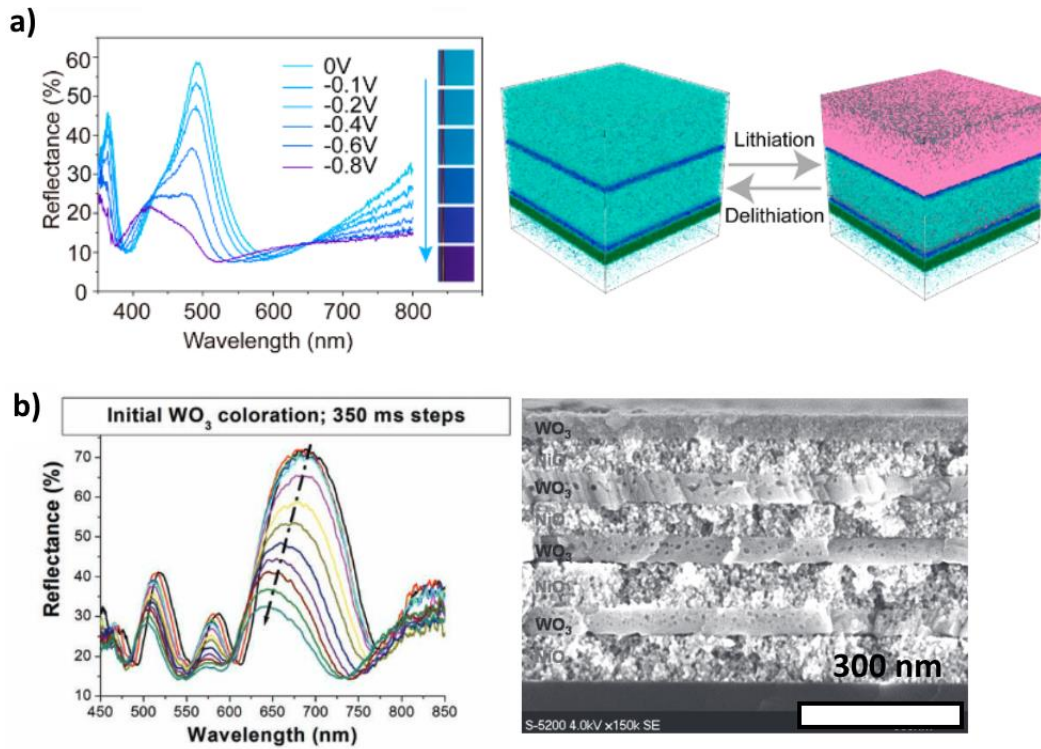


Fig. 1.11: EC Bragg-Reflector type color displays. (a) Sputtering process showing sharp resonances in the reflectance spectra (left) and a schematic of the device (right). (b) Colloidal fabrication process based on alternating layers of NiO and WO<sub>3</sub> nanoparticles spin coated onto FTO substrates. Reflectance spectra during coloration and SEM image of device architecture.<sup>74,76</sup>

Chen *et al.* recently improved the concept of an active EC nanocavity by means of a complex device design which allows switching between the Fabry-Perot (F-P) cavity resonance and a Fano resonance through the lithiation of WO<sub>3</sub> (Fig. 1.12(a,b)).<sup>77</sup> Such a multifunctional nanophotonic platform consists of a simple F-P cavity on top of an ITO layer that sandwiched between an Ag mirror and a thin Ag reflector/absorber. In the delithiated state, the F-P cavity resonance dominates,

and the device reflects a blue light color. However, when the device is lithiated, the Fano resonance dominates since the  $\text{WO}_3$  layer becomes highly semiconducting, making ITO the main cavity material and color changes to purple due to the mixing of the blue light color cavity resonance and the red-light color arising Fano resonance. The lithiation dependent reflection spectra are shown in Fig. 1.12(c). Through the lithiation process of the device, a distinct fixed peak around 610 nm appears. Interestingly, when the Ag mirror is replaced with a 10 nm thick Ag film, the device exhibits different colors for transmission and reflection, as such functioning as a color filter.

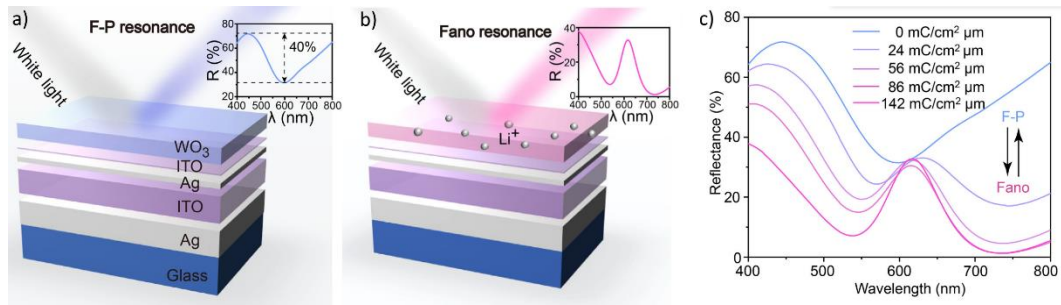


Fig. 1.12: (a) Schematic diagram of cavity operating in the F–P resonance mode. Inset: Reflection spectra of the proposed structure operating in the F–P resonance mode. (b) Same device operating in the Fano resonance mode. (c) Reflection spectra as a function of lithiation with resonance mode

Recently, Gugole *et al.* appended the work presented in this thesis (see Section 4.3) by introducing Pt NHA in an active EC plasmonic cavity having a  $\text{WO}_3$  modulation layer (Fig. 1.13(a)). By reversing the layer architecture and measuring light reflection through the glass substrate rather than the electrolyte, the reflectivity

of the cavity can be increased by up to 15%. The introduced devices operate between  $V = \pm 1.5$  V and achieve a wide ( $\Delta\lambda = 110$  nm) spectral shift. By adjusting the thickness of the  $\text{WO}_3$  layer, light colors between violet and red are achieved. Notably, this ECD power consumption is quite low. A single switching cycle requires approximately  $40 \text{ mJ/cm}^2$ , which is below the energy density required to operate an e-ink reader.

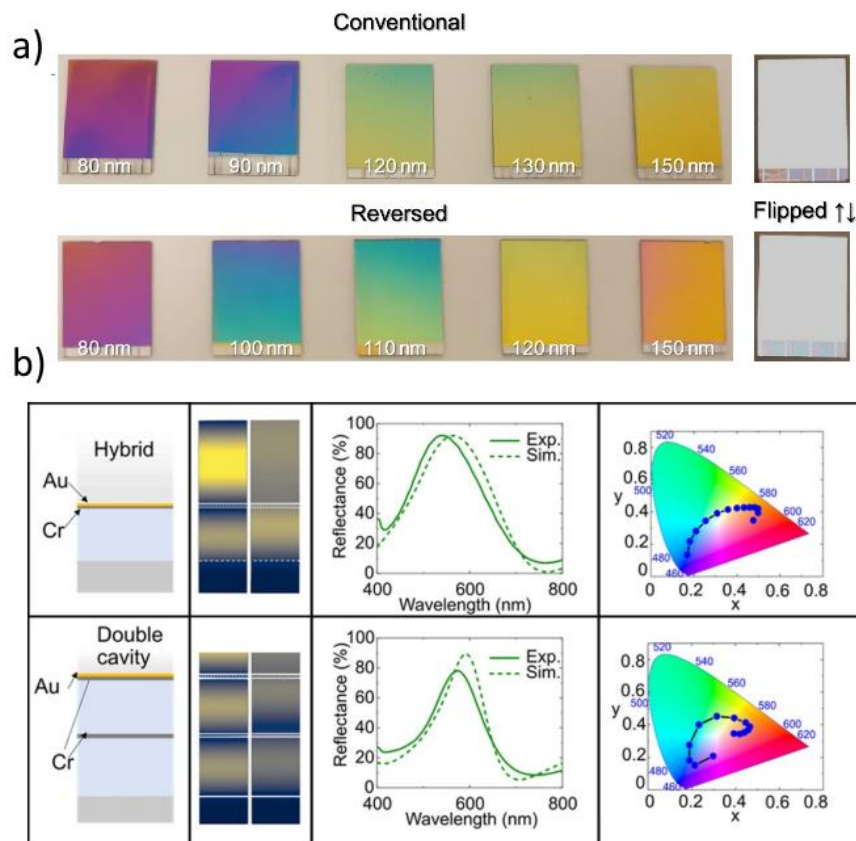


Fig. 1.13: (a) Images of the large-scale color printing devices fabricated by Gugole *et al.* (b) Fabry-Perot type EC cavity with absorber for higher chromaticity.<sup>78,79</sup>

Further development of F-P cavity type color devices makes use of broadband absorbers in the same device architecture to enhance chromaticity of the main reflected color wavelength. Ma *et al.* introduced a Cr-based absorber in front of the F-P cavity to spectrally shape the reflectance.<sup>78,80</sup> The combination of these two device layers does not impede on the available color shift and only reduces the reflectance by less than 5%. Other possibilities to increase optical transmission modulation and chromaticity are the introduction of several layers of NHA into the WO<sub>3</sub> active dielectric. Evidently, the NHA based devices provide another degree of freedom that can be used to tune the optical properties of the cavity. To date, two distinct types of resonant cavity devices have been investigated: static cavities having EC on-off switching capability and dynamic cavities having WO<sub>3</sub> as the resonator material. While the EC on-off switching based on conductive polymer coatings achieve video frequencies (25 Hz), their electrochemical stability is limited. On the other hand, EC cavity materials lead to a wide range of dynamically achievable light colors, but they lack the speed and optical transmission modulation necessary to compete with other display technologies. However, both platforms exhibit low power consumption and offer scalable fabrication approaches that make device integration favorable. The last drawback to overcome is that all investigated devices to date incorporate liquid electrolytes, which limits the potential for integration into e-readers or similar display devices.

Table 5: Comparison of selected Fabry-Perot type cavity devices. Values for color range, FWHM and optical transmission modulation are extracted from figures and graphs from the cited references.

Technology	Type	Color Range (nm)	FWHM (nm)	Modulation	Ref.
Al <sub>2</sub> O <sub>3</sub> cavity, Au NHA, EC Polypyrrole	On-off	> 300 (static)	70	85%	68
W/WO <sub>3</sub> SC	Active	~ 120	120	35%	32
Ti/Mn <sub>2</sub> O <sub>3</sub> ZIB	Active	~ 130	140	10%	73
Au/WO <sub>3</sub> /Au NHA	Active	~ 105	110	70%	81
Ag/WO <sub>3</sub> /Ag nanodisks	Active	~ 107 (reflection) ~ 23 (transmission)	60	20%	75
W/WO <sub>3</sub> Multilayer	Active	~ 55	55	40%	74

### 1.4.3 Modulation Materials for Integrated Photonics

The propagation of electromagnetic (EM) waves in photonic devices, such as waveguides and ring resonators is fundamentally determined by the dimensions of the device, the refractive indices of the waveguide core material, cladding, and the difference between the two refractive indices. In the case of a planar waveguide having an isotropic dielectric and a permittivity  $\epsilon_i(x)$  (or a refractive index  $n_i(x)$ ) which varies only along the  $x$ -direction, the wavevector for a medium  $i$  is:

$$k_i^2 = \omega^2 \mu_0 \epsilon_i(x) = \frac{\omega^2}{c^2} n_i^2(x) \quad (1.12)$$

However, such a simplistic relation needs to be adjusted for 3D waveguides, such as ridge and strip waveguides, by means of introducing a dimension-dependent effective refractive index. Since the propagating optical mode does extend out of the waveguide core material, the effective index experienced by such a mode is not only dependent on the refractive index of the core material, but also by its surrounding medium. This leads to a propagation constant along the waveguide to be defined as:

$$\beta = n_{\text{eff}}k_0. \quad (1.13)$$

The complex nature of the 3D waveguide configuration necessitates that the solution(s) for the effective refractive index are best found through numerical approaches. The direct influence of the dielectric environment on the electric field properties of an optical mode propagating along a waveguide allows direct manipulation of such a mode.

Conventional approaches for stimuli responsive nanophotonics, such as thermo-optic and electro-optic modulators suffer from the volatility of the respective effect as well as the need for continuously applying power. Furthermore, Phase-change materials (PCM), such as  $\text{Ge}_2\text{Sb}_2\text{Te}_5$  (GST),  $\text{Sb}_2\text{Se}_3$  or  $\text{VO}_2$  are investigated to dynamically alter the refractive index in photonic waveguides, and thereby, provide tunability of the phase and transmission of such devices.<sup>82–86</sup> In Si waveguide modulator based on  $\text{Sb}_2\text{Se}_3$  (Fig. 1.14(a)), metal bow tie contacts acting as electrical microheaters are used to heat up the  $\text{Sb}_2\text{Se}_3$  strip to induce the phase change. The modulation depth induced in a 220 nm wide Si waveguide by a 6  $\mu\text{m}$

long  $\text{Sb}_2\text{Se}_3$  strip is  $\sim 3000$  dB/cm. In a Mach-Zehnder Interferometer (MZI) configuration, an optical modulation of  $\sim 30$  dB is achieved at  $< 0.1$  nm FWHM for the extinction profile.<sup>87</sup>

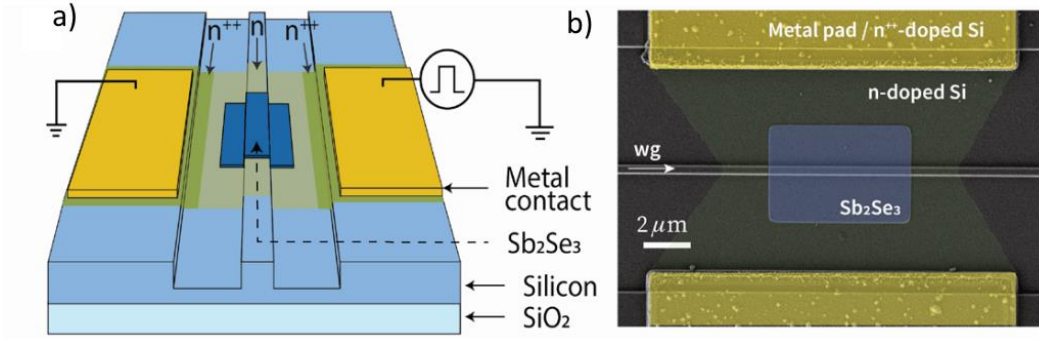


Fig. 1.14: (a) Microheater design with doped silicon profiles to create an electrical resistor in a half-etched 220 nm SOI waveguide. (b) SEM image of a fabricated 6  $\mu\text{m}$ -long bowtie microheater on a 6  $\mu\text{m}$ -long  $\text{Sb}_2\text{Se}_3$ .<sup>87</sup>

However, the phase change in GST and  $\text{VO}_2$  is introduced by heating over a threshold temperature. Since the optical modulation process requires high current for contact heating or high-power laser pulses, the device power consumption and thermal dissipation can be very high, thus making this class of devices impractical for on-chip applications.

Due to their large change in refractive index induced through ionic gating, more recently, 2D materials, such as  $\text{WS}_2$  and other transition metal dichalcogenides, have been employed in photonic circuits.<sup>88–94</sup> It has been shown that 2D  $\text{WS}_2$  experiences a change in its refractive index  $\Delta n = 0.6$  when it is ionically gated with  $N = 8 \times 10^{13} \text{ cm}^{-2}$  charge carriers.<sup>88</sup> The charge-modulated dielectric constants

are utilized in a Mach-Zehnder interferometer (MZI) where it induces a change in the effective index in the  $\text{Si}_3\text{N}_4$  waveguide core of up to  $\Delta n_{\text{eff}} = 5 \times 10^{-3}$ . The corresponding structure shown in Fig. 1.15(a) illustrates the MZI having  $\text{WS}_2$  on both arms. When a voltage is applied and the monolayer is ionically gated on one side of the MZI, the transmittance curve is red shifted (Fig. 1.15(b)). While the loss induced by the small overlap of optical mode and conductive material is negligible ( $\Delta k = 1.3 \times 10^{-5}$ ), the wavelength shift in the MZI is directly proportional to  $\Delta n_{\text{eff}}$  but the modulation depth decreases with increasing  $\Delta k$ , thus a trade-off has to be made for optical performance.

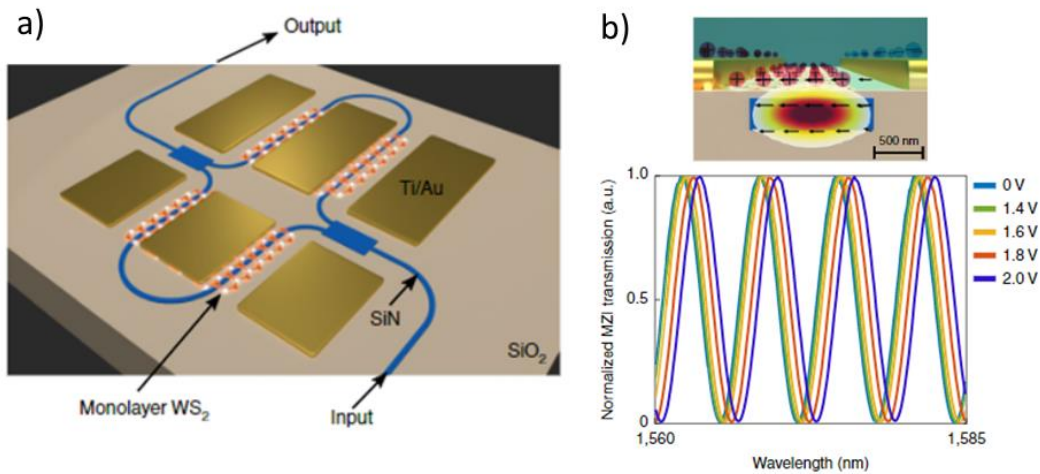


Fig. 1.15: Schematic of an on-chip MZI having a patterned monolayer  $\text{WS}_2$  on both arms of the MZI. Optical transmittance of the MZI for the TE mode at different voltages. The top figure shows the optical mode profile for the TE mode where the arrows illustrating the field lines aligned along the plane of  $\text{WS}_2$  monolayer.<sup>88</sup>

Gating of 2D materials has further shown promise in electrically gated graphene modulators on Si waveguides.<sup>95</sup> Through strong coupling of the optical mode to the graphene layer, this platform achieves up to 35 dB optical transmission modulation. However, a spacer thickness of 10 nm SiO<sub>2</sub> is necessary to mitigate the loss to this level. Other technologies make use of the high change in dielectric properties of 2D materials through illumination and achieve high photodetection sensitivity.<sup>80</sup>

Unfortunately, processing of 2D materials is a quite challenging feat and to date have proven to be unscalable for large area integration.<sup>96</sup> Furthermore, ionic, and electric gating of these materials is not bistable and requires constant supply of the electrical power. Hence, a non-volatile, low operating voltage alternative for these materials is necessary for on-chip manipulation of optical signals.

EC materials operating in voltage windows  $\Delta V = \pm 2$  V are poised to offer the necessary change in optical properties to actively and dynamically manipulate the dielectric environment of photonic and plasmonic devices needed for novel functionalities. While the modulation of resonant effects is mainly reliant on the change in the refractive index of the EC material, the inherent increase of optical extinction can be utilized in optical transmission modulation for photonic devices such as optical waveguides. To date, EC modulation of optical waveguide transmission is realized in devices based on the conventional smart window architecture where the electrical contact are in direct proximity to the waveguide core and as plasmonic slit waveguides.<sup>29-31</sup>

The first report of EC waveguide fabrication and measurements was by Page *et al.* in 1990<sup>97</sup>. However, the authors rather focused on utilizing the EC effect as a method of proving the optical poling of an electro-optic polymer exhibiting EC properties. However, the clear dependence on the optical poling and the induced absorption, due to the EC effect, inspired further investigations of such a platform. In 1992, Piraud *et al.* presented the first EC waveguide modulator based on a planar optical waveguide.<sup>98</sup> Their waveguide platform was based on the EC effect in lutetium biphthalocyanine ( $\text{Lu}(\text{PC})_2$ ). The device consisted of planar potassium-exchanged sodalime glass waveguide with a silica buffer layer between the core material and the ITO electrode on which the  $\text{Lu}(\text{PC})_2$  film is deposited (Fig. 1.16(a)). The resulting device having a 10 nm thick  $\text{Lu}(\text{PC})_2$  film and 200 nm buffer thickness between waveguide core and 10 nm ITO film exhibits modulation of the TE mode absorption along the waveguide from 10 dB/cm to 22.5 dB/cm for  $\lambda = 680$  nm (Fig. 1.16(b)). Due to the EC effect in  $\text{Lu}(\text{PC})_2$ , which switches the maximum extinction between green and red, the absorption behavior reverses around 750 nm wavelength. Notwithstanding the high modulation depth, it was further found, that the thickness of the spacer layer, as well as the EC material have a strong influence on device performance. Interestingly, since, the EC effect in  $\text{Lu}(\text{PC})_2$  is triggered by the presence of the  $\text{Cl}^-$  ions, this particular experiment was realized as an integrated EC sensor. However, the electrochemical cell is by no means integrated into the device.

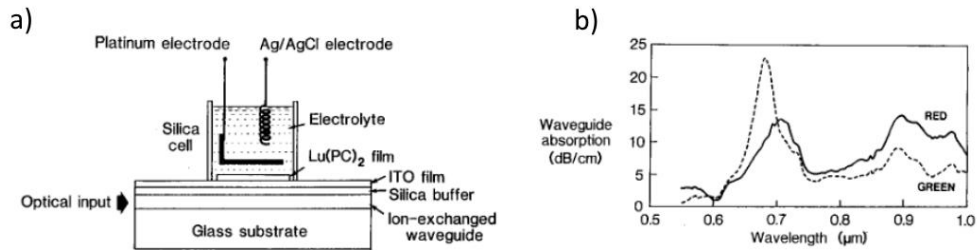


Fig. 1.16: Planar waveguide with EC modulation layer. (a) Schematic of the device including planar waveguide, buffer layer and EC cell. (b) Achievable modulation in reduced (labeled: red) and oxidized (labeled: green) state of Lu(PC)<sub>2</sub>.

The concept of EC modulation for integrated optics and photonics was later realized in the form of an electrochromic variable optical attenuator (ECVOA), as introduced by O'Brien *et al.*<sup>99</sup> In this optical modulator, operating in the NIR spectral region, an all-solid-state WO<sub>3</sub> ECD, composed of a Ta<sub>2</sub>O<sub>5</sub> layer as the proton conductor, is utilized to modulate the attenuation of a gradient index lens by up to 12 dB at an insertion loss of 0.5 dB. Remarkably, the attenuator exhibits up to 5 dB/cm s switching rate owing to the fast proton conduction with stability over 70000 switching cycles. However, Cowin *et al.* remarked how little attention the ECVOA achieved despite its notable dynamic properties.<sup>100</sup>

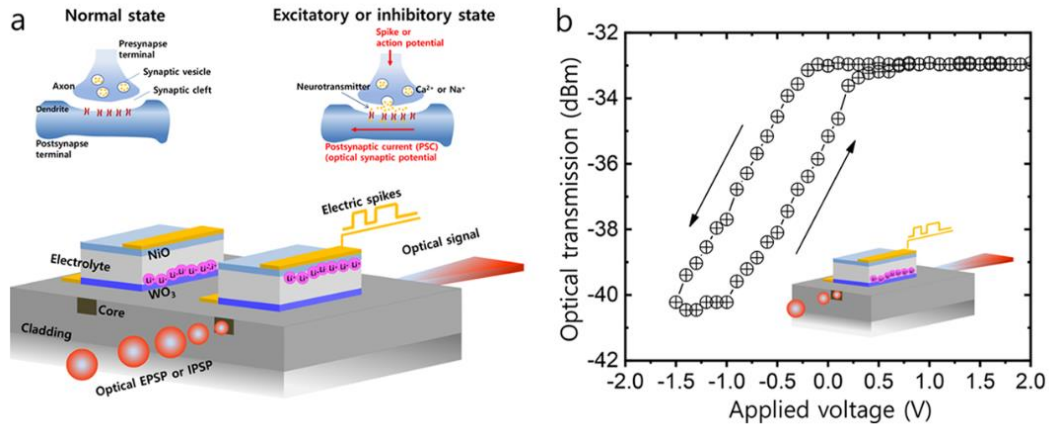


Fig. 1.17: (a) Schematic of synaptic transmission modulation via Ca<sup>2+</sup> ions and corresponding device design. (b) Voltage dependent optical transmission in the artificial synapse.<sup>29</sup>

Agrawal *et al.* exploited the EC behavior of Prussian Blue (K<sub>4</sub>Fe(CN)<sub>6</sub> – PB) in a nanoplasmonic slit structure ( $w = 50 \text{ nm} \times 100 \text{ }\mu\text{m} = 5 \text{ }\mu\text{m}^2$ ) milled into a 250 nm thick gold film via a focussed ion beam (FIB). The EC PB films are deposited from 5 mM K<sub>4</sub>Fe(CN)<sub>6</sub> in 0.1 M HClO<sub>4</sub>, leading to a continuous increase in the EC optical transmission modulation of the device. The authors reported ~ 96% optical transmission modulation at fill factors of 25%.<sup>101</sup> In comparison to a flat gold surface with electrodeposited PB films, the nanoslit device achieves 60% higher optical transmission modulation.

Kim *et al.* introduced optically readable EC waveguide modulator devices acting as artificial synapses for ionically driven bio-applications.<sup>29,31</sup> Ionic gating of EC materials has shown promise for bistable resistive switching devices and on-chip memory. However, utilization of the optical signal modulation is lacking in

these devices.<sup>102–106</sup> To incorporate EC-based optical modulation at increased speed and optical transmission modulation, a conventional smart window type ECD is built on top of a buried polymer waveguide with cladding (Fig. 1.17(a)). The  $\text{WO}_3$  layer on top of the waveguide core modulates the optical signal traversing through the waveguide, effectively increasing the light-matter interaction with the EC oxide to the length of the waveguide. The devices introduced here achieved 10 dB optical switching modulation with sub-second switching speeds, which is up to 5 times faster than conventional EC cycling of  $\text{WO}_3$ .

However, the initial loss due to the coupling of the optical mode to the electrical contact (required to drive ions into the EC material) are rather large and prevent these devices from reaching the full optical transmission modulation potential. A major challenge for EC waveguide technology is its miniaturization into the nanoscale since all devices published to date rely on liquid electrolytes on the scale of several millimeter. To achieve full, on-chip optical transmission modulation for EC waveguides, truly nanoscale device design and all-solid-state approaches are essential. Furthermore, introducing enhanced light-matter interaction through plasmonic structures can help enhance the inherent absorption of the EC material.<sup>107</sup>

While we previously focused on introducing EC optical transmittance modulation, active manipulation of effective refractive indices and group indices along a waveguide open further possibilities for novel EC nanophotonic platforms. Furthermore, the exploitation of nonlinear phenomena in photonic devices is an important field of research that seeks for solutions to alter phase and propagation

properties dynamically.<sup>108–110</sup> Efficient generation and wavelength tenability of higher order harmonic light requires phase matching of the involved optical modes at different wavelengths. Such a tunability of the phase-matched wavelength can be achieved through altering the effective refractive index of the optical modes inside the waveguide core. Often, direct heating of the waveguide core material is employed to achieve such a change in the phase-matching conditions.<sup>111</sup> Luo *et al.* demonstrated thermal modulation of the phase matching conditions for a nanophotonic LiNbO<sub>3</sub> waveguide over  $\Delta\lambda_{\text{PM}} = 37$  nm at a temperature dependent modulation rate of  $\zeta = 0.69$  nm/K (Fig. 1.18). To provide thermally inert devices exhibiting low power consumption integration of EC materials is crucial to the evolution of nonlinear photonic waveguides.

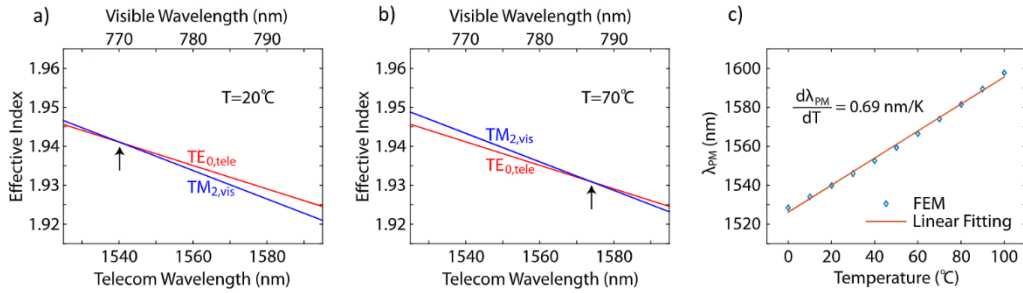


Fig. 1.18: Wavelength-dependent effective indices of  $\text{TE}_{0,\text{tele}}$  and  $\text{TM}_{2,\text{vis}}$  at (a)  $20^\circ\text{C}$ , and (b)  $70^\circ\text{C}$ , with black arrows indicating phase matching; (c) simulated phase-matched pump wavelength  $\lambda_{\text{PM}}$  as a function of temperature.

## 1.4.4 Summary

Electrochromic materials, especially PANI, PEDOT and  $\text{WO}_3$ , have shown great potential for applications in nanoscale devices based on plasmonic resonances and waveguide structures. The high change in the dielectric properties of these materials during redox cycling can be exploited to change the resonance conditions for LSPR and SPP propagation through changes in the dielectric environment of a single nanoparticle or an array. Wavelength shifts up to  $\Delta\lambda = 180$  nm for PEDOT:PSS have been realized for nanostructure arrays coated with the conductive polymer. To shift of the initial resonance wavelength away from the NIR spectral region, active F-P cavity type devices which incorporate plasmonic superstructures are employed. Such devices light modulation spans the visible spectrum from green to red. Chromaticity and lifetime are issues that are being actively solved through a manifold of solutions. Especially the combination of cavity resonance and plasmonic effects provides an interesting path to device improvements.

In photonic waveguides, EC materials, especially  $\text{WO}_3$ , have shown to allow high optical transmission modulation which is paired with synaptic functionality. While introduced in the 20<sup>th</sup> century, the technology of EC photonics is in its infancy when compared to other approaches for active nanophotonic devices. Through its high refractive index change in the visible and NIR spectrum,  $\text{WO}_3$  is so far considered to be the prime candidate for dynamically EC modulated nanophotonics. Nonetheless, the high on-state and coupling losses, as well as the

long switching times need to be further improved for on-chip photonic implementation of  $\text{WO}_3$ .

## 1.5 Objectives

The main goal of this thesis is to evaluate and demonstrate the feasibility of EC materials, mainly  $\text{WO}_3$ , for integration in nanophotonic and nanoplasmonic devices aiming to provide additional functionality and tunability. To achieve functionality on the nanoscale, the EC effect and the behavior of the employed ion conducting materials need to be investigated and understood. Applications of the introduced devices include ultra-high on-off transmission modulation in optical waveguides, highly sensitive ion detection, phase tuning in nonlinear waveguides and full color tunability of plasmonic, resonant nanocavities.

The objectives of the thesis can be chronologically ordered as the following: (1) evaluate different methods of  $\text{WO}_3$  thin film deposition for suitability in nanofabrication and gather data on the optical properties of such films; (2) investigate the optical and electronic properties of liquid, solid and polymer ion conductors, as well as their compatibility with conventional nanofabrication techniques; (3) gain an understanding of the influence the EC effect in  $\text{WO}_3$  has on photonic and plasmonic devices through the use of FDTD simulations based on ellipsometric material data; (4) design a dynamically tunable resonant nanocavity having a plasmonic superstructure and determine its intercalation dependent reflectance; (5) develop a process to fabricate optical waveguide modulators based on CMOS compatible fabrication standards and integrated  $\text{WO}_3$  modulation layers.

(6) Exploit the EC effect to create a dynamic nonlinear waveguide to actively tune the SHG. The work in this thesis bears the promise of a deeper understanding of EC effects and its benefits in nanoscale photonic and plasmonic devices.

## 1.6 Structure of the Thesis

The thesis is structured into five main chapters as follows:

Chapter 1 discusses the motivation and research objectives of the thesis. It further presents a comprehensive review of the resonant and nonresonant nanoplasmonic, and nanophotonic effects currently employed in multifunctional and advanced ECDs.

Chapter 2 summarizes the theoretical background relating to several of the topics discussed in this thesis. First, electrochromism and its origins are discussed and explained briefly. Next, ionic conduction necessary for EC functionality is reviewed and the most important dependencies are laid out. Furthermore, the resonant and nonresonant optical effects utilized in this work are introduced. Finally, the basic principles of plasmon resonances as well as fundamentals of photonic waveguides are outlined.

Chapter 3 introduces several different methods for the deposition of EC materials from wet chemical and dry physical processes. The resulting films are investigated regarding their suitability for nanofabrication processes and application in optical devices. In combination with different ionic conductors, the EC materials  $\text{WO}_3$  and  $\text{NiO}$  are employed in different ECD architectures to explore

their electrochemical dynamic and static properties.  $\text{WO}_3\text{-NiO}$  supercapacitors incorporating polymeric and solid-state electrolytes are compared regarding switching times and EC optical transmission modulation. A hydrogel-based EC battery is introduced as a mean to evaluate a method to increase the electrochemical lifetime of hydrogel electrolytes. Finally, a scalable approach to EC oxide protection by means of a self-assembled monolayer (SAM) is introduced.

In Chapter 4, a variety of applications for EC materials in plasmonic resonant and nonresonant devices are presented. A  $\text{WO}_3$  solid-state ECD is utilized to change the coupling conditions for a surface plasmon polariton to an Au thin film. Furthermore, a plasmonic NHA is employed to achieve highly chromatic color printing from a resonant cavity. Finally, nonresonant SPP propagation along a plasmonic waveguide is utilized for all-solid-state transmission modulation.

In Chapter 5, a novel photonic waveguide platform based on PECVD Silicon Nitride is introduced. The platform utilizes EC materials in a low loss architecture to provide ultra-high transmission modulation and to induce a change in the nonlinear properties of such waveguides. The chapter introduces the fabrication process as well as the FDTD simulations that lead to the final devices. Such a platform is then employed as a highly sensitive  $\text{Na}^+$  ion sensor for potential microfluidic measurements. Lastly, a solid-state ECD is utilized to change the phase matching conditions inside a Silicon Nitride waveguide to such an extent that the generated second harmonic light can be actively tuned and modulated.

Finally, in Chapter 6, a summary of the major results from the thesis, along with future work and suggestions for continuation of the project, are presented.

# Chapter 2

## Background

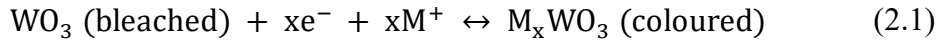
This chapter presents a literature survey on the topics related to the thesis. Section 2 provides a summary and explanation of the electrochromic effect in transition metal oxides (TMO) along with a description of the origins of the EC effect. Furthermore, a brief summary of ionic conductors is given, outlining the most important differences between solid and polymeric ionic conduction. A short overview of up-to-date applications of solid-state ion conductors shows the potentials and shortcomings of such a technology. Next, in Section 2.2 the basic electromagnetic properties of the devices presented in this thesis are derived from Maxwell's equation. Section 2.3 then goes further into detail about the fundamental description of plasmon resonances and surface plasmon propagation. Finally, Section 2.4 presents an introduction into nonlinear optical materials by means of second harmonic generation (SHG) in Silicon Nitride.

### 2.1 Electrochromism

Electrochromism, the change in color or transparency of a given material by applying an electrical potential, has been studied since the 19<sup>th</sup> century. However, tremendous progress has been made since the 1980s.<sup>1</sup> Electrochromic (EC) smart windows based on TMOs have been improved continuously and provide effective optical transmission and heat modulation for energy efficient buildings.<sup>4,13,112</sup> Constant progress is made through nanostructuring of EC materials, doping of EC



(coloration upon deintercalation/oxidation) EC materials. In cathodic EC materials, such as  $\text{WO}_3$ ,  $\text{TiO}_2$ ,  $\text{Nb}_2\text{O}_5$ ,  $\text{MoO}_3$ , and  $\text{Ta}_2\text{O}_5$ , positively charged ionic species (i.e.  $\text{H}^+$ ,  $\text{Li}^+$ ,  $\text{Na}^+$ ,  $\text{Zn}^{2+}$  or  $\text{Al}^{3+}$ ) can effectively diffuse through the cathodic EC oxide lattice and intercalate randomly in their highly distorted  $\text{MO}_6$  octahedral unit cell.<sup>116</sup> The introduced positive charge is offset by an electrical current from a contact, which leads to the accumulation of free charge carriers in the empty  $d$ -bands and thus free carrier absorption in the material.<sup>14,16,116</sup>  $\text{WO}_3$  as the most prominent EC oxides experiences a change in its dielectric properties following this reaction:



Here,  $\text{M}^+$  can be a proton or one of the aforementioned ionic species. Notably, the change in dielectric properties for  $\text{WO}_3$  is significant, leading to over 80% optical transmission modulation in an EC smart window based on  $\text{Al}^{3+}$  ion intercalation (Fig. 2.2). While the extinction coefficient of  $\text{WO}_3$  increases from  $k_{\text{ex}} = 0$  to  $k_{\text{ex}} = 0.5$  at 632 nm wavelength, the refractive index decreases from  $n = 2.1$  to  $n = 1.8$ .<sup>35,81,117</sup>

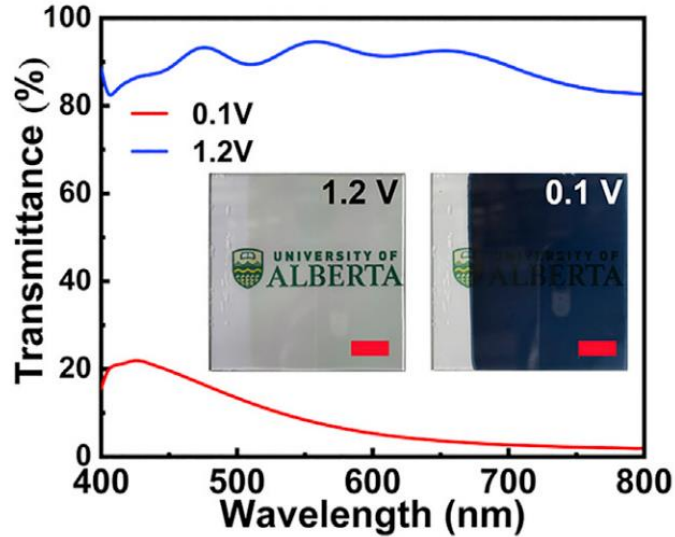


Fig. 2.2: Optical transmittance of a 300 nm thick  $\text{WO}_3$  film on ITO in its oxidized (blue) and reduced (red) state.<sup>50</sup>

Anodic EC oxides ( $\text{NiO}_x$ ,  $\text{IrO}_2$ ,  $\text{Cr}_2\text{O}_5$ ,  $\text{MnO}_2$ ...) are most commonly employed as counter electrodes. Counter electrodes serve as ion storage layers during bleaching of the device. Anodic EC materials as counter electrodes are often used in EC smart windows and devices, since their coloration occurs upon deintercalation, and hence, compliments the EC effect in cathodic EC materials. The significance of octahedral crystal coordination becomes obvious when investigating the electronic properties of EC oxides. In their pristine state EC oxides exhibit filled oxygen 2p bands (Fig. 2.3), with the metal 3d bands split into  $t_{2g}$  and  $e_g$  bands due to the octahedral symmetry. In case of pure  $\text{WO}_3$ , the O 2p band is filled with electrons and separated from the empty  $t_{2g}$  state by a large energy bandgap ( $E_G \approx 3.5$  eV), which renders the material transparent in the optical regime. Once cations are inserted by applying an electric field, the balancing

electrons, from the conductive electrode, fill the  $t_{2g}$  state and introduce free charges in the  $d$  band. These free electrons, in turn, lead to a change in the dielectric properties of  $\text{WO}_3$ . Complimentary, anodic EC oxides have unoccupied  $t_{2g}$  states which are filled upon ion insertion and thus lead to an optical bandgap between the separated  $d$  bands. Due to the presence of different crystal phases,  $\text{V}_2\text{O}_5$  experiences both types of EC coloration. The break in octahedral symmetry leads to a narrow split-off band in the material's  $3d$  band.

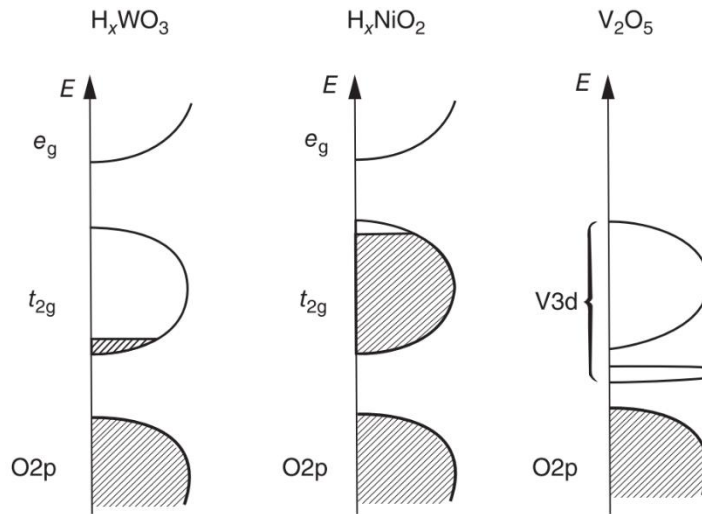


Fig. 2.3: Schematic band structures for different types of electrochromic oxides. Shaded regions signify filled states and  $E$  denotes the energy. From Ref. <sup>118</sup>

The optical absorption in EC oxides is often attributed to charge transfer between different metal sites in the host crystal. In  $\text{WO}_3$ , the intercalated charges lead to a distortion of the crystal and as a result, injected electrons are localized in trap states approximately  $\Delta E = 0.1 - 0.2$  eV below the bandgap. These strongly localized electrons form small polarons through strong electron-phonon coupling.

The transfer of charges from one site  $i$  to another  $j$  is accompanied by the absorption of a photon:<sup>119</sup>



## 2.1.2 Ion Conductors and Electrolytes

An ion conductor or an electrolyte of an ECD provides the physical barrier between the active electrodes allowing ion diffusion but preventing electrical conduction. As such, ion conductors must exhibit certain key optical, electronic, and electrochemical material characteristics. Depending on the application of the ECD, ion conductors can be liquid, polymeric or inorganic solid electrolytes. Liquid electrolytes (e.g., aqueous solutions of NaCl, LiCl or AlCl<sub>3</sub> or Li, Al, or Na perchlorates solved in propylene or ethylene carbonate) offer the highest conductivity but are disadvantageous in most applications due to leakage, thermal and optical stability, or incompatibility to fabrication standards. On the other hand, solid ion conductors (e.g., H<sup>+</sup> conducting Ta<sub>2</sub>O<sub>5</sub> or Li<sup>+</sup> conducting LiNbO<sub>3</sub>) lack the high conductivity of liquid conductors but are compatible with most nanofabrication standards and exhibit high thermal, electrochemical and optical stability. The key property for all ionic conductors for integration in ECDs however is their optical transmittance. Especially for smart window applications and nanophotonic devices, optical loss free electrolytes are an absolute necessity. Unfortunately, this criterion precludes most of the commonly known solid electrolytes.

The comparison of different types of ionic conductors with every other type (polymeric, solid, liquid) is difficult. Such a comparison is a research field on its own. There are three types of mass transport that play a part in ionic conduction (i.e., migration, convection, and diffusion). While convection can be neglected when looking at physically static samples, migration and diffusion provide ion conduction in an additive manner. Migration becomes important when the number of mobile ions becomes sufficiently small, which is the case in solid-state and polymer electrolytes, but is negligible in liquid electrolytes. Hence, diffusion becomes the most important mode of comparison for all ionic conductors. Furthermore, they must obey the Nernst-Einstein relation representing the ionic conductivity,  $\sigma_{\text{ion}}$ , through the following:

$$\sigma_{\text{ion}} = \frac{nq^2D}{k_B T} = \frac{nq^2 \lambda^2}{k_B T 6\tau_i} \quad (2.3)$$

Where,  $n$  is the concentration of mobile ions in the electrolyte,  $q$  is the valency charge of the ionic species, (i.e., the charge of the ion),  $D$  is the diffusion coefficient expressed as a random walk having an ion length hop of  $\lambda$  and an average time between hopping of  $\tau_i$ . The valency of the ionic species in liquid electrolytes can be freely chosen to fit the application, while in solid ion conductors it is limited to protonic conduction or small ionic species (i.e.,  $\text{Li}^+$ ,  $\text{Na}^+$ ). Hence, the ionic conductivity is mainly governed by the concentration of mobile ions and their diffusion coefficient. Obviously, certain simplifications have been made here since every conduction process is thermally activated and thus it is temperature dependent. Hence, assuming a constant temperature for all ionic conductors and

simplifying the ionic conductivity to the Nernst-Einstein relation, the factors influencing the ionic conductivity of a medium depend strongly on both  $n$  and  $D$ . Given a specific ionic specie (e.g.,  $\text{Li}^+$ ) the concentration in liquids and polymers is usually adjustable and of similar concentration  $\sim 10^{23} \text{ cm}^{-3}$ ,<sup>120</sup> while the typical ionic concentration for excess ions in solids is on the order of  $< 10^{21} \text{ cm}^{-3}$ .<sup>35,121</sup> Moreover, the diffusion coefficients for liquids, polymers and solids are around  $D = 10^{-4} \text{ cm}^2/\text{s}$ ,  $D = 10^{-7} \text{ cm}^2/\text{s}$  and  $D = 10^{-10} \text{ cm}^2/\text{s}$ , respectively.<sup>122,123</sup> It is clear that the ionic conductivity of liquids is higher than that of polymers or solids. However, for application in devices, other key parameters such as suitability for nanofabrication standards, chemical stability and optical transparency have to be taken into account. Some of the recent developments regarding ionic conductors for ECDs are presented in the following.

Even though, liquid electrolytes, such as aqueous salt solutions of  $\text{LiCl}$ ,  $\text{NaCl}$ ,  $\text{AlCl}_3$ ,  $\text{KOH}$ ,  $\text{Zn}_2\text{SO}_4$  and others, as well as perchlorates solved in propylene carbonate (i.e.,  $\text{LiClO}_4$ ), provide excellent ionic conductivity and are easily adjustable,<sup>124,125</sup> liquid ion conductors are difficult to integrate into nanoscale devices. To overcome the shortcomings of aqueous electrolytes, quasi-solid hydrogels, such as polyacrylamide, are used as a host matrix for high loadings of water.<sup>126–128</sup> Hydrogels as ion conductors have emerged as contenders in energy storage devices and ECDs due to their high conductivity, mechanical flexibility, and low processing cost.<sup>126,127,129</sup> Moreover, the intrinsic biocompatibility of hydrogels allows their application in wearable smart batteries and sensors. However, a major limitation of polyacrylamide (PAM) and other hydrogels (e.g.,

Poly(ethylene-glycol), Poly(ethylene-oxide)) is their short lifetime ion conduction which is rooted in the fast evaporation of water from the host matrix. A proposed solution was presented by exploiting the ionic hydration effect to bind water molecules to the host gel and, thereby, increasing the gel's water retention. Though, this mechanism has been mainly focused on LiCl as the hydrated salt, which limits the application to only Li-ion based batteries.<sup>128,130</sup> Hence, a long lifetime hydrogel having high electrolyte retention based on a different approach is needed for implementation in solid-state batteries and ECDs. Recently, we have shown that dimethyl sulfoxide (DMSO) modification of PAM hydrogels can increase the lifetime of the ionic conduction and the water retention tremendously, while providing up to 30 mS/cm ionic conductivity.<sup>131</sup>

While polymer electrolytes exhibit high optical transparency and chemical stability necessary for electrochromic applications.<sup>132,133</sup>, polymeric ion conductors based on poly(ethylene-oxide) (PEO), poly(methyl methacrylate) (PMMA), or poly(butyl acrylate) (PBA) exhibits slightly lower ionic conductivity ( $10^{-6}$  -  $10^{-4}$  S/cm) than liquids or hydrogel ion conductors.<sup>120,134</sup> A common method of increasing the intrinsic conductivity of such polymer ion conductors is to load the host matrix with inorganic nanoparticle fillers.<sup>135</sup> Hu *et al.* showed an increase of the ionic conductivity of a PVA based polymer electrolyte from  $10^{-7}$  S/cm to  $1.51 \times 10^{-4}$  S/cm through the addition of up to 30 wt-% silica particles.<sup>136</sup>

Solid ion conductors, such as proton conducting  $\text{Ta}_2\text{O}_5$  and  $\text{Li}^+$  ion conducting  $\text{LiNbO}_3$ ,  $\text{LiTaO}_3$  or  $\text{LiAlO}_4$ , exhibit low ionic conductivities around  $10^{-7}$  S/cm.<sup>123,137,138</sup> However, inorganic solid ion conductors can be readily integrated

with common nanofabrication techniques and possess superior cycle life.  $\text{Li}^+$  containing oxide electrolytes can be sputtered directly onto the EC electrode, which makes EC oxides as the working material necessary. A major difference between proton conducting thin films and the  $\text{Li}^+$  ion conductors is that most lithium oxides act as their own source of excess ions, which eliminates the need for implanting excess ions.  $\text{Li}^+$  ions are further prone to diffuse out of the ECD, which leads to longer lifetimes.

All-solid-state ECDs have been investigated for decades, with early devices making use of proton conduction in  $\text{SiO}_2$ ,  $\text{Cr}_2\text{O}_3$  and other simple oxides.<sup>139,140</sup> Shimizu *et al.* demonstrated  $\Delta T = 50\%$  optical transmission modulation in a  $\text{WO}_3/\text{NiO}$  ECD with a  $\text{Cr}_2\text{O}_3$  ion conductor having a remarkable lifetime of  $10^6$  switching cycles.<sup>140</sup> In 1997, Mathew *et al.* introduced a proton conducting  $\text{Ta}_2\text{O}_5$  thin film into a an ECD. Their large devices  $> 20 \text{ cm}^2$  exhibited up to  $\Delta T = 50\%$  optical transmission modulation. The authors estimated the lifetime of the ECD to be a few years.<sup>141</sup> Nagai *et al.* reported ionic conductivities for  $\text{Ta}_2\text{O}_5$  and  $\text{LiNbO}_3$  to be on the order of several  $\mu\text{S}/\text{cm}$  and demonstrated  $\Delta T = 55\%$  optical transmission modulation.<sup>142</sup> Using a  $\text{IrO}_2/\text{Ta}_2\text{O}_5$  solid electrolyte reflective type device, Tajima *et al.* achieved a fast EC switching time of  $< 15 \text{ s}$ .<sup>143</sup> An ionic conductivity of  $\sigma = 3 \mu\text{S}/\text{cm}$  of  $\text{Ta}_2\text{O}_5$  was further confirmed Niwa *et al.* in a  $\text{IrO}_x/\text{Ta}_2\text{O}_5$  ECD with  $\text{WO}_3$  and  $\text{NiO}$  as the active EC materials.<sup>144</sup> This ECD allows for  $\Delta T = 60\%$  optical transmission modulation and  $< 200 \text{ ms}$  EC switching time. The high ionic conductivity was further improved to  $\sigma = 6.2 \mu\text{S}/\text{cm}$  Niwa *et al.* through a modified sputtering process<sup>145</sup> Notably, this improved ECD was shown

to exhibit  $\Delta T = 72\%$  optical transmission modulation over more than  $t = 50000$  s consequent redox cycling. The main driving factor behind the high protonic conductivity in  $Ta_2O_5$  is due to hopping of  $H^+$  along  $OH^-$  groups adsorbed on the surface of the  $Ta_2O_5$ .

$Li^+$  ion conducting solid electrolytes based on  $LiNbO_3$  have been introduced in 1988 by Goldner *et al.*. They reported that when the ionic conductivity is  $> 10^{-7}$  S/cm, it drastically outweighs the electrical resistivity of the sputtered thin films ( $\rho = 10^{11} \Omega\text{cm}$ ) and hence allows for purely ionic conduction.<sup>146</sup> The same authors reported ECDs, based on  $WO_3$  and  $NiO$  EC electrodes, that achieved up to  $\Delta T = 65\%$  optical transmission modulation in a comprehensive study investigating the theoretical limits to  $Li^+$  based ECDs.<sup>147</sup> Notably, the  $LiNbO_3$  thin films showed good mechanical and chemical stability. In the following years, several ionic conductors incorporating  $Li^+$  ions were introduced and studied. Ashrit *et al.* developed a  $LiBO_2$  based ECD having up to  $\Delta T = 40\%$  optical transmission modulation and a switching time of  $\sim 120$  s.<sup>148</sup> By employing  $LiAlF_4$  as a solid-state electrolyte and  $WO_3$  and  $V_2O_5$  EC electrodes, Daneo *et al.* reported up to  $\Delta T = 60\%$  optical transmission modulation with. The switching speed here was reduced to  $t < 60$  s.<sup>149</sup> More recently,  $LiTaO_3$  was investigated as the ion conduction layer in a flexible ECD achieving up to  $\Delta T = 74.5\%$  optical transmission modulation at exceptional coloration efficiencies exceeding  $CE_{ec} = 68 \text{ cm}^2/\text{C}$  at  $\lambda = 550 \text{ nm}$ .<sup>150</sup> This a  $LiTaO_3$  based ECD was shown to exhibit coloration and bleaching of  $\tau_c < 13$  s and  $\tau_b < 3.5$  s, respectively.<sup>151</sup> It can be concluded that all  $Li^+$  based solid ion

conductors exhibit ionic conductivity around  $\sigma = 10^{-7}$  S/cm and at the same time exhibit high electrical resistivity.<sup>152</sup>

### 2.1.3 Electrochemical Description and Analysis

The electrochemical processes involved in determining the EC metrics are governed by the change in the Gibbs free energy,  $G$ , in an electrochemical cell:

$$\Delta G = -mFE_{\text{Cell}} \quad (2.4)$$

Where,  $m$  is the number of electrons transferred in a redox reaction and  $F$  is the Faraday constant ( $= 96\,485.3321$  sA/mol – i.e., the electric charge of  $6.022 \times 10^{23}$  electrons, or the charge in a mole of a complete reaction). If a meter is connected to a redox pair, it indicates  $E_{\text{Cell}}$  as a voltage occurring via the transfer of charge,  $nF$ . The electrochemical cell consists of two electrodes, of which both exhibit at least two distinct charged states. In solid electrodes, these charged states are the oxidation state of the material. At a single electrode, either one reaction occurs when an electrical potential is applied, either the electrode material gains an electron and is reduced:



Or the material undergoes an oxidation reaction. If an inert metal, such as a platinum wire is brought into contact with the two redox states, it experiences the redox potential  $E_{O,R}$ . Applying a potential  $E_{O,R}$  to the electrochemical half-cell does not change the oxidation state of the electrode, since electron flow and redox reactions occur at the same rate. If no potential is applied, the redox pair determines

the potential in the metal contact and, thereby, the cell voltage. To measure a cell voltage, two redox half-cells are necessary since electrochemical potential can only be determined as the difference between half-cells. Hence, a  $H^+/H_2$  couple is used as a reference for all other cell potentials. The redox potential for sufficiently fast redox couples is described as:

$$E_{O,R} = E_{O,R}^\ominus + \frac{RT}{mF} \ln \left( \frac{a(O)}{a(R)} \right) \quad (2.6)$$

Where  $E_{O,R}^\ominus$  is the standard electrode potential,  $R$  is the gas constant (8.3145 J/(molK)),  $F$  is the Faraday constant and  $n$  is the number of electrons transferred in the redox reaction. The variable  $a$  describes the reactivity of the oxidative species and can be perceived as the thermodynamic concentration. At the equilibrium cell potential, cathodic (electrons are relinquished from electrode) and anodic (electrons are acquired by electrode) current are equal and, hence, no current flow. When an overpotential,  $\eta$ , is applied to the cell, the overall current flow is non-zero and either cathodic current,  $I_{cath}$ , or anodic current,  $I_{an}$ , dominate and describe a rate of reaction at the electrode according to:

$$I_{cath} = -mFk_{cath}c_O \quad \text{and} \quad I_{an} = mFk_{an}c_R \quad (2.7)$$

Here, the rate constants  $k_{cath}$  (i.e., cathode reaction rate) and  $k_{an}$  (anode reaction rate) are both dependent on  $\eta$  and can be obtained from literature values according to Tafel's law.<sup>14</sup>  $c_O$  and  $c_R$  describe the concentration of species oxidized or reduced. At the equilibrium potential  $E_{O,R}^\ominus$  both currents are equal. However, at this equilibrium rate  $k^\ominus$ , the rate constant includes an exponential activation term, which

indicates the potential barrier that has to be overcome in either direction of a redox reaction. Such a term includes  $u = 0.4 - 0.6$  depending on the symmetry of the energy barrier (i.e., the barrier for electron transfer). Taking  $u$  into account the reaction rate constants are:

$$k_{\text{cath}} = k^{\ominus} \exp\left(-\frac{unF\eta}{RT}\right) \text{ and } k_{\text{an}} = k^{\ominus} \exp\left(-\frac{(1-u)nF\eta}{RT}\right) \quad (2.8)$$

These thermally activated rate constants lead to the Butler-Volmer equation for the transferred current  $i$ , wherein the description remains valid until  $\eta$  becomes large enough that reactant consumption becomes problematic:

$$i = i_0 \left\{ \exp\left(-\frac{unF\eta}{RT}\right) - \exp\left(-\frac{(1-u)nF\eta}{RT}\right) \right\} \quad (2.9)$$

EC materials and ion conductors must undergo the same characterization techniques to determine electrochemical and dependent optical properties. As such, the charge capacity and reversibility of an EC material are usually determined via cyclic voltammetry (CV) measurements. In a CV measurement, the potential at the working electrode (WE) is measured independently from the counter electrode (CE) via a reference electrode (RE) (Fig. 2.4(a)). Via a potentiostat, a constant voltage sweep rate is applied over time, which leads to the typical CV curve (Fig. 2.4(b)). The CV measurement shows the current flow as a function of applied potential to the WE with peak values for  $I_p$  close to  $E_{O, R}$ .

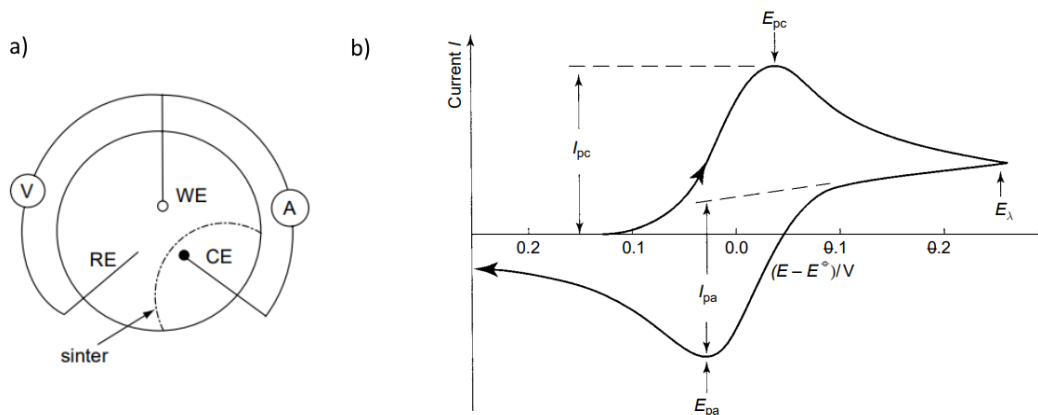


Fig. 2.4: Cyclic voltammetry for electrochemical analysis. (a) Schematic of the CV measurement cell. (b) Typical CV curve with anodic and cathodic peak currents ( $I_{PC,PA}$ ) and potentials ( $E_{pa,pc}$ ) indicated.<sup>14</sup>

The sweep rate can be adjusted to determine diffusion dependent properties, such as the charge capacity of the WE:

$$Q = \frac{\int Idt}{2v\Delta VA} \quad (2.10)$$

Evidently, the stored charge,  $Q$ , is dependent on the integrated current over time, the voltage window  $\Delta V$  and the sweep rate  $v$ . CV is the most important electrochemical analysis method for the intercalation dynamics of ionic species into EC materials and is often combined with simultaneous optical transmission measurements or voltage dependent investigation of the spectral response. Furthermore, detailed CV measurements allow linking the peak current density  $J_n$  to the diffusion coefficient  $D$  via the Randles-Sevcik equation:<sup>14</sup>

$$J_n = 2.69 \times 10^5 n^{3/2} C_0 D^{1/2} \nu^{1/2} \quad (2.11)$$

Additionally, electrochemical impedance spectroscopy (EIS) is utilized to determine the ionic conductivity of a given material through frequency dependent application of an external potential. Since most electrochemical conductors exist as complex elements acting as several resistances and parallel capacitors due to electrochemical potentials and interface effects, the measured impedance is conventionally comprised of a real and imaginary part. Through a Nyquist plot, it is possible to relate the high-frequency intercept of the  $x$ -axis to the ionic conductivity of the material.<sup>14</sup>

## 2.2 Optical Fields and Electromagnetic Waves in Photonic Devices

Photonics describes the engineering of devices and applications utilizing direct control of light (photons). Especially in photonic devices it is important to consider both the wave and particle nature of light. The temporal evolution and propagation of electromagnetic radiation in photonic devices is governed by its wave equation, while the energy of traversing photons leads to frequency conversion and light-matter interactions. Particularly in modern telecommunications, the photon energy ( $E_{ph} = 1.6 - 3.1 \text{ eV}$ ) is in the range of bandgap energies for most semiconductors.<sup>153</sup>

Table 6: Regions of the electromagnetic spectrum

Region of light	Frequency	Wavelength	Applications
Radio	kHz-GHz	km-cm	Electronics
Micro/MM-wave	1 GHz – 1 THz	300 mm – 300 $\mu\text{m}$	Telecommunication
Optical	1 THz – 10 PHz	300 $\mu\text{m}$ – 30 nm	Photonics
X-ray	10 PHz – 10 EHz	30 nm – 300 pm	Imaging and Diagnostics

The wave equation for light propagating in a linear medium, such as a photonic device composed of linear optical dielectrics and/or metals can be derived from the fundamental Maxwell's equations.<sup>153,154</sup>

$$\nabla \cdot \mathbf{D} = \rho \quad (2.12)$$

$$\nabla \cdot \mathbf{B} = 0 \quad (2.13)$$

$$\nabla \times \mathbf{E} = - \frac{\partial \mathbf{B}}{\partial t} \quad (2.14)$$

$$\nabla \times \mathbf{H} = \mathbf{J} + \frac{\partial \mathbf{D}}{\partial t} \quad (2.15)$$

Here,  $\mathbf{D}$  is the electric flux density and  $\mathbf{E}$  is the electric field, while  $\mathbf{B}$  is the magnetic flux density and  $\mathbf{H}$  is the magnetic field. Furthermore,  $\mathbf{J}$  is the current density, and  $\rho$  is the free charge density within the medium. Since Eqns. 2.14 and 2.15 describe the temporal evolution of the electric and magnetic fields, they can be used to derive the propagation of electromagnetic (EM) waves in an isotropic and linear medium

having no charges ( $\rho = 0$ ) or current ( $J = 0$ ). Solving the curl equation for 2.14 yields:

$$\nabla \times (\nabla \times \mathbf{E}) = \nabla \times \left( -\frac{\partial \mathbf{B}}{\partial t} \right) \quad (2.16)$$

With the vector identity  $\nabla \times (\nabla \times \mathbf{A}) = \nabla(\nabla \cdot \mathbf{A}) - \nabla^2 \mathbf{A}$ , Eq. 2.16 can be described as:

$$\nabla(\nabla \cdot \mathbf{E}) - \nabla^2 \mathbf{E} = -\frac{\partial}{\partial t} (\nabla \times \mathbf{B}) \quad (2.17)$$

Here, it is necessary to relate the microscopic electric field to the macroscopic electric flux density and polarization,  $\mathbf{P}$ , of the material as well as the magnetic field to the magnetic flux density and the magnetization,  $\mathbf{M}$ , of the material according to:

$$\mathbf{D} = \epsilon_0 \mathbf{E} + \mathbf{P} \quad (2.18)$$

$$\mathbf{B} = \mu_0 \mathbf{H} + \mu_0 \mathbf{M} \quad (2.19)$$

Where, the permittivity  $\epsilon_0 = 8.854 \times 10^{12}$  F/m and permeability of vacuum  $\mu_0 = 4\pi \times 10^{-7}$  H/m. Since a linear and isotropic medium is assumed, the polarization  $\mathbf{P}$  and magnetization  $\mathbf{M}$  can be directly related to the fundamental fields via:

$$\mathbf{P} = \epsilon_0 \chi_e \mathbf{E} \quad (2.20)$$

and

$$M = \chi_m H \quad (2.21)$$

With  $\epsilon_r = 1 + \chi_e$  and  $\mu_r = 1 + \chi_m$  Eqns 2.18 and 2.19 can be expressed as:

$$D = \epsilon_0 \epsilon_r E \quad (2.22)$$

and

$$B = \mu_0 \mu_r H \quad (2.23)$$

Within this work  $\mu_r = 1$ , since the magnetization of a material response time is much slower than the period of the oscillating optical electric field. With the help of Eqns. 2.12 - 2.15 and taking  $\rho = 0$ , Eq. 2.17 can be simplified to:

$$\nabla^2 E = \mu_0 \frac{\partial}{\partial t} (\nabla \times H) \quad (2.24)$$

Since  $J = 0$ , substituting 2.15 results in:

$$\nabla^2 E = \mu_0 \frac{\partial^2 D}{\partial t^2} \quad (2.25)$$

Using Eq. 2.20 and the speed of light  $c = 1/\sqrt{\mu_0 \epsilon_0} = 2.998 \times 10^8$  m/s as well as the refractive index  $n$  of the material defined as  $n = \sqrt{\epsilon_r}$ , the propagation of an electromagnetic wave in a medium can be described with:

$$\nabla^2 E = \frac{n^2}{c^2} \frac{\partial^2 E}{\partial t^2} \quad (2.26)$$

Similarly, one can obtain the following wave equation for the magnetic field:

$$\nabla^2 H = \frac{n^2 \partial^2 H}{c^2 \partial t^2} \quad (2.27)$$

It is further necessary to acknowledge the complex nature of the refractive index  $\tilde{n} = n + ik_{\text{ex}} = \sqrt{\varepsilon}$  with  $\varepsilon = \varepsilon_1 + i\varepsilon_2$ . Substituting the complex refractive index yields the optical properties of a given material where:

$$\varepsilon_1 = n^2 - k_{\text{ex}}^2 \quad (2.28)$$

$$\varepsilon_2 = 2nk_{\text{ex}} \quad (2.29)$$

$$n^2 = \frac{\varepsilon_1}{2} + \frac{1}{2} \sqrt{\varepsilon_1^2 + \varepsilon_2^2} \quad (2.30)$$

$$k_{\text{ex}} = \frac{\varepsilon_2}{2n} \quad (2.31)$$

Here,  $k_{\text{ex}}$  is the extinction coefficient of a given material and relates to the absorption of electromagnetic radiation in a lossy medium via Lamberts' law and the absorption coefficient:

$$\alpha = \frac{2k_{\text{ex}}\omega}{c} \quad (2.32)$$

The fundamental wave equation will be used in following paragraphs to explain linear and nonlinear optical properties of materials and structures investigated in this thesis.

## 2.2.1 Harmonic Oscillations in the Free Electron Gas

The optical properties of linear and isotropic materials and, hence, their interaction with light can be modeled by a plasma mass-spring harmonic oscillator model, where a bound electron cloud is displaced with respect to a fixed positively charged nucleus. The total driving force,  $F_{\text{tot}}$ , behind such a process due to the applied electric field force,  $F_{\text{app}}$ , resulting from the electric field  $E(t) = E_0 \cdot e^{-i\omega t}$  of the EM wave, the damping force,  $F_{\text{damp}}$ , due to collisions, and the restoring force,  $F_{\text{rest}}$ , which is modeled as a simple spring force of a spring constant  $k_{\text{sp}}$ . This force acting on the electron cloud leads to a displacement of  $x(t) = x_0 \cdot e^{-i\omega t}$ . In a one-dimensional scenario, this mass-spring damped harmonic oscillator force and displacement can be described respectively as:

$$F_{\text{tot}} = F_{\text{app}} + F_{\text{rest}} + F_{\text{damp}} \quad (2.33)$$

$$m_e \ddot{x} = eE(t) - k_{\text{os}}x - m_e \gamma \dot{x} \quad (2.34)$$

Where,  $\gamma = 1/\tau$  is the damping coefficient which is related to the is the relaxation time of the electron cloud,  $\tau$ , ( $\sim 10^{-14}$  s),  $m_e = 9.1 \times 10^{-31}$  kg is the mass of an electron, and  $e = -1.6 \times 10^{-19}$  is the electric charge of an electron. With the resonant frequency of the harmonic oscillator,  $\omega_0 = \sqrt{k_{\text{os}}/m_e}$ , Eq. 2.34 yields the time dependent displacement:

$$x(t) = \frac{e}{m_e(\omega_0^2 - i\gamma\omega - \omega^2)} E(t) \quad (2.35)$$

The displacement of electrons relative to the fixed nucleus leads to an induced dipole moment for every single atom, which in sum creates a macroscopic polarization  $P = Np = Nex(t)$ . Assuming small, linear displacements, the polarization of a material can hence be related to the electric field via:

$$P(t) = \frac{n_e e^2}{m_e (\omega_0^2 - i\gamma\omega - \omega^2)} E(t) \quad (2.36)$$

Substituting and defining the plasma frequency of the displaced electrons as  $\omega_p =$

$\sqrt{\frac{n_e e^2}{\epsilon_0 m_e}}$  yields:

$$D(t) = \epsilon_0 \left( 1 - \frac{\omega_p^2}{\omega_0^2 - i\gamma\omega - \omega^2} \right) E(t) \quad (2.37)$$

Hence, it is obvious that:

$$\epsilon_r = 1 + \frac{\omega_p^2}{\omega_0^2 - i\gamma\omega - \omega^2}. \quad (2.38)$$

## 2.2.2 Bulk Plasmons

Bulk plasmons describe the quantized oscillation of the free electrons along a metal or conductor. When considering an EM wave transparency regime, where  $\omega > \omega_p$ , the propagation of waves in a metallic substance can be described with the properties derived from Maxwell's equations. In case of a monochromatic and transverse EM wave (i.e.,  $\nabla \cdot E = 0$ ), the dispersion relation has the form:

$$\omega^2 \epsilon(\omega) = c^2 k^2 \quad (2.39)$$

With  $k$  the wave vector. Using Drude's dispersion law, Eq. 2.39 simplifies to:

$$\omega^2 = \omega_p^2 + c^2 k^2 \quad (2.40)$$

Hence, the dispersion for bulk plasmons follows:

$$\omega = \sqrt{\omega_p^2 + c^2 k^2} \quad (2.41)$$

It becomes obvious, that even when wave vectors are small, the frequency of the electron cloud is not zero, but tends towards the bulk plasmon frequency. It is further stated here, that when Eq. 2.41 is fulfilled, the permittivity becomes positive and, thus, the metal is transparent to the propagating EM wave.

## 2.3 Nanoplasmonics

The field of nanoplasmonics is the study of optical properties of metallic nanostructures as determined by the oscillations of their conduction electrons. Two distinct effects usually come together when discussing nanoplasmonics: First, the optical field is strongly localized and enhanced due to structure's nanoscale dimensions. Second, the plasma frequency of the investigated structure is in the visible or NIR spectral range. Two classes of plasmons will be explained in the following, surface plasmon polaritons (SPP) as observed on metal-dielectric interfaces and localized surface plasmon resonances (LSPR) occurring around metallic nanostructures or nanovoids.

### 2.3.1 Helmholtz Equation for Propagating Waves

To describe the propagation of plasmons at a perfectly flat metal-dielectric interface, the wave equation Eq. 2.26 can be rearranged to the Helmholtz equation for harmonic time dependence of the electric field:

$$\nabla^2 E + k_0^2 \epsilon E = 0 \quad (2.42)$$

With  $k_0$  the wavevector in vacuum. If the propagation symmetry is defined as a perfectly flat surface, then  $\epsilon = \epsilon(z)$  and  $z = 0$  defines the propagation plane of the wave. Furthermore, propagation occurs in  $x$ -direction with no variation of  $\epsilon$  along the  $y$ -direction (Fig. 2.5). Hence, the propagating wave can be described as:

$$E(x, y, z) = E(z) e^{i\beta x} \quad (2.43)$$

With  $\beta = k_x$  being the complex plasmon wavevector in  $x$ -direction which includes the corresponding part of the wavevector in the propagation direction. Inserting Eq. 2.43 into Eq. 2.42 yields the spatially dependent wave equation:

$$\frac{\partial^2 E(z)}{\partial z^2} + (k_0^2 \epsilon - \beta^2) E(z) = 0 \quad (2.44)$$

Notably, a similar solution exists for the magnetic field. With the harmonic time dependence  $(\partial/\partial t = -i\omega)$  and propagation in  $x$ -direction  $(\partial/\partial x = i\beta)$ , as well as homogeneity in  $y$ -direction  $(\partial/\partial y = 0)$  a set of coupled equations for the electric and magnetic field components in  $x$ -,  $y$ - and  $z$ -direction can be derived from the curl equations:

$$\frac{\partial E_y}{\partial z} = -i\omega\mu_0 H_x \quad (2.45a)$$

$$\frac{\partial E_x}{\partial z} - i\beta E_z = i\omega\mu_0 H_y \quad (2.45b)$$

$$i\beta E_y = i\omega\mu_0 H_z \quad (2.45c)$$

$$\frac{\partial H_y}{\partial z} = i\omega\epsilon_0 \epsilon E_x \quad (2.45d)$$

$$\frac{\partial H_x}{\partial z} - i\beta H_z = -i\omega\epsilon_0 \epsilon E_y \quad (2.45e)$$

$$i\beta H_y = -i\omega\epsilon_0 \epsilon E_z \quad (2.45f)$$

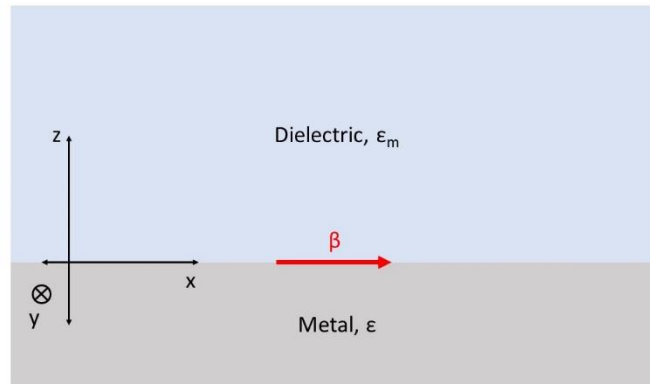


Fig. 2.5: Schematic of the propagating wave at the metal-dielectric interface

This set of equations has two sets of self-consistent solutions with p-polarization, defined with  $E_x$ ,  $E_y$  and  $H_y$  being non-zero and s-polarization defined here as the transverse electric wave (TE) with  $H_x$ ,  $H_z$  and  $E_y$  non-zero. Hence, the wave equation for TM waves is:

$$\frac{\partial^2 H_y}{\partial z^2} + (k_0^2 \varepsilon - \beta^2) H_y = 0 \quad (2.46)$$

And similarly, the wave equation for TE modes can be written as:

$$\frac{\partial^2 E_y}{\partial z^2} + (k_0^2 \varepsilon - \beta^2) E_y = 0 \quad (2.47)$$

Notably, these equations are generally valid for propagating electromagnetic waves and can describe optical modes in waveguiding arrangements as well as plasmon propagation.

### 2.3.2 Surface Plasmon Polaritons

Surface plasmon polaritons (SPP) are propagating, dispersive electromagnetic waves coupled to the free electrons at the interface between a metal (or a good conductor) and a dielectric. In the simplest case, SPPs are sustained at the perfect, flat interface defined in Section 2.3.1. For a metal-dielectric interface, where the half-space  $z > 0$  occupied by a dielectric having a positive real permittivity  $\varepsilon_2$  and the  $z < 0$  half-space is a metal having a dielectric function  $\varepsilon_1(\omega)$ . For frequencies below  $\omega_p$ , the metallic character of this half-space implies that  $\text{Re}[\varepsilon_1] < 0$ . To describe SPP propagating wave, we seek a wave propagating along the  $x$ -direction and evanescently decaying in  $z$ -direction. As such, for  $z > 0$ , the TM solutions are:

$$H_y(z) = A_2 e^{i\beta x} e^{-ik_2 z} \quad (2.48a)$$

$$E_x(z) = iA_2 \frac{1}{\omega \varepsilon_0 \varepsilon_2} k_2 e^{i\beta x} e^{-ik_2 z} \quad (2.48b)$$

$$E_z(z) = -A_1 \frac{1}{\omega \epsilon_0 \epsilon_2} \beta e^{i\beta x} e^{-ik_2 z} \quad (2.48c)$$

And for  $z < 0$ :

$$H_y(z) = A_1 e^{i\beta x} e^{ik_1 z} \quad (2.49a)$$

$$E_x(z) = -iA_1 \frac{1}{\omega \epsilon_0 \epsilon_1} k_1 e^{i\beta x} e^{ik_1 z} \quad (2.49b)$$

$$E_z(z) = -A_1 \frac{1}{\omega \epsilon_0 \epsilon_1} \beta e^{i\beta x} e^{ik_1 z} \quad (2.49c)$$

Here,  $A_i$  is the amplitude of the propagating field and  $k_i$  is the component of the wavevector perpendicular to the interface between the metal and the dielectric. Due to the continuity of  $H_y$  and  $E_z$  at the interface,  $A_1 = A_2$  and hence:

$$\frac{k_2}{k_1} = -\frac{\epsilon_2}{\epsilon_1} \quad (2.50)$$

Since,  $\text{Re}[\epsilon_1] < 0$  and  $\epsilon_2 > 0$ , these modes can only exist at the interface of the metal and the dielectric. Furthermore, since Eq. 2.46 has to be fulfilled, we obtain:

$$k_1^2 = \beta^2 - k_0^2 \epsilon_1 \quad (2.51)$$

$$k_2^2 = \beta^2 - k_0^2 \epsilon_2 \quad (2.52)$$

With the above equations (2.52 and 2.53), the dispersion relation for a SPP at an interface can be expressed as:

$$\beta = k_0 \sqrt{\frac{\epsilon_1 \epsilon_2}{\epsilon_1 + \epsilon_2}} \quad (2.53)$$

Starting above derivations for TE modes shows that SPP only exist for p-polarization or as TM modes.

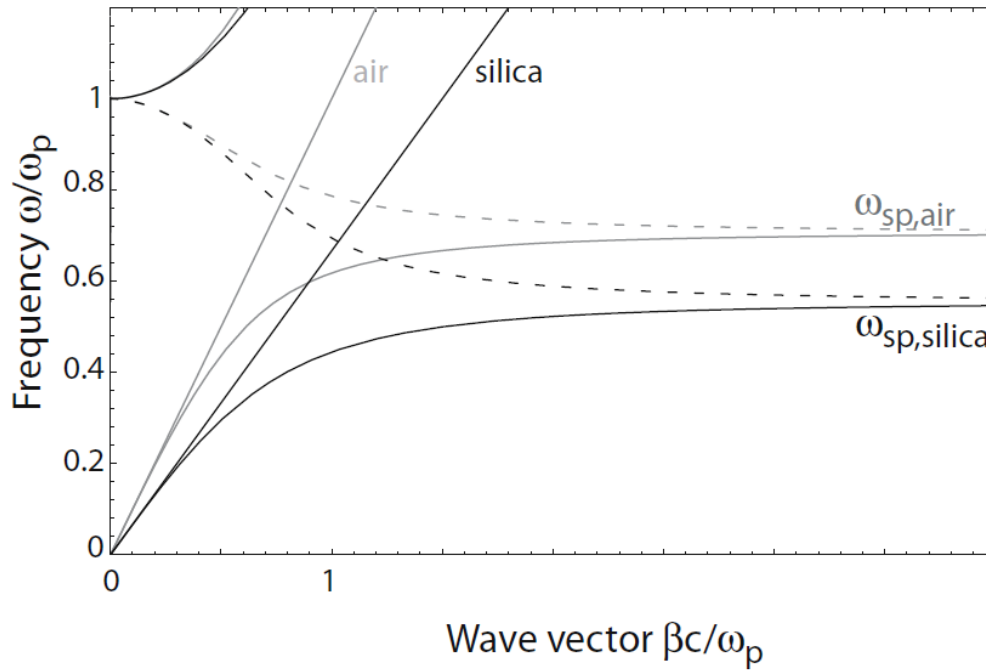


Fig. 2.6: SPP dispersion relation at an interface between a lossless metal and air (grey) and silica (black). The dashed lines indicate purely imaginary propagation constants between the bound and the radiative states.<sup>155</sup>

Fig. 2.6 shows the dispersion relation for SPPs at the interface between a (i) Drude metal ( $\epsilon_1 < 0$ ) and air ( $\epsilon_2 = 1$ ) and (ii) the same Drude metal and silica ( $\epsilon_2 = 2.25$ ). Shown are the real parts of the wavevector  $\beta$  (continuous lines) and the imaginary parts (dashed lines). Due to their bound nature, the SPPs lay to the right

of their respective lightlines (i.e., the straight lines), which indicates that direct coupling of an optical field to these states is impossible since conservation of momentum is not satisfied. Hence, light field coupling through gratings or higher refractive index prisms is necessary.<sup>156</sup> As can be seen from the figure, the lightline for silica intersects the SPP line for air which implies that conservation of momentum is possible when a metal-air plasmon is excited with an optical beam incident from silica. The dashed lines indicate purely imaginary propagation constants between the bound and the radiative states. For small frequencies (i.e., in the NIR and MIR region), the SPP propagation constant is close to  $k_0$ , while for large frequencies, the SPP approaches the characteristic surface plasmon frequency,  $\omega_{SP}$ , is:

$$\omega_{SP} = \frac{\omega_P}{\sqrt{1 + \epsilon_2}} \quad (2.54)$$

The most important property of SPPs is their inherent localization and, thus, the confinement of the electric field wherein,

$$\beta > \frac{\omega}{c} \sqrt{\epsilon_2} \quad (2.55)$$

With the wavevector of the surface plasmon  $\beta$ . Since the  $z$ -components of the wavevector are purely imaginary, the electric field decays exponentially away from the metal-dielectric interface. In case of a lossy metal, (i.e., a metal that exhibit inherent losses ( $\epsilon = \epsilon' - i\epsilon''$ ) with  $\epsilon'$  the real and  $\epsilon''$  the imaginary part of the permittivity),  $\beta$  is small, indicating that  $(\epsilon'_1 + \epsilon'_2)^2 \gg \epsilon_2''$  and the decay length,  $\delta_{SPP}$ , for the SPPs along their propagation direction is given by:

$$\delta_{\text{SPP}} = \frac{1}{2\beta''} \approx \frac{c}{\omega} \left( \frac{\epsilon'_1 + \epsilon_2}{\epsilon'_1 \epsilon_2} \right)^{3/2} \frac{\epsilon_1'^2}{\epsilon_1''} \quad (2.56)$$

Where  $\beta''$  is the imaginary part of the surface plasmon wavevector. In reality,  $\delta_{\text{SPP}} \approx 20 \mu\text{m}$  and the localization parameter perpendicular to the surface  $\delta_z (= \frac{1}{k_z}) \approx 200 \text{ nm}$ , for a silver-air interface at short wavelengths frequencies (e.g.,  $\lambda = 450 \text{ nm}$ ). The propagation length and the confinement increase dramatically at telecommunication wavelengths ( $\sim \lambda = 1550 \text{ nm}$ ) with  $\delta_{\text{SPP}} \approx 1 \text{ mm}$  and  $\delta_z \approx 3 \mu\text{m}$ . SPPs are utilized in plasmonic waveguides for high field enhancement and strong localization.<sup>86,157,158</sup> Such devices exhibit strong subwavelength confinement, which can be utilized for enhanced light-matter interaction in nonlinear waveguides.<sup>159,160</sup> In waveguiding applications, a trade-off has to be made between field-enhancement and propagation length. The strong dependence of SPP coupling on the dielectric environment is further exploited for sensing applications. In the so-called Kretschmann configuration,<sup>155</sup> the incident light field is coupled to a metal-air interface through a glass prism ( $n_g = 1.44$ ), so that the in-plane momentum of the plasmon can be described as:

$$\beta = n_g k_0 \sin(\theta_i) \quad (2.57)$$

With  $\theta_i$  the internal (i.e., inside the glass prism) incident angle of the photon onto the metal layer. The reflectance of the interface decreases sharply when the resonance angle  $\theta_{\text{SP}}$  is reached. This is achieved when the wavevector of the plasmon equals the parallel component of the incident beams wavevector. If the dielectric properties of the metal-air interface change, the SPP resonance angle

changes. This phenomenon is used to detect molecule adhesion and other changes in the environment.<sup>156,161</sup>

### 2.3.3 Localized Surface Plasmon Resonance

Localized surface plasmon resonances (LSPR) occur as non-propagating oscillations of the electron plasma of a metal or a good conductor having nanoscale dimensions. When an electromagnetic wave couples to the conduction electrons of a metallic nanostructure, the non-flat surface of the particle acts as a restoring force on the excited electrons. Hence, a resonance with field amplifications inside the structure and in its near-field environment can arise. The easiest description of such LSPRs can be made in the case of the quasi-static approximation, where the particle dimensions  $d \ll \lambda$ . This approximation is valid for nanoparticles with dimensions below 100 nm. For the purpose of the discussion, the following derivation assumes an isotropic, homogenous sphere having radius  $a$ . The surrounding medium is a dielectric having permittivity of constant  $\epsilon_m$  and the dielectric response of the sphere is described by a complex permittivity,  $\epsilon$ .

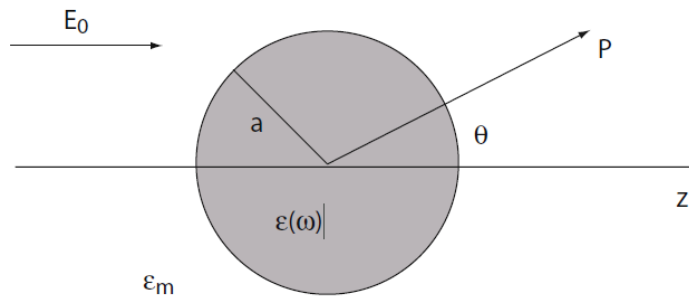


Fig. 2.7: Sketch of a homogeneous sphere placed into an electrostatic field.<sup>155</sup>

Such a sphere is placed at the origin in a static electric field  $E = E_0 \hat{z}$  with field lines parallel to the  $z$ -axis (Fig. 2.7). The solution for such a problem is given by solving the electrostatic potential,  $\Phi$ , using Laplace equation  $\nabla^2 \Phi = 0$  and consequently the solution for the electric field is obtained from  $E = -\nabla \Phi$ . This approach leads to solutions for the potential inside ( $\Phi_{\text{in}}(r, \theta)$ ) and outside ( $\Phi_{\text{out}}(r, \theta)$ ) of the sphere as:

$$\Phi_{\text{in}}(r, \theta) = \sum_{l=0}^{\infty} A_l r^l P_l(\cos(\theta)) \quad (2.58)$$

$$\Phi_{\text{out}}(r, \theta) = \sum_{l=0}^{\infty} [B_l r^l + C_l r^{-(l+1)}] P_l(\cos(\theta)) \quad (2.59)$$

Here,  $P_l(\cos(\theta))$  are Legendre Polynomials of order  $l$  and  $\theta$  is the angle between the position vector,  $r$ , at point  $P_1$  and the  $z$ -axis. The solutions for  $A_l$ ,  $B_l$  and  $C_l$  can be determined from the boundary conditions at the sphere surface ( $r = a$ ) and at  $r \rightarrow \infty$ . For  $r \rightarrow \infty$ , the potential outside the sphere is given by  $\Phi_{\text{out}} = -E_0 z = -E_0 r \cos(\theta)$ , so that  $B_1 = -E_0$  and  $B_l = 0$  for  $l \neq 1$ .  $A_l$  and  $C_l$  can be determined via the equality of the tangential components of the electric field at  $r = a$ :

$$-\frac{1}{a} \frac{\partial \Phi_{\text{in}}}{\partial \theta} \Big|_{r=a} = -\frac{1}{a} \frac{\partial \Phi_{\text{out}}}{\partial \theta} \Big|_{r=a} \quad (2.60)$$

and equating the normal components of the displacement field:

$$-\epsilon_0 \epsilon \frac{\partial \Phi_{\text{in}}}{\partial r} \Big|_{r=a} = -\epsilon_0 \epsilon_m \frac{\partial \Phi_{\text{out}}}{\partial r} \Big|_{r=a} \quad (2.61)$$

For these boundary conditions,  $A_l$  and  $C_l = 0$  for  $l \neq 1$  and, hence, using only the real parts of the respective permittivities, the potentials can be expressed as:

$$\Phi_{\text{in}}(r, \theta) = -\frac{3\varepsilon_m}{\varepsilon + 2\varepsilon_m} E_0 r \cos(\theta) \quad (2.62)$$

$$\Phi_{\text{out}}(r, \theta) = -E_0 r \cos(\theta) + \frac{\varepsilon - \varepsilon_m}{\varepsilon + 2\varepsilon_m} E_0 a^3 \frac{\cos(\theta)}{r} \quad (2.63)$$

Interestingly, Eq. 2.63 describes the superposition of an external electric field and a dipole moment at the center of the particle. Introducing the dipole moment,  $p$ , as:

$$p = 4\pi\varepsilon\varepsilon_m a^3 \frac{\varepsilon - \varepsilon_m}{\varepsilon + 2\varepsilon_m} E_0 \quad (2.64)$$

And substituting in Eq. 2.63 yields:

$$\Phi_{\text{out}} = -E_0 r \cos(\theta) + \frac{p \cdot r}{4\pi\varepsilon\varepsilon_m r^3} \quad (2.65)$$

The induced dipole moment is proportional to the outside electric field following its polarizability via  $p = \varepsilon_0 \varepsilon_m \alpha E_0$  where,

$$\alpha = 4\pi a^3 \frac{\varepsilon - \varepsilon_m}{\varepsilon + 2\varepsilon_m} \quad (2.66)$$

Such a complex polarizability experiences a resonance when  $|\varepsilon + 2\varepsilon_m|$  is minimum. Under the assumption of slowly varying  $\text{Im}[\varepsilon_1]$ , the resonance condition simplifies to:

$$\text{Re}[\varepsilon(\omega)] = -2\varepsilon_m \quad (2.67)$$

Evidently, this condition can only be satisfied for a metal-dielectric interface due to the negative sign of the real part of the permittivity of the metal. This Fröhlich condition describes the dipole surface plasmon for a metal nanoparticle. For a metallic particle situated in air, the resonance condition is met at:

$$\omega = \frac{\omega_p}{\sqrt{3}} \quad (2.68)$$

It is further evident, that the resonance experiences a red shift when  $\varepsilon_m$  is increased. This property is commonly exploited in LSPR based metal nanoparticle sensing applications.

### 2.3.4 Plasmonic Loss

The inherent loss experienced by SPPs and LSPR can be explained through the conservation of energy in an optical resonator. If the characteristic length of a dielectric is larger than the wavelength  $l \gg \lambda$ , every half-period of oscillation, the electric field energy density,  $u_E$ , is transferred to magnetic field energy density,  $u_H$ , and vice versa. That is,

$$u_E = u_H \quad (2.69)$$

Or

$$\frac{1}{2} \varepsilon E^2 = \frac{1}{2} \mu H^2 \quad (2.70)$$

This phenomenon is similar to a mass on a spring, with conservation of energy between kinetic and potential energies. In the case of the large optical resonator, both E and H field sinusoidally oscillate as  $\sin\left(\frac{2\pi x}{\lambda}\right)$ . As such, Maxwell equations are satisfied when  $H = \sqrt{\epsilon/\mu}E$  and, hence,  $u_E = u_H$  (Fig. 2.8(a)). If the characteristic size is reduced to  $l < \frac{\lambda}{2n}$ , with n the refractive index of the medium, the field dependency becomes  $\sin\left(\frac{\pi x}{l}\right)$ . Hence, for cavities with sub-wavelength dimensions, the magnetic field energy is much less than the electric field energy and the cavity radiates. Self-sustaining oscillations are only possible if energy is stored as kinetic energy,  $u_K$ , where:<sup>162</sup>

$$u_E = u_H + u_K \quad (2.71)$$

With:

$$u_K \sim \frac{1}{2} \epsilon_0 \frac{\omega_p^2}{\omega^2} E^2 \quad (2.72)$$

The plasma frequency  $\omega_p$  for most metals is in the UV spectral region. The energy balance can be restored at frequencies  $\omega_{SP}$ . Hence, SPPs and LSPRs can be propagating or be localized with characteristic wavelength  $\lambda_p < \frac{\lambda_0}{2n}$ . Since the magnetic field strength is less than, the electric field resembles an electrostatic field, fulfilling the quasi-static approximation in Section 2.3.3. Even though this approach effectively beats the diffraction limit, storing energy in form of kinetic energy leads to scattering of electrons in the metal. The rate of scattering in metals

is on the order of 10 fs, which indicates that SPP energy is lost on the same time scale.

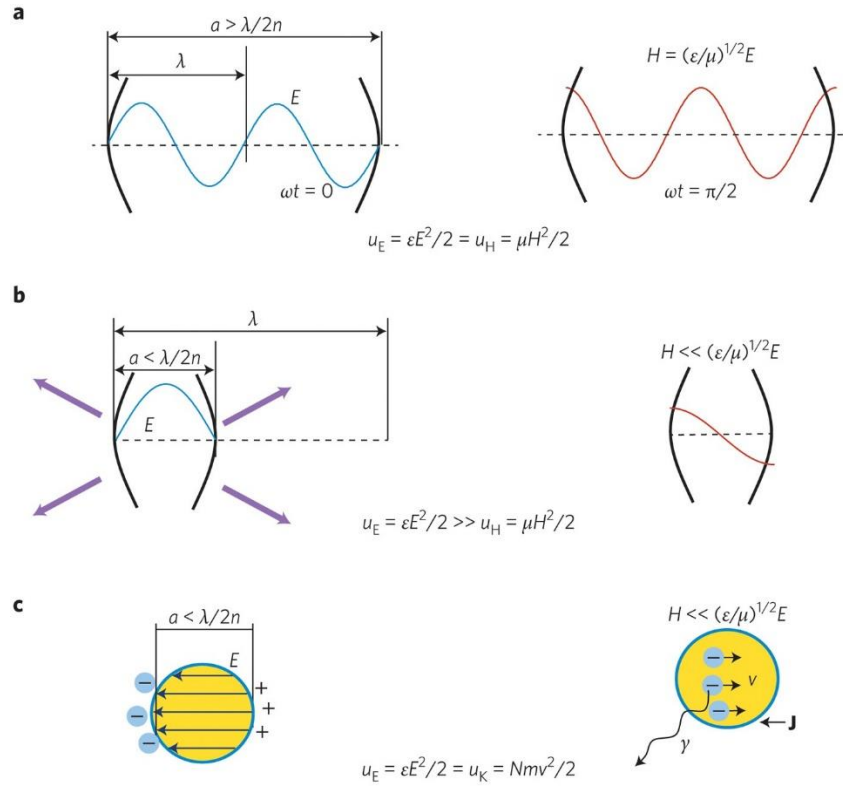


Fig. 2.8: (a) In an optical cavity with dimensions larger than half wavelength  $\lambda/2n$  energy alternates between  $u_E$  (left), and  $u_H$  (right). (b) In a cavity with a characteristic size  $< \frac{\lambda}{2}$ ,  $u_H$  is too small; hence, the cavity radiates energy out (purple arrows). (c) Free carriers lead to a current flow,  $J$ , and the energy alternates between  $u_E$  and kinetic energy of carriers  $u_K$ . The optical diffraction limit is overcome, but the motion of carriers is strongly damped at a rate  $\gamma$ , and the SPP mode becomes lossy.<sup>162</sup>

## 2.4 Nonlinear Optical Materials

In Section 2.2 a linear and isotropic material is assumed to derive the equations necessary to describe the propagation of an electromagnetic wave. However, under sufficiently high optical excitation, the response of a given material deviates from the linear response case and nonlinear phenomena occur. First demonstrations of nonlinear effects in form of second-harmonic generation (SHG) date back to 1961.<sup>163</sup> Frequency doubled radiation is generated by the part of the material's response that scales quadratically with the power of the excitation electric field. Higher orders of the material's response scale accordingly. Hence, it is necessary to append Eq. 2.20 and formulate the polarization to include nonlinear polarization terms accordingly,

$$P(t) = \epsilon_0 [\chi^{(1)}E(t) + \chi^{(2)}E(t)^2 + \chi^{(3)}E(t)^3 + \dots] \quad (2.73)$$

where,  $\chi^{(n)}$  describes the n-order of the optical susceptibility of the material. The first term (i.e., for  $n = 1$ ,  $\epsilon_0\chi^{(1)}E(t)$ ) in Eq. 2.75 denotes the linear polarization of the material. It is important to note that  $\chi^{(2n)}$  vanishes in centrosymmetric crystals, so that only polarization effects of uneven order occur in such materials. The nonlinear polarization,  $P^{NL}(= \epsilon_0[\chi^{(2)}E(t)^2 + \chi^{(3)}E(t)^3 + \dots])$ , can act as the source for new components of the electromagnetic field and, hence, the wave equation in nonlinear optics is given as:

$$\nabla^2 E - \frac{n^2}{c^2} \frac{\partial^2 E}{\partial t^2} = \frac{1}{\epsilon_0 c^2} \frac{\partial^2 P^{NL}}{\partial t^2} \quad (2.74)$$

Where,  $n$  is the linear refractive index and  $c$  is the speed of light in vacuum. This inhomogeneous wave equation indicates the nonlinear polarization  $P^{NL}$  as a source for the electric field. Notably, the  $\frac{\partial^2 P^{NL}}{\partial t^2}$  term describes the acceleration of electrons, which in turn generates electromagnetic radiation at various frequencies.

### 2.4.1 Second Harmonic Generation

Second harmonic generation (SHG) describes a nonlinear process in which an incident laser beam at frequency  $\omega$  induces a second order nonlinear polarization which in turn leads to the generation of EM radiation at a frequency  $2\omega$ . For an incident electric field strength represented as:

$$E(t) = Ee^{-i\omega t} + E^*e^{i\omega t} = Ee^{-i\omega t} + c. c. \quad (2.75)$$

The second order nonlinear polarization,  $P^{(2)}(t)$ , induced by such an optical electric field in a medium where  $\chi^{(2)} \neq 0$  is:

$$P^{(2)}(t) = 2\varepsilon_0\chi^{(2)}EE^* + \varepsilon_0\chi^{(2)}E^2e^{-i2\omega t} + c. c. \quad (2.76)$$

Here, the second-order polarization consists of two terms: the first term is a none oscillating polarization and the second term is polarization oscillating at frequency  $2\omega$ . According to Eq. 2.78, the nonlinear polarization can, hence, lead to the generation of second harmonic radiation. The first term in Eq. 2.77 leads to a process called optical rectification, which generates a static electric field across the medium.

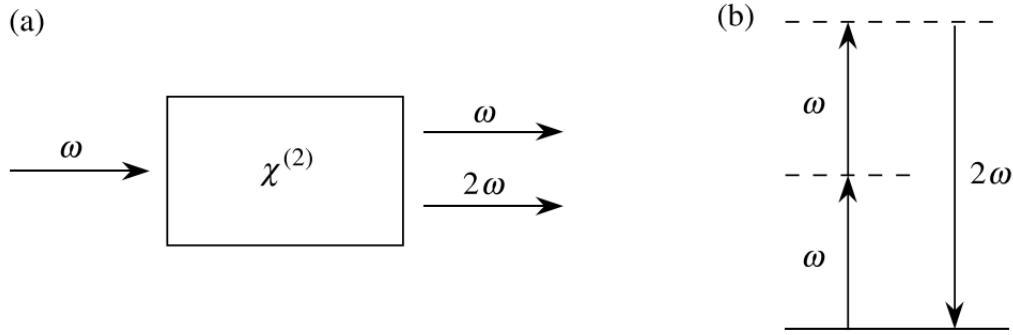


Fig. 2.9: Second harmonic generation process. (a) Schematic of the SHG process. (b) Energy level description of SHG.

## 2.4.2 Second Order Nonlinearity in Silicon Nitride

To create even order nonlinearities in complementary metal-oxide semiconductor (CMOS) compatible centrosymmetric crystals, surface inhomogeneities and induced stress are utilized to locally break such a crystalline symmetry. As such, the centrosymmetric Silicon crystal has been found to exhibit strong second order nonlinearities ( $\chi_{\text{eff}}^{(2)} = 0.6 \text{ pm/V}$ ) if strained with Silicon Nitride cladding.<sup>164</sup> While it is conventionally believed that surface stress or strain induce the second order nonlinearity, Castellán *et al.* found that a UV treatment could eliminate such a nonlinearity in Si waveguides having  $\text{Si}_3\text{N}_4$  cladding.<sup>164</sup> The authors suggested that K centers at the cladding interface, a site where one Si atom is bound to three N atoms, induce a DC electric field through differently charged dangling bonds. The K centers exist in three differently charged states, with the  $\text{K}^+$  state (no electron in the dangling bond) being the most favorable. Due to the cladding interface,  $\text{K}^+$  centers form and induce a second order nonlinearity through electric-field-induced second harmonic generation (EFISH) as a third order

nonlinear process  $\chi_{\text{EFISH}}^{(2)} = 3\chi^{(3)}E_{\text{DC}}$ . Similarly, Silicon Nitride films and waveguides have been investigated for their second order nonlinear properties when cladded with SiO<sub>2</sub>. Lettieri *et al.* found the second order nonlinear response of amorphous SiN<sub>x</sub> films to be strongly localized to the interfaces with other materials.<sup>165</sup> On the other hand, Lipson *et al.* attributed the second harmonic generation (SHG) in a Si<sub>3</sub>N<sub>4</sub> ring resonator to symmetry breaking through cladding induced stress.<sup>166</sup> Second order nonlinearities values have been reported to be between  $\chi_{\text{eff}}^{(2)} = 0.1$  and 1 pm/V.<sup>108,167,168</sup> It is suggested, that such a nonlinearity can be adjusted by varying the chemical composition and the deposition parameter. Si rich SiN<sub>x</sub> films have shown enhanced nonlinear properties, which suggests that not just interfacial, but also dangling bonds in the bulk film can lead to induced nonlinearities.<sup>169</sup>

In another approach, the electric field necessary for the EFISH process is induced optically. By exciting a waveguide structure with a sufficiently strong CW-laser beam, free charges accumulate periodically along the waveguide. These free charges not only form a DC field which can induced second harmonic generation via EFISH, but also lead to efficient quasi-phase matching through self-induced optical poling.<sup>168,170</sup> The induced grating has a period of:

$$\Lambda = \frac{\lambda}{2(n_{\text{SH}} - n_{\text{FE}})} \quad (2.77)$$

With  $n_{\text{SH}}$  and  $n_{\text{FE}}$  the effective refractive indices for the optical mode at the second harmonic (SH) wavelength and the fundamental wavelength (FE), respectively.

# Chapter 3

## Materials for Electrochromic Devices

EC technology and applications have spawned a variety of routinely used deposition methods for EC materials, as well as ionic conductors. As such, dip- and spray coating,<sup>37</sup> electrodeposition,<sup>171–174</sup> chemical bath deposition,<sup>114,175,176</sup> reactive magnetron sputtering,<sup>121,177,178</sup> and several sol-gel methods have been employed to deposit EC oxides.<sup>179,180</sup> Most commonly, these approaches target to increase the EC optical transmission modulation and switching speed along with the chemical and thermal stability of the EC material. Additionally, liquid electrolytes based on aqueous alkali solutions or organic solvents are used,<sup>6,37,131</sup> along with solid-state and quasi-solid-state electrolytes based on polymer ion conductors or metal oxides.<sup>123,131,132,181</sup> An electrolyte for ECDs needs to possess high optical transparency paired with sufficient ionic conductivity. The performance of an ECD is, hence, dependent on the performance of these components individually and ultimately their interactions with each other. However, to date, no studies have been reported on the compatibility of these fabrication methods with common nanofabrication techniques. As such, in the following chapter, several processes for the fabrication of EC  $\text{WO}_3$  and suitable ion conductors are presented and compared regarding their suitability for microfabrication.  $\text{WO}_3$  is chosen over other EC oxides due to its large change in dielectric properties during redox ion intercalation and ready availability.

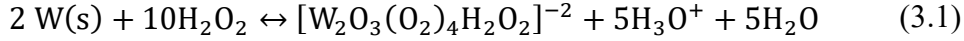
This chapter is organized as follows: first, several different deposition methods for  $\text{WO}_3$  are investigated and compared for their suitability for nanofabrication processes (Section 3). Next, Section 3.2 presents a comparison of common polymeric and solid-state ion conductors for application in ECDs. In Section 3.3 the properties of a liquid electrolyte based  $\text{WO}_3$ -NiO supercapacitors are investigated for EC optical transmission modulation switching and charge capacity. Next, Section 3.4 presents a novel dual-ion EC battery based on a modified DMSO based hydrogel electrolyte which is shown to exhibit superior thermal properties and prolonged lifetime.<sup>131</sup> An approach to increased EC electrode lifetime, through modification with a self-assembled monolayer, are presented in Section 3.5.<sup>182</sup>

### 3.1 Deposition Methods for EC $\text{WO}_3$

Electrochromic  $\text{WO}_3$  undergoes a strong insulator to semiconductor transition during electrochemical cycling,<sup>183-185</sup> and, hence, creates the large change in optical properties necessary for integrated ECDs. There is, however, a variety of fabrication techniques for EC  $\text{WO}_3$  that involve wet and dry chemical methods. Here, the EC and morphological properties of  $\text{WO}_3$  deposited via electrodeposition, spray coating, and reactive magnetron sputtering are investigated and compared to each other.

Electrodeposition and spray coating of  $\text{WO}_3$  thin films start with the same precursor solution. 1.8 g of metallic tungsten powder are dissolved in 60 ml 30%  $\text{H}_2\text{O}_2$  under constant stirring at  $T = 60^\circ\text{C}$ . After 24 h, the W forms peroxo tungstic

complexes with the peroxide, such as  $[\text{W}_2\text{O}_3(\text{O}_2)_4\text{H}_2\text{O}_2]^{2-}$ .<sup>186</sup> The main chemical reaction occurring during dissolution of W powder is:



The precursor solution can then be used to reduce W(IV) to W(VI)O<sub>3</sub> via direct reduction in electrodeposition or thermal annealing of spray coated films at temperatures above  $T > 200^\circ\text{C}$ .

On the other hand, WO<sub>3</sub> thin films can also be directly sputtered onto the ECD electrode. Reactive magnetron sputtering of WO<sub>3</sub> is realized from a metallic W sputtering target under oxygen atmosphere. Gas flow ratios, plasma power, and chamber pressure determine the EC and optical properties of the deposited films.

### 3.1.1 Morphological Comparison

Electrodeposition of WO<sub>3</sub> through direct reduction at the working electrode is conducted in a three-electrode setup with a Pt wire as the counter electrode and a Ag/AgCl reference electrode in saturated KCl. The deposition is conducted at a constant potential  $V = -500 \text{ mV}$  for different periods of time. Consequently, the time-dependent deposition current and corresponding film thicknesses are measured. Typically, the WO<sub>3</sub> films are grown onto  $1 \times 2 \text{ cm}^2$  pieces of ITO on glass ( $R_{\text{Sh}} < 20 \text{ } \Omega/\text{sq}$ ). As shown in Fig. 3.1, the deposition current density,  $J$ , increases rapidly in the first 15 s and reaches a maximum value of  $J = 5.25 \text{ mA/cm}^2$ . Beyond this time,  $J$  decreases rapidly from  $J = 5.25 \text{ mA/cm}^2$  to  $J = 4.1 \text{ mA/cm}^2$  during the first  $t = 100 \text{ s}$  of deposition. Afterwards, the current density stabilizes at  $J = 4.1 \text{ mA/cm}^2$ .

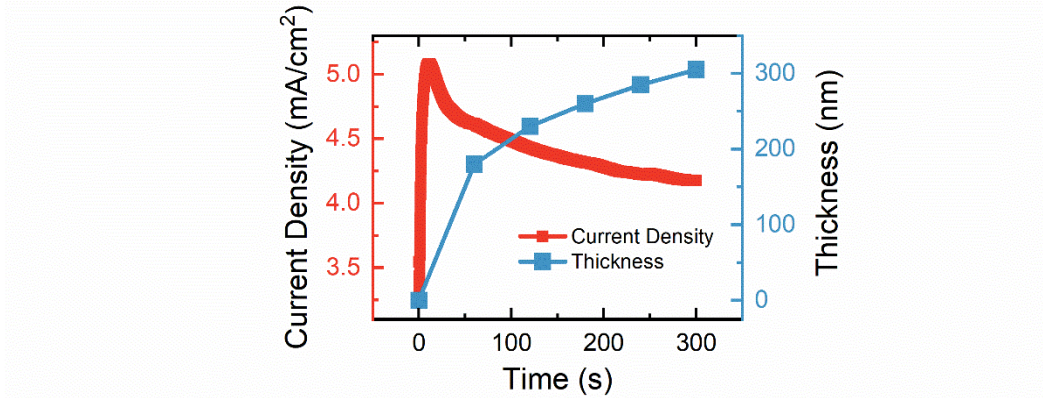


Fig. 3.1: Electrodeposition of  $\text{WO}_3$  from peroxy tungstic solution. The deposition current density saturates and tends towards  $J = 4 \text{ mA/cm}^2$  (red). Simultaneously, the deposition rate decreases for time beyond 60 s.

Correspondingly, the deposited film thickness is measured, via contact profilometry, in 15 s intervals to monitor the change in deposition rate. It is evident, that the change in deposition current, effects the deposition rate. Up to a deposition time of 110 s, the deposition rate stays stable around 1.8 nm/s. After the drop in deposition current, the deposition rate decreases to 0.5 nm/s. The transition in deposition rate and current is consistent enough to estimate the time for the desired film thickness. For three different samples, the thickness of electrodeposited  $\text{WO}_3$  films is inferred to be in a range of  $\Delta d_t = \pm 20 \text{ nm}$ . The surface roughness and morphology of the deposited films are determined via optical profilometry and SEM images (Fig. 3.2(a)). For a 250 nm thick  $\text{WO}_3$  film, the optical profilometry measurements show that such a film exhibits a surface roughness of  $\Delta r = \pm 12.3 \text{ nm}$ . This roughness is in good agreement with the particulates seen in the SEM image of the sample. Hence, electrodeposition leads to a nanoparticular film having

particulate sizes between 20 nm and 50 nm. Over an area of  $1 \times 1 \text{ cm}^2$ , the electrodeposited sample exhibits a thickness inhomogeneity of  $\Delta t = \pm 16 \text{ nm}$ . Notably, the thickness of the sample decreases with increasing distance to electrical contact of the deposition electrodes, so that the thickness decreases along the electrode. This is due to that fact that the voltage drop across the conductive ITO substrate leads to different deposition rates along the sample. In a deposition test with a Cr film on  $\text{SiO}_2$  substrate, the inhomogeneity can be decreased to  $\Delta t = \pm 9 \text{ nm}$ .

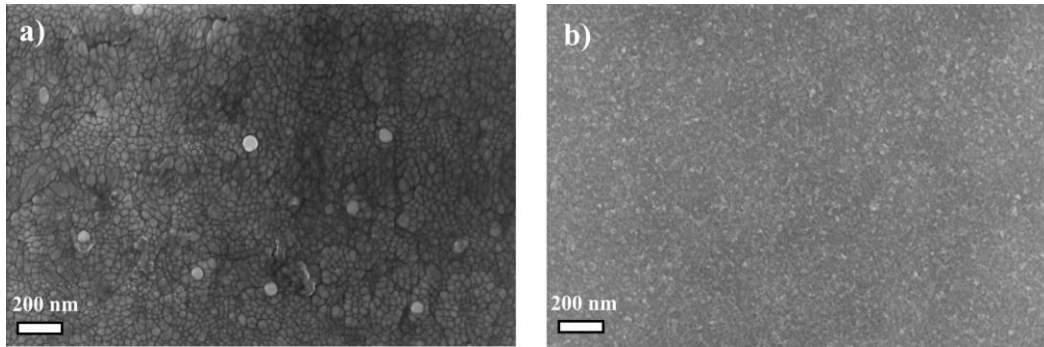


Fig. 3.2: SEM images of the surface of EC  $\text{WO}_3$  deposited via (a) electrodeposition and (b) spray coating.

$\text{WO}_3$  spray coated samples are fabricated by directly spraying the peroxotungstic precursor solution onto ITO substrates which are kept at a temperature of  $T = 260^\circ\text{C}$ . Here, the  $\text{WO}_3$  spray coated samples show a strong dependence of the film thickness on the amount of precursor, as well as process parameter, such as pressure of the airbrush gun, dwell time, and substrate temperature. For a typical spray process, the deposition thickness can be adjusted with an accuracy of  $\Delta d = \pm 25 \text{ nm}$  which can be further improved by using a slow deposition rate. For 250 nm

thick  $\text{WO}_3$  samples, the films exhibit a surface roughness of  $\Delta r = \pm 22.4$  nm, with some notable outliers ( $\pm 102$  nm). SEM imaging of the spray coated surface suggest a porous network of EC  $\text{WO}_3$  (Fig. 3.2(b)). The thickness inhomogeneity ( $\Delta t = \pm 21$  nm) of the sample suggests a poor distribution of the spray coated solution.

For reactive magnetron sputtering of  $\text{WO}_3$ , a gas mass flow rate from Ar at  $\dot{m}_{\text{Ar}} = 20$  sccm to  $\text{O}_2$  at  $\dot{m}_{\text{O}_2} = 5$  sccm at a plasma power of 125 W and a pressure of 20 mTorr lead to a constant  $\text{WO}_3$  deposition rate of 0.1 nm/s. Film thicknesses of  $d_t = 250$  nm can be achieved with an accuracy of  $\Delta d_t = \pm 3$  nm. In accordance with the investigations for electrodeposition and spray coating, the surface roughness is determined as  $\Delta r = \pm 7.3$  nm, and the thickness inhomogeneity of the film is found to be  $\Delta t = \pm 3.7$  nm. A comparison of the investigated morphological properties can be found in Table 7. Due to re-occurring surface irregularities resulting from the spray coating method, it was decided to further pursue it.

Since NiO experiences anodic coloration and provides good ion storage properties, it is investigated as the counter-electrode in integrated ECDs. Similar to  $\text{WO}_3$ , EC NiO is deposited via reactive magnetron sputtering from a pure Ni target. A plasma power of 200 W and a pressure 20 mTorr with a gas mass flow ratio of  $\dot{m}_{\text{Ar}} = 20$  sccm to  $\dot{m}_{\text{O}_2} = 1$  sccm lead to a NiO deposition rate of 0.08 nm/s. The deposited film thickness can be reproduced with an accuracy of  $\Delta d = \pm 4$  nm, while having a surface roughness of  $\Delta r = \pm 6.2$  nm and thickness inhomogeneity of  $\Delta t = \pm 4.3$  nm.

Table 7: Comparison of morphological properties of 250 nm thick WO<sub>3</sub> film deposited by different methods.

<b>Deposition Method</b>	<b>Thickness Accuracy (nm)</b>	<b>Surface Roughness (nm)</b>	<b>Thickness Inhomogeneity (nm)</b>
Electrodeposition	20	12.3	16
Spray Coating	25	22.4	21
Reactive Magnetron Sputtering	3	7.3	3.7

### 3.1.2 Electrochemical Properties of EC Thin Films

In addition to topological and morphological properties fulfilling necessities for integration in nanoscale optical devices, EC thin films are required to meet a variety of demands regarding their electrochemical and EC metrics. Hence, both electrodeposited and sputtered thin films are investigated through cyclic voltammetry (CV), current-voltage-time dynamics, and the corresponding spectro-electrochemical properties.

CV measurements are conducted in a 1 M LiClO<sub>4</sub> in PC electrolyte using a three-electrode setup where a Pt wire is used as the counter electrode and a 1 M KCl Ag/AgCl acts as a reference electrode. During measurements, the voltage applied between the EC electrode and the counter electrode is swept with a variable speed, that is fixed during a respective cycle and the corresponding current flow at the EC electrode is measured. The resulting CV curves for EC WO<sub>3</sub> at multiple different sweep speeds, ranging from  $v = 100$  mV/s to  $v = 1$  mV/s, are shown in Fig. 3.3(a) for an electrodeposited WO<sub>3</sub> film and in Fig. 3.3(b) for a sputtered film.

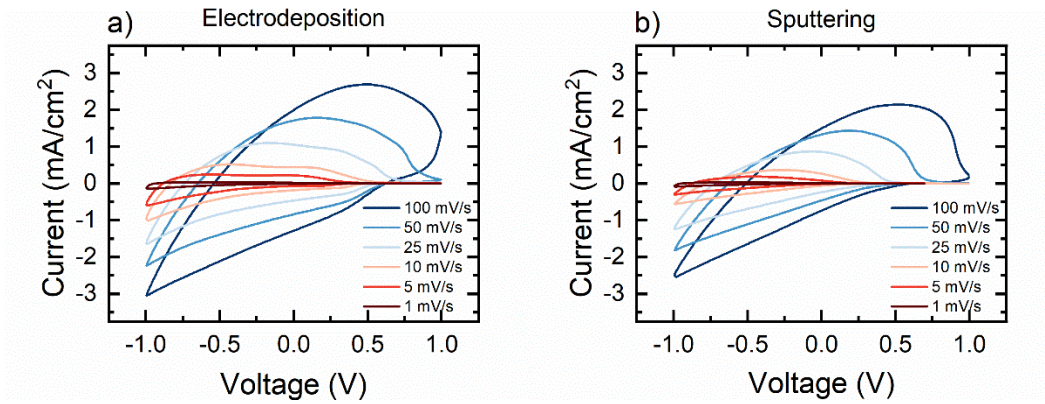


Fig. 3.3: CV measurements of a 250 nm thick EC WO<sub>3</sub> film deposited on ITO via (a) electrodeposition and (b) reactive magnetron sputtering. The applied voltage is measured with respect to an Ag/AgCl reference electrode. Voltage sweep rates are varied from 100 mV/s to 1 mV/s as indicated.

CV cycling of electrodeposited WO<sub>3</sub> leads to a typical shape for the current-voltage curve. The negative current flow indicates intercalation of Li<sup>+</sup> ions into the WO<sub>3</sub> film, while the positive current flow is due to bleaching or deintercalation of the Li<sup>+</sup> ions. For the investigated samples (i.e., the electrodeposited and sputtered), the ratio of intercalated/deintercalated charge is  $\Gamma = \frac{Q_{\text{int}}}{Q_{\text{deint}}} \approx 1.01$  and  $\Gamma = 0.97$ , respectively, indicating that no detrimental effects, such as irreversible ion intercalation or detachment of the EC material take place. Furthermore, the intercalated charge is strongly dependent on the voltage sweeping rate where faster sweeps result in higher current flow. While the electrodeposited sample demonstrates a maximum intercalation current flow density of  $J = 2.9 \text{ mA/cm}^2$ , the magnetron sputtered sample exhibits slightly lower current densities of  $J = 2.7$

mA/cm<sup>2</sup>. Via the Randles-Sevcik equation, the anodic current density can be related to the diffusion coefficient D for the Li<sup>+</sup> ions into WO<sub>3</sub>:

$$J_n = 2.69 \times 10^5 N^{3/2} C_0 D^{1/2} v^{1/2} \quad (3.2)$$

where,  $J_n$  is the peak current density,  $N$  is the number of electrons involved in the redox reaction,  $C_0$  is the electrolyte concentration in [mol/cm<sup>3</sup>], and  $v$  the sweep rate in [V/s].<sup>187</sup> Hence, the diffusion coefficient for intercalation,  $D_{\text{int}}$ , and deintercalation,  $D_{\text{deint}}$ , of Li<sup>+</sup> in the electrodeposited samples are  $1.45 \times 10^{-10}$  cm<sup>2</sup>/s and  $1.32 \times 10^{-10}$  cm<sup>2</sup>/s, respectively.

The discrepancy in the intercalated charge between the electrodeposited and the sputtered WO<sub>3</sub> films becomes evident when the curves are compared for a voltage sweep rate of  $v = 10$  mV/s (Fig. 3.4). The CV curve for electrodeposited WO<sub>3</sub> shows overall higher current densities, resulting in more intercalated/deintercalated charge. Moreover, the electrodeposited sample exhibits three distinct features in its curve. A shoulder at  $V = 0.3$  V during intercalation and two peaks at  $V = -0.52$  V and  $V = 0.35$  V during deintercalation. These distinct features can be attributed to reduction of tungsten from W<sup>6+</sup> to W<sup>5+</sup> and vice versa. The occurrence of such distinct redox peaks indicates simultaneous intercalation throughout the depth of the film and, hence, high diffusivity of ionic species inside the host lattice.

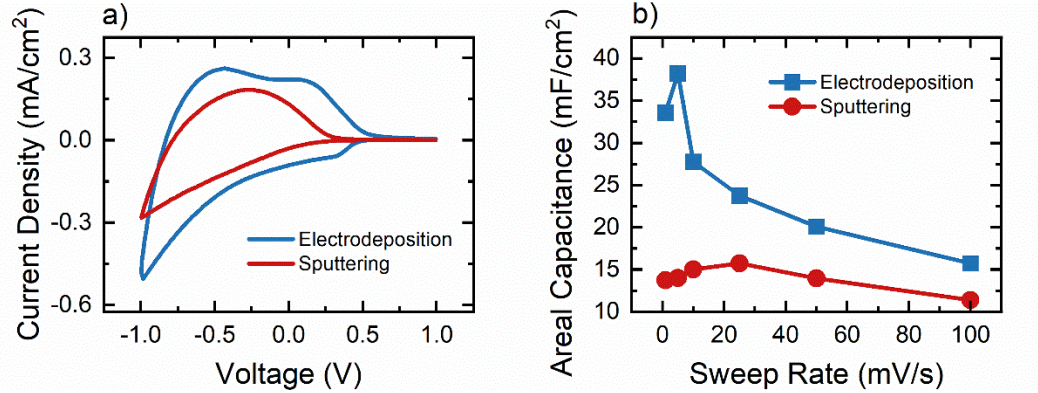


Fig. 3.4: CV measurements of 250 nm thick  $\text{WO}_3$  films deposited via electrodeposition (ED) and sputtering (SP) compared. (a) CV curve for a voltage sweep rate of 10 mV/s. (b) Areal capacitance of the investigated films as a function of the sweep rate.

In sputtered  $\text{WO}_3$  films, the redox processes occur continuously along the depth of the film, indicating that higher potentials are necessary to intercalated into deeper layers of the  $\text{WO}_3$  film. Fig. 3.4(b) depicts the areal capacitance of the investigated samples as a function of the voltage sweep rate. Here, AC is calculated from:

$$AC = \frac{\int Idt}{2 \cdot v \cdot \Delta V \cdot A} \quad (3.3)$$

where,  $v$ , is the voltage sweep rate,  $\Delta V$  is the voltage range of the measurement, and  $A$  is the active electrode area. As predicted from the CV curves, the electrodeposited sample exhibits higher capacitance throughout, achieving a high maximum  $AC = 39 \text{ mF/cm}^2$ . Notably, this high value is in good agreement with maximum values reported for  $\text{WO}_3$  (Table 2). For both the electrodeposited and the

sputtered samples, the areal capacitance decreases at higher sweep rates. Again, the findings here are in good agreement with those presented in Section 3.1.1.

It is evident that the EC thin films of the reactively sputtered  $\text{WO}_3$  provide more homogenous film thicknesses and lower surface roughness. Both of these features ultimately lead to denser film possessing lower diffusivity of ionic species. On the other hand, the nanoparticulate microstructure of the electrodeposited samples allows for efficient penetration of the electrolyte into the EC film and, hence, deeper layers of the EC material can be intercalated more efficiently. The investigated films show good retention of their electrochemical properties, with the electrodeposited sample retaining 89% of its areal charge capacitance over 1000 continuous CV measurements ( $v = 200 \text{ mV/s}$ ), while the sputtered sample retains as high as 94% of its capacitance.

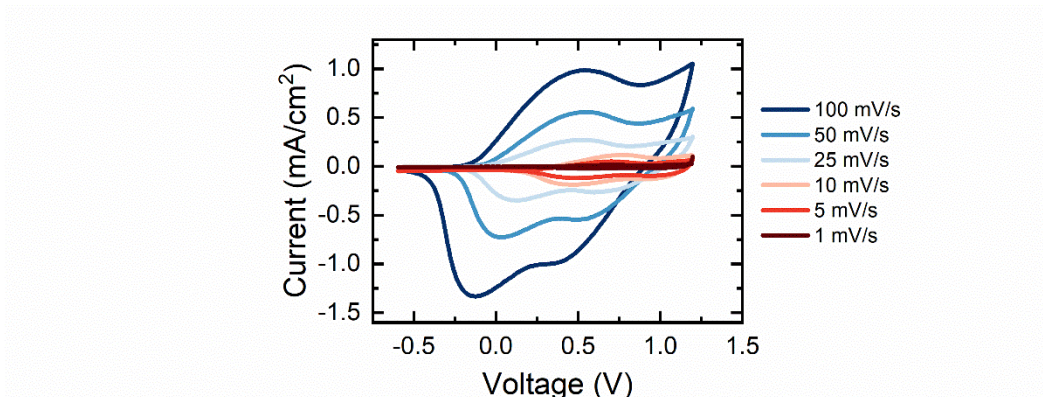


Fig. 3.5: CV measurement of a 250 nm thick NiO film deposited via reactive magnetron sputtering.

Reactive magnetron sputtering of 250 nm thick NiO films yields a substantially lower areal capacitance derived from CV than for  $\text{WO}_3$ . The films investigated here

exhibit a maximum current density  $J = -1.32 \text{ mA/cm}^2$ . Hence, the maximum achievable areal capacitance of such films is  $AC = 7.9 \text{ mF/cm}^2$  (Fig. 3.5). The films show good reversibility of the redox intercalation process where  $\Gamma \approx 0.95$ . Furthermore, the characteristic peaks for the reduction and oxidation of NiO at  $V = 0.4 \text{ V}$  and  $V = -0.125 \text{ V}$  are clearly present. The NiO film display a high retention of its capacitance of 97% over 1000 continuous CV measurements at  $v = 200 \text{ mV/s}$ .

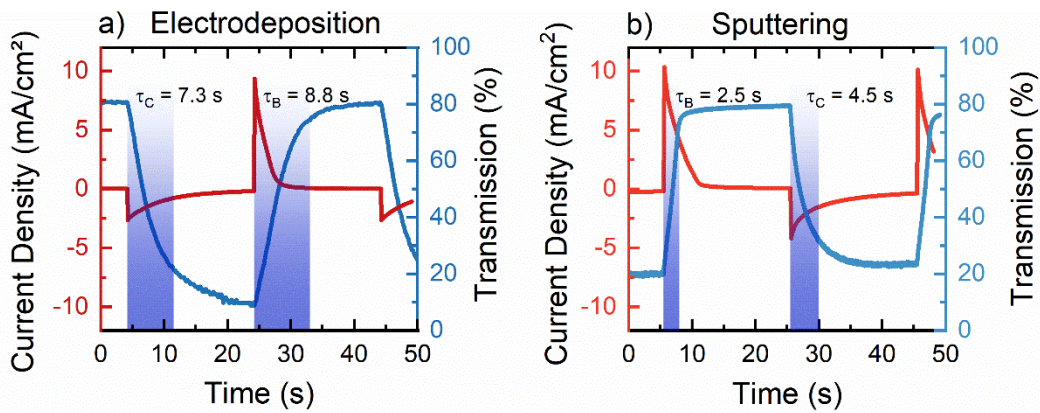


Fig. 3.6: Spectro-electrochemical analysis of 250 nm thick  $\text{WO}_3$  films prepared via electrodeposition and sputtering. An alternating voltage of  $V = \pm 1 \text{ V}$  is applied to the EC electrode and the current profile, as well as the optical transmission are measured.

In addition to the charge capacitance and electrochemical stability of the investigated films, ECDs require fast, high optical transmission modulation. To investigate the switching properties, the  $\text{WO}_3$  samples are subjected to an alternating voltage of  $\pm 1 \text{ V}$  and the corresponding current, as well as the optical transmission at a wavelength of 632 nm are recorded (Fig. 3.6). As shown in Fig. 3.6(a), the electrodeposited sample allows for an optical transmission modulation

of up to 71% at an intercalated charge of  $C = 15.5 \text{ mC/cm}^2$  (i.e., corresponds to a coloration efficiency  $CE_{cc} = 62 \text{ cm}^2/\text{C}$ ). The corresponding time constants for coloration and bleaching states of the films are  $\tau_c = 7.3 \text{ s}$  and  $\tau_b = 8.8 \text{ s}$ , respectively. Interestingly, even though the achievable optical transmission modulation for the sputtered film is lower (i.e.,  $\Delta T = 58\%$ ), the coloration and bleaching times are significantly faster ( $\tau_c = 4.5 \text{ s}$  and  $\tau_b = 2.5 \text{ s}$ ). The faster switching speed results from the intercalation dynamics explained earlier, where only  $\text{WO}_3$  unit cells close to the surface of the sputtered material contribute to the charge intercalation and hence to the coloration of the film. However, due to the lower optical transmission modulation, the coloration efficiency of the sputtered sample reaches a maximum of  $CE_{cc} = 45 \text{ cm}^2/\text{C}$ .

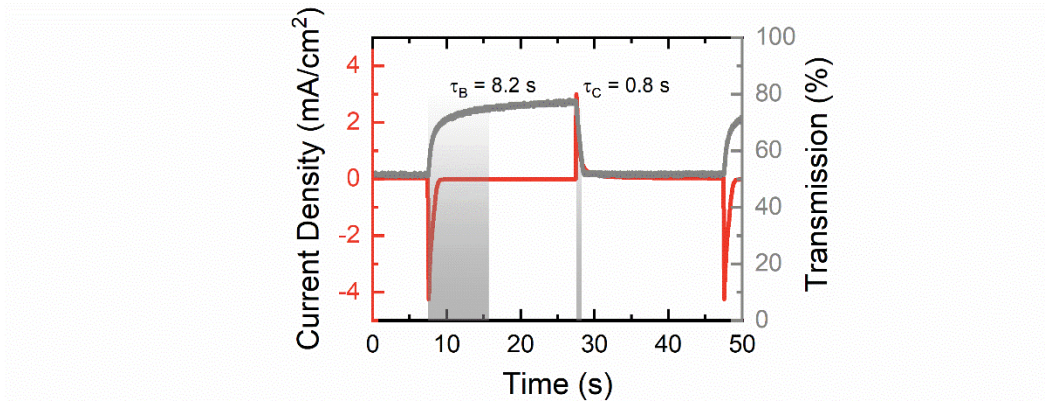


Fig. 3.7: Spectro-electrochemical analysis of a 250 nm thick NiO film.

The EC NiO thin film exhibits a maximum achievable optical transmission modulation of  $\Delta T = 29\%$ , which allows for a coloration efficiency of  $CE_{cc} = 13 \text{ cm}^2/\text{C}$  (Fig. 3.7). While intercalation time of the  $\text{Li}^+$  ions into the NiO film occurs at  $\tau_B = 8.2 \text{ s}$ , the coloration (i.e., deintercalation) takes place in  $< 1 \text{ s}$  (i.e.,  $\tau_C = 0.8$

s). The discrepancy of switching times can be explained by considering the energy necessary to overcome diffusion and intercalation barriers for the  $\text{Li}^+$  ions into the NiO host. While it takes more energy to drive ions into the host lattice, the repulsive force from the material supports the deintercalation process.

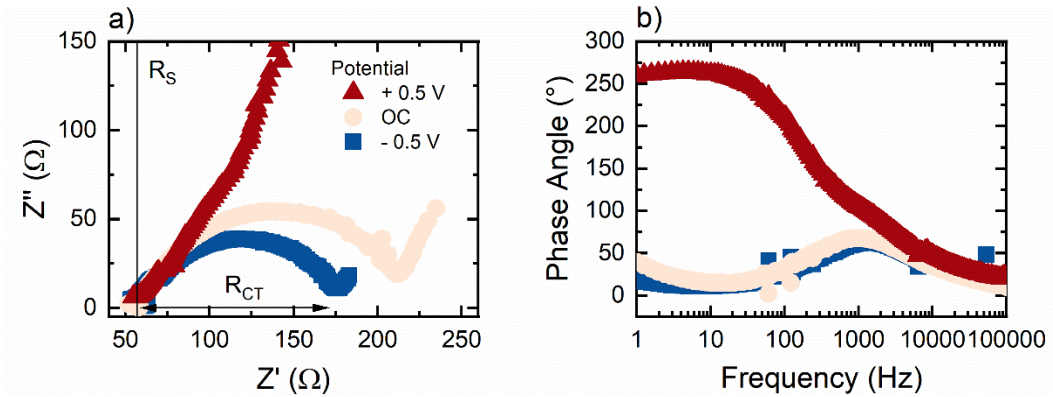


Fig. 3.8: EIS analysis of a 250 nm thick sputtered  $\text{WO}_3$  sample on ITO in 100 mM  $\text{LiClO}_4$  in PC. a) Nyquist plot of the real and imaginary part of the resistance as a function of applied voltage (vs.  $\text{Ag}/\text{Ag}^+\text{Cl}^-$ ). b) Bode plot of the phase angle over frequency.

To investigate the influence of ion insertion on the impedance of the sputtered EC  $\text{WO}_3$  thin film, EIS measurements are performed with applied voltages of +0.5 V (fully deintercalated), -0.5 V (fully intercalated) and in equilibrium (OC) (Fig. 3.8). When no external potential is applied, the series resistance of the sample as determined for the high frequency end of the Nyquist plot is  $R_s = 57 \Omega$ . A similar value is found when applying a potential with  $\pm 0.5$  V. However, the charge transfer resistance  $R_{CT}$  (i.e., the resistance at the interface between electrode and electrolyte) is strongly lithiation dependent. As determined by fitting the semi-circle of the

Nyquist plot,  $R_{CT}$  is 118  $\Omega$  and 162  $\Omega$  for an applied potential of -0.5 V and the open circuit configuration, respectively. The charge transfer resistance gives an indication of the availability of electrons for compensation of ionic charges and hence is directly correlated to the electrical conductivity of the sample. For  $WO_3$ , the electrical conductivity increases with every intercalated charge, due to accumulation of free electrons in the conduction band. In case of an actively deintercalated sample (i.e., -0.5 V applied potential), the electrical resistance of the  $WO_3$  film has to be overcome and no electrons are readily available at the interface to mitigate charge transfer. Accordingly, the Bode plot in Fig. 3.8(b) is used to determine the time constant for electron recombination as:<sup>188</sup>

$$\tau_e = \frac{1}{2\pi f_{\max}} \quad (3.4)$$

Where  $f_{\max}$  is the frequency at maximum phase angle. Hence, the recombination time is 27 ms for an actively deintercalated  $WO_3$  sample, while the recombination time drops to 15.6  $\mu$ s and 9.8  $\mu$ s for an OC potential and a lithiated sample, respectively. The recombination time can be interpreted as the time it takes for the electron to eliminate a positive ionic charge and hence it directly influences the switching time of the EC thin film. However, due to the low diffusion coefficient of  $WO_3$  with  $D \leq 1.45 \times 10^{-10}$   $cm^2/s$ , the EC coloration is mainly governed by ionic diffusion through the  $WO_3$  film. With  $\tau_D \sim \frac{d_f^2}{D} \geq 3$  s, the limiting factor for EC switching speed is regarded to be the interplay between film thickness and diffusion coefficient.<sup>35</sup> When reducing film thicknesses to  $\leq 10$  nm, the charge transfer resistance has to be regarded in terms of limiting the switching speed of an ECD.

Similarly, high film thicknesses will lead to an increased electrical resistance and low switching speeds. In the present configuration with 250 nm film thickness, the electrical conductivity is measured to be  $\sigma_e \geq 1 \frac{\text{mS}}{\text{cm}}$ , while the ionic conductivity as determined from the diffusion coefficient is  $\sigma_i \leq 10^{-4} \frac{\text{mS}}{\text{cm}}$ .

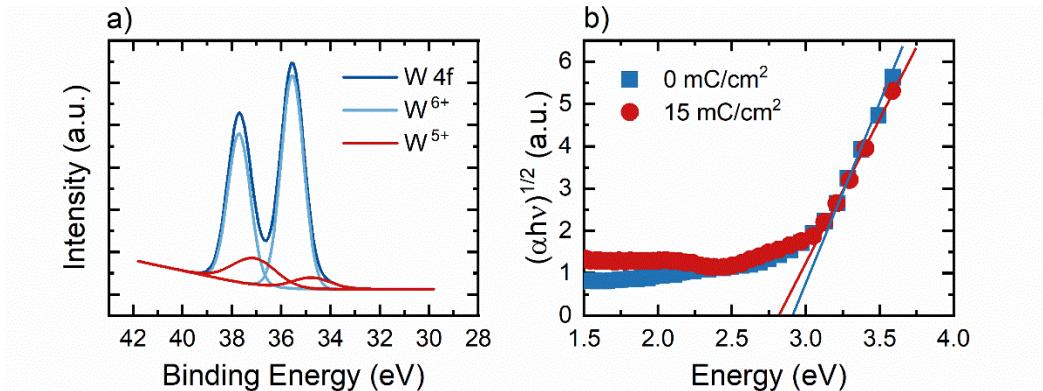


Fig. 3.9: a) XPS spectrum of W4f region for a pristine sample indicating  $\text{W}^{6+}$  and  $\text{W}^{5+}$  contributions. b) Tauc plot of  $\text{WO}_3$  as a function of lithiation.

Furthermore, the magnetron sputtered  $\text{WO}_3$  sample is investigated towards its bandstructure and influence of defects. Fig. 3.9(a) shows the W4f XPS spectrum of a  $\text{WO}_3$  sample deposited via reactive magnetron sputtering. The indicated fits are used to determine the relative amounts of W in its fully oxidized state and W with an oxygen vacancy or other defect. The presence of the  $\text{W}^{5+}$  phase indicates that defects are present and lead to the local reduction of W in  $\text{WO}_3$ . The peak ratios for  $\text{W}^{5+}$  and  $\text{W}^{6+}$  for  $\text{W}4\text{f}_{5/2}$  at 38 eV and  $\text{W}4\text{f}_{7/2}$  at 35 eV are 14% and 8% respectively. The Tauc plot of the absorption measurements performed for a lithiated and delithiated  $\text{WO}_3$  sample in Fig. 3.9(b) indicate the optical band gap as the intercept of the x-axis with the linear fit of the absorption on-set. The optical band gap for

the delithiated sample was determined to be  $E_g = 2.91$  eV, which shifts slightly red when the sample is lithiated ( $E_g = 2.82$  eV). Lithiation further leads to a significant increase in the absorption across the visible range at energies below the band gap.

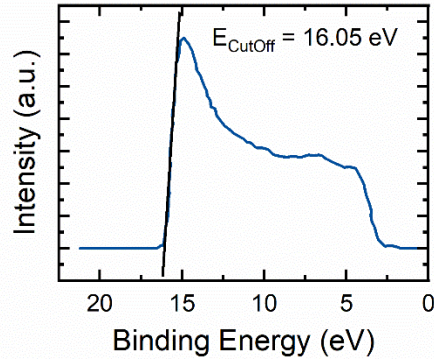


Fig. 3.10: UPS spectrum of  $\text{WO}_3$  thin film on W with its corresponding secondary electron energy cut-off value. The Fermi energy is determined to be 0 eV.

Furthermore, Ultraviolet photoemission spectroscopy (UPS) is used to determine the electronic band structure of the  $\text{WO}_3$  film. A He I source with 21.22 eV excitation energy is utilized to verify the work function of the investigated sample. Following the relation  $\Phi = 21.22 \text{ eV} - E_{\text{CutOff}}$ , the work function for  $\text{WO}_3$  can be calculated as 5.17 eV, which is significantly lower than literature values for fully oxidized  $\text{WO}_3$  determined by in-situ measurements indicate ( $\Phi = 6.47$  eV).<sup>189</sup> Exposure to air was found to reduce the work function of  $\text{WO}_3$  by more than 1 eV. Such a reduced work function indicates the existence of defect states and confirms the presence of oxygen vacancies, which lead to an n-type doping of the  $\text{WO}_3$  film.

Such a presence of defect states is confirmed via valence band spectra obtained for  $\text{WO}_3$  thin film samples (Fig. 3.11). As seen in Fig. 3.11(a), the valence band

maximum (VBM or  $E_v$ ) lies 2.83 eV below the Fermi level, suggesting that the Fermi level is close to the optically determined band gap. Hence, the Fermi level position confirms the intrinsic n-type doping of the investigated  $\text{WO}_3$  sample due to defect states. Such defect states are visible in the UPS spectrum shown in Fig. 3.11(b), where a shoulder in the spectrum around 0.5 eV indicates deep lying trap states.<sup>190</sup> All values for the positions of energy levels as determined via UPS measurements agree with measured values for mixed phase  $\text{WO}_3$ .<sup>191</sup>

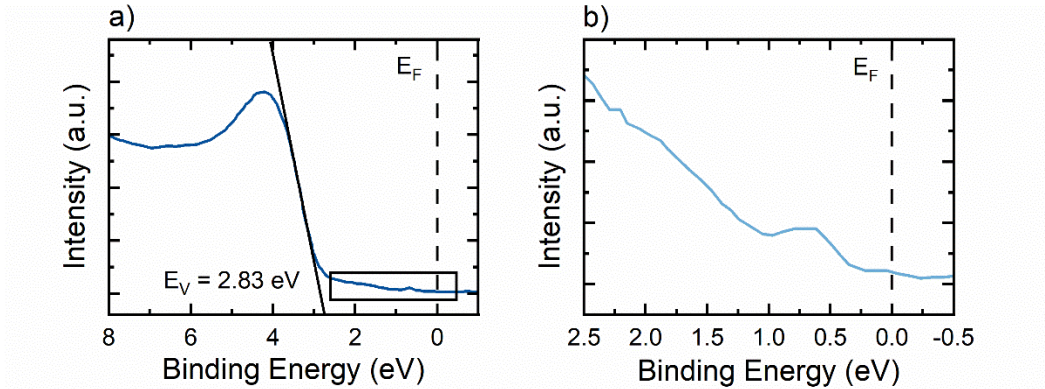


Fig. 3.11: Valence band edge spectrum for  $\text{WO}_3$ . a) Valence band determination for  $\text{WO}_3$  on W. b) Close-up of defect states close to  $E_F$

In summary, spectro-electrochemical analysis of the investigated EC films suggests advantages for the sputtered  $\text{WO}_3$  film in terms of switching dynamics, while the electrodeposited film allows for the higher optical transmission modulation. Combined with the findings in 3.1.1, it is evident that that electrodeposited  $\text{WO}_3$  is more favorable for energy storage applications where switching dynamics are less important. The smooth surface of the sputtered  $\text{WO}_3$ , as well as its superior switching speed make it a better candidate for integrated

photonic devices. The electrochemical and morphological properties of the samples are clearly in good agreement with the reported literature values related to charge capacitance, optical transmission modulation and switching speed.<sup>178,192–196</sup>

### 3.2 Ion Conductors for ECDs

Electrochromic windows and smart devices employ a wide range of ion conductors and electrolytes. However, their suitability for nanofabrication processes and long-term stability must be tailored to the specific application. The most common solid-state and quasi solid-state electrolytes employed in ECDs are hydrogels (i.e., polyacrylamide PAM), long chain polymers, such as Poly(methyl methacrylate) (referred to as PMMA) and  $\text{Li}^+$  conducting oxides, such as  $\text{LiNbO}_3$ . These three classes of ionic conductor are compared here in terms of their electrochemical and physical properties.

Polyacrylamide (PAM) hydrogels contain aqueous electrolytes of varying ionic species. The investigated sample is fabricated from 1.5 g acrylamide (AM) monomer per 10 ml of water. *n,n'*-Methylenebisacrylamide acts as the crosslinking agent and potassium persulfate acts as the thermal initiator. After 30 minutes of degassing in a vacuum chamber, the samples are left to polymerize in petri dishes at a temperature of  $T = 70^\circ\text{C}$ . After which, the polymerized hydrogel is soaked in a 1 M  $\text{LiCl}$  aqueous electrolyte. The samples are then cut into  $1 \times 1 \text{ cm}^2$  pieces and characterized for its ionic conductivity, optical transmittance, and conductivity retention. The hydrogel samples are compared to a PMMA based gel electrolyte containing 1 M  $\text{LiClO}_4$ , and magnetron sputtered  $\text{LiNbO}_3$ .<sup>19,123,131</sup> The PMMA gel

electrolyte is fabricated following previously reported procedure by Lee *et al.*<sup>197</sup> It is well known that reactive magnetron sputtering of LiNbO<sub>3</sub> poses several challenges regarding the deposition rate, the oxygen flow during the sputtering process, and the purity of the material.<sup>181,198,199</sup> In this work, the sputtering target used is a 99.99% pure LiNbO<sub>3</sub> ceramic disc purchased from Angstrom Engineering. 120 nm thick films are sputtered at a plasma power of 88 W, a pressure of 5 mTorr, and an Ar gas mass flow rate  $\dot{m}_{\text{Ar}} = 20$  sccm. The base pressure of the system is set at  $2 \times 10^{-7}$  mTorr. In case of no additional oxygen flow, the deposition rate reaches  $\dot{r} = 45$  nm/h, while the addition of oxygen at mass flow rate of  $\dot{m}_{\text{O}_2} = 1$  sccm decreases the rate to  $\dot{r} = 24$  nm/h. Accordingly, the produced films strongly differ in composition. As indicated by the X-ray photoemission spectroscopy (XPS) analysis, both samples exhibit the typical O 1s spectrum for strong O<sup>2-</sup> bonds and the C 1s peak at binding energy, BE = 285.5 eV (Fig. 3.12). However, the C 1s spectrum of the sample without oxygen addition show another feature at BE = 290 eV that can be attributed to carbonate bonding. The Nb 3d regions of the XPS analysis for both samples are similar in position and the ratio of the Nb 3d<sub>3/2</sub> and Nb 3d<sub>5/2</sub> peaks. Potential shifts of the peaks are below the resolution of the measurement tool ( $\Delta\text{BE} = 0.1$  eV). While no evidence for compositional or chemical differences can be found from the Nb 3d spectra, the Li 1s region that also contains the Nb 4s spectrum indicates a strong dependence of LiNbO<sub>3</sub> formation on the oxygen content of the deposition plasma. In both XPS spectra, the Li 1s peak is strongly pronounced and centered around BE = 56 eV. However, the spectrum of the sample deposited with additional oxygen flow presents a strong peak at BE

= 61 eV. This peak is attributed to Nb 4s and the formation of  $\text{LiNbO}_3$ . In the case of no additional oxygen flow, the peak at BE = 61 eV is present but barely stronger than the noise ratio. The XPS analysis indicate that without the addition of oxygen to the reactive plasma, the prevalent phases deposited are  $\text{Nb}_2\text{O}_5$  and  $\text{Li}_2\text{CO}_3$ . Through the addition of oxygen, the formation of  $\text{Li}_2\text{CO}_3$  is suppressed while  $\text{LiNbO}_3$  films grow. While both samples show electrochemical activity and ionic conduction, the process employing the addition of oxygen offers higher optical transparency and better ionic conduction than the mixed phase oxide.

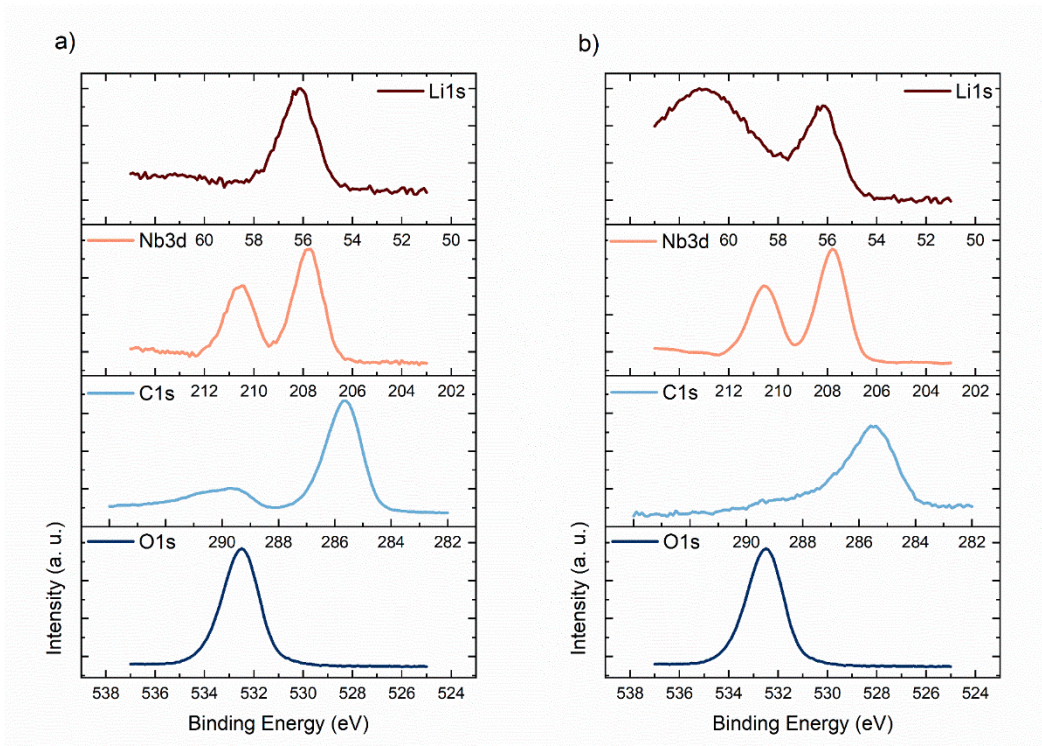


Fig. 3.12: XPS analysis of the  $\text{LiNbO}_3$  samples sputtered under the same conditions for (a) without the addition oxygen flow (b) with 1 sccm  $\text{O}_2$  flow.

Electrochemical impedance spectroscopy (EIS) is employed to determine the ionic conductivity. All samples are sandwiched between two 1 cm<sup>2</sup> gold electrodes. A HeNe laser operating at a wavelength of 632 nm is used to determine the optical transmittance of the samples grown on 500 μm quartz wafers. To determine the respective suitability for device integration, the three samples (PAM hydrogel, PMMA gel and LiNbO<sub>3</sub>) are deposited on a 250 nm thick sputtered WO<sub>3</sub> thin films and cycled to simulate the operation of ECDs. A summary of optical, ionic and EC properties of the PAM hydrogel, PMMA gel and LiNbO<sub>3</sub> solid electrolytes is presented in Table 8.

All three samples provide sufficient ( $\geq 94\%$ ) optical transmittance at a wavelength of 632 nm to be employed in ECDs. At the same time, the ionic conductivity of the investigated samples differs drastically. While the hydrogel sample having a water loading of nearly 90 wt-% offers ionic conductivity of up to  $\sigma = 30$  mS/cm, the gel electrolyte ionic conductivity does not exceed  $\sigma = 50$  μS/cm. On the other hand, the solid-state ion conduction in LiNbO<sub>3</sub> reaches ionic conductivities of  $\sigma \sim 2 \times 10^{-7}$  S/cm, which is in good agreement with literature reported values.<sup>123,181</sup> It should be noted that, the electrical conductivity of the LiNbO<sub>3</sub> samples was determined by a four-point probe measurement to be  $\sigma \sim 1.4 \times 10^{-9}$  S/cm. This value is  $\sim 0.7\%$  of the ionic conductivity, thus, creates an ohmic offset for the electrochemical properties and the coloration efficiencies.

When employed in an ECD consisting of a 300 nm thick WO<sub>3</sub> film sputter deposited onto an ITO substrate, the PAM hydrogel, PMMA gel and LiNbO<sub>3</sub> solid electrolytes, provide sufficient Li<sup>+</sup> ion intercalation to create optical transmission

modulations of  $\Delta T = 68\%$ ,  $\Delta T = 62\%$  and  $\Delta T = 46\%$ , respectively. Interestingly, the difference in ionic conductivity between the PAM hydrogel and PMMA electrolyte does not lead to a significant variance in the optical transmission modulation. Meanwhile, lower achievable transmission modulation when utilizing  $\text{LiNbO}_3$  can be attributed to the low ionic conductivity, as well as the overall concentration of excess  $\text{Li}^+$  ions contributing to redox intercalation. Accordingly, the coloration time for the three different ECDs relies significantly on the ionic conductivity, with the hydrogel based ECD switching in  $\tau_c = 3.7$  s, the PMMA sample achieving 90% transmission modulation in  $\tau_c = 8.2$  s and the  $\text{LiNbO}_3$  ECD needing nearly  $\tau_c = 54$  s to reach coloration. However, a key advantage of the solid-state electrolyte is it effectively prevents degradation of the  $\text{WO}_3$  during electrochemical cycling. While the polymer based ECDs reach 50% capacitance retention in less than 5000 cycles, the solid-state device drops to 82% capacitance retention after 10000 cycles. However, the liquid components of the PAM hydrogel and PMMA gel electrolyte can lead to degradation of the EC film where the high number of excess ions cause permanent ion intercalation.<sup>200-202</sup>

It is interesting to note that the solid-state electrolyte facilitates enhanced bistability of the EC film. Here, the devices are first fully colored and optical transmittance is continuously monitored after removing the external bias. The bistability time is determined as the time to a 10% drop in maximum optical transmittance modulation. Bistability in solid-state electrolytes can be further improved by utilizing thin diffusion barrier films such as  $\text{Ta}_2\text{O}_5$ .<sup>203</sup> Lastly, the compatibility of the respective electrolytes to common nanofabrication processes

and conditions is determined in terms of resistance against solvents and vacuum. While the hydrogel sample, as well as the gel electrolyte dissolve in common organic solvents, such as Acetone, the LiNbO<sub>3</sub> films withstand organic, as well as alkali-based solvents (photoresist developer), oxygen plasma cleaning (at power > 250 W), ultra-high vacuum (< 10<sup>-5</sup> mTorr), and piranha (a mixture of sulfuric acid and hydrogen peroxide) cleaning. Notably, the PMMA gel electrolytes retain their mechanical and electrochemical properties after vacuum treatment and submersion in developers.

Table 8: Summary of the optical, ionic, and EC properties of PAM hydrogel, PMMA gel and LiNbO<sub>3</sub> solid electrolytes.

	<b>3mm thick PAM Hydrogel 1 M LiCl</b>	<b>0.1 mm thick PMMA/PC 1 M LiClO<sub>4</sub></b>	<b>120 nm thick LiNbO<sub>3</sub> Li<sup>+</sup></b>
<b>ΔT at 632 nm</b>	96%	97%	94%
<b>Ionic conductivity</b>	max. 30 mS/cm	max. 50 μS/cm	~10 <sup>-7</sup> S/cm
<b>Transmission Modulation</b>	68%	62%	46%
<b>Switching time τ<sub>c</sub></b>	3.7 s	8.2 s	54 s
<b>50% cycle life of 300 nm WO<sub>3</sub></b>	3000	4200	> 10000
<b>Bistability time</b>	30 s	25 s	6 min
<b>Compatibility to CMOS fabrication</b>	No vacuum / No organic solvents	No organic solvents	Yes

### 3.3 WO<sub>3</sub> – NiO supercapacitor

When integrating the ECD on-chip or in nanostructured devices, the interplay between the EC modulation layer and the ion storage layer becomes important for device performance. To compare Li<sup>+</sup> containing PMMA gel and LiNbO<sub>3</sub> as ionic conductors, they are employed in smart window type supercapacitors consisting of WO<sub>3</sub> and NiO layers as the active EC materials. Both devices are fabricated by sputtering 250 nm thick WO<sub>3</sub> films onto ITO on glass substrates. In the case of the LiNbO<sub>3</sub> electrolyte, the ion conductor, counter electrode (i.e., 250 nm thick NiO film) and an electrical contact (i.e., 200 nm thick W film) are sputtered sequentially. For the gel electrolyte device, the NiO film on an ITO substrate is connected to the WO<sub>3</sub> electrode via a 300 μm thick adhesive tape to form a cavity. The space in between the electrodes is then filled with the liquid electrolyte monomer. After complete filling, the liquid electrolyte monomer is cured with a UV light (See Section 3.2).

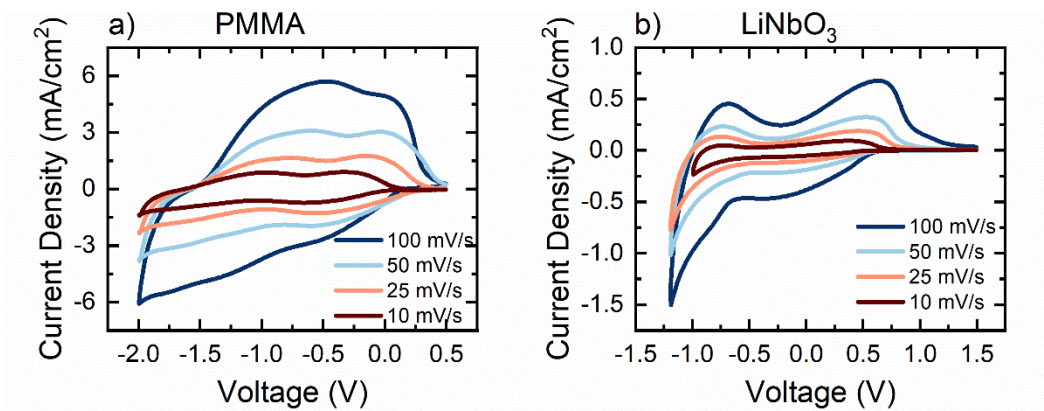


Fig. 3.13: CV measurements of supercapacitor type smart devices. (a) a WO<sub>3</sub>/NiO ECD having PMMA gel electrolyte, and (b) a WO<sub>3</sub>/NiO having a reactively sputtered Li<sup>+</sup> containing LiNbO<sub>3</sub> ion conductor.

In terms of charge capacitance as determined by electrochemical CV measurements, the gel electrolyte-based supercapacitor device achieves high anodic and cathodic current density of  $J = 3 \text{ mA/cm}^2$ . This high value is attributed to high diffusion of the Li<sup>+</sup> ions through the respective electrolyte and into the WO<sub>3</sub> and NiO electrode materials. Accordingly, the areal capacitance at  $v = 10 \text{ mV/s}$  sweep rate reaches  $AC = 27 \text{ mF/cm}^2$  for the PMMA-based supercapacitor (Fig. 3.13(a)). Remarkably, such an AC is much higher than that previously reported in devices.<sup>204–207</sup>

As depicted in Fig. 3.9(a), several anodic ( $V = 0 \text{ V}$  and  $V = -0.5 \text{ V}$ ) and cathodic peaks ( $V = -1.4 \text{ V}$ ) are present, indicating the distinct redox reactions for  $\text{Ni}^{2+} \leftrightarrow \text{Ni}^+$  and  $\text{W}^{6+} \leftrightarrow \text{W}^{4+}$ . It is interesting to note that the reversibility of the intercalation process is high where  $\Gamma \approx 0.93$  and that the retention of charge capacitance exceeds 90% after 1000 cycles. On the other hand, the supercapacitor based on the solid-

state ion conductor shows a capacitance retention of 97.2% after 1000 cycles but exhibits significantly lower values for current density and capacitance in the pristine state (Fig. 3.13(b)).

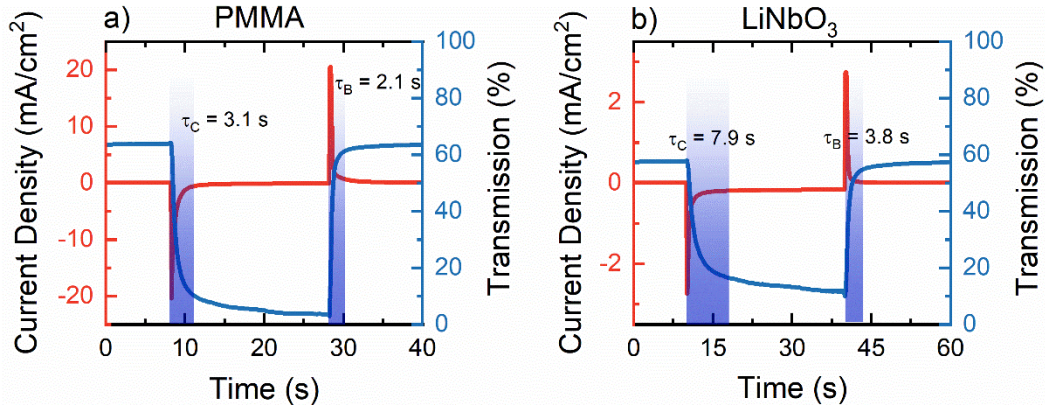


Fig. 3.14: Spectro-electrochemical analysis of supercapacitor type smart window ECDs having (a) PMMA gel electrolyte and (b) LiNbO<sub>3</sub> solid ion conductor.

With a maximum anodic current density of  $J = -1.5 \text{ mA/cm}^2$ , the areal capacitance at  $v = 100 \text{ mV/s}$  sweep rate is  $3.3 \text{ mF/cm}^2$ . Accordingly, the switching time in the PMMA based ECD is faster and more efficient than the solid-state based ECD. As shown in Fig. 3.14. The PMMA gel electrolyte sample achieves  $\tau_c = 3.1 \text{ s}$  and  $\tau_B = 2.1 \text{ s}$ , which are in good agreement with the previously reported values.<sup>197</sup>, whereas the solid-state LiNbO<sub>3</sub> based ECD exhibits longer coloration and bleaching times of  $\tau_c = 7.9 \text{ s}$  and  $\tau_B = 3.8 \text{ s}$ , respectively. The optical transmission modulation for the PMMA ECD exceeds  $\Delta T = 60\%$  with as low as 2% optical transmission at  $\lambda = 632 \text{ nm}$ . On the other hand, the LiNbO<sub>3</sub> sample achieves  $\Delta T = 47\%$  optical transmission modulation while passing through both EC layers twice (optical transmission modulation measured in reflectance). Hence, the ion dynamics

indicated through the CV measurements lead to better EC properties for the PMMA sample, with coloration efficiencies exceeding  $CE_{ec} = 135 \text{ cm}^2/\text{C}$ .

### 3.4 Hydrogel Based $\text{WO}_3$ Dual Ion EC Battery<sup>131</sup>

Ion conductors for EC applications still suffer some major shortcomings including low ionic conductivity and short lifetimes. While the ionic conductivity of the hydrogels introduced in 3.2 is sufficient for EC applications, their intrinsic lifetime is limited due to the evaporation of the aqueous electrolyte. Based on a dimethyl sulfoxide (DMSO) modification process, polyacrylamide hydrogels having longer lifetime and high conductivity are developed and implemented in a dual-ion  $\text{Zn}^{2+}/\text{Al}^{3+}$  EC battery consisting of a Zn anode and a  $\text{WO}_3$  cathode.<sup>131</sup> To ensure increased electrolyte retention at ambient conditions, dimethyl-sulfoxide (DMSO): $\text{H}_2\text{O}$  mixtures are used in the gelation process of the acrylamide. DMSO: $\text{H}_2\text{O}$  mixed solvents exhibit unique properties that are not found in the pure solvents, such as low freezing temperatures of down to 60 K and increased hygroscopicity.<sup>208,209</sup> The significant changes in physical and chemical properties of the mixed solvent are based on the formation of nanoclusters triggered by the polar interaction of the DMSO and water molecules. Following our published work (presented in the following chapter), multiple proofs of the concepts introduced here have been published.<sup>210-212</sup>

#### 3.4.1 DMSO Modified PAM Hydrogel Electrolytes

PAM hydrogels are prepared by dissolving different amounts of potassium persulfate as the initiator in water/DMSO mixtures to create three different samples

(10/25/150 mg per 10 ml) followed by stirring at 45°C for 30 minutes. Next, 1.5 g of acrylamide (AM) monomer is added to the heated mixture and stirred for 5 minutes. The crosslinking n,n-Methylenebisacrylamide is added (10 mg per 10 ml) and stirred for 10 minutes. The resultant transparent solution is poured into a 100 mm polystyrene petri dish and kept at 60°C. Depending on the amount of the initiator, polymerization of the hydrogel is completed within 30 to 120 minutes. Next, the hydrogels are washed in deionized water (DI) water and soaked in an aqueous solution containing the dual-ion electrolyte. In order to determine the success of the modification process, hydrogels having 25 mg PP initiator with and without DMSO modifications are investigated via Fourier transform infrared spectroscopy (FTIR) and energy dispersive X-ray spectroscopy (EDX). Fig. 3.15(a) presents the results of the FTIR investigation of an unmodified and a DMSO modified PAM hydrogel after a DI wash. Clearly, both samples exhibit strong absorption peaks at 3327 and 3185  $\text{cm}^{-1}$  originating from the N-H-stretch and a strong absorption at 1650  $\text{cm}^{-1}$  correlated with stretching of C=O bonds.<sup>213</sup> However, the DMSO- modified hydrogel exhibits stronger absorption peaks at 1310  $\text{cm}^{-1}$  and 1412  $\text{cm}^{-1}$  associated with CH-bending and two additional absorption peaks at 951  $\text{cm}^{-1}$  and 1022  $\text{cm}^{-1}$ . The absorption at 951  $\text{cm}^{-1}$  occurs due to the enhanced CH-bending, while the newly arising absorption around 1020  $\text{cm}^{-1}$  can be attributed to S=O stretching. EDX analysis of freeze-dried hydrogels further supports the claim that DMSO is incorporated into the hydrogel microstructure as shown in Fig. 3.15(b). For hydrogels polymerized in DMSO mixed solvent, the amount of elemental sulfur increases from approximately 5.6 % in the unmodified

sample to 13.5% in the 50/50-mixture (Samples were soaked in 1M  $\text{ZnSO}_4$  for 72h to ensure to have the same standard). On the contrary, the atomic weight concentration of elemental nitrogen is greatly reduced from 13.6% in the pure DI sample to 3.7% in the DMSO modified sample, suggesting the substitution of the acrylamide's amino group by DMSO. This is also supported by the FTIR where magnitude of the N-H stretch absorption is reduced in the spectra of DMSO modified samples.

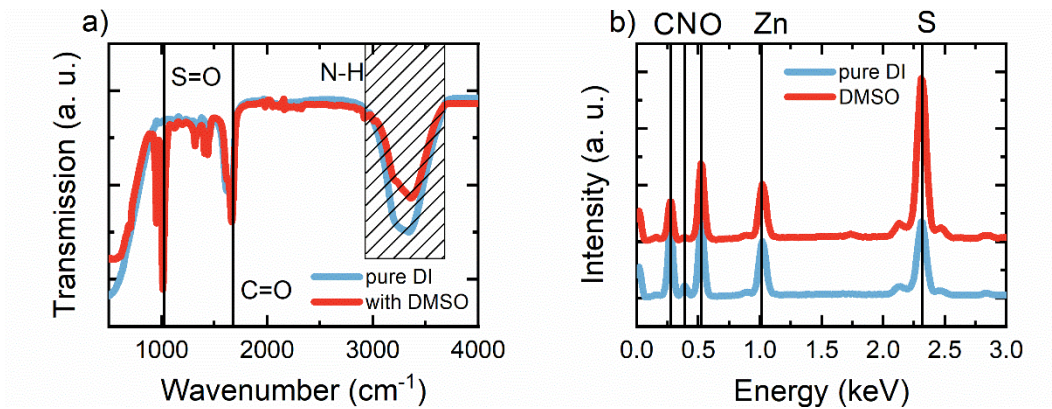


Fig. 3.15: Characterization of modified and unmodified PAM hydrogels. (a) FTIR spectra of a DMSO-modified and a DI hydrogel. The important absorption peaks are indicated. (b) EDX spectra of freeze-dried hydrogels with and without DMSO modification. Samples are soaked in 1 M  $\text{ZnSO}_4$  prior to the drying process.

The modification of PAM hydrogels with DMSO molecules also leads to morphological differences of the polymerized structure. For comparison, Fig. 3.16 depicts the morphology of PAM-hydrogel synthesized in pure DI water and when synthesized in a 50/50 mixture of DMSO:H<sub>2</sub>O. It can be seen from the SEM images that the addition of DMSO to the solvent changes the appearance of the hydrogel.

Instead of a “ropy lava”-like lamellar microstructures, DMSO introduces a certain degree of randomization to the polymerization process. The formation of these randomized structures can be attributed to reaction-induced phase separation.<sup>214</sup>

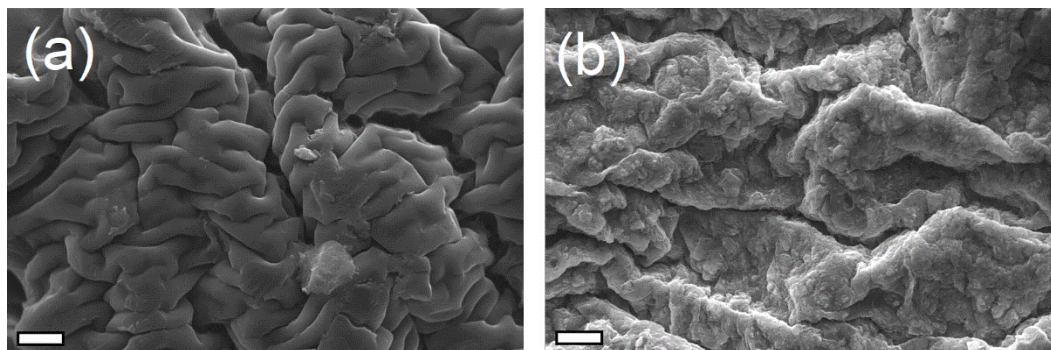


Fig. 3.16: SEM image of freeze-dried hydrogels without (a) and with DMSO (b) modification. Scale bar: 2 $\mu$ m

Notably, it is possible for the DMSO molecule to polymerize upon interaction with  $\text{SO}^{4-}$  radicals along two pathways.<sup>215</sup> DMSO can be incorporated into the hydrogel by strong polar interaction or copolymerization (Fig. 3.17).<sup>216,217</sup> The polar S=O group can form hydrogen bonds with water molecules and, thereby, adheres to the hydrophilic amino group (Fig. 3.17(a)). As depicted, radical sulfate ions may also interact with DMSO to form dimethyl-sulfone, which in turn polymerizes with acrylamide (AM) (Fig. 3.17(b)).<sup>215</sup> As a result, the polar S=O group of the dimethyl sulfoxide forms highly stable nanoclusters with the water molecule via hydrogen bonds. These nanoclusters significantly alter the physical and chemical properties of the mixed solution<sup>208,218</sup> and the resulting hydrogel where the S=O bond enhance water retention of the gel as water molecules are held at sulfoxide sites.

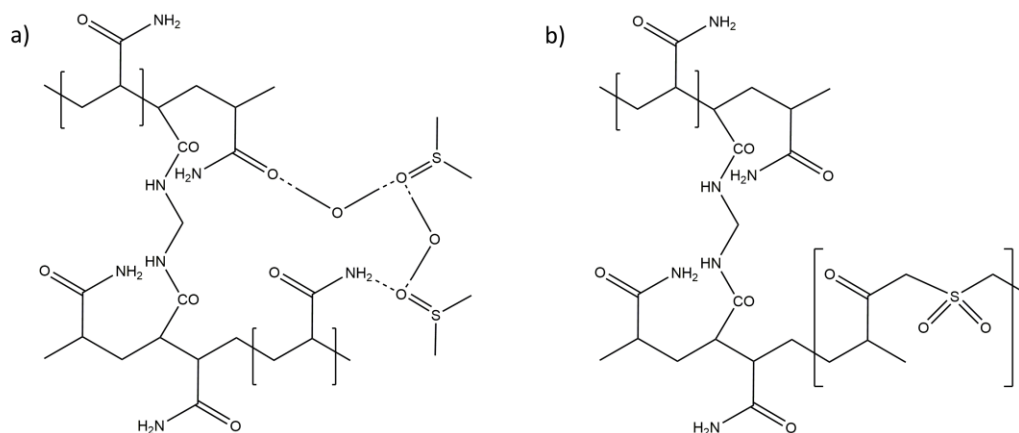


Fig. 3.17: Possible mechanisms of DMSO incorporation into PAM-hydrogel. (a) Water molecule mediated dipolar interactions. (b) Copolymerization of sulfone with acrylamide.

The retention of water in the PAM hydrogels is investigated in terms of the relative weight of samples over time and ionic conductivity retention. Long term investigations of the relative weight of unmodified and modified hydrogels show drastically increased retention of the electrolyte incorporated in the modified hydrogel. As such, the relative weight over time is monitored for samples at 30% relative humidity (RH), while the ionic conductivity over time is monitored for samples stored at 40% RH. This difference is due to ambient air ventilation in the laboratories. In both cases the relative humidity fluctuated  $\pm 2.5\%$ . Fig. 3.18(a) presents the relative weight of different hydrogel samples over a period of four weeks in 30% relative humidity (RH) atmosphere. After synthesis, all samples are soaked in DI water for 24h to ensure maximum water loading. Here, 10 g of hydrogel sample are placed into a petri-dish and left in the controlled environment

while RH is monitored via a commercially available humidity sensor. Samples synthesized with DMSO show significantly higher water retention, exhibiting between 50% and 72% of their initial weight. Clearly, the concentration of radical initiator influences the water holding capability of the modified hydrogels. Samples polymerized with 1 mg/ml initiator show 51% weight retention after 4 weeks, while increasing the initiator concentration leads to 60% and 72% weight retention for concentrations of 2.5 mg/ml and 15 mg/ml, respectively. Even though, decreasing initiator concentration leads to a decrease in water retention of the DMSO samples, the experiment shows that the concentration of initiator plays a minor role in electrolyte retention. The initiator can crosslink the acrylamide chains and, thus, slightly increasing the surface area. This, in turn, enhances the water holding capability of the hydrogels,<sup>219</sup> but does not affect the weight retention of hydrogel in a way the polar S=O interaction does. This is evident as the unmodified hydrogel sample polymerized with 15 mg/ml initiator have poor weight retention; wherein, the rest weight of the sample without DMSO modification after 28 days is that of its polymeric components.

To investigate the ionic conductivity time evolution, the samples were soaked for 72 h in an electrolyte mixture consisting of 1M AlCl<sub>3</sub> and 1M ZnSO<sub>4</sub> and placed between 2 cm × 2 cm stainless steel electrodes. To ensure the evaporation of any excess electrolyte, the first measurements are taken 3hrs later. As shown in Fig. 3.18(b), the gel-electrolytes fabricated with DMSO exhibit ionic conductivity as high as 20 mS/cm after the first 3hrs and retained an ionic conductivity of 1 mS/cm even after four weeks of storage in 40% RH. The measured ionic conductivity is in

agreement with the values reported previously, while a retention of 5% ionic conductivity over a period of four weeks is remarkable when compared to other approaches used for electrolyte retention.<sup>130,213,220</sup> The initial conductivity of the unmodified hydrogel sample exhibits values up to 28 mS/cm. However, the unmodified hydrogel dries out quickly, reducing its ionic conductivity to 0.2 mS/cm in only 5 days.

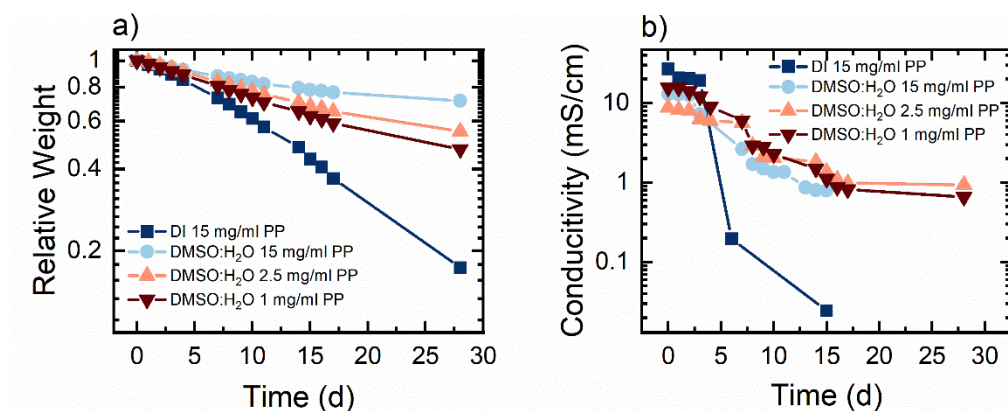


Fig. 3.18: Long-term retention measurements weight and ionic conductivity of PAM hydrogels. (a) Relative weight of unmodified and modified hydrogel samples over 30 days at 30% RH. (b) Ionic conductivity as a function of time of DI and DMSO:H<sub>2</sub>O hydrogel samples. The samples were soaked in ZnAl-electrolyte for 24h before the measurements were taken.

A notable feature of the hydrogel prepared with a 2.5 mg/ml initiator is its high optical transparency ( $T = 93\%$ ), over the whole visible spectrum. Interestingly, when placed in contact with an ITO substrate, their combined optical transparency is measured to be  $>95\%$ . This is due to the fact that this modified hydrogel has a refractive index close to that of water (i.e.,  $n = 1.33$ ), and when contact with the

ITO glass, it reduces scattering of light from the rough ITO. The high liquid retention of the gel allows it to be highly transparent even after four weeks of storage at ambient condition. Together with its high optical transparency, long lasting conductivity (e.g., 1 mS/cm after 28 days), and over 1500% stretchability, the hydrogel having 2.5 mg/ml initiator concentration is chosen as the electrolyte matrix for a rechargeable dual-ion EC battery.

### 3.4.2 Dual-Ion EC Battery

Taking advantage of the similarity of the physical and chemical mechanisms involved in electrochemically triggered chromatic response and capacitive ion storage allows for envisioning novel battery materials having EC functionality. Due to the zinc's high charge capacity of 820 mAh g<sup>-1</sup>, zinc-ion batteries are considered to be the main contenders for lithium ion-based batteries.<sup>221,222</sup> The multivalent nature of zinc combined with its non-toxic nature have inspired a multitude of research in liquid and solid electrolyte-based devices.<sup>221,223</sup> Unfortunately, Zn<sup>2+</sup> ions cannot be efficiently intercalated into EC tungsten oxide.<sup>125</sup> However, a dual-ion electrolyte can overcome such constraints by combining the redox reactions of zinc electrodes and the high coloration efficiency of WO<sub>3</sub> intercalated with trivalent aluminum ions (Al<sup>3+</sup>).<sup>21,224</sup> The comparably small (relative to the ionic Zn<sup>2+</sup> ions) radius (53 pm) of the Al<sup>3+</sup> ions enables superior and reversible intercalation into WO<sub>3</sub>. Furthermore, along with its exceptionally high charge capacities in WO<sub>3</sub> (347 mAh g<sup>-1</sup>), the trivalent nature of the Al<sup>3+</sup> ions have been shown to allow faster intercalation than that of monovalent sodium ions and lithium ions<sup>193,225</sup>

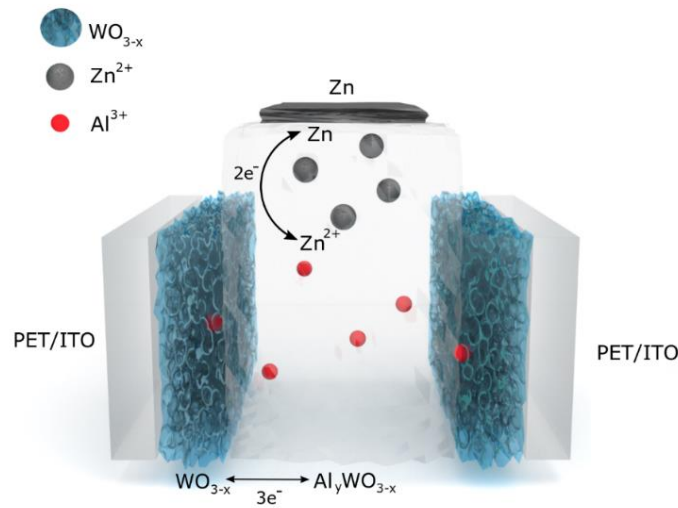


Fig. 3.19: Schematic of the proposed double layer device with  $\text{Al}^{3+}$  intercalation at the  $\text{WO}_{3-x}$  cathode and  $\text{Zn}/\text{Zn}^{2+}$  redox reaction at the zinc anode.

The basic schematic of the dual-ion rechargeable battery is illustrated in Fig. 3.19. The EC  $\sim 270$  nm thick  $\text{WO}_3$  film is electrodeposited onto a flexible and optically transparent polyethylene terephthalate (PET) coated with 130 nm thick ITO. Strips of zinc sheet metal with 0.5 mm thickness (polished with sandpaper under DI water flow) served as the anode material. To avoid short circuiting, a highly transparent DMSO modified hydrogel forms the electrode separator. Because of the high mechanical flexibility of the PAM-based electrolyte, bending of the device is only limited by the mechanical rigidity of ITO on the respective substrate. By employing two  $\text{WO}_3$  electrochromic electrodes, both the areal capacity and the optical transmission modulation between the colored and the bleached states are further increased. The small ionic radius of  $\text{Al}^{3+}$  and its high diffusion coefficient into the hydrogel ensure fast coloration even at a few

millimeters electrode distance.<sup>226,227</sup> As discussed in section 3, electrodeposition is chosen over sputtering, because it offers higher specific capacitance and potential large area scalability.<sup>228,229</sup> To ensure full optical contact,  $\text{WO}_3$  electrodes are wetted with a thin layer of aqueous mixed ZnAl electrolyte before they are brought into contact with the hydrogel.

Notably, this EC battery type device operates under different condition than supercapacitor type devices. A battery-like ECD offers a maximum optical transmission in the charged state, while supercapacitor ECDs are fully colored when charged. The difference arises from the self-charging effect introduced by the electrochemically active counter-electrode, such as zinc.<sup>6</sup>

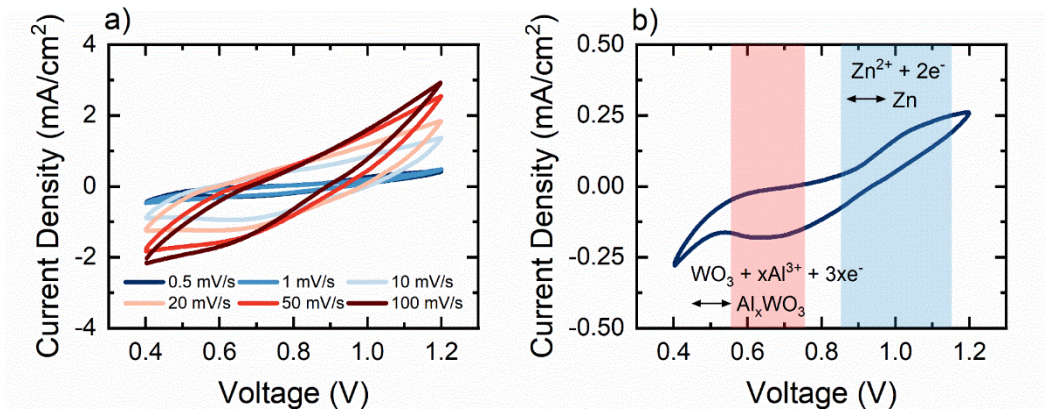
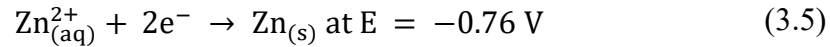


Fig. 3.20: Cyclic voltammetry of a hydrogel-based EC battery. (a) CV measurement of the EC dual-ion battery assembled with DMSO-modified hydrogel electrolyte between 0.4 V and 1.2 V vs  $\text{Zn}/\text{Zn}^{2+}$  at different cycling speeds. (b) CV measurement of  $\text{WO}_3$ -zinc EC battery at 0.5 mV/s sweep rate. The pink and light blue colored bars indicate the oxidation and the reduction regions.

Current-voltage characteristics for the assembled EC dual-ion WO<sub>3</sub>-zinc battery are presented in Fig. 3.16. The highest current density of  $J = 3.6 \text{ mA/cm}^2$  is achieved at a sweeping rate of  $v = 100 \text{ mV/s}$ . At  $v = 0.5 \text{ mV/s}$ ,  $J$  is reduced to  $0.25 \text{ mA/cm}^2$ . The EC WO<sub>3</sub>-zinc battery achieves high faradaic capacitance of  $122.9 \text{ mF/cm}^2$  at a sweeping speed of  $100 \text{ mV/s}$  and up to  $375 \text{ mF/cm}^2$  for  $v = 0.5 \text{ mV/s}$  (referenced against the area of the WO<sub>3</sub> electrode). The battery architecture increases the achievable areal charge capacity by nearly a factor of 6 when compared to the supercapacitor type devices introduced earlier. Clearly, slower cycling allows for efficient Al<sup>3+</sup> ion diffusion into the WO<sub>3</sub> layer, which in return, leads to intercalation of Al<sup>3+</sup> ions at deeper lying oxygen vacancies. Moreover, since the total area enclosed by the oxidation/reduction curves are similar (i.e.,  $\Gamma = 0.96$ ), intercalation and dissolution processes occur reversibly between  $V = 0.4 \text{ V}$  and  $V = 1.2 \text{ V}$ . Accordingly, the expected reduction/oxidation reactions follow:



Following the theoretical redox potentials, a maximum nominal cell voltage meaning the maximum achievable potential difference between anode and cathode potentials, of  $1.1 \text{ V}$  is expected, but irreversibility increases tremendously for higher cell voltages, reaching as low as  $\Gamma = 0.82$  for  $V_{\text{cell}} = 1.1 \text{ V}$ . As can be seen in Fig. 3.20(b), the Al<sup>3+</sup> intercalation into WO<sub>3</sub> creates a distinct peak at  $0.65 \text{ V}$ , while the zinc redox reaction occurs steadily. The lower potential window is mainly due to irreversible effects occurring when increasing the potential window. The

resistance of the hydrogel electrolyte leads to diffusion-based voltage drops, leading to increased stripping of the Zn electrode.

The CV curves can further be analyzed for ion insertion or diffusive contribution dependency on sweep rate to the overall capacity ( $q_c$ ).<sup>230</sup> Based on the following equation,

$$q_{\text{tot}} = q_c + \text{const}(v^{1/2}), \quad (3.7)$$

the capacitive part of the energy storage can be determined from the y-intercept of the plot of the capacity as a function of  $v^{-1/2}$ . The diffusive contribution towards the overall capacity increases from 22% at a sweep rate of  $v = 100$  mV/s to 63% for  $v = 1$  mV/s. Such an increase is attributed to the resistance of the hydrogel electrolyte.

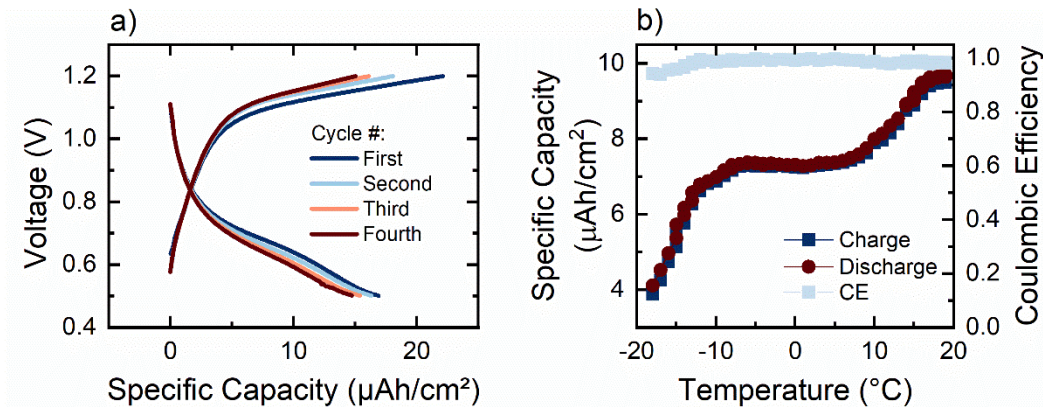


Fig. 3.21: (a) First four charge-discharge profiles of dual-ion  $\text{Zn}^{2+}/\text{Al}^{3+}\text{WO}_3$  battery under constant current of  $J = 10$  mA/cm<sup>2</sup>. (b) Temperature dependence of charge-discharge capacity and CE of  $\text{WO}_3$ -zinc battery having a DMSO-modified hydrogel electrolyte.

In addition to the faradaic capacitance, the galvanostatic charge capacity is the most important metric for battery characterization. Fig. 3.21(a) shows the galvanostatic measurement of the flexible dual-ion ( $\text{Zn}^{2+}/\text{Al}^{3+}$ )  $\text{WO}_3$ -zinc battery. As shown in Fig. 3.21(a), the observed intercalation peak at  $V = 0.65$  V, present in the CV measurements, is visible as a shoulder in the discharge current. In constant current charge-discharge measurements at high current densities of  $200 \mu\text{A}/\text{cm}^2$ , the dual-ion device exhibits areal discharge capacities of up to  $16.9 \mu\text{Ah}/\text{cm}^2$ . However, at lower current densities ( $< 200 \mu\text{A}/\text{cm}^2$ ), the initial charge-discharge cycles exhibit poor reversibility ( $\Gamma < 0.75$ ). This is mainly due to irreversible stripping of zinc at the anode during discharging as the  $\text{Zn}^{2+}$  ions go into solution and do not get plated on the Zn electrode during charging. When increasing the current density to 0.4 and 1 mA/cm, the discharge capacity reduces to 14.2 and 9.3  $\mu\text{Ah}/\text{cm}^2$ , respectively. The Coulombic efficiency increases at higher charging currents, resulting from the shorter time spans for irreversible zinc stripping. Faster cycling is, therefore, favors reversibility, while offers less capacity.

Interestingly, DMSO modification of the PAM hydrogel allows for operation in a large temperature range (Fig. 3.21(b)). While commercial Li-ion batteries should not be operated at temperatures below  $5^\circ\text{C}$ , remarkably, the EC dual-ion ( $\text{Zn}^{2+}/\text{Al}^{3+}$ )  $\text{WO}_3$ -zinc has a specific capacity of  $4 \mu\text{Ah}/\text{cm}^2$  at  $T = -15^\circ\text{C}$  at a charging current of  $J = 1 \text{ mA}/\text{cm}^2$ . The low temperature ( $T = -15^\circ\text{C}$ ) capacity is 40% of room temperature value. The DMSO-modified hydrogel electrolyte also exhibits an increased ionic impedance at  $T = -10^\circ\text{C}$  with the conductivity decreasing to  $\sigma_{\text{ion}} = 6 \text{ mS}/\text{cm}$ . Furthermore, the DMSO modification of the hydrogel

electrolyte leads to several beneficial electrochemical properties of the assembled battery. In addition to the increased temperature range, which has been increased to  $\Delta T = 120^\circ\text{C}$  following this work,<sup>210</sup> the modification process enables longer lifetimes and high mechanical flexibility. Hence, the assembled EC battery retains 20% initial discharge capacity after 10 days of storage at 60% RH and  $T = 22^\circ\text{C}$ , while a similar device with an unmodified hydrogel electrolyte exhibits only 2% capacity retention after 24hrs of storage. Furthermore, the DMSO modification enabled hydrogel battery, shows no noticeable decrease in capacity retention when bent or compressed for over 50 times.

The results of the spectro-electrochemical investigation of the EC dual-ion ( $\text{Zn}^{2+}/\text{Al}^{3+}$ )  $\text{WO}_3$ -zinc battery can be found in Fig. 3.22. In the double layer architecture, the EC battery achieves nearly full coloration at minimum optical transmission of 0.25%. As such, this increases a single layer optical transmission modulation by 4.5% from 95% to 99.5%. In both cases, the coloration efficiency is found to be  $\text{CE}_{\text{ec}} = 54 \text{ cm}^2/\text{C}$ . Compared to the single  $\text{WO}_3$  electrode (3.1.2), while the EC dual-ion ( $\text{Zn}^{2+}/\text{Al}^{3+}$ )  $\text{WO}_3$ -zinc battery exhibits higher optical transmission modulation, it comes at the cost of increased switching times. The coloration and bleaching times increase to  $\tau_c = 15.8 \text{ s}$  and  $\tau_b = 24.3 \text{ s}$ , respectively. Increased switching times can be attributed to the complex dynamics of the  $\text{Zn}^{2+}/\text{Al}^{3+}$  interaction in the hydrogel electrolyte, as well as to the relatively low ionic conductivity of the hydrogel electrolyte compared to a liquid  $\text{Li}^+$  solution (i.e.,  $\sigma_{\text{gel}} = 20 \text{ mS/cm} < \sigma_{\text{sol}} \approx 500 \text{ mS/cm}$ ). In the mixed electrolyte, the applied field cannot directly drive  $\text{Al}^{3+}$  ions into  $\text{WO}_3$ , but rather leads to a stepwise process

intercalation in which  $\text{Zn}^{2+}$  ion goes into solution first in order for the  $\text{Al}^{3+}$  ion to intercalate and effectively compensate the charge density in the solution. Furthermore, the high charge capacity of the EC dual-ion ( $\text{Zn}^{2+}/\text{Al}^{3+}$ )  $\text{WO}_3$ -zinc battery, limits the achievable coloration efficiency, as zinc ions are physically plated onto the Zn electrode during cycling. The voltage dependent optical spectral transmission of the battery is measured with a single EC electrode and the results are presented in Fig. 3.21(b). In the bleached state (i.e.,  $V = 1.2$  V), the battery is fully charged and exhibits 80% optical transmission over the whole visible spectrum. When a load is connected to the battery, the cell voltage decreases to a minimum of  $V = 0.1$  V, thus, gradually reducing the optical transmission of the battery. By increasing the intercalated charge, the on-set of light absorption starts in the NIR and shifts into the visible spectrum,<sup>231</sup>. For example, the optical transmission at  $\lambda = 500$  nm reaches a minimum of 18%, while at  $\lambda = 700$  nm the optical transmission is nearly 0%. The voltage dependent optical transmission of the EC battery shows high retention of optical transmission modulation where the bleached state optical transmission decreases by only 2% over 1000 cycles and the colored state optical transmission increases by 9%. This reduction in the optical transparency can be attributed to the irreversible  $\text{Al}^{3+}$  intercalation into the  $\text{WO}_3$ .<sup>232</sup>

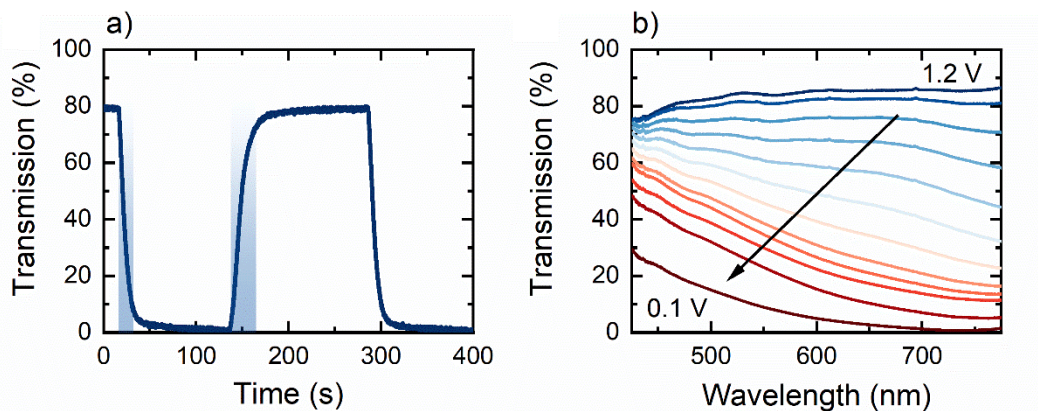


Fig. 3.22: (a) Rise and fall of colored-bleached cycling of electrochromic double layer device with DMSO-modified electrolyte between 0.1 V and 1.2 V. (b) Transmission spectra of single layer EC battery with DMSO-modified hydrogel electrolyte at  $\lambda = 632$  nm.

### 3.5 Stability Enhancement for Electrochromic Thin Films<sup>233</sup>

To ensure the highest possible optical transmission modulation for ECDs, complimentary electrodes need to be incorporated into the electrochromic device. NiO and PB are just two of many anodic coloration materials, that have been used to compliment the cathodic coloration of  $\text{WO}_3$ .<sup>124,138,234</sup> However, for an ECD, the electrolyte plays an important role in the coloration and bleaching processes. While NiO exhibits excellent performance in basic electrolytes containing hydroxides (e.g., potassium hydroxide or lithium hydroxide)<sup>173</sup> and PB reaches its optimum coloration in potassium chloride electrolyte,<sup>20</sup>  $\text{WO}_3$  is incompatible with basic electrolytes and aqueous KCl solutions. The cycling stability of  $\text{WO}_3$  electrodes in alkali-ion containing aqueous electrolytes is poor, as water itself is detrimental to

the longevity of the  $\text{WO}_3$  electrode. It has been theorized, that hydrous  $\text{WO}_3$  species tend to form a fully hydroxylated solid-water interface which leads to a more reactive surface and breaking of the crystal integrity. Additionally,  $\text{Li}^+$  or  $\text{K}^+$  ions in aqueous solution form hydrated complexes. With such effective large radii of the formed complexes, the unit cell experiences a substantial volumetric expansion upon ion intercalation.<sup>235</sup> These effects lead to a destabilization of the  $\text{WO}_3$  electrode and subsequent irreversible etching by the solvent.

Despite tungsten oxide being the most intensively studied and widely used EC material, its instability in KCl and LiCl aqueous electrolytes remains to be a formidable challenge. Mostly, the issue is solved by employing organic solvents or polymeric quasi-solid-state electrolytes,<sup>130,202,234</sup> however, not only do these electrolytes suffer from low ionic conductivity when compared to the aqueous electrolytes,<sup>131,236</sup> they can also be potentially flammable or often hazardous. Degradation protection against detachment of  $\text{WO}_3$  has been realized via atomic layer deposition (ALD) coatings.<sup>237</sup> Moreover, increasing crystallinity through annealing improves the stability of  $\text{WO}_3$ ; however, this process leads to lower coloration speeds due to the increased density of the material. Since the degradation process is a surface phenomenon, a simple approach and a promising solution is to apply self-assembled monolayers (SAM) to  $\text{WO}_3$  to improve its stability.

By self-assembly of a *n*-dodecylphosphonic acid (DDPA) monolayer on  $\text{WO}_3$  film, an effective protection layer against degradation in 1M KCl and LiCl aqueous electrolytes is realized. The monolayer creates an artificial solid-electrolyte interface (SEI), which passivates the oxide surface sites and protects the electrode

against electrochemical etching in aqueous alkali-ion containing electrolytes. The strong covalent bonds between SAM and the electrode increase the stability of the  $\text{WO}_3$  surface layer by forming a net-like superstructure.

The DDPA protection layer is formed by self-assembly in a modified tethering by aggregation and growth (T-BAG) method.<sup>238</sup> Briefly, a solution of 1mM DDPA in 15 ml ethanol is poured into a clean petri dish. The  $\text{WO}_3$  coated substrate is rinsed with DI water and is slowly submerged into the DDPA-ethanol solution such that it is covered by approximately one millimeter by the DDPA-ethanol solution. The  $\text{WO}_3$  coated substrate is left covered for 24 h and then uncovered to dry under ambient conditions. After completely drying, the  $\text{WO}_3$  coated substrate is cured at  $60^\circ\text{C}$  for 4hrs, after which it is washed with ethanol. When an electrodeposited  $\text{WO}_3$  film on an ITO substrate is submerged in a 1 mM DDPA-ethanol solution and left to dry, monolayers of DDPA form in solution and bind to the  $\text{WO}_3$  surface. As shown in Fig. 3.23(a), the formation process is attributed to the following processes: phosphonic acid binds to the hydroxide groups of the  $\text{WO}_3$  layer by a Lewis acid base reaction. The hydroxide group of the phosphonic acid creates to surface hydroxide groups under the release of water. DDPA then binds the mono- and bidentate to hydroxide groups as well as to surface oxygen. As such, the  $\text{WO}_3$  layer is passivated (i.e., exterminating surface groups, e.g., hydroxides), due to the lowered reactivity of the strong covalent bonds between the DDPA and the surface of the  $\text{WO}_3$ . The SEI arising from the surface modification for the alkali-ions in aqueous electrolyte solution is depicted in Fig. 3.23(b). Even though, the hydrophobic nature of the SAM leads to a physical barrier for water, both  $\text{K}^+$  and

$\text{Li}^+$  ions can freely pass the protection layer, while possible etching products or detached particulates are blocked. Moreover, the highly ordered monolayer hinders etching of the electrode by providing a physical barrier for the solvent. In this respect, the self-assembled DDPA monolayer degradation protection provides these two functionalities: (i) passivation of the surface and subsequent stabilization of the nanocrystalline  $\text{WO}_3$  surface and (ii) protection of the  $\text{WO}_3$  electrode against solvent chemical etching reactions.

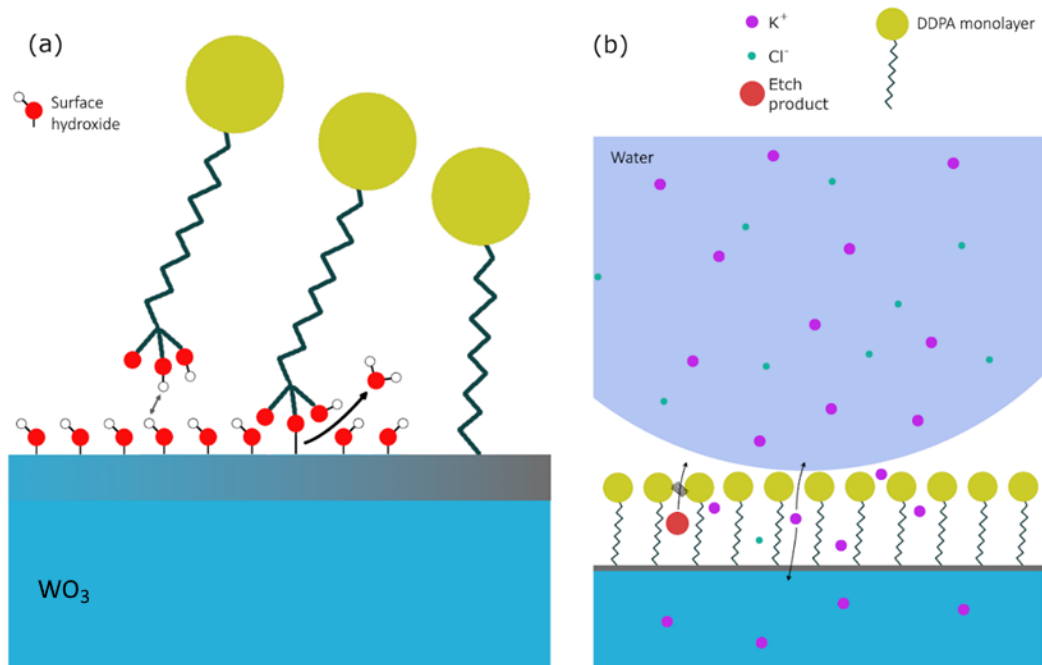


Fig. 3.23: (a) Schematic of the protection layer functionality where the grey layer represents the passivated metal oxide surface. DDPA molecules bind to the surface covalently by Lewis acid base reaction between surface hydroxide groups and the phosphonic acid head group. (b) Schematic of the resulting artificial SEI. DDPA forms a well-ordered monolayer on the  $\text{WO}_3$  surface, resulting in a hydrophobic surface. Nonetheless,  $\text{K}^+$  ions can freely pass the protection layer, while the integrity of the tungsten oxide is maintained, and possible etching products are blocked.

To examine the modification of the nanocrystalline  $\text{WO}_3$  surface, the surface properties of bare ITO substrates, ITO/ $\text{WO}_3$  and DDPA SAM modified  $\text{WO}_3$  samples are analyzed by contact angle measurements with DI water (Fig. 3.24). The bare ITO surface shows a contact angle of  $77^\circ$ , which is reduced to less than  $32^\circ$  for the electrodeposited  $\text{WO}_3$  film. Surface modification with DDPA SAM results

in a hydrophobic surface having a contact angle of  $99^\circ$ . The reduced wettability of the surface indicates a change in the surface energy, which is caused by the formation of a DDPA SAM.

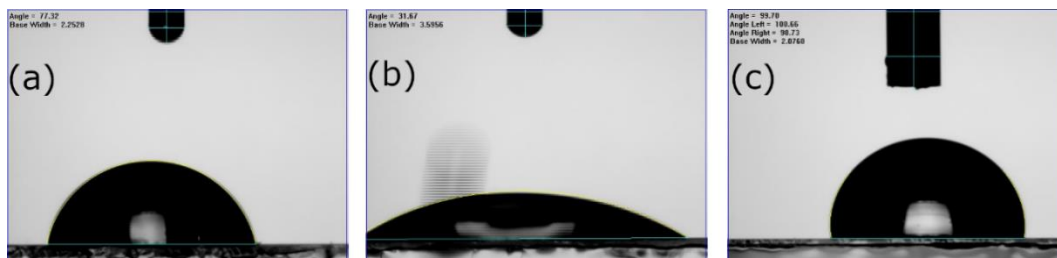


Fig. 3.24: Contact angle analysis of (a) cleaned ITO surface, (b) electrodeposited WO<sub>3</sub> thin film and (c) DDPA SAM modified WO<sub>3</sub> surface. DI water is used for the droplets.

To provide further evidence of the WO<sub>3</sub> surface modification, XPS measurements are conducted on a WO<sub>3</sub> surface with no SAM and with DDPA SAM. Fig. 3.25(f) illustrates the spectral region of phosphor 2p photoelectron emission, revealing the presence of phosphor on the surface. The relatively low signal is due to the monolayer nature of the DDPA SAM protective layer. Since photoemission originates from the first 10-20 nm regions from the sample, the P2p signal is relatively weak compared to O, W and C, because the number of P atoms is comparably low. spectra for samples with no SAM and with DDPA SAM. (f) Phosphor 2p spectrum of the DDPA SAM modified surface.

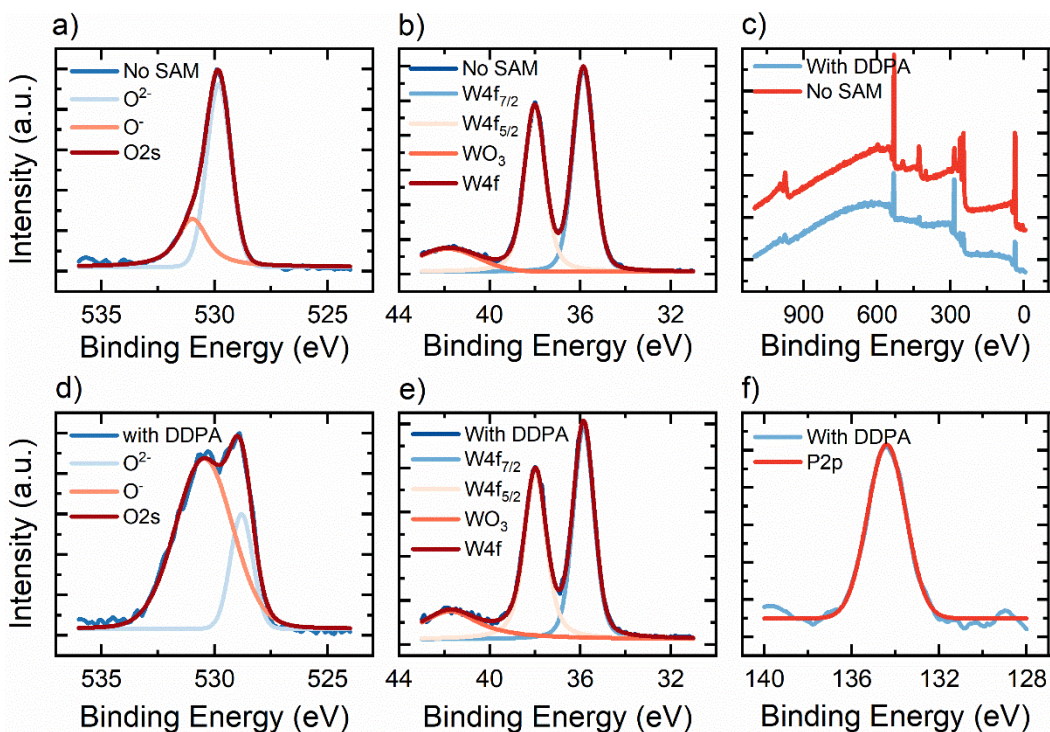


Fig. 3.25: XPS spectra of  $\text{WO}_3$  sample with no SAM and with DDPA SAM modification. (a,d) and (b,e) show the oxygen 2s and tungsten 4f region of the sample with no SAM and with DDPA modification, respectively. (c) Full survey

The effect of the SAM protection layer on the electrochemical properties of the  $\text{WO}_3$  thin film is investigated via EIS and CV measurements. The EIS spectra for the modified and unmodified samples of a 40 nm  $\text{WO}_3$  on ITO, as measured in 1 M KCl, show insignificant difference in ionic conductivity at the high frequency cut off, wherein, the ionic conductivities of  $\sigma_{\text{ion}} = 1.2 \times 10^{-6}$  S/cm for the modified sample and  $\sigma_{\text{ion}} = 9.5 \times 10^{-7}$  S/cm for the unmodified sample, respectively (Fig. 3.26). However, the unmodified sample exhibits a higher imaginary impedance at low frequencies, indicating losses due to unsaturated  $\text{OH}^-$  bonds that capture  $\text{K}^+$  ions during intercalation.

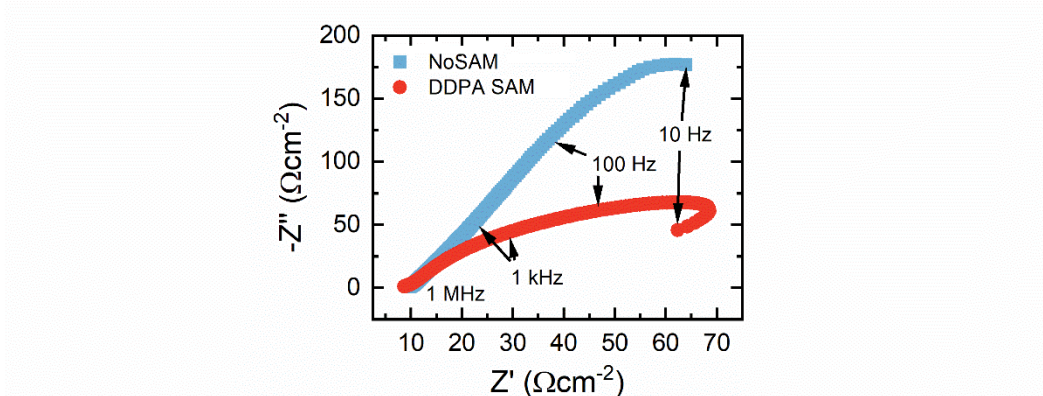


Fig. 3.26: Electrochemical impedance spectra of a 40 nm thick  $\text{WO}_3$  electrodes on ITO with and without DDPA SAM modifications. The frequency regions as indicated by arrows. Measurements are conducted in 1 M KCl aqueous electrolyte.

Fig. 3.27 presents the CV curves of 40 nm thick  $\text{WO}_3$  electrodes with no SAM (Fig. 3.26(a)) and with a DDPA SAM protection layer (Fig. 3.26(b)) measured in 1M KCl. The most significant difference is that the protected sample still exhibits high retention of the initial charge capacity after 1000 cycles, while the unprotected sample exhibits no measurable charge capacity after 100 cycles. The DDPA SAM modification lowers the initial charge capacity of the electrode (attributed to the eliminating of the surface hydroxyl-groups), compared to an unprotected sample.

While the unprotected sample loses over 33% initial capacity after 10 cycles in KCl, the modified electrode retains over 99% of its initial capacity. Furthermore, it is noticeable that the intercalation peak for  $\text{K}^+$  ions at  $V = -0.2$  V is clearly distinguishable for the unprotected sample, while it smears out for the protected electrode. The protection layer leads to a rather continuous intercalation process by sterically hindering immediate intercalation. The steric hindrance also leads to

higher deintercalation potentials necessary indicated by the peak at around  $V = -0.4$  V for the sample with no SAM, while the modified sample shows a deintercalation peak at around  $V = -0.15$  V (indicated in green). For the protected sample a slight shoulder arises around  $V = 0.2$  V, possibly arising from a second deintercalation path.

The protection of the sample leads to significantly higher current retention over time. As depicted in Fig. 3.27(c), the unprotected samples current saturates after around 1000 s, which resembles the CV curves shown in Fig. 3.27(a). The DDPA SAM protected sample in 1M LiCl; however, shows high current retention over time and exhibits great performance even after 1000 cycles or 13600s. Interestingly, the unprotected (no SAM) sample loses all capacitive behavior after only 10 cycles or approximately 200s, while the DDPA SAM protected sample retains that capacity for over 1000s. It should be noted that the etching effect in LiCl is stronger than that of KCl, because  $\text{Li}^+$  ions are of a smaller ionic radius, thus, leading to higher lattice mismatch when intercalated into the  $\text{WO}_3$  electrodes. Electrodes cycled in the respective electrolytes long enough show no apparent  $\text{WO}_3$  material left on the ITO substrate, while protected samples retain the  $\text{WO}_3$  film. The degradation of the electrode is due to other effects, possibly irreversible intercalation through ion trapping.<sup>201</sup> The detachment of  $\text{WO}_3$  nanostructures from the surface has been observed for nanoparticulate oxide in 1M  $\text{LiClO}_4$ .<sup>237</sup>

The electrodeposited films of  $\text{WO}_3$  exhibit poor cyclability in both the KCl and the LiCl electrolytes, as such, preventing a wide array of possible anodic materials. Self-assembly of a DDPA layer on  $\text{WO}_3$  presents an easily scalable and cost-

efficient method to hinder degradation of the electrode in KCl and LiCl electrolytes. The modified samples exhibit greatly enhanced durability when cycled in 1M KCl, with the sample retaining a high amount of current density even after 1000 CV cycles. In LiCl, the degradation rate is dramatically decreased. Hence, modification of electrochromic electrodes by self-assembly of protection layers is a promising way to increase the cycle life even in hostile electrochemical environments.

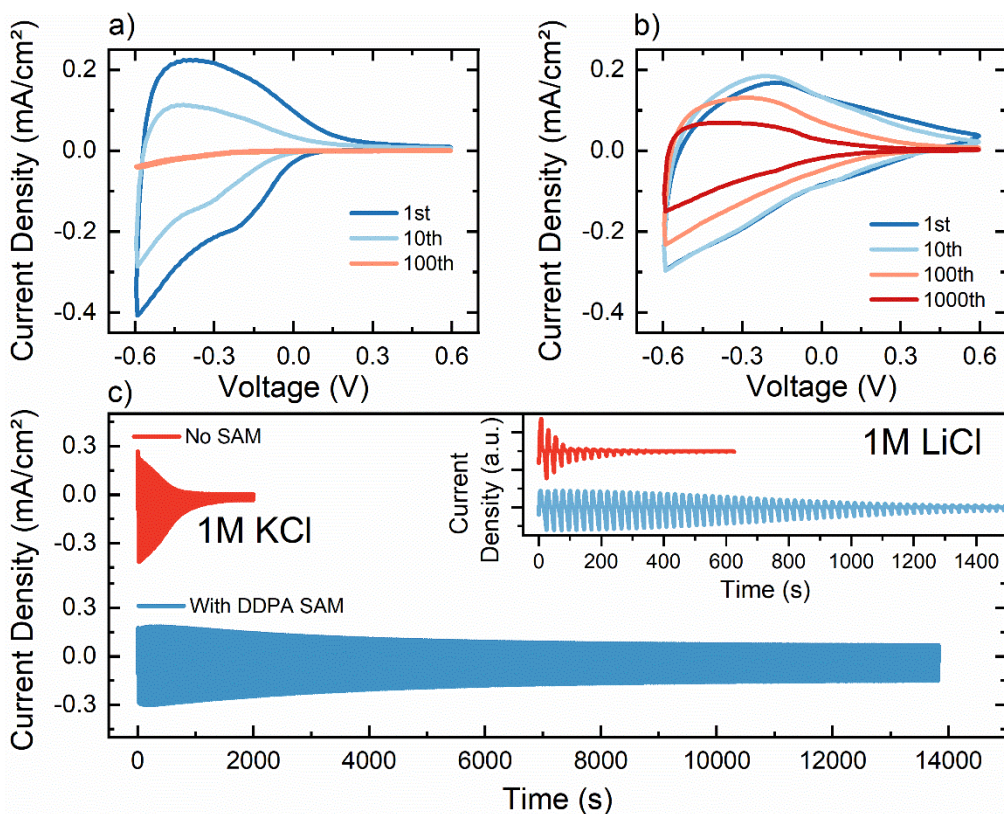


Fig. 3.27: Electrochemical analysis of modified and unmodified  $\text{WO}_3$  electrodes. (a) CV analysis of electrode with no SAM and (b) with DDPA SAM at 100 mV/s sweep rate in 1M KCl. (c) Current density as a function of time for cyclic

voltammetry in 1M KCl for WO<sub>3</sub> electrodes with no SAM and with DDPA SAM. The inset depicts the same measurement in 1M LiCl.

### 3.6 Summary

In summary, this chapter laid out the methods needed to fabricate nanoscale EC architectures for novel and efficient ECDs. It outlined the deposition and synthesis of several different materials involved in the fabrication of an ECD. Deposition methods for WO<sub>3</sub> including electrodeposition, spray coating, and reactive magnetron sputtering are studied and compared. Reactive magnetron sputtering of WO<sub>3</sub> films are shown to have higher optical quality, while electrodeposited WO<sub>3</sub> films exhibit higher charge capacity and, hence, are considered to be more suitable in energy storage applications.

Furthermore, representatives of the most common electrolyte materials for ECDs have been compared in terms of their ionic conductivity, optical transmittance, and nanofabrication suitability. The synthesized electrode and ion conduction materials were then integrated into EC smart window type to investigate the interplay between electrode materials and determine ECD properties. A WO<sub>3</sub> – NiO supercapacitor has shown the advantages of high ionic conductivity in liquids over the solid ion conductors. A novel dual function EC battery type smart window, based on electrodeposited WO<sub>3</sub>, was shown to express superior charge capacity of porous and wet-chemically deposited ECDs. Lastly, a simple approach to increase the lifetime of fragile EC electrodes was presented. The self-assembled monolayer of DDPA significantly prolonged EC operation lifetime in aqueous electrolytes.

# Chapter 4

## Plasmonic-Electrochromic “Plasmochromic” Devices

The interplay of the ionically triggered, EC effect and propagation of surface plasmon polaritons (SPP) or the resonances of localized plasmonic resonances (LSPR) is envisioned to give rise to novel and fast EC enabled devices.<sup>15,34,61</sup> Nonresonant plasmonic field localization increases the light matter interaction and, hence, reduces necessary EC material volume and film thickness needed for a typical ECD. Through enhanced field localization, several attributes of ECDs can be altered and tailored to suit the respective application. Switching speed and dynamic optical transmission modulation are directly dependent on the thickness of the EC material and, hence, strongly influenced by light spatial localization. Due to their extremely small footprint and field enhancement, plasmonic waveguides have been successfully implemented in light-based device.<sup>158,159</sup> On the other hand, the strong dependence of the LSPR on its dielectric environment is utilized to create devices whose response can be dynamically altered through intercalation of ionic species into EC  $\text{WO}_3$ . LSPR resonance of nanohole arrays (NHA) have shown to increase chromaticity in color printing devices,<sup>79,239</sup> while colloidal and lithographical nanocavities were introduced to directly alter the reflectance of the device through EC redox cycling.<sup>33</sup> In this chapter, ECDs having plasmonic, electrochromic (“plasmochromic”) functionalities are designed, fabricated and

investigated. Resonant plasmonic structures are integrated with EC  $\text{WO}_3$  to determine the influence of redox cycling on plasmonic properties.

This chapter is organized as follows. First, a standard Kretschmann architecture plasmochromic device (PCK) is studied to determine the influence of EC cycling on the plasmonic coupling in an MIM structure (Section 4.1). In Section 4.2, nonresonant SPP propagation in a waveguide structure is examined for high optical modulation depth and fast switching speeds in an all-solid-state plasmochromic waveguide (PCWG). Next, a plasmonic nanohole array is employed as superstructure in a Fabry-Perot cavity type EC color display (Section 4.3).

## 4.1 Surface Plasmon Propagation

Probing the SPP resonance of metallic films for bio sensing or to determine dielectric properties of an insulator is one of the most common utilizations of plasmonic resonance modulation.<sup>240–243</sup> Here, the Kretschmann-setup, with excitation through a quartz prism is employed to excite plasmonic resonances on a thin Au metal film. The Au film is deposited on nanopolished quartz substrates with surface roughness  $\leq 0.5$  nm, which increases film homogeneity for the metal film and the ECD. Such a glass substrate is then attached to the cleaned prism via an index matching adhesive. The prism and the glass substrate with  $n > 1$  is necessary to achieve matching of the surface plasmon wavevector  $k_{SP}$  and the in-plane component of the wavevector of the incident p-polarized light  $k_x$ . The SPP experiences a sharp resonance at the angle of incidence, where  $k_x$  and  $k_{SP}$  match. Through physisorption of molecules or other changes in the dielectric environment, this resonance angle  $\theta$  altered accordingly.

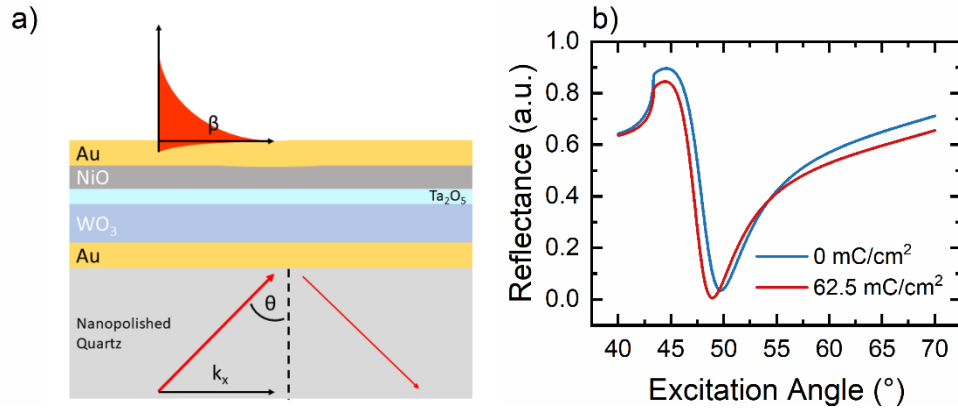


Fig. 4.1: Schematic of the Kretschmann-type SPP measurement. (a) Schematic of measurement device with MIM EC structure with a thin  $\text{Ta}_2\text{O}_5$  ion conduction layer. Light is coupled through a prism and a nanopolished quartz substrate attached to the prism via index matching adhesive. (b) Calculated reflectance for a fully oxidized/reduced  $\text{WO}_3$  film at  $\lambda = 633$  nm excitation.

#### 4.1.1 Plasmochromic Kretschmann Stack (PCK): Design and Simulation

The change of dielectric properties of  $\text{WO}_3$  and  $\text{NiO}$ , as triggered by ion intercalation, can lead to a change in the dielectric environment of the plasmonic Au film. Since two electrically conductive contacts are necessary for the coloration of a solid-state EC device, the device design incorporating two Au electrodes here can be considered as a modified Kretschmann architecture as illustrated in Fig. 4.1. The Au contacts ( $d_{\text{Au}} = 20$  nm) were chosen because of their low surface roughness  $< 3$  nm and high electrical conductivity. Meanwhile, the insulator needs to be thin enough to support coupling to the top electrode. The plasmon propagates on the top electrode of the metal-insulator-metal (MIM) type structure; the EC stack however influences its resonance by changing the refractive index of the medium the light

couples from. A simple device consisting of two 20 nm thick Au electrodes sandwiching layers of  $\text{WO}_3$  (thickness:  $d_{\text{WO}_3}=25$  nm),  $\text{Ta}_2\text{O}_5$  (thickness:  $d_{\text{Ta}_2\text{O}_5} = 10$  nm), and NiO (thickness:  $d_{\text{NiO}} =20$  nm), is a simple manifestation of a plasmochromic device. The thickness of the respective films can be adjusted to achieve favorable device parameter, i.e., achieve certain resonance angles and contrast. Notably, the  $\text{Ta}_2\text{O}_5$  film acts as a diffusion barrier for  $\text{Li}^+$  ions where it effectively supports bistable redox states of the device.<sup>203,244</sup> Excess  $\text{Li}^+$  ions are intercalated into the  $\text{WO}_3$  and  $\text{Ta}_2\text{O}_5$  before deposition of NiO through wet lithiation. In such a process, the electrode is submerged in 0.1 M  $\text{LiClO}_4$  in PC and a negative bias (-2.5 V) is applied until the current flow saturates. Afterwards the device is cleaned in PC and the NiO film, as well as the top electrode are deposited.  $\text{Ta}_2\text{O}_5$  acts as a barrier between NiO and  $\text{WO}_3$  that mitigates  $\text{Li}^+$  ion diffusion when a potential is applied but promotes bistability in the OC configuration.

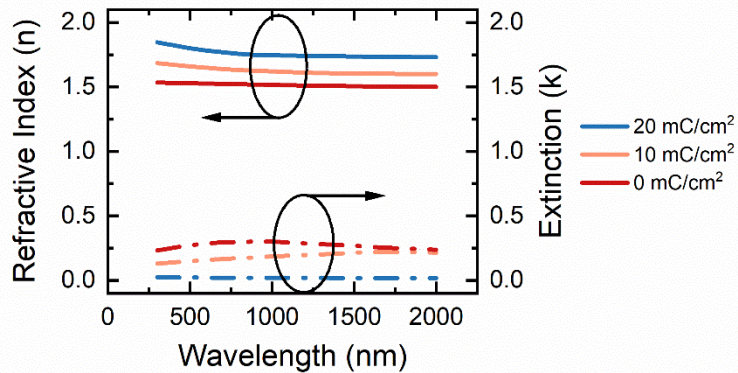


Fig. 4.2: Refractive index (n) and extinction coefficient (k) for NiO under different intercalation levels for a 200 nm thick film.

The refractive index change of NiO at  $\lambda = 633$  nm excitation is comparably small where  $n_{\text{NiO}} = 1.76$  in the bleached state and  $n_{\text{NiO}} = 1.5$  in the colored state (Fig. 4.2). Fig. 4.1(b) shows that at  $\lambda = 633$  nm excitation wavelength, the simulated SPP resonance shifts from  $\theta = 49.81^\circ$  to  $\theta = 48.72^\circ$  during redox cycling of the plasmochromic Kretschmann stack (PCK). Meanwhile, the reflectance at resonance of the PCK significantly decreases from 3.6% to 0.32%. Fig. 4.3 presents FDTD simulation of the electric field distribution in a PCK device due to the coupling of the  $\lambda = 633$  nm excitation wavelength. In Fig. 4.3(a), the laser light electric field reaches the PCK structure, propagates through the bottom electrode and the ECD that form an effective medium metal to the top Au electrode, and couples as an SPP. The oxidation state of the ECD, hence, directly influences the coupling of the optical laser electric field to the top Au electrode. Fig. 4.3(b) shows electric field distribution in the PCK device  $t = 5$  fs later, with most of the E-field coupled to the top electrode and propagating along the Au film in  $x$ -direction as a SPP wave. Notably, in Fig. 4.2(b), the electric field is normalized to the maximum value reached for the coupled SPP, as such, it is evident that the SPP not only propagates, but also localizes the electric field and leads to an enhancement at the metal-air interface.

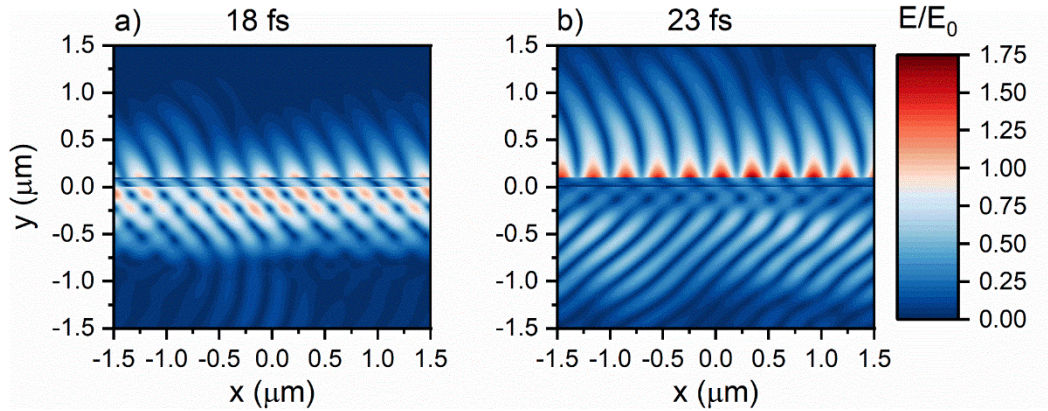


Fig. 4.3: FDTD simulation of the electric field distribution in a PCK device. (a) 633 nm laser light excitation coupling to the PCK at  $t = 18$  fs after the start of simulation. (b) SPP propagation along the top Au surface at  $t = 23$  fs after the start of simulation.

The SPP resonance angle, as well as the modulation depth, can be adjusted through changing the  $\text{WO}_3$  thickness. As illustrated in Fig. 4.4, the absorption peak for the resonance angle broadens for thicker  $\text{WO}_3$  films and shifts to larger angles. Furthermore, the minimum reflectance increases for thicker EC films. For a completely oxidized  $\text{WO}_3$  film ( $0 \text{ mC/cm}^2$ ), the resonance angle shifts from  $\theta = 48^\circ$  for 10 nm thickness to  $\theta = 65^\circ$  at 40 nm thickness. Meanwhile, a lithiation of the  $\text{WO}_3$  film ( $62.5 \text{ mC/cm}^2$ ) leads to deeper resonances, shifting from  $\theta = 49^\circ$  to  $\theta = 55^\circ$  for  $d = 10 \text{ nm}$  and  $d = 40 \text{ nm}$ , respectively. In reality, both EC films (i.e.,  $\text{WO}_3$  and  $\text{NiO}$ ) thicknesses have to be adjusted to be able to accommodate the access of  $\text{Li}^+$  ions during redox cycling.

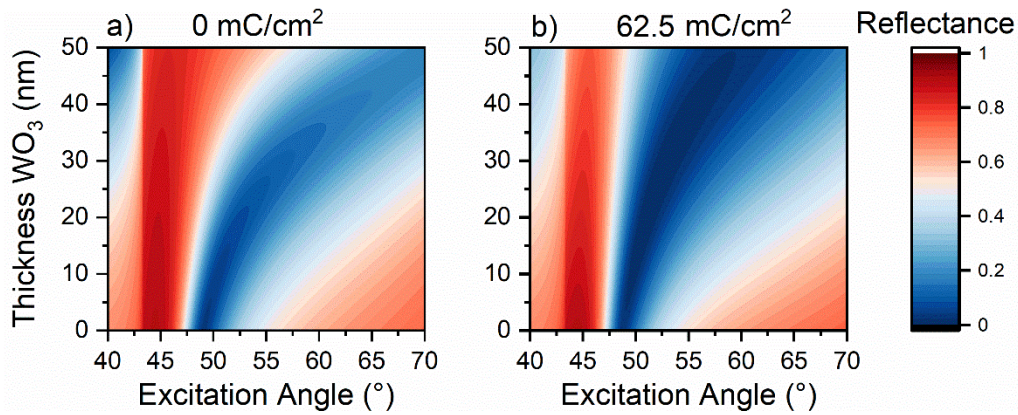


Fig. 4.4: Calculations of the reflectance of a PCK as a function of excitation angle and WO<sub>3</sub> thickness. (a) Reflectance for  $C = 0 \text{ mC/cm}^2$  intercalated charge and (b) Reflectance for  $C = 62.5 \text{ mC/cm}^2$  intercalated charge.

#### 4.1.2 PCK Experimental Results

The PCK is fabricated on nanopolished quartz substrates. First, an Au bottom electrode is deposited using evaporation ( $d_{\text{Au}} = 20 \text{ nm}$ ). Afterwards, the thin film ECD is deposited using reactive magnetron sputtering where optical profilometry after every oxide film deposition is used to determine the oxide layer thicknesses. The oxide films are deposited with approximate thicknesses of  $d_{\text{WO}_3} = 25 \text{ nm}$ ,  $d_{\text{Ta}_2\text{O}_5} = 10 \text{ nm}$  and  $d_{\text{NiO}} = 30 \text{ nm}$ . Consequently, the deposited films are wet-lithiated by immersion in 0.1 M LiClO<sub>4</sub> and application of  $V = -2.5 \text{ V}$  potential.<sup>245</sup> The films are cleaned with pure PC and dried by flowing N<sub>2</sub> gas. Finally, another 20 nm thick Au top electrode is evaporated.

The SPP resonance measurements are conducted with a HeNe laser delivering p-polarized optical radiation at a wavelength  $\lambda = 632.8 \text{ nm}$ . The excitation angles are swept through via a high-precision stepper motor driving a rotation stage having

a resolution of  $0.05^\circ$ . The reflected light intensity is measured using a Si photodiode and captured by a digital oscilloscope.

Fig. 4.5(a) shows the angle dependent optical reflectance for the fabricated the PCK in its fully lithiated (i.e.,  $V = +3$  V)  $\text{WO}_3$  and delithiated  $\text{WO}_3$  (i.e.,  $= -3$  V) states. The applied voltage is referenced to the top electrode. The resonance angle shifts from  $\theta = 47.8^\circ$  in the delithiated state to  $\theta = 46.7^\circ$  in the lithiated state. At these resonance angles, the optical reflectance decreases from  $R = 0.08$  to  $R = 0.02$ . Both states show high stability, with the optical reflectance at  $\theta = 46.7^\circ$  increasing by only  $+0.015$  to  $R = 0.035$  after 1h when no potential is applied ( $\Delta R = -0.02$  for the delithiated state at resonance). Furthermore, switching of the device between the two states occurs in less than  $t = 1$  s.

Fixing the excitation angle at  $\theta = 47.5^\circ$  and sweeping the applied voltage at  $v = 25$  mV/s sweeping rate leads to a hysteresis of the optical reflectance curve as shown in Fig. 4.5(b). During redox cycling of the device, intercalation and deintercalation potential barriers exist similar to conventional ECDs, making the device bistable. The measurements here indicate several hours of bistability and hence potential applications as plasmochromic memories are possible. Interestingly, the corresponding IV measurement and the resulting curve show a similar hysteric behavior as shown in Fig. 4.5(c). Starting the potential sweep at 0 V going to positive voltages, the PCK device is in a high resistive state until enough  $\text{Li}^+$  ions are extracted from the NiO layer by applying a potential ( $V = +2.5$  V), hence, increasing the conductivity of the PCK device. Intercalation of  $\text{Li}^+$  ions into  $\text{WO}_3$  also leads to increased conductivity of the EC film, but no hysteresis is visible.

The reason for the absence of the hysteresis could have to do with the intercalation process in the thin  $\text{WO}_3$  film that might favor pseudocapacitive intercalation over a redox reaction. At  $V = 1.2$  V, the PCK device reaches its highest resistance state with both EC films exhibiting their lowest conductivity (Fig. 4.5(d)). This state can be interpreted as the equilibrium state in which both EC films exhibit the lowest amount of free charge carriers. However, by applying a negative voltage to NiO, the current flow stays low until a threshold of -2 V is reached when the current increases by two orders of magnitude. When sweeping the voltage back up, the current stays at levels over  $10^{-9}$  A until -0.65 V applied voltage are reached. The bistability of electrochemical intercalation into NiO changes the electrical properties of the film and induces resistive switching, while the redox reaction happening to the device leads to a change in the coupling of the SPP. Thus, the PCK device presents a way of relating plasmochromic functionality with electrical switching.

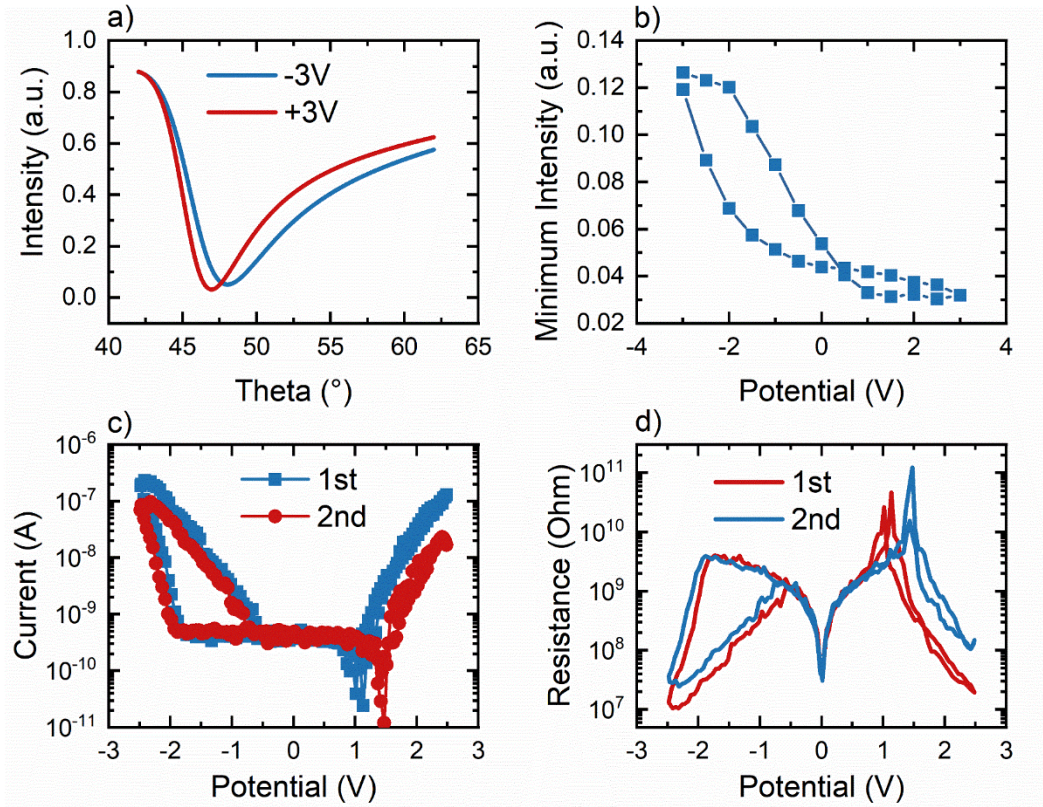


Fig. 4.5: Experimental results for EC dependence of the PCK device. (a) SPP resonance measurements for EC cycling at +3V and -3V. (b) Fixed angle measurement light intensity as a function of the applied potential. (c) I-V curves of the PCK device. (d) Electrical resistance resulting from the I-V measurements.

## 4.2 Nanoplasmonic Waveguide Nonresonant Modulator<sup>117</sup>

To increase the light matter interaction on a nanoscale, plasmonic nanostructures are integrated into waveguiding devices, thus, leading to radically enhanced linear and nonlinear effects. On-chip hybrid plasmonic waveguides exhibit strong light confinement in structures having dimension much less than the wavelength of light,<sup>158,246</sup> while also providing an excellent platform for enhancing the electromagnetic mode interaction within the waveguide's core.<sup>159,247</sup> Dynamic control of plasmon transport and propagation loss in waveguides has been realized mainly through thermal activation, where micro heaters or high power laser pulses are employed to either change the properties of a thermochromic material (e.g. vanadium oxide<sup>83,248</sup>) or by directly heating the waveguide's core.<sup>249</sup> Despite thermal modulation of plasmonic waveguides offering direct control over light transmission, the high energy consumption and excessive heat dissipation are inferior in comparison to their optical or electrical counterparts. ECDs, having their low operating voltages and bistable nature, can dynamically and moreover reversibly change the dielectric environment of the propagating plasmon, either by changing its resonance wavelength or its dielectric loss. To achieve ultra-high EC-based optical transmission modulation depth based in an all-solid-state waveguide device, an active metal-insulator-metal plasmochromic waveguide (PCWG) is designed. The PCWG consists of nanometer thick  $\text{WO}_3$  and  $\text{LiNbO}_3$  layers sandwiched between two plasmonic gold electrodes. Through the reversible process of intercalation and deintercalation of  $\text{Li}^+$  into the  $\text{WO}_3$  film, both the real

and imaginary components of the refractive indices are modified, thus, altering the loss in the plasmonic waveguide.

#### 4.2.1 PCWG Design and FDTD Simulations

A Schematic of the PCWG device is illustrated in Fig. 4.6. The PCWG is designed to exhibit two distinct optical states: “On” and “Off”. Through lithiation or delithiation of  $\text{WO}_3$  by means of  $\text{Li}^+$  ion intercalation, the optical transmission of the PCWGs can be dynamically altered. Upon applying a voltage bias, and depending on the voltage polarity, to the Au electrodes,  $\text{Li}^+$  ions move through the  $\text{LiNbO}_3$  ion conductor and are transferred into (by applying positive voltage) or out of (by applying a negative voltage) the  $\text{WO}_3$  film. Ion intercalation into  $\text{WO}_3$  leads to a reduction from  $\text{W}^{6+}$  in the delithiated state ( $0 \text{ mC/cm}^2\mu\text{m}$  intercalated charge) to  $\text{W}^{4+}$  in the fully lithiated state ( $\sim 68 \text{ mC/cm}^2\mu\text{m}$ ). Simultaneously, electrons balance the intercalated charge, leading to charge carrier densities of up to  $10^{22}/\text{cm}^3$ .<sup>33,35</sup> While the fully oxidized state of  $\text{WO}_3$  acts as an optically transparent insulator, the semiconducting reduced state is highly absorbing to light due to the presence of excess valence electrons. Amorphous  $\text{WO}_3$  has been shown to exhibit higher EC optical modulation and faster switching speed compared to its crystalline phase,<sup>201</sup> while amorphous  $\text{LiNbO}_3$  offers good ionic conductivity. Since the directions of  $\text{Li}^+$  ion transport and the plasmon propagation are orthogonal to each other (Fig. 4.6(c)), optical modulation and switching speed can be decoupled and independently optimized. The 250 nm  $\text{LiNbO}_3$  thin film hence offers multiple functionalities in this device, with ion conduction and storage and SPP propagation

along the film. The waveguide is excited through a 1550 nm wavelength laser coupled through a high numerical aperture in free space.

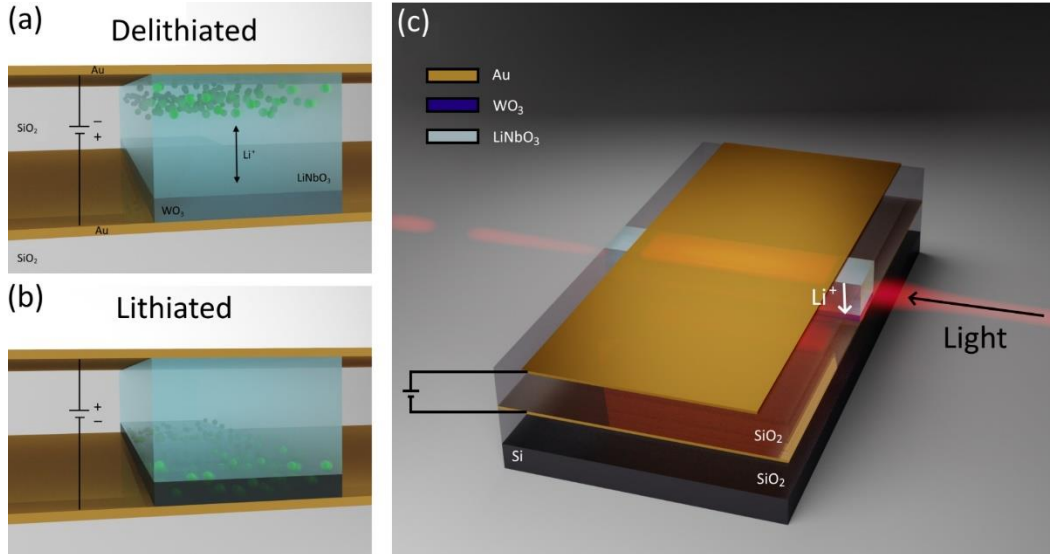


Fig. 4.6: Schematic of the PCWG device operation. (a) Delithiated state: WO<sub>3</sub> is transmissive - On. (b) Lithiated State: WO<sub>3</sub> is absorptive - Off. (c) Overview of the device structure with light and ion diffusion paths indicated.

To examine device properties and optimize fabrication parameters, the PCWG structure is simulated using FDTD. The material parameters are adjusted using measurement data and the simulation region is chosen as a 3D structure having a height of 5  $\mu\text{m}$  and a width of 5  $\mu\text{m}$ . The length of the simulation region is set to fit the waveguide length. A 1550 nm wavelength mode light source and the subsequent fundamental TE mode are used to excite the structure, while a 2D power monitor is placed at the end of the waveguide to record the transmitted light power. Around the waveguide a refined mesh with a spacing equivalent to 10% of the respective film thickness is placed. Perfectly matched layer (PML) boundary conditions are

used in all directions. Refractive indices data for Au, SiO<sub>2</sub>, Si, LiNbO<sub>3</sub>, and Cr were used as pre-installed. The dielectric properties for WO<sub>3</sub> are extracted from ellipsometry measurements of a 200 nm thick WO<sub>3</sub> film on a W metallic substrate. The results of the analysis are shown in Fig. 4.7. As evident from the ellipsometric measurements, the lithiation dependent refractive index,  $n$ , as well as the extinction coefficient,  $k_{ex}$ , undergo dramatic changes upon WO<sub>3</sub> redox reaction. While the refractive index in the NIR increases by up to  $\Delta n_{NIR} = 0.45$ , the change in the visible spectrum is less and in the opposite direction  $\Delta n_{VIS} = -0.3$ . The change in extinction coefficient is highest around the wavelength  $\lambda = 1250$  nm, reaching a value  $\Delta k = 0.5$ . Hence, the results suggest optimal device performance in the NIR around the telecommunication wavelengths of 1330 nm and 1550 nm.

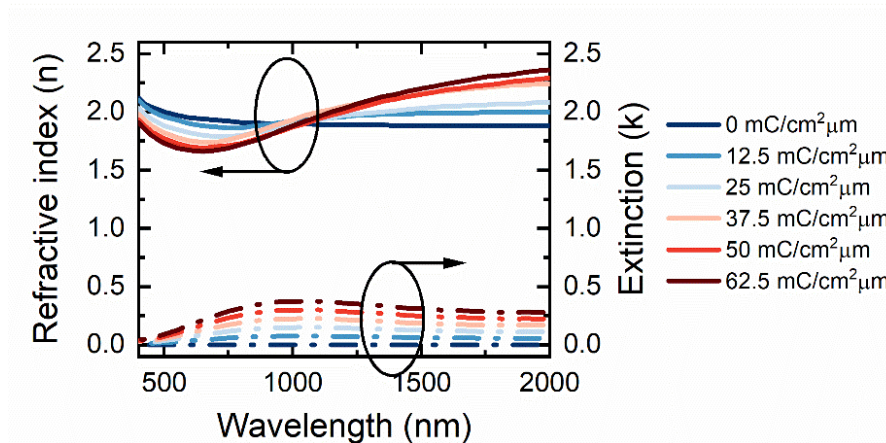


Fig. 4.7: The refractive index and the extinction coefficient of a 200 nm thick WO<sub>3</sub> film on W at different intercalation levels of Li<sup>+</sup> ions. Li<sup>+</sup> ions are intercalated through a constant applied current in a 0.1 M LiClO<sub>4</sub> electrolyte. Intercalated charge is the product of current over time.

A potential EC effect in  $\text{LiNbO}_3$  is not measurable, since the refractive index of a 100 nm thick film remains unchanged after the intercalation of  $3.7 \text{ mC/cm}^2 \text{ Li}^+$  ions. Based on the measured values for the intercalation dependent  $\text{WO}_3$  refractive index, and the extinction coefficient, light interaction with a  $2 \mu\text{m}$  wide PCWG can be simulated via FDTD (Fig. 4.8). Fig. 4.8(a) presents the plasmon transmittance of the  $2 \mu\text{m}$  wide PCWG as a function of lithiation for lengths  $l = 5 \mu\text{m}$  and  $l = 10 \mu\text{m}$ . For comparison, the transmittance of a 50 nm thick  $\text{WO}_3$  layer on ITO is included in the graph (i.e., planar EC). Evidently, the  $5 \mu\text{m}$  long PCWG exhibits a greatly enhanced EC optical transmission modulation achieving up to  $5.6 \times 10^{-3}$  transmission modulation at a wavelength of 1550 nm. The low optical transmission in the On-state is due to plasmonic loss of 57% when the PCWG.

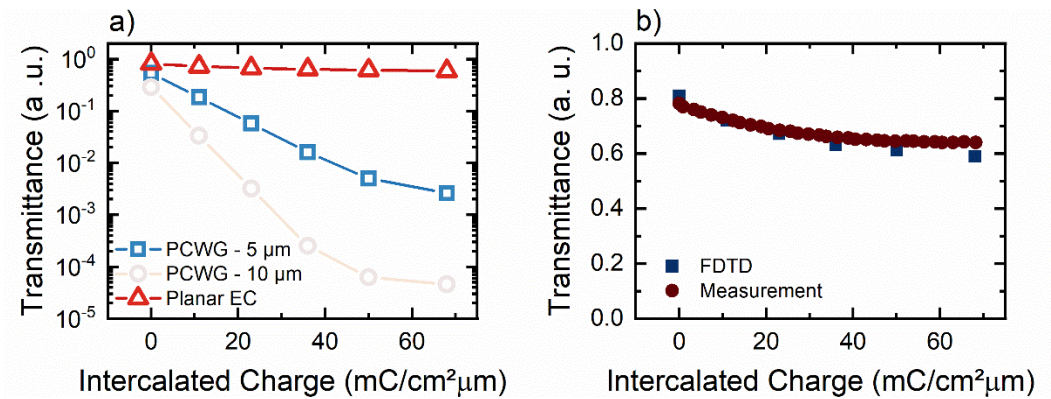


Fig. 4.8: (a) FDTD simulated plasmon transmittance at 1550 nm for PCWGs of width  $w = 2 \mu\text{m}$  and lengths  $L = 5 \mu\text{m}$  and  $10 \mu\text{m}$ . Shown also is the optical transmittance of a 50 nm thick  $\text{WO}_3$  film. (b) Comparison of simulated and measured transmittance of a 50 nm thick  $\text{WO}_3$  on ITO for different intercalation levels.

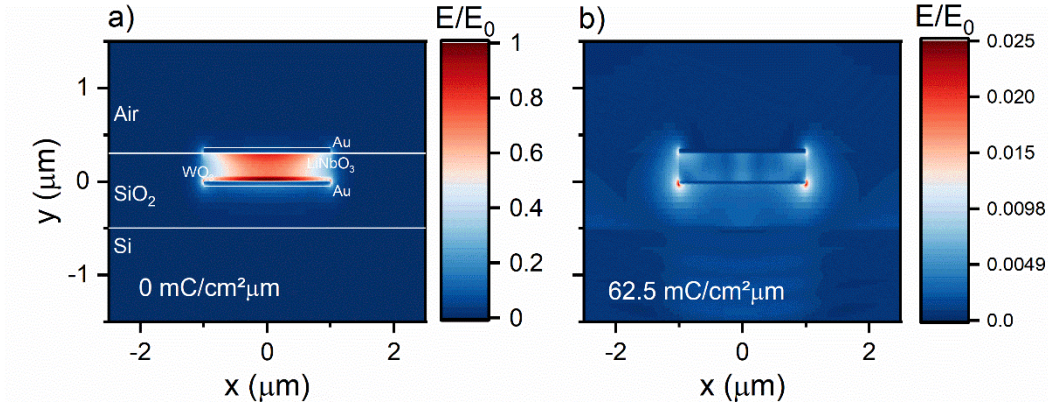


Fig. 4.9: FDTD simulations of the normalized magnitude of the E-field distribution in a 2  $\mu\text{m}$  wide PCWG captured at 5  $\mu\text{m}$  propagation length: (a) with fully oxidized  $\text{WO}_3$  and (b) after the  $\text{Li}^+$  ion intercalation.

In contrast, the planar ECD consisting of a 50 nm thick  $\text{WO}_3$  layer exhibits a maximum modulation of 26%. Here, a glass substrate is assumed for the film, even though, in reality a conductive electrode is necessary for coloration of the film. When increasing the waveguide length to 10  $\mu\text{m}$ , the optical modulation increases to  $2.5 \times 10^{-5}$  with an On-state optical transmission of  $\sim 25\%$ . It becomes obvious that the modulation depends strongly on the PCWG length, and, as such the plasmonic loss can be calculated as 12.5% per  $\mu\text{m}$ , wherein the maximum achievable modulation is 69.8% per  $\mu\text{m}$ . Hence, a 40  $\mu\text{m}$  long PCWG will exhibit roughly 1% On-state optical transmittance and over  $10^{20}$  Off-state modulation.

The accuracy of the FDTD optical transmittance results is verified by spectro-electrochemical measurement of a 50 nm thick  $\text{WO}_3$  deposited on an ITO coated glass substrate. A comparison between the respective FDTD simulations optical transmittance and the experimentally measured one are shown in Fig. 4.8(b).

Remarkably, the measurement data fit the FDTD simulations very well with small differences at higher charge intercalation levels. The difference is attributed to the different substrates (i.e., W and ITO) when measuring the dielectric properties (W) and the transmittance (ITO). However, in the case of the waveguide samples, additional factors, such as lithiation profiles, surface roughness and coupling losses have to be considered when evaluating the maximum achievable transmission modulation.

As shown in Fig. 4.9, FDTD simulations further help to predict the shape and the distribution of the plasmonic mode propagating along the waveguide for a fully oxidized  $\text{WO}_3$  and after the  $\text{Li}^+$  ion intercalation. The 50 nm thin  $\text{WO}_3$  film, sputtered onto the bottom Au electrode, contains 76% of the electric field, as such sufficient overlap of the plasmon and the modulation layer is possible as shown in Fig. 4.9(a). While the electric field intensity is localized at the  $\text{WO}_3$  near the bottom Au electrode when no  $\text{Li}^+$  ions are injected (i.e., 0  $\text{mC}/\text{cm}^2\mu\text{m}$ ), the intensity in the waveguide core decreases by more than three orders of magnitude during the  $\text{Li}^+$  ion intercalation. By increasing the  $\text{Li}^+$  ion intercalation level to 68  $\text{mC}/\text{cm}^2\mu\text{m}$ , the maximum electric field intensity decreases by two orders of magnitude due to increased losses, while the plasmon mode is forced out of the PCWG core and mainly propagates along the edges of the metallic electrode. Simulation results indicate that PCWGs having a width  $w = 2 \mu\text{m}$ , height  $h = 300 \text{ nm}$  and lengths  $l > 10 \mu\text{m}$  can exhibit high optical modulation and sufficient modal overlap between the plasmon and the EC  $\text{WO}_3$  layer.

## 4.2.2 PCWG Fabrication

The PCWG devices are fabricated on a 500  $\mu\text{m}$  Silicon wafer having a 500 nm thick thermal oxide layer. Multiple optical lithography steps are employed to pattern the waveguides and chips for processing. Alignment between the subsequent steps is conducted automatically on the Heidelberg MLA150 lithography tool and is measured to have an accuracy of  $< \pm 100$  nm. In the first processing step, 350  $\mu\text{m}$  deep scores are sawed into the back of the, dividing it into 5 mm  $\times$  10 mm pieces.

The scored wafers are cleaned in Piranha solution and subsequently dehydrated to deposit a monolayer of hexamethyldisilazane (HMDS) for photoresist adhesion. For the first lithography step, a lift-off resist bilayer consisting of 500 nm thick layer of LOR 5B and 1.1  $\mu\text{m}$  thick layer of AZ1512 positive photoresist, is spin-coated onto the wafer. The resist is exposed in a Heidelberg MLA 150 maskless alignment system at 160 mJ/cm<sup>2</sup> to transfer the pattern for the bottom Au contacts. After development, a 5 nm/25 nm/5 nm trilayer of Cr/Au/Cr is electron beam evaporated onto the wafer. Following the first lift-off procedure, a 300 nm thick film of SiO<sub>2</sub> is deposited through plasma-enhanced chemical vapor deposition (PECVD). A second lithography step of a single layer of AZ1512 is needed to facilitate the transfer of the waveguide pattern onto the bottom Au contacts. The waveguide trenches are etched through reactive ion etching in a CHF<sub>3</sub> plasma at 50 W (Oxford PlasmaPro 80).

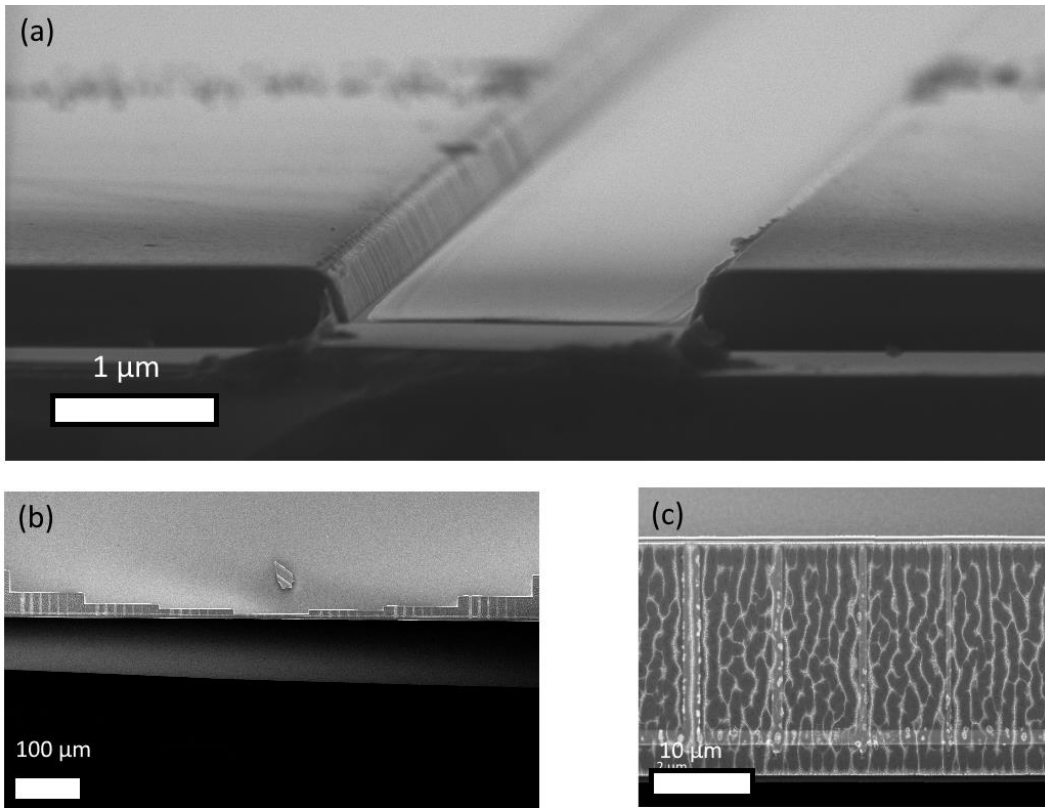


Fig. 4.10: SEM images of the PCWG device at different stages of the fabrication process. (a) Etched trench after waveguide patterning. (b) Beam structure after DRIE etch. (c) Close-up of defined PCWG devices.

A SEM image of the etched trench is shown in Fig. 4.10(a). Next, 50 nm thick film of  $\text{WO}_3$  and 250 nm thick film of  $\text{LiNbO}_3$  are deposited through a reactive magnetron sputtering process. During deposition of the  $\text{WO}_3$ , the Ar plasma is ignited at 50 W over the  $\text{LiNbO}_3$  target while shutter on the  $\text{LiNbO}_3$  remains closed (Appendix A). This process is important as it leads to  $\text{Li}^+$  ion diffusion into the  $\text{WO}_3$  film and, therefore, helps in building up an excess reservoir of mobile  $\text{Li}^+$  ions.<sup>123</sup>  $\text{LiNbO}_3$  is deposited from an oxide target in a RF sputtering process. The deposition processes are discussed earlier (see Section 3). Both films are

simultaneously deposited on a clean Si wafer to investigate their crystal structure. Amorphous films of  $\text{WO}_3$ , as well as  $\text{LiNbO}_3$  offer better coloration efficiency and improved ion dynamics. Fig. 4.11 shows the respective XRD spectra of the deposited  $\text{WO}_3$  and the  $\text{LiNbO}_3$  films. For the  $\text{WO}_3$  film, the significant peaks at  $23^\circ$  and  $52.5^\circ$  are indicated. The broadened peaks indicated an amorphous nature with small crystalline structures. XRD analysis of the  $\text{LiNbO}_3$  thin film suggests a fully amorphous crystalline structure as only the Si peaks are distinctly visible (denoted by \*) while a broad shoulder between  $20^\circ$  and  $40^\circ$  arises from the deposited  $\text{LiNbO}_3$ .

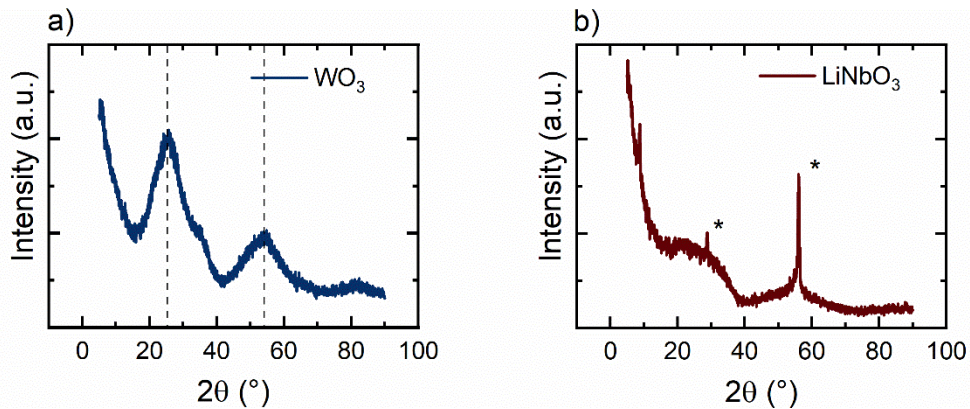


Fig. 4.11: XRD spectra of: (a) reactively sputtered  $\text{WO}_3$  film on Si. (b) 100 nm thick sputter deposited  $\text{LiNbO}_3$  film on Si. The peaks indicated by (\*) are due the Si substrate.

After the deposition of the waveguide core materials, the AZ1512 photoresist is lifted-off. It is imperative to stress that the wafers do not encounter water contact for at least one day after lift-off process, as the organic solvents lead to a dehydration of the EC film and an abrupt rehydration leads to expansion and

delamination of the oxide films. Following the rehydration period, a layer of 50 nm thick Au and a 20 nm thick Cr are deposited onto the wafer. The metal films are patterned through a third lithography step utilizing a 4.1  $\mu\text{m}$  thick AZ1529 photoresist film. The metals are etched in respective wet etchants, followed by a reactive-ion etching (RIE) to etch the  $\text{SiO}_2$  layer and a deep reactive ion etch (DRIE) to etch the Silicon wafer to separate the wafer into dies Fig. 4.10(b). The resulting chips are cleaned in a low power oxygen plasma for 30 minutes to remove the DRIE scum (Fig. 4.10(c)). As shown in Fig. 4.12, the fabricated devices exhibit a slightly roughed surface over the waveguide structures, which is attributed to evaporation of solvents intercalated into  $\text{LiNbO}_3$  during the Au deposition process. As depicted in Fig. 4.12, the SEM images show a 250 nm thick  $\text{LiNbO}_3$  ion conductor and a 50 nm thick  $\text{WO}_3$  film. Light and ion propagation paths are indicated for convenience. It becomes evident, that  $\text{Li}^+$  ion diffusion occurs over a maximum distance of 250 nm, while the light interacts with such layer for a distance of 10  $\mu\text{m}$ . Assuming the switching time is directly proportional to the diffusion length  $l_D$  and the diffusion coefficient  $D$ ,  $\tau$  can be expressed as follows:<sup>250</sup>

$$\tau \propto l_D^2/D \quad (4.1)$$

Hence, the waveguide device is expected to function similar to an EC smart window device having an optical thickness of  $d_t > 10 \mu\text{m}$  but expressing ion diffusion dynamics of a thin film with a thickness of 50 nm.

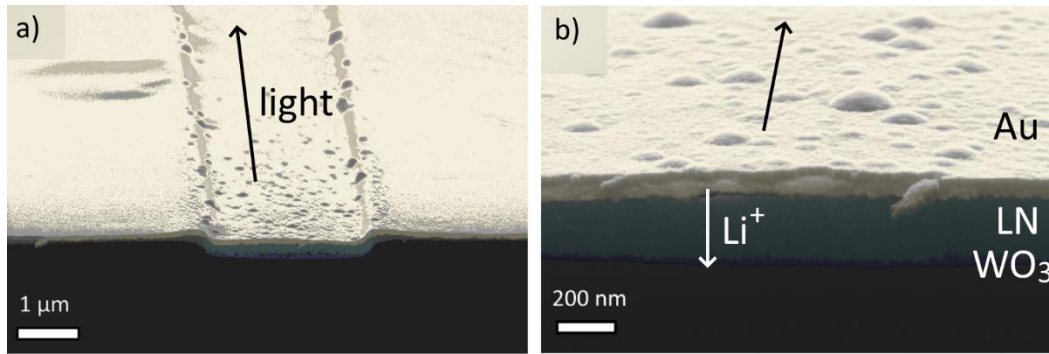


Fig. 4.12: SEM images of finished PCWG devices. (a) Overview of the fabricated PCWG (light propagation direction is indicated by the black arrow). (b) Close-up of MIM waveguide structure ( $\text{Li}^+$  ions diffusing path is indicated by the white arrow).

### 4.2.3 Photo-Electrochemical Analysis of PCWG

The lithiation dependent dynamics of the PCWG are determined by sweeping an applied voltage at  $v = 10 \text{ mV/s}$  and simultaneously recording the transmitted optical power with a ThorLabs D100 power meter. The voltage is swept via a Keithley 2400 source meter. The PCWG is excited by 1550 nm laser radiation delivered from Toptica FemtoPro  $\text{Er}^{3+}$  fiber laser and coupled through an objective with  $\text{NA} = 0.85$ . A lensed single mode fiber having 2  $\mu\text{m}$  working distance is used for collection of transmitted light. For a wavelength  $\lambda = 1550 \text{ nm}$  and the objective's  $\text{NA} = 0.85$ , the calculated coupling efficiency is 18.35%. However, for an excitation power of  $P_0 = 1 \text{ mW}$ , the transmitted power in the On-state,  $P_{\text{on}}$ , of a 10  $\mu\text{m}$  long is 32  $\mu\text{W}$ . The low transmitted optical power (total loss of 96.8%) is attributed to the plasmonic loss at the metal electrodes and inhomogeneities of the coupling facet.

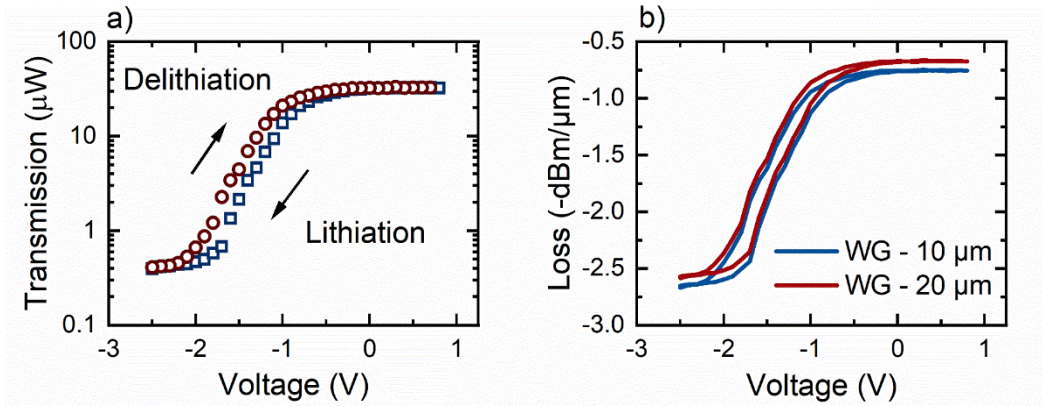


Fig. 4.13: Photo-electrochemical analysis of PCWG devices. (a) Voltage dependent optical transmission of a 10  $\mu\text{m}$  long PCWG. (b) Comparison of loss per unit length of a 10  $\mu\text{m}$  and a 20  $\mu\text{m}$  long PCWGs.

The results of the voltage dependent optical transmission measurements for different PCWGs are shown in Fig. 4.13. Over one complete reversible process, the lithiation and the delithiation processes shown in Fig. 4.13(a) exhibit a slight hysteresis, which is strongly correlated to the shape of the EC CV curves for  $\text{WO}_3$ . Starting at  $V = 0.8 \text{ V}$ , the optical transmission remains constant until a voltage threshold of around  $V = -0.6 \text{ V}$  is reached. The negative potential attracts the  $\text{Li}^+$  ions to overcome the insertion barrier and diffuse into the  $\text{WO}_3$  thin film, where both the refractive index and the extinction coefficient start to change. Applying higher negative voltages increases these changes until a minimal light transmittance of 395 nW is reached at  $V = -2.5 \text{ V}$  (i.e., an optical modulation depth of  $\sim 20 \text{ dB}$ ). When the voltage is swept back up to 0.8 V,  $\text{Li}^+$  ion deintercalation onsets around  $V = -1.8 \text{ V}$ , which leads to a slight hysteresis of the light transmittance curve before the initial transmittance level is recovered under positive bias. For the 20  $\mu\text{m}$  long

waveguide having the same cross-section, a modulation depth of nearly 38 dB has been achieved. When comparing the loss per length of the two waveguides referenced to the coupled power of 184  $\mu\text{W}$  (Fig. 4.13(b)), it is evident that the plasmochromic modulation is constant along the waveguide. The small offset of the two curves is attributed to constant parasitic losses. At 0  $\text{mC}/\text{cm}^2\mu\text{m}$  lithiation, the 20  $\mu\text{m}$  long PCWG exhibits a slightly reduced loss per  $\mu\text{m}$  of 0.1  $\text{dB}/\mu\text{m}$  compared to the 10  $\mu\text{m}$  long PCWG, which can be attributed to a better coupling or reduced surface roughness. Nonetheless, this leads to a loss that is  $\sim 0.2$   $\text{dBm}/\mu\text{m}$  higher than that of the simulated device. While the loss modulation per unit length in both PCWGs is high, they do not achieve the theoretically predicted modulation of 5  $\text{dB}/\mu\text{m}$ . This discrepancy is attributed to a  $\text{Li}^+$  ion shortage in the electrolyte and to the incomplete reduction of the thin  $\text{WO}_3$  layer. Nonetheless, the modulation data presents the same trend as the simulations for intercalation levels and waveguide length.

Fig. 4.14 compares the simulated and measured transmission of the 10  $\mu\text{m}$  long PCWG at different lithiation levels. The measured data is normalized to 18.4% coupling efficiency. To obtain lithiation dependent data a constant current of  $J = 1$   $\text{mA}/\text{cm}^2$  is applied to the device and the resulting transmission is measured. The intercalated charge is then calculated as current density over time. Due to malicious current flow and the finite electrical resistance of  $\text{LiNbO}_3$ , the calculated lithiation is most likely higher than the actual amount of intercalated  $\text{Li}^+$  ions. Nonetheless, a similar saturation of the coloration effect can be seen for both the simulated and the measured PCWG device for high degrees of lithiation. However, the actual

device exhibits  $\sim 1.5$  orders of magnitude lower optical transmission modulation, which is attributed to incomplete reduction of  $\text{WO}_3$  due to the parasitic currents.

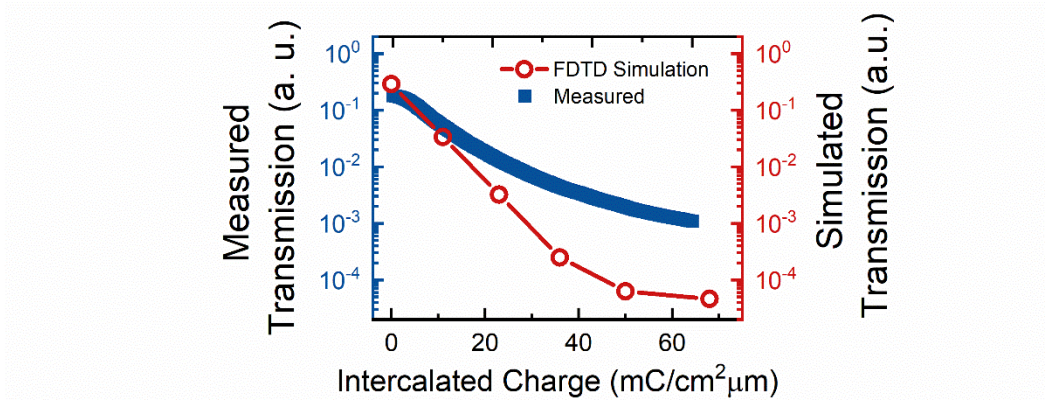


Fig. 4.14: Comparison of lithiation dependent optical transmission of a simulated and a measured 10  $\mu\text{m}$  long PCWG. Measured values for intercalated charge are determined as current over time.

While the lithiation dependent behavior of the PCWGs can be predicted through FDTD simulations, the dynamic response time cannot be simply inferred from the model. The experimentally measured dynamics of the optical response to the redox reaction are presented in Fig. 4.15. As shown in Fig. 4.15(a), when comparing the lithiation times of the 10 and 20  $\mu\text{m}$  long PCWGs with a planar EC device, the normalized time-dependent transmission modulation is greatly enhanced for the PCWGs (Fig. 4.15(b,c)). While the PCWGs' full lithiation achieves 90% optical transmission modulation in  $\tau_c = 3.3$  s, the planar EC device takes  $\tau_c = 14.7$  s to reach the same optical modulation level. The faster lithiation time of the PCWG is a result of the incorporation of the thin (50nm)  $\text{WO}_3$  film, which permits short  $\text{Li}^+$  ion diffusion paths, while ultra-high modulation is retained through the long optical

path in the PCWG. Interestingly, since the absorption loss is proportional to the light propagation length,  $x$ , according to Lambert's law:

$$I(x) = I_0 e^{-\left(\frac{4\pi k_{ex}(C)}{\lambda} + \gamma_{SP}\right)x} \quad (4.2)$$

where  $I$  is the modulated light intensity,  $I_0$  is the coupled light intensity into the PCWG,  $k_{ex}(C)$  is the  $\text{Li}^+$  ion concentration-dependent extinction coefficient,  $\lambda$  is the light wavelength, and  $\gamma_{SP}$  is the plasmon propagation loss coefficient. During the lithiation process of the EC film  $k(C)$  gradually increases with the insertion of the  $\text{Li}^+$  ions, thus, the overall optical can far exceed the plasmon propagation loss. As such, longer PCWGs can achieve the same modulation depth at lower lithiation levels and subsequently at lower voltages in comparison to shorter PCWGs. Relative to the 10  $\mu\text{m}$  long waveguide, the measured switching time for a 20  $\mu\text{m}$  long waveguide exhibits significantly decreased lithiation ( $\Delta\tau_c = 0.82$  s) and delithiation ( $\Delta\tau_b = 2.7$  s) times.

The achieved optical modulation depth per volt (8 dB/V) in the PCWG modulator (10  $\mu\text{m}$  long) is an order of magnitude higher than that of other state-of-the-art voltage-driven plasmonic electrooptic modulators. Since the optical modulation depth greatly depends on the length of the PCWG, the optical modulation depth could be further enhanced to exceed 50 dB by using longer ( $> 20$   $\mu\text{m}$ ) waveguides, while operating at much lower voltages.

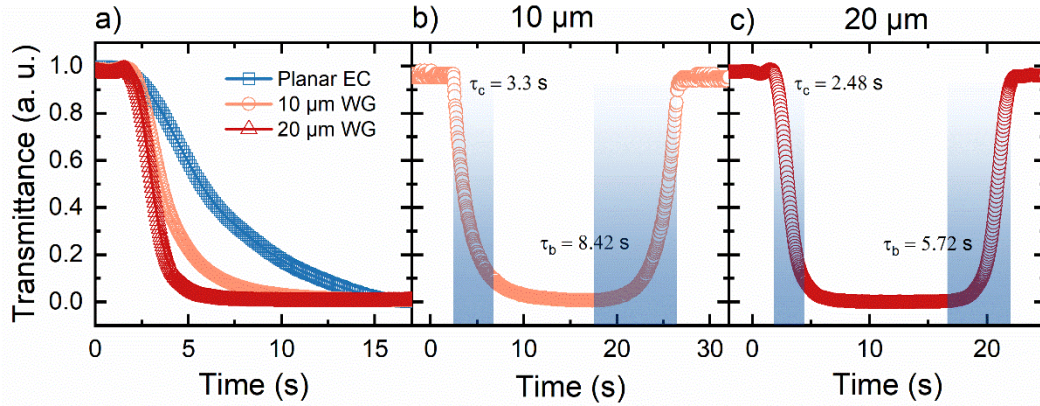


Fig. 4.15: Switching dynamics of PCWG devices. (a) Comparison of time dependent optical transmission for PCWGs and planar EC at  $V = -2.5$  V. (b) Coloration dynamics and indicated switching times for 10  $\mu\text{m}$  long PCWG. (c) Switching times for 20  $\mu\text{m}$  long PCWG.

To discern the relationship between the optical modulation depth and the duty cycle, Fig. 4.16(a) presents the optical transmission as a function of time for  $t = 15$  s, 5 s, 2 s, and 1 s duty cycles. Under an alternating bias of  $\pm 2.5$  V, the 10  $\mu\text{m}$  long PCWG exhibits the full 20 dB modulation for the 15 s duty cycle. Reducing the duty cycle to 5 s reduces the optical modulation depth to 13 dB which indicates that the PCWG has not reached the fully delithiated state. Further decreasing the duty cycle to 1 s enhances this effect where the modulation depth reaches 3 dB.

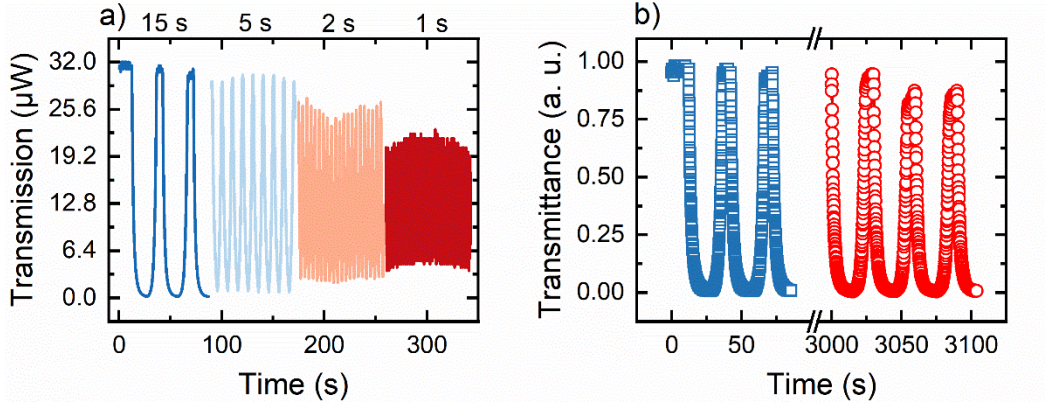


Fig. 4.16: Switching times of the PCWGs. (a) Time-dependent light transmission switching behavior under various  $\pm 2.5$  V duty cycles. (b) Transmittance modulation of the PCWG over 3000 s, or 200 cycles.

Along with the advantages of high optical modulation depth and fast switching speed, the PCWGs show good reversible transmittance modulation (Fig. 4.16(b)). Over 50 minutes of repeated cycling, the maximum optical transmittance in the delithiated state of the 10  $\mu\text{m}$  long PCWG decreases only by 12%, while the optical transmittance in the fully lithiated state remained unaltered at 150 nW. The decrease in maximum optical transmittance is attributed to irreversible  $\text{Li}^+$  ion intercalation into the  $\text{WO}_3$  thin film. Notwithstanding, after 50 minutes of reversible cycling, the process of permanent  $\text{Li}^+$  ion intercalation into the  $\text{WO}_3$  layer saturates at 12% permanent loss.

#### 4.2.4 Discussion

The PCWGs investigated show greatly enhanced EC switching resulting in faster speeds and higher optical transmission modulation than the planar counterparts. However, the experimentally obtained modulation of the PCWGs is orders of magnitude lower than that simulated via FDTD. A possible solution to the incomplete lithiation of the  $\text{WO}_3$  film that could be a source of this discrepancy is the dry lithiation of the active EC films and the waveguide core.<sup>251,252</sup> Furthermore, electron-beam lithography could be employed to further down-scale the waveguide dimensions. Miniature PCWGs would lead to further increased light-matter interaction and, hence, could increase modulation depth and switching speed.

### 4.3 Plasmochromic Nanocavity<sup>81</sup>

Highly chromatic reflectance was realized in metal-insulator-nanostructured (MIN) plasmonic cavities composed of nanohole array metasurfaces.<sup>52,65,253</sup> Such an MIN platform offers high integration density of  $10^5$  dpi<sup>254</sup>, while promising low fabrication cost. The large scale realization of nanostructured metal surfaces is made possible either through nanoimprint,<sup>254–256</sup> or colloidal lithography.<sup>65,257–259</sup> While both approaches bring the advantages of cost-effectiveness and reproducibility, to date, only On-off-switching was realized through electrochromic polymers,<sup>68,239</sup> through hydration of magnesium nanostructures,<sup>260,261</sup> or through a conventional liquid crystal filter.<sup>255</sup> Nonetheless, color selectivity can only be achieved through physical alterations of the size and shape of the plasmonic pixel element.<sup>53,261</sup> Hence, despite the multifarious potential applications for plasmonic MIN devices, they lack the versatility to enable dynamical light reflectance or

transmission spectra.<sup>239,260</sup> Indeed, overcoming the monochromatic nature of MIN devices requires active modulation of the dielectric properties of the insulator medium.

A prime class of candidate material which allows for reversible changes in the permittivity are electrochromic oxides. Electrochromic oxides, such as MoO<sub>3</sub>, NiO<sub>x</sub>, V<sub>2</sub>O<sub>5</sub>, WO<sub>3</sub> and their hybrids are mainly employed for broadband optical transmission modulation through dynamic control of light absorbance upon ion intercalation from an electrolyte medium in an applied electric field.<sup>8,131,234,262,263</sup> However, the process of intercalation not only tunes the dielectric loss, but also alters the refractive index of the material resulting in varying resonances for a cavity.<sup>264</sup> In a plasmonic MIN cavity, actively changing the refractive index and extinction of the insulator (i.e., electrochromic oxide) modulates the plasmonic resonance frequency of the metal nanohole array and subsequently its wavelength selective light reflection and transmission properties.

Here, a fully inorganic, high chromaticity, and highly stable plasmochromic color modulation device based on WO<sub>3</sub> as the active EC layer in a gold plasmonic nanocavity is developed and investigated. The MIN device architecture allows for tunable resonance wavelength selectivity and is scalable through the utilization of polystyrene (PS) nanospheres colloidal lithography. Wide resonant light reflectivity modulation is achieved through intercalation and deintercalation of Lithium ions (Li<sup>+</sup>) into the WO<sub>3</sub> film.

### 4.3.1 Plasmochromic Nanocavity Design and Simulations

The schematic for the plasmochromic nanocavity (PCNC) is shown in Fig. 4.17(a). The PCNC consists of a 100 nm thick Au film mirror, a 120 nm thick WO<sub>3</sub> insulator, and 20 nm Au manholes array (NHA). The Au mirror film is evaporated onto a 5 nm Titanium adhesion layer, upon which the EC WO<sub>3</sub> film is reactively magnetron sputtered. To increase the surface wettability of the WO<sub>3</sub> film for the colloidal lithography process, the oxide layer is activated in a weak oxygen plasma to break saturated surface bonds and enhance its hydrophilicity. The plasmonic nanohole array, is formed by sputtering 20 nm of gold onto a sub-monolayer of 224 nm diameter polystyrene nanospheres, which were self-assembled on the EC WO<sub>3</sub>. The assembled PCNC consists of an ITO coated glass substrate as the counter electrode placed 1 mm from the plasmonic nanohole array and adhered to it via double sided tape. The space between ITO and plasmonic nanohole array is filled with an organic electrolyte containing 1 M LiClO<sub>4</sub> in PC to provide the Li<sup>+</sup> ions for the EC redox reaction. Here, the nanohole array serves both as a plasmonic light-confinement superstructure and as transport conduits for Li<sup>+</sup> ion insertion into the EC WO<sub>3</sub> layer in the nanocavity as depicted in Fig. 4.17(b). For active color modulation, a DC voltage is applied between the ITO counter electrode and Au mirror. During EC coloring of WO<sub>3</sub>, the refractive index decreases from approximately  $n = 2.1$  (the initial state in the visible region) to approximately  $n = 1.7$  in the colored state. Miller *et al.* showed a linear dependence for the plasmon resonance shift over the change in refractive index for different metallic nanostructures.<sup>265</sup> Based on the refractive index dependence investigated here, the

plasmonic resonance of the NHA structure will blue shift with increasing  $\text{Li}^+$  insertion, thus, leading to a “cutoff” of the broad cavity resonance in the red region of the spectrum. The device is envisioned to experience two convoluted resonances with the F-P cavity resonance and the NHA resonance interacting to form a narrower reflectance than with either one of these elements alone.

The “quasi random holes” of the NHA exhibit short-range ordered pattern which is effectively determined by the characteristic spacing  $\zeta$ . As such, the effective periodicity of the MINs resembles that of a long-range ordered structure:<sup>65,266–268</sup>

$$\zeta = \frac{2\pi}{\text{Re}(k_x)} \quad (4.3)$$

Where  $k_x$  is the wavevector in the dielectric’s plane. Collectively, the quasi-random nature of the MIN cavities provided a broad plasmonic resonance which is highly desirable for full-color light reflection modulation. The interplay between the modulation of the localized surface plasmon resonances and the dynamic reflectivity of the nanocavity yields highly tunable light wavelength selectivity.

Such a device can be modeled via FDTD simulations using Lumerical. The material parameters are adjusted using measurement data and the simulation region is chosen as a 3D structure having a height of 3  $\mu\text{m}$  and a width representing the periodicity of the random NHA. A plane wave light source ( $\lambda = 300$  to 1200 nm) is used to excite the structure, while a 2D power monitor is placed above the source to measure reflectance. Around the cavity a refined mesh with a spacing equivalent

to 10% of the respective film thickness is placed. Perfectly matched layer (PML) boundary conditions are used in  $z$ -direction, while periodic boundaries are utilized in  $x$ - and  $y$ -directions. Refractive indices data for Au,  $\text{SiO}_2$ , Si, and Ti are used as pre-installed. The dielectric properties for  $\text{WO}_3$  are extracted from ellipsometry measurements of a 200 nm thick  $\text{WO}_3$  film on a W metallic substrate.

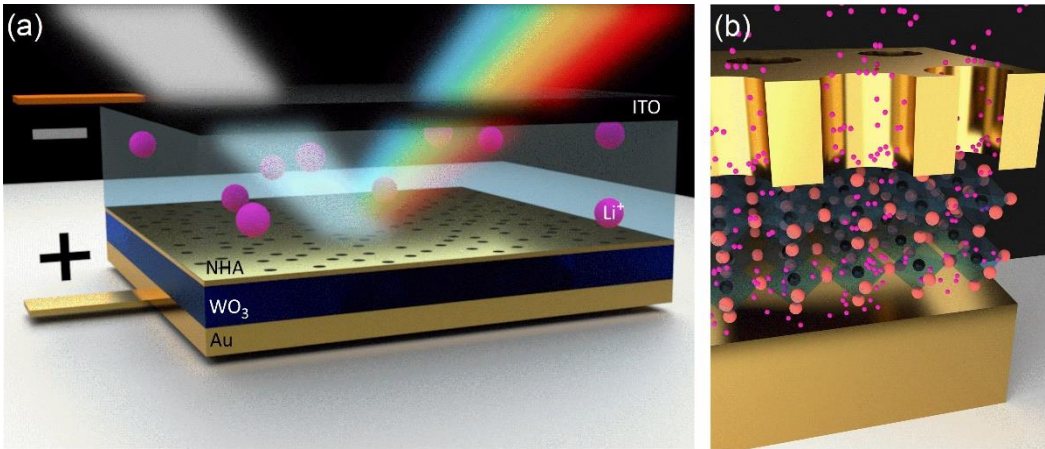


Fig. 4.17: PCNC based on EC  $\text{WO}_3$  insulator layer able to modulate reflectance over broad spectral range. (a) Schematic of the plasmochromic device based on an electrochromic  $\text{WO}_3$  layer and a gold resonator (not to scale). Lithium ions are contained in the 1 M  $\text{LiClO}_4$  electrolyte and represented as pink spheres (exaggerated in size). The top ITO film on glass serves as the counter electrode. (b) Close-up schematic of the Lithium ions (pink) diffusing through the gold nanohole channels into the tungsten (black) oxide (red) film. Depicted here is the cubic phase of  $\text{WO}_3$ .

As shown in Fig. 4.18(a), the NHA plays a vital role in increasing the chromaticity of the PCNC by “shaping” the reflectance peak through a cut-off on

the red side of the spectrum. The reflectance for a nanocavity without the NHA is broad spanning a broad spectral range between  $\lambda = 400 \text{ nm} - 800 \text{ nm}$ . The reflection signature from the nanocavity is also present around  $580 \text{ nm}$ . The NHA exhibits a clear plasmonic absorption above  $\lambda_P = 700 \text{ nm}$ , thus, spectrally-shaping the nanocavity reflectance to a single peak ( $450 \text{ nm} - 700 \text{ nm}$ ).

Fig. 4.18(b) presents results for the simulation of the active PCNC during lithiation. Shown are the simulated reflectance spectra for  $\text{Li}^+$  ion injection ranging from  $0 \text{ mC/cm}^2$  to  $8 \text{ mC/cm}^2$  (in a  $120 \text{ nm}$  thick  $\text{WO}_3$  film), spanning a reflectance  $R = 0.96$  to  $R = 0.48$  within the spectral range from  $\lambda = 400 \text{ nm}$  wavelength to  $\lambda = 700 \text{ nm}$  wavelength. Notably, the spectral peaks are cut off on the long wavelength side by the plasmonic resonance of the NHA ( $\lambda_P$ ). When no  $\text{Li}^+$  ions are injected (i.e.,  $0 \text{ mC/cm}^2$ ), the reflected peak wavelength is at  $595 \text{ nm}$  and having a full width at half maximum (FWHM) range between  $500 \text{ nm}$  and  $680 \text{ nm}$ . At the highest lithiation level of  $6 \text{ mC/cm}^2$ ,  $R = 0.48$  and the wavelength at peak reflected intensity blue-shifts to  $505 \text{ nm}$  while the FWHM narrows by  $40\%$  to  $110 \text{ nm}$ . The plasmon resonance wavelength is inversely proportional to the  $\text{Li}^+$  ion concentration, as such, the plasmon resonance wavelength decreases from  $700 \text{ nm}$  at  $0 \text{ mC/cm}^2$  to  $622 \text{ nm}$  at  $6 \text{ mC/cm}^2$ . Furthermore, the reflectance in the delithiated case shows fringes on the main reflection peak, which are due to additional Fabry-Perot modes.

Throughout the  $\text{Li}^+$  ion insertion process, broadband optical absorption arises from free electrons withdrawn from the Au electrode to balance the charge due the  $\text{Li}^+$  ion insertion. Therefore, starting at longer wavelengths, the attenuation of the reflected optical intensity increases with higher degrees of lithiation.

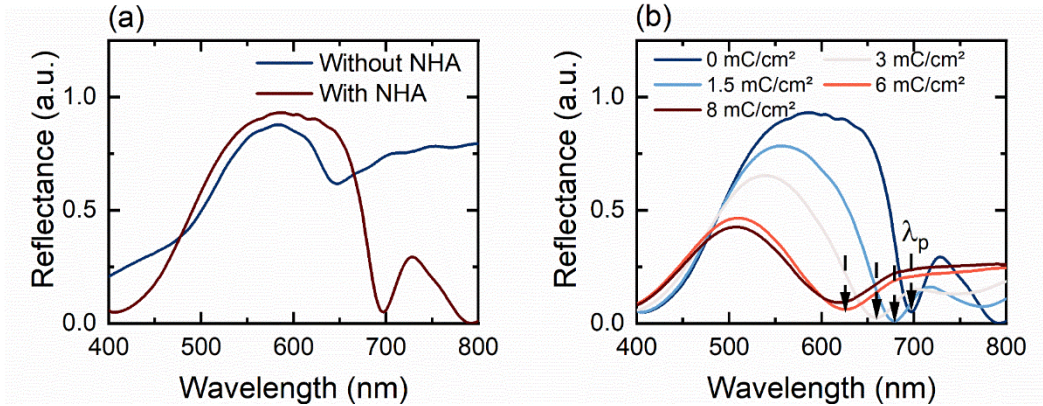


Fig. 4.18: FDTD simulations of PCNC. (a) Simulated reflectance spectra of a PCNC with a periodicity of 452 nm and a hole diameter of 224 nm with and without NHA. (b) Reflectance as a function of lithiation. The arrows indicate the location of the plasmon resonance wavelength absorption  $\lambda_p$ .

### 4.3.2 PCNC Fabrication

Colloidal lithography is employed to fabricate the nanohole arrays.<sup>258,269</sup> Polystyrene nanobeads are synthesized following a modified recipe presented by Chiappini *et al.*<sup>270</sup> Briefly, 90 ml of DI-water is heated in an oil bath to 80°C in a 250 ml three-neck flask, followed by the addition of cleaned styrene to create polystyrene (PS) nanospheres. As seen in Fig. 4.19(a), the relative amount of styrene directly influences the average particle size of the resulting colloids where the average particle size increases with increasing amounts of precursor. While 7.5 ml styrene lead 192 nm diameter nanospheres, 15 ml styrene result in 320 nm diameter for the synthesized nanospheres. Notably, the standard deviation of the particle size reaches a minimum for 8.5 ml styrene, where the particles exhibit a size of  $d = 224 \text{ nm} \pm 5.7 \text{ nm}$  (Fig. 4.19(b)). Hence, 8.5 ml styrene are optimal to

create monodisperse nanosphere solutions. The particle size and standard deviation are determined via ImageJ software and particle size plugin. For the measurements, particles are spin-coated onto Si substrates (Fig. 4.20(a)). The 8.5 ml of styrene are added to the DI water and the mixed solution is kept at 80°C for 5 minutes, under constant N<sub>2</sub> purging and refluxing. 350 mg of potassium persulfate, as the initiator and 50 mg of sodium dodecyl sulfate (SDS), are solved in 10 ml DI-water and are kept at 65°C. The solution is added to the three-neck flask to start the synthesis. Here, SDS acts as the stabilizing and capping agent, so that a change in the amount of SDS can also directly influence the particle size. The synthesis is completed after 4 hours. PS nanosphere solutions are centrifuged at 6000 rpm and washed with DI water 4 times prior to use. The final solution is adjusted to approximately 1 wt-% for further processing.

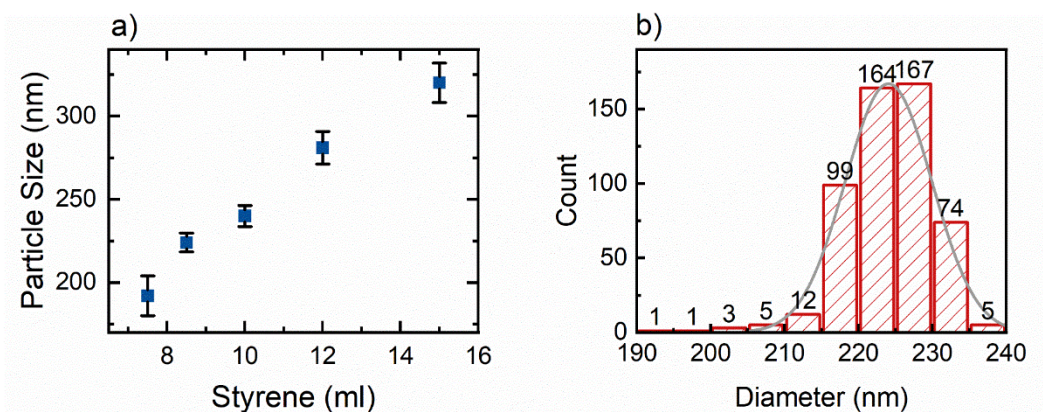


Fig. 4.19: Polystyrene nanosphere synthesis results. (a) Average particle size as a function of amount of styrene added to the reaction. (b) Histogram of PS nanosphere size distribution for 8.5 ml styrene addition to the reaction.

The PCNC is assembled on glass substrates, sonicated in Acetone and Ethanol for 30 minutes, and rinsed with IPA before drying with N<sub>2</sub>. First, the reflective 100 nm thick film Au back mirror is sputter deposited onto of 5 nm Titanium for adhesion. Next, 120 nm thick WO<sub>3</sub> film is reactively sputtered from a pure W target onto the Au mirror. The sputtered WO<sub>3</sub> films is subjected to a weak oxygen plasma (at 50 W of power) for 60 s to increase the wettability of the surface. In a modified liquid-air self-assembly approach, densely packed layers of PS nanoparticles can be achieved.<sup>271</sup> To increase the wettability of the surface and thus increases adhesion,<sup>272</sup> the substrate with the Au/WO<sub>3</sub> coating is immersed in 2.5 wt-% Polydiallyldimethylammonium chloride (PDDA) solution for 2 minutes, followed by rinsing in DI water and N<sub>2</sub> blow drying. As a result, the PDDA modified substrate is covered with a thin layer PS solution (approximately 20 μl per cm<sup>2</sup>). Upon carefully drop-casting the solution onto the substrates, the liquid fully wets the WO<sub>3</sub> layer without further assistance. Next, the substrate is placed in a covered 10 cm wide Petri-dish to prevent evaporation. PS nanospheres adsorbed onto the surface for 30 min, before the substrate was tilted to a nearly 90° angle and held in that position for 5 s to allow the excess solution to run off. Afterwards, the substrate is immersed in boiling water for 5 s and blow dried with N<sub>2</sub>. Adsorption of the PS nanospheres for less than 30 min leads to lower packing densities and higher run-off of PS nanospheres. When adsorption is carried out without the PDDA layer, the nanospheres often adhere to each other, leading to a broadening of the plasmonic resonance as shown in Fig. 4.20(b). After the random assembly of PS spheres on the WO<sub>3</sub> surface, a top 20 nm thick Au film is deposited via magnetron sputtering.

Consequently, the PS spheres are lifted-off by applying a strip of standard wafer tape and physically removing the excess spheres and the Au film. The resulting NHA distribution is random but exhibits short range order as discussed earlier. Notably, the sputtering process leads to rough edges of the holes as depicted in Fig. 4.20 (c,d). The roughness of the nanoholes is expected to broaden the plasmonic resonance. The fabricated PCNC electrode is then connected to an ITO counter electrode through a 1 mm thick double sided silicone tape. Finally, the space between the electrodes is filled with a 1 M LiClO<sub>4</sub> liquid electrolyte.

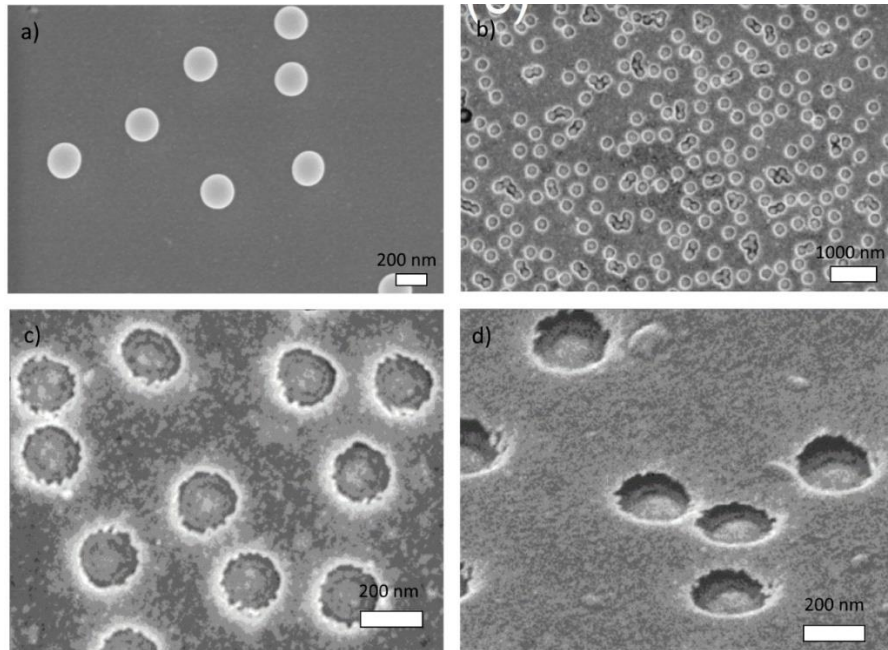


Fig. 4.20: FESEM images of PS nanospheres during lithography process. (a) PS nanospheres on Si substrate for size determination. (b) NHA showing defects due to the absence of the PDDA coating. (c,d) Nanoholes after Au sputtering.

### 4.3.3 Experimental Results

For plasmochromic color modulation, a PCNC device is assembled and analyzed using a spectro-electrochemical setup. Here, a Zahner Zennium potentiostat is utilized to apply referenced voltages or currents (vs. Ag/AgCl) to the device to achieve coloration or bleaching of the  $\text{WO}_3$  thin film (Fig. 4.21). A standard white light source is collimated, send through a custom 3D-printed dark field aperture, and focused onto the samples through a  $5\times$  microscope objective. The measurements are taken through the ITO counter electrode and normalized to its transmittance. Raw micrographs of the reflected color images taken with a CMOS camera are shown in Fig. 4.22(a). The images are taken during the lithiation process at lithiation states from  $0 \text{ mC/cm}^2$  to  $8 \text{ mC/cm}^2$ . While the PCNC in its delithiated state and upon lithiation with  $1.5 \text{ mC/cm}^2$  charge reflects red, with increasing lithiation, the wavelength of reflected light blue shifts. For  $3 \text{ mC/cm}^2$ , the color changes to orange, becoming brownish yellow at  $4 \text{ mC/cm}^2$ . At highest lithiations ( $6 \text{ mC/cm}^2$  and  $8 \text{ mC/cm}^2$ ) the reflection becomes green and deep green. Over the whole lithiation process, the images show highly uniform and vivid colors which are highly sought after for high resolution display technology.

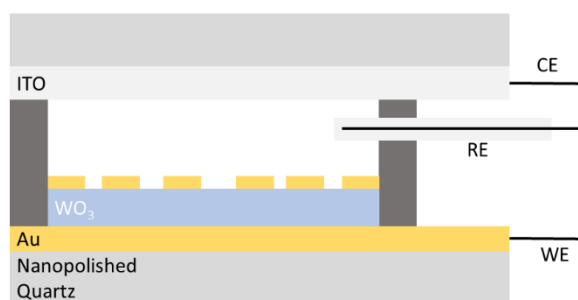


Fig. 4.21: Schematic of the experimental measurement cell used to investigate the PCNC device. The space between ITO and  $\text{WO}_3$  electrode is filled with 1 M  $\text{LiClO}_4$ .

The corresponding reflectance spectra from the PCNC as a function of lithiation are shown in Fig. 4.22(b). The delithiated sample ( $0 \text{ mC/cm}^2$ ) exhibits a spectral peak at 616 nm (red). During lithiation to  $8 \text{ mC/cm}^2$ , the resonant peak wavelength shifts from 616 nm to 552 nm, resulting in a reflected green color. Due to the dielectric loss induced by the ion intercalation process, the light intensity at 552 nm is reduced to 32% in comparison to the delithiated sample. The spectra are normalized to the obtained reflectance before lithiation, not the source spectrum. It should be noted that the surface roughness of the  $\text{WO}_3$  further suppresses any unwanted Fabry-Perot fringes.

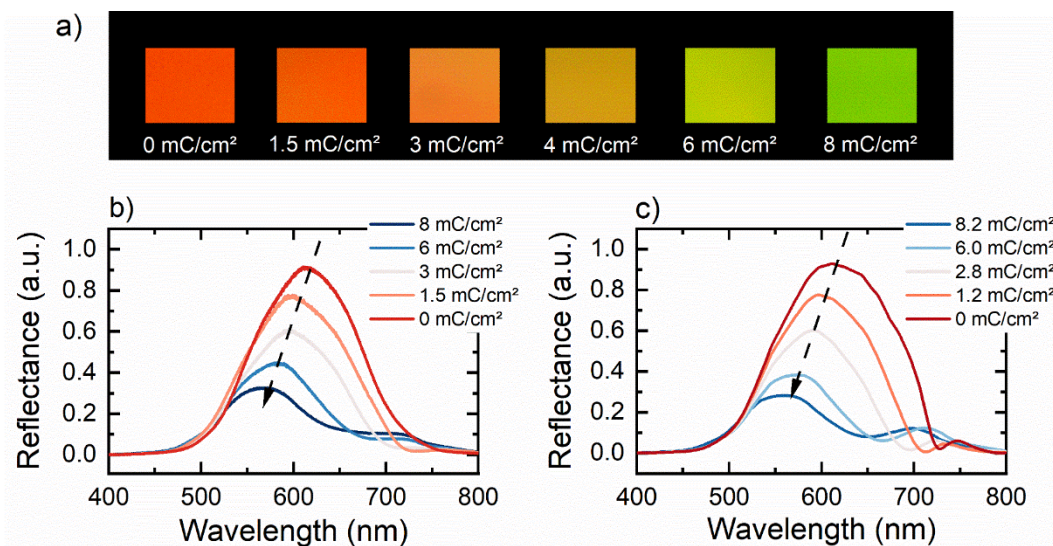


Fig. 4.22: Spectro-electrochemical characteristics of the PCNC. (a) 100 μm × 100 μm size raw images of the reflected color at various stages of the lithiation process. Images are taken with a CMOS camera. (b) Experimentally obtained reflectance at various stages of the lithiation. (c) FDTD simulated reflectance spectra multiplied by experimentally obtained source spectrum at various stages of the lithiation process. The dashed arrow is the same as that in (b).

Fig. 4.23 illustrates the peak wavelength and its peak intensity as a function of lithiation for simulated and experimental results. The experimentally measured blue shift of the ( $\Delta\lambda_{\text{peak}}$ ) peak spectrum is inversely proportional to the degree of lithiation with a linear dependence of  $\Delta\lambda_{\text{peak}} = -7.7 \text{ nm/mCcm}^{-2}$ . This matches well with the blue shift of the simulated spectra, which experiences a  $\Delta\lambda_{\text{peak}} = -7.1 \text{ nm/mCcm}^{-2}$  (Fig. 4.23(b)). In both the experiment and the simulations, the color change is accompanied by a comparable decrease in the reflected intensity.

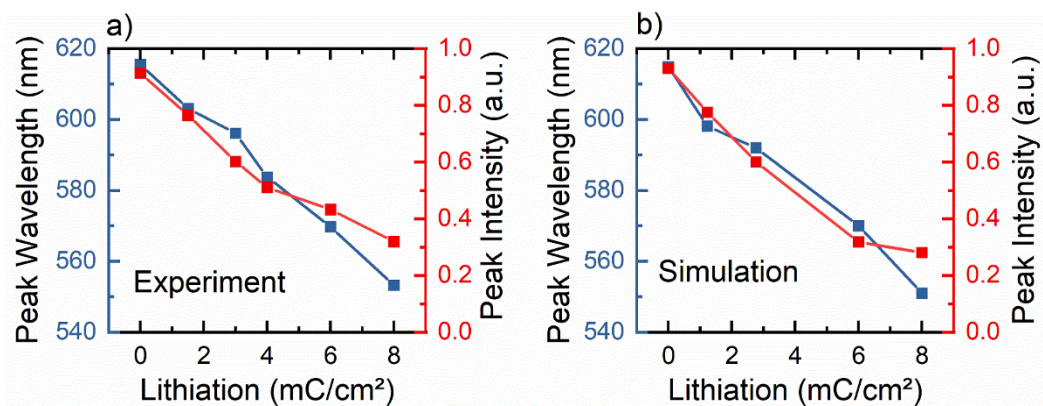


Fig. 4.23: Comparison of experiment and simulation. (a) Experimentally measured peak reflected wavelength and the reflected intensity as a function of increasing lithiation. (b) Peak wavelength and intensity for the FDTD simulated results. The simulated data follow the same experimental data shown in (a).

Remarkably, the obtained experimental results for the reflectance spectra are in very good agreement with to the FDTD predictions shown in Fig. 4.22(c). The general trend for the spectral shift, as well as the attenuation are similar to the experimentally measured values (Fig. 4.24). The minor differences arise mainly from broadening of the plasmonic resonance frequency due to polydispersity of the employed PS nanospheres and possible agglomeration during the colloidal lithography process. The high similarity between simulated and measured reflectance spectra further indicates, that there are no measurable changes in the WO<sub>3</sub> film thickness due to volumetric changes upon Li<sup>+</sup> intercalation. Even though, the unit cell of WO<sub>3</sub> expands up to 17% upon lithiation, the porosity of the film can accommodate the microscopic volumetric change without leading to macroscopic effects.<sup>273</sup> The shoulders of the reflection peak at long wavelengths arise due to the

blue shift of the plasmonic extinction, which allows reflection at longer wavelengths. In the case of the real device, the shoulders are less defined due to broader extinction arising from the polydispersity of the nanospheres.

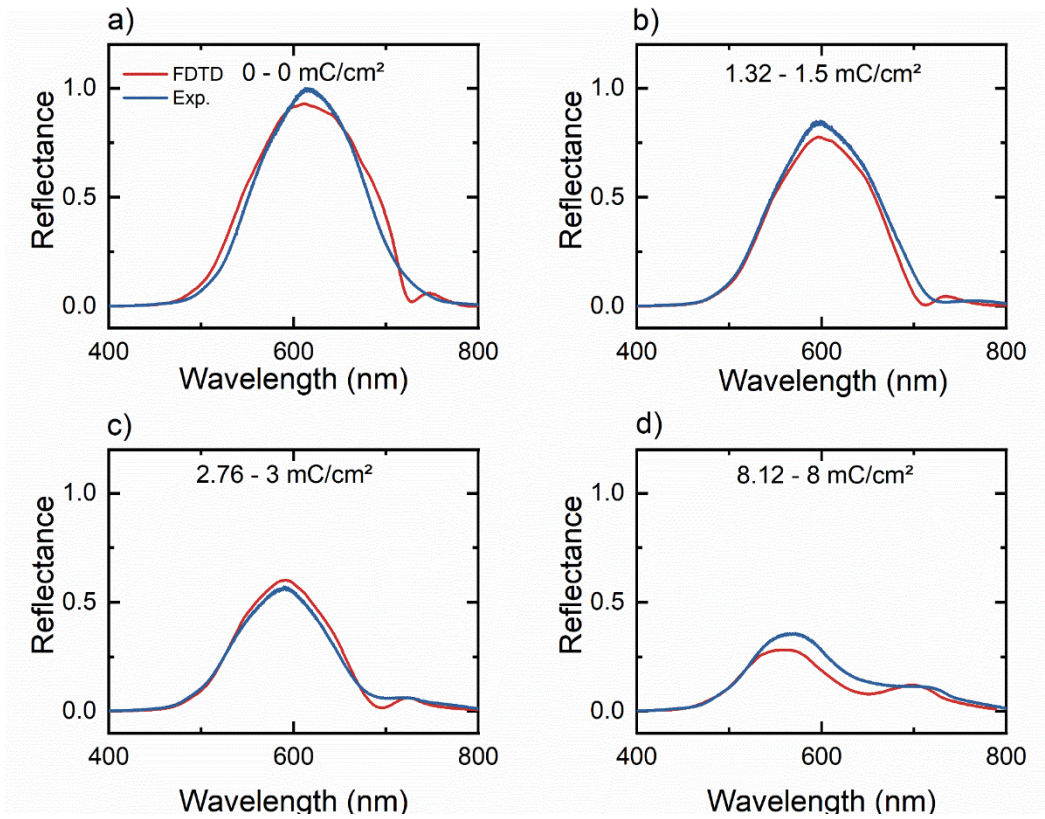


Fig. 4.24: Comparison of measured (blue) and simulated (red) reflectance using the same light source for different lithiation states (0 – 8 mC/cm<sup>2</sup>). To model a realistic light source, FDTD simulation reflectivities were normalized to the source spectrum to achieve absolute reflectivity (i.e., reflectance). The resulting reflectance was multiplied with the experimentally obtained source spectrum, yielding the corrected reflectance spectra plotted in red.

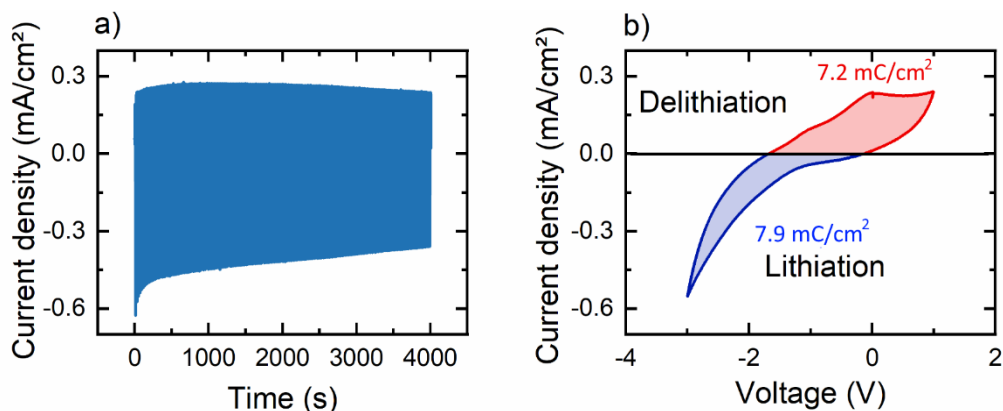


Fig. 4.25: CV of a PCNC under a constant sweep rate of 100 mV/s in 1 M LiClO<sub>4</sub>. (a) 100 cycles of CV measurement plotted versus time to illustrate the high electrochemical stability of the device. After 100 cycles of voltage sweep, the PCNC shows 85% charge capacity retention. (b) Single CV measurement at 10 cycles of voltage sweep. The lithiation and delithiation processes show a high reversibility (7.9 mC/cm<sup>2</sup> intercalation vs. 7.2 mC/cm<sup>2</sup> extracted charge).

In addition to its dynamic spectral properties, the PCNC exhibits electrochemical properties, that provide an insight into their long-term stability. Fig. 4.25 displays the CV curves of a PCNC device under  $v = 100$  mV/s sweep rate vs an Ag/AgCl reference electrode. For 100 cycles of constant CV cycling, the PCNC exhibits a retention of faradaic capacity of 88%. The drop in current density for the first 10 redox cycles contributes 9% of the decrease in charge capacity (Fig. 4.25(a)). As seen in Fig. 4.25(b), the retention of charge capacity is mainly influenced by the irreversible intercalation of the Li<sup>+</sup> ions. A higher lithiation charge indicates irreversible intercalation, which in turn decreased the achievable optical transmission modulation and capacity for the PCNC. Nonetheless, CV analysis shows high reversibility (91.1 % charge recovery), and low power

consumption ( $\Delta P = 1/2 \cdot \Delta C \cdot V^2 = 5.6 \text{ mW/cm}^{-2}$ ), as lithiation and delithiation require similar amount of charge. The high stability of the PCNC is owed to the inorganic  $\text{WO}_3$  modulation layer, which has been shown to exhibit a high electrochromic lifetime of over 1000 cycles in organic electrolytes. Notably, this lifetime can be further extended through ion detrapping<sup>274</sup> or via various protection layers (see section 3.5).<sup>233,237</sup>

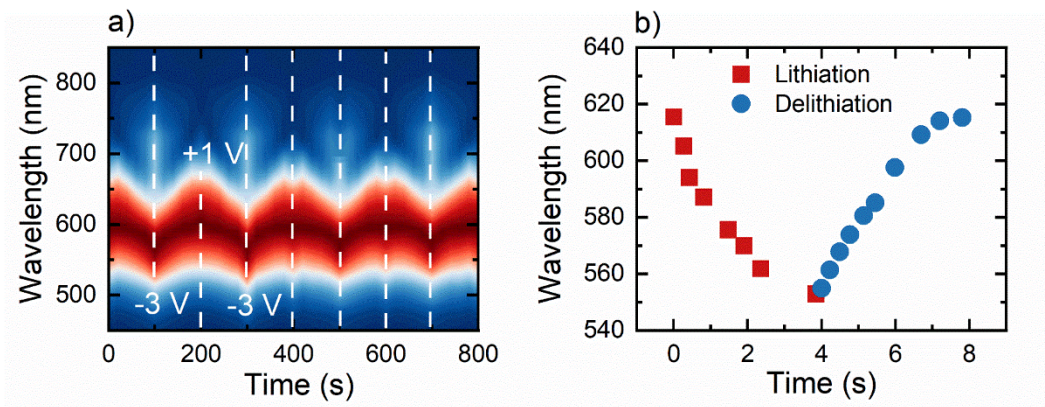


Fig. 4.26: (a) Color modulation over time. The spectra are normalized to show the high reproducibility of spectral colors. (b) Time dependence of the color modulation process of the plasmochromic device by applying -3 V to 1 V potential. Full color modulation takes place in a duration of ~ 4 seconds.

The electrochemical stability of the PCNC leads to a high reproducibility of the reflectance spectra exhibited during voltage cycling. Fig. 4.26(a) displays the normalized reflectance spectra of five consequent CV cycles at  $v = 25 \text{ mV/s}$ . The applied voltage is alternated between  $V = -3 \text{ V}$  and  $V = +1 \text{ V}$ . Over the course of the measurement, the respective peak wavelengths at comparable voltages are consistent. Furthermore, the spectral response follows the applied voltage (i.e., the

lithiation/delithiation process). Similarly, the wavelength switching dynamics of the PCNC are presented in Fig. 4.26(b) an alternating applied voltage having fast rise and fall times of less than 10  $\mu$ s. Remarkably, both the red and the blue shifts are achieved in times of less than 4 s, with wavelength shift rates as high as 33 nm/s and 19 nm/s for the blueshift and for the redshift, respectively.

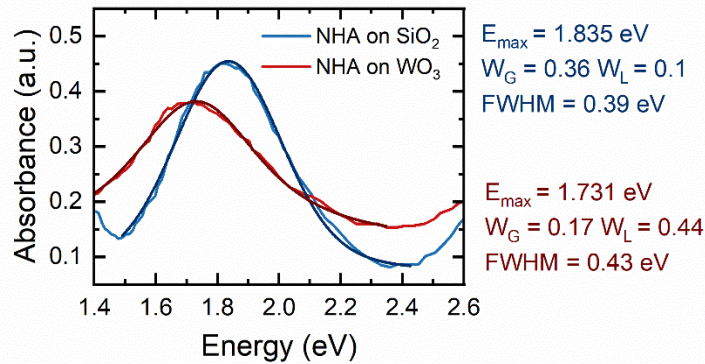


Fig. 4.27: Absorbance spectrum of thin NHA sample on  $\text{SiO}_2$  and  $\text{WO}_3$  as well as the respective Voigt fit.

The fabricated NHAs are further analyzed regarding their absorbance spectra and corresponding broadening features (Fig. 4.27). As seen in Fig. 4.27, the absorbance spectra for a 25 nm thick NHA fabricated on  $\text{SiO}_2$  and  $\text{WO}_3$  show distinct peaks at 1.835 eV and 1.731 eV respectively. Both samples exhibit the same average hole diameter of 220 nm and comparable periodicities ( $\Delta_{\text{SiO}_2} = 414$  nm,  $\Delta_{\text{WO}_3} = 459$  nm). The difference in periodicity can be attributed to the different wettability of the surface even after PDDA treatment. Due to the difference in permittivity of  $\text{SiO}_2$  and  $\text{WO}_3$ , the resonance peak shifts red when the NHA is fabricated on top of a  $\text{WO}_3$  film. The effect of the change in periodicity is assumed

to be small in comparison to the refractive index difference. Furthermore, the samples differ in line shape with the NHA fabricated on top of SiO<sub>2</sub> showing mostly Gaussian contribution to the spectral shape indicating inhomogeneous broadening. The quality factor is determined to be  $Q = 4.71$ . Meanwhile the WO<sub>3</sub> sample exhibits a higher degree of homogenous broadening with a quality factor of  $Q = 4.02$ . The origin of the different broadening contributions could lie in the higher electrical conductivity of WO<sub>3</sub> when compared to SiO<sub>2</sub>, which leads to faster dephasing of the plasmon and is directly related to  $Q$ . Moreover, surface roughness of the Au film, roughness of the etched holes and size distribution of the used PS spheres all contribute to homogenous broadening. The occurrence of touching nanoholes with clusters from 2 to 5 holes leads to inhomogeneous broadening. The overall shape of the plasmon resonances measured here is in good accordance with literature.<sup>275</sup>

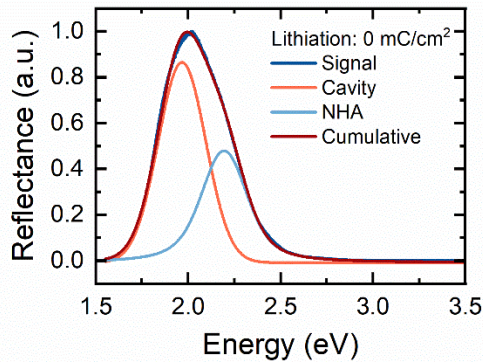


Fig. 4.28: PCNC reflectance at 0 mC/cm<sup>2</sup> intercalated charge with Voigt fits indicating the cavity mode and reflection from the NHA.

Moreover, the PCNC reflectance spectra can be fitted to determine its spectral components. Here, two Voigt fits are used to replicate the PCNC reflectance. Fig. 4.28 indicates the two peaks with maxima at  $E = 2.02$  eV and  $2.25$  eV, accordingly. The reflectance at  $2.02$  eV coincides with the cavity mode for normal incidence simulated via FDTD (Fig. 4.29(a)), while the peak at  $2.25$  eV can be attributed to the decrease in absorbance of the NHA. Correspondingly, the cavity peak presents completely Gaussian features, while the NHA peak is mixed Gaussian and Lorentzian in nature, which indicates homogenous and inhomogeneous broadening as seen for the NHA resonances.

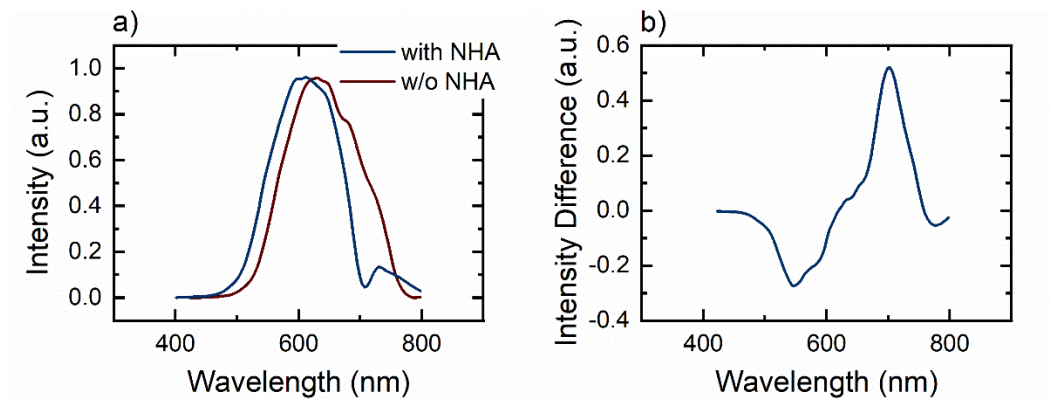


Fig. 4.29: Comparison of PCNC with and without NHA. a) Experimental reflected spectra obtained for PCNC in delithiated state through white light measurement and b) difference in reflection spectra indicated as additional absorption due to NHA.

To ascertain the necessity for the plasmonic NHA superstructure, a nanocavity with and without the hole array are compared. Both structures consist of the gold bottom mirror, a delithiated EC  $\text{WO}_3$  film and a thin gold top electrode. In the case of the NHA sample, the top electrode is patterned via colloidal lithography. As seen

in Fig. 4.29(a), the reflected intensity spectrum for the sample with the NHA shows a slightly narrower spectrum with a maximum at 605 nm wavelength. While the maximum for the sample without NHA stays unchanged, the spectrum broadens and its cutoff shifts from 695 nm to 740 nm. The difference between the two spectra is shown in Fig. 4.29(b). Evidently, the plasmonic superstructure increases the chromaticity of the nanocavity device by introducing an additional absorption feature between 650 nm and 750 nm wavelength, while the reflectance at around 580 nm is slightly increased. To investigate the difference between PCNCs with and without the plasmonic NHA, FDTD simulations are performed for devices with different lithiation levels (Fig. 4.30). As seen in Fig. 4.30(a) the NHA leads to a suppression of reflectance at  $\lambda \geq 620$  nm, which helps define chromatic red color. Simultaneously, the NHA leads to a decrease of reflection around 400 nm wavelength, effectively shaping the reflectance on the low wavelength side. A similar effect is shown for the fully lithiated device at  $8 \text{ mC/cm}^2$  intercalated charge (Fig. 4.30(b)). In general, the NHA leads to slightly reduced reflectance from the sample, even at desired wavelengths. However, the quality factor of the reflectance peak is improved due to the lower reflectance at undesired wavelengths.

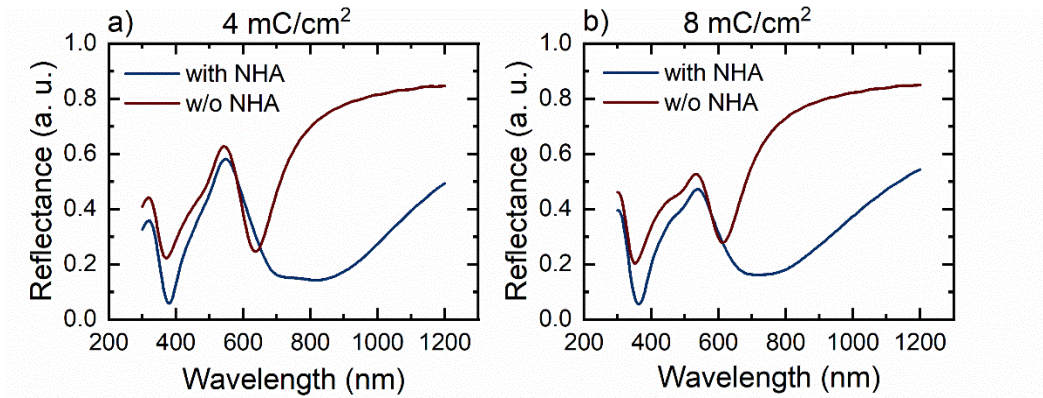


Fig. 4.30: Simulated reflectance spectra for PCNCs with and without NHA. a) Reflectance for PCNC under  $1.5 \text{ mC/cm}^2$  lithiation and b)  $4.5 \text{ mC/cm}^2$  lithiation.

## 4.4 Summary and Discussion

This chapter investigated the potential for plasmochromic device technologies employing nonresonant and resonant approaches for plasmonic light-matter interaction paired with EC functionality. First, the change of dielectric properties of a solid-state ECD in a simple Kretschmann architecture was utilized to shift the resonance angle for SPP coupling. The introduced PCK device experienced optical and electrical hysteresis effects that can be employed in miniaturized opto-electrical memory devices. Next, nonresonant SPP propagation, in an all-solid-state plasmochromic waveguide (PCWG), was shown to increase switching speeds and to significantly enhance the optical modulation depth of a 50 nm thick EC  $\text{WO}_3$  layer. The results were verified and compared with FDTD simulations of the PCWG and suggest that even higher optical modulation depth could be achievable if excess  $\text{Li}^+$  ions could be provided. Finally, by employing a scalable colloidal lithography approach, a nanocavity, having both photonic and plasmonic

resonances, has been successfully designed and demonstrated to display various colors of the visible spectrum ranging from green to red with high chromaticity.

The devices fabricated here show that EC materials, including  $\text{WO}_3$ , NiO and  $\text{Ta}_2\text{O}_5$ , can be incorporated into nano- and microfabrication processes and can provide enhanced EC functionality on the nanoscale. The interaction with plasmonic nanostructures will need further investigation to fully understand the effect of  $\text{WO}_3$  conductivity on resonance broadening.

# Chapter 5

## EC for Linear and Nonlinear Nanophotonic Applications

In this chapter, the potential for dynamic EC powered Silicon Nitride ( $\text{SiN}_x$ ) photonics on a CMOS compatible basis are explored in the form of functional nanophotonic waveguides.  $\text{SiN}_x$  has gained attention as a waveguiding material due to its high optical transmission in the optical communication wavelength range and its CMOS compatibility. Moreover, the strain induced high nonlinear optical properties of  $\text{SiN}_x$  offer a cost-efficient alternative to conventional nonlinear crystalline materials, such as  $\text{LiNbO}_3$ .<sup>110,167,170,276–280</sup> Since PECVD deposition of  $\text{SiN}_x$  is realized at temperatures below  $T = 300^\circ\text{C}$ , PECVD deposition is favorable for incorporating  $\text{SiN}_x$  into a wide range of EC applications, in particular, nonlinear nanophotonic devices.

In this chapter, the utilization of  $\text{WO}_3$  in nanophotonic  $\text{SiN}_x$  waveguides as a modulation material is investigated. As demonstrated in section 4.2, the integration of EC into waveguiding structures has the potential to increase the optical transmission modulation and to improve the EC switching speeds. In contrast to the PCWG device introduced earlier, the waveguides introduced in this chapter offer high On-state optical transmission combined with the advantages of higher optical modulation depth and switching times. The device architecture employed in these EC  $\text{SiN}_x$  based photonic waveguides improves upon the previously mentioned

existing designs by eliminating the coupling of the optical mode to electrical contacts. By offsetting the electrical contacts relative to the cladded waveguide core and utilizing the finite resistance of EC  $\text{WO}_3$  films (which act as their own electrical contacts), the On-state optical transmission and resulting optical modulation depth are enhanced.

The following chapter is arranged as follows. First, the experimental setup which is used for linear and nonlinear optical investigations is introduced. Next, a  $\text{SiN}_x$  waveguide with ion sensing properties through EC modulation is proposed. Device design, FDTD simulations and fabrication steps are laid out before the experimental results for a  $\text{Na}^+$  ion sensing device are presented (Section 5.2). This is followed by introducing a novel waveguiding platform for nonlinear optical applications; in particular, for active control over the phase matching conditions in second harmonic generation (SHG) (Section 5.3). Lastly, a summary of the chapter's findings for EC nanophotonics is given (Section 5.4).

## 5.1 Experimental Setup

The waveguides presented in this chapter are utilized for their linear and nonlinear optical properties at  $\lambda = 1550$  nm. The laser radiation is delivered from an 84 fs  $\text{Er}^{3+}$  doped fiber femtosecond laser operating at a repetition rate of  $f_{\text{rep}} = 90$  MHz and delivering an average power of  $P = 270$  mW (i.e.,  $\sim E = 3$  nJ/pulse). The laser pulses are focused onto the waveguides through a  $\text{NA} = 0.85$  microscope objective (Fig. 5.1).

The experiments are conducted with a maximum excitation power of  $P = 100$  mW since higher powers are shown to damage the waveguide's input facet. On the collection side, a tapered fiber (OZ Optics #TSMJ-3A-1550-9/125-1-7-2-12-2) is used to pick up the second harmonic (SH), at  $\sim 775$ nm, signal and the IR at 1550nm, signal. The transmitted optical power, as well as the SH signal are measured using a Thorlabs PM100D fiber coupled powermeter. The spectra are recorded using either an OceanOptics 2000 spectrometer for SH signals or a Yokogawa AQ6370C Spectrum Analyzer for the IR signals. When collecting either signal, a respective filter is used to block the other signal.

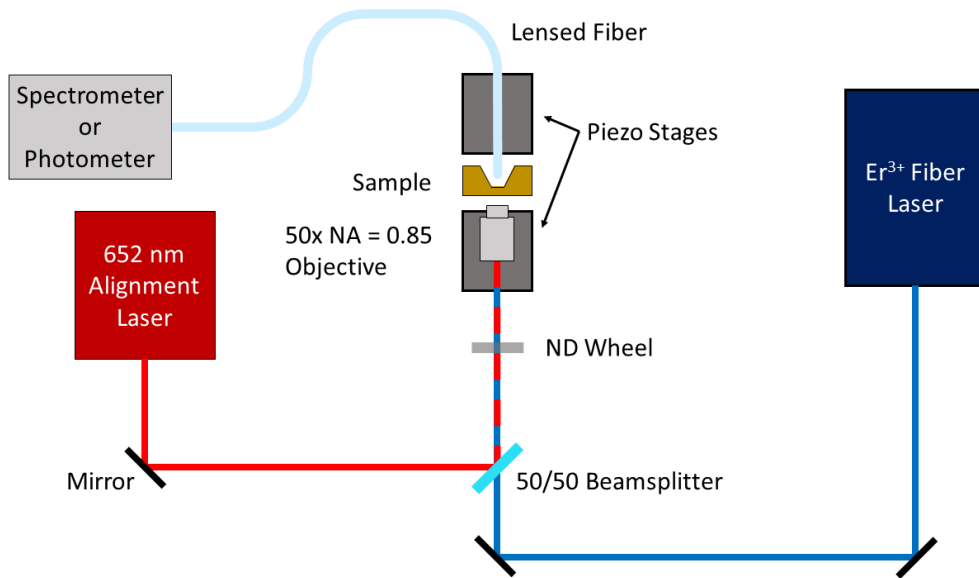


Fig. 5.1: Schematic illustration of the free-space coupling setup used to investigate the linear and nonlinear optical properties of EC  $\text{SiN}_x$  based photonic waveguides. A  $\text{Er}^{3+}$  doped fiber laser is coupled via a  $\text{NA} = 0.85$  objective into the waveguide samples. Spectro- or photometer are used to analyze the transmitted signal

The intercalated charge is determined as the applied current over time, thickness, and area of the respective ECD. Currents and voltages are applied via a Zahner Zennium Potentiostat chemical station or Keithley 2400 source meter. In the configuration for dynamic measurements, a potential is applied between the bottom electrode of the waveguide samples and a top electrode. In case of the liquid electrolyte, a micro reference electrode is carefully inserted into the solution.

## 5.2 Ion Sensing in EC Waveguide<sup>281</sup>

Most ECDs do not inherently utilize the direct relation between the change in dielectric properties and ion concentration to measure ionic movement, intercalation, or diffusion. However, EC sensor technology makes use of the ion concentration dependency of the EC effect for pH sensing,<sup>282,283</sup> ion concentration sensing in gases and liquids,<sup>23,284</sup> and simulating artificial synapses.<sup>29</sup> The coloration effect in EC materials (e.g., WO<sub>3</sub>) is found to strongly correlate with the concentration of ionic species within the electrolyte. As such, EC sensor devices have found basic applications in health care,<sup>285</sup> and environmental science.<sup>286,287</sup>

Optical transmission modulation in conventional ECDs is limited to about 80% and switches on time scales of several seconds.<sup>4,288,289</sup> To achieve higher optical transmission modulation and to reduce the switching times, various EC photonic devices have been introduced. EC infrared photonic waveguides have been implemented for artificial synapses.<sup>29</sup> Additionally, when compared to traditional ECD architectures, this platform exhibited improved switching times of < 1 s and enhanced optical transmission modulation to ~90%. However, the waveguide

optical modulation suffers from poor penetration of the optical mode into the EC material due to the presence of an indium tin oxide (ITO) electrode separating the waveguide core and the EC layer.

To mitigate the optical loss from the electrical contact, a multifunctional EC nanophotonic SiN<sub>x</sub> waveguide (SNWG) platform, offering a high optical modulation depth ( $\Delta T = 10^6$ ), fast switching times ( $\tau_{10\%} < 0.56$  s), and strong ion concentration dependency is investigated. When used as a sodium ion sensor, the nanophotonic waveguide device achieves an excellent Na<sup>+</sup> concentration detection accuracy of > 95% over a concentration range of 1000 mM within an effective interaction volume of several  $\mu\text{m}^3$ . The device architecture allows for the sampling of solutions with volumes as low as 20  $\mu\text{l}$ , which corresponds to  $10^{16}$  ions in solution.

### 5.2.1 SiN<sub>x</sub> waveguide (SNWG) Design and Simulations

The basic architecture of the SiN<sub>x</sub> nanophotonic waveguide EC ion sensor/light modulator is illustrated in Fig. 5.2. A SiN<sub>x</sub> nanophotonic waveguide core, having a facet area of 750 nm by 2000 nm, is cladded with a plasma enhanced chemical vapor deposition (PECVD) SiO<sub>2</sub> layer. The waveguide core is deposited via PECVD, which leads to slightly Si-rich Si<sub>3</sub>N<sub>4-x</sub>, also referred to as SiN<sub>x</sub>. A WO<sub>3</sub> EC layer is deposited on top of the SiO<sub>2</sub> spacer layer, thus, isolating the EC material and the waveguide core by 150 nm from the top side and 100 nm on the sides. The WO<sub>3</sub> layer uniformly covers the device and continuous at the step created by the waveguide and cladding, which is confirmed via resistance measurements. A

bottom metallic Cr (25 nm)/W (25 nm) electrode provides electrical connection to the WO<sub>3</sub> layer only. This electrode is offset by 10 μm away from the SiN<sub>x</sub> nanophotonic waveguide core so as to minimize any plasmonic coupling losses.

The EC layer is covered with an ion-containing electrolyte (NaClO<sub>4</sub> in Propylene Carbonate (PC)) and is countered by a platinum electrode and referenced with an Ag/AgCl micro electrode. A thick photoresist film (AZP4620) is used to keep the electrolyte in place. By applying a voltage between the Pt wire and the bottom electrode, Na<sup>+</sup> ions are either intercalated into the WO<sub>3</sub> film (Fig. 5.2(a)) or extracted from it (Fig. 5.2(b)). The intercalated Na<sup>+</sup> ions lead to an accumulation of free electrons in the WO<sub>3</sub> layer as these electrons balance the positive charge introduced by the intercalated Na<sup>+</sup> ions. Notably, the free electron density can be as high as 10<sup>22</sup> cm<sup>-3</sup>, effectively leading to free carrier absorption of the light in the WO<sub>3</sub> layers and altering its extinction coefficient,  $k_{ex}$ , from  $k_{ex} = 0$  to  $k_{ex} = 0.5$  (Fig. 4.7).

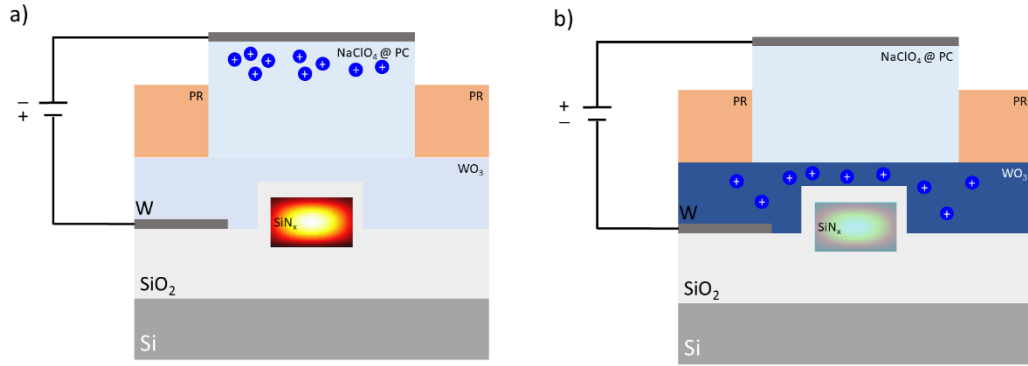


Fig. 5.2: Schematic of the EC nanophotonic waveguide Na<sup>+</sup> ion sensor and light modulator. (a) A positively biased WO<sub>3</sub> layer drives Na<sup>+</sup> ions out of the EC material and renders it transparent. (b) A negatively biased WO<sub>3</sub> layer leads to an accumulation of Na<sup>+</sup> ions inside the EC material. The balancing charge (electrons) from the W electrode dope the WO<sub>3</sub> to a high charge carrier density of  $\sim 10^{21} \text{ cm}^{-3}$ , resulting in a lossy EC optical modulation layer and low light transmission.

To ascertain the behavior of the EC nanophotonic waveguide device and its critical design parameters, FDTD simulations combined with experimentally determined material parameters data are used to model the device and light mode interaction with the EC WO<sub>3</sub> layer. FDTD simulations are performed using the same general layout as in section 4.2.1 with measured values for  $n$  and  $k_{\text{ex}}$  for SiN<sub>x</sub>. Fig. 5.3 illustrates the results of modelling of a SNWG having a  $w = 2 \mu\text{m}$  wide and  $h = 0.75 \mu\text{m}$  high SiN<sub>x</sub> core. As depicted in Fig. 5.3 the optical mode inside the waveguide core partially penetrates the EC WO<sub>3</sub> light modulating layer. The degree of penetration, however, can be optimized by tuning the thickness of the SiO<sub>2</sub> spacer layer. For a 250 nm thick SiO<sub>2</sub> spacer layer, only 5% of the intensity of the

electric field of the optical mode is found to be confined inside the waveguide's  $\text{WO}_3$  layer (Fig. 5.3(a)), while for a 50 nm thick  $\text{SiO}_2$  spacer layer 23% of the optical mode resided inside the  $\text{WO}_3$  layer (Fig. 5.3(b)).

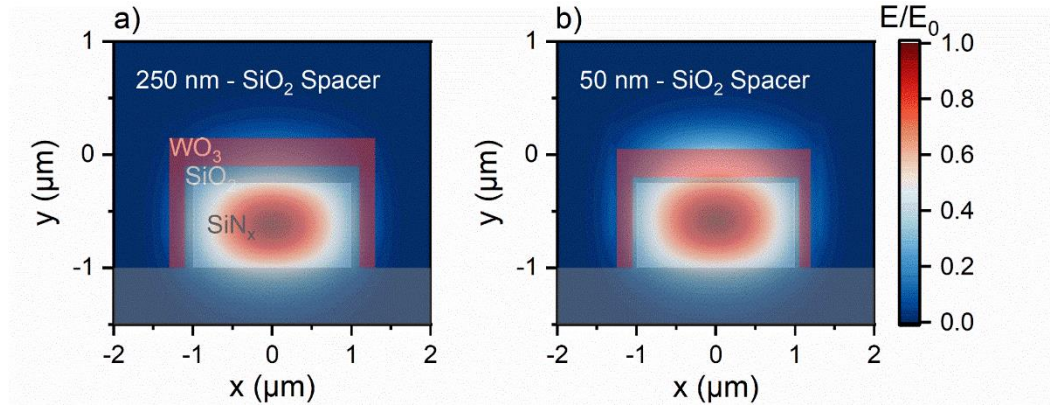


Fig. 5.3: Representation of FDTD simulation results of a  $2 \mu\text{m}$  wide and a  $0.75 \mu\text{m}$  high  $\text{SiN}_x$  waveguide core. (a,b) E-field distribution in and around the  $\text{SiN}_x$  waveguide for different  $\text{SiO}_2$  spacer thicknesses. Material thicknesses and geometries are indicated through the shaded areas.

The propagation loss is inversely proportional to the spacer thickness. However, while the FDTD simulations provide a very reasonable prediction of the optical propagation loss, intrinsic material defects (i.e., not included in the calculations) can contribute further to the optical loss. The EC  $\text{WO}_3$  layer even in its oxidized state contains defects that can further increase the losses. Such a lossy  $\text{WO}_3$  film through defects and vacancies was confirmed in Section 3.1.2.

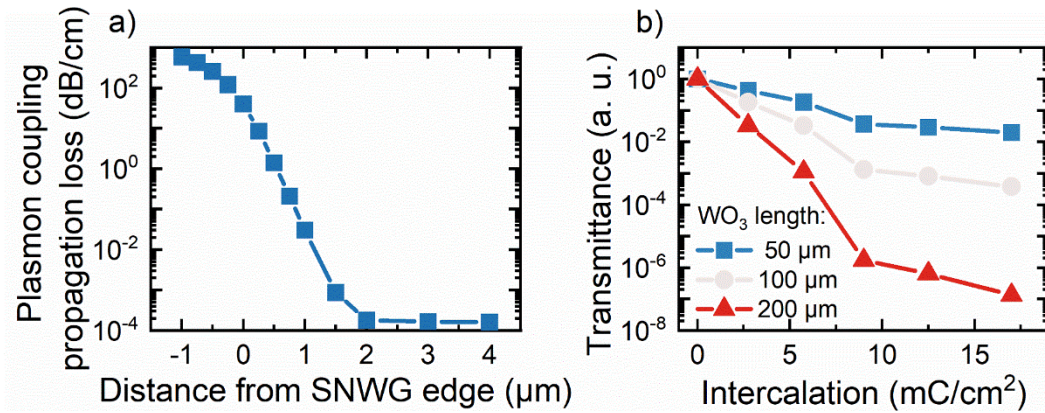


Fig. 5.4: (a) Calculated plasmonic loss resulting from optical mode coupling to the metallic contact for a SiO<sub>2</sub> spacer thickness of 150 nm. Optical loss becomes negligible for a distance greater than 2 μm. (b) FDTD simulation of the modulated optical transmission at 1550 nm through the SiN<sub>x</sub> waveguide having various WO<sub>3</sub> lengths.

A key factor contributing to the achievable modulation depth as well as to the switching speed is the location of the metallic electrical contact relative to the SiN<sub>x</sub> waveguide core. To avoid coupling between the optical mode and the electrical contacts, the contacts must be placed so as to provide a sufficiently strong electric field for the EC functionality, but far enough from the SiN<sub>x</sub> core to minimize plasmonic loss. While the electric field driving ions into WO<sub>3</sub> is strongest when the electrode distance is low, the plasmonic loss increases for close proximity of contact and waveguide. Fig. 5.4(a) depicts the calculated waveguide's plasmonic loss at various positions for a W electrical contact where at the position indicated by '0', is where the W electrical contact is right at the edge of the waveguide SiN<sub>x</sub> core. Notably, when the electrical contact is in contact with the waveguide core (0

$\mu\text{m}$  relative to the side edge of the waveguide), the loss in dB/cm is nearly  $10^2$ , which would make device operation impossible. The induced loss decreases sharply once the electrical contacts are positioned slightly off to the side. When the electrical contact is placed 500 nm away from the side edge of waveguide core, the induced loss decreases to 1 dB/cm, while at distances  $> 2 \mu\text{m}$  the induced loss becomes negligible ( $< 10^{-4}$  dB/cm), especially when compared to the propagation loss of  $\text{SiN}_x$  (7 dB/cm). The contact-waveguide distance is acceptable, due to the electrical properties of  $\text{WO}_3$  and the electrolyte.  $\text{WO}_3$ , even in its deintercalated (i.e., fully oxidized state), exhibits a finite resistivity of approximately  $10^2 \Omega\text{cm}$ , and the voltage drop over the waveguide-contact distance for distances  $< 100 \mu\text{m}$  is negligible compared to the voltage drop across the electrolyte ( $> 100 \Omega\text{cm}$ ).<sup>290</sup> Considering that the electrical contact-waveguide distance is  $10 \mu\text{m}$  and the electrolyte layer thickness is 1 mm, the voltage drop along the  $\text{WO}_3$  is 100 times lower than that in the electrolyte. Furthermore, the resistivity of  $\text{WO}_3$  decreases by several orders of magnitude during intercalation, leading to a minimal resistivity ratio of  $1/10^7$  in the case of fully intercalated/reduced  $\text{WO}_3$ .<sup>105</sup>

The selected waveguide length ( $1000 \mu\text{m}$ ), facet dimensions ( $2000 \text{ nm} \times 750 \text{ nm}$ ) and spacer thickness ( $150 \text{ nm}$ ), along with the  $\lambda = 1550 \text{ nm}$  excitation wavelength and different modulation layer lengths ( $l_{\text{EC}} = 50 - 200 \mu\text{m}$ ), are used in the FDTD simulation to calculate the intercalation dependent modulation properties of the SNWG. Fig. 5.4(b) shows the calculated optical transmission for waveguides having a  $50 \mu\text{m}$ ,  $100 \mu\text{m}$  and  $200 \mu\text{m}$  long EC  $\text{WO}_3$  optical modulation layer as a function of ion intercalation. In the fully oxidized state, the optical transmission is

nearly 100% since the optical losses of both  $\text{WO}_3$  and  $\text{SiN}_x$  are negligible. For the three EC nanophotonic waveguide lengths, the optical transmission exponentially decreases during the electrochemical reduction of  $\text{WO}_3$ , with a maximum achievable optical modulation of  $10^2$ ,  $6 \times 10^3$  and  $10^7$  for the 50  $\mu\text{m}$ , 100  $\mu\text{m}$  and 200  $\mu\text{m}$  long EC  $\text{WO}_3$  layer, respectively. For the 200  $\mu\text{m}$  long EC  $\text{WO}_3$  optical modulation layer, the optical transmission along the waveguide decreases from nearly unity to  $10^{-3}$  at 5.75  $\text{mC}/\text{cm}^2$  intercalated  $\text{Na}^+$  ions and to  $10^{-7}$  at 17  $\text{mC}/\text{cm}^2$  intercalated  $\text{Na}^+$  ions. For shorter EC layer lengths, the maximum achievable transmission modulation decreases accordingly.

### 5.2.2 SNWG Fabrication

SNWGs are fabricated on a 4" Si wafer having a 2  $\mu\text{m}$  thermal oxide layer. First, an 800 nm thick  $\text{SiN}_x$  film is deposited via plasma enhanced chemical vapor deposition (PECVD – Oxford Trion PECVD) in a standard process involving  $\text{NH}_3$  and diethyl silane. Next, chromium patterns, serving as etch masks, are defined through maskless optical lithography (Heidelberg MLA 150) and deposited onto the samples via electron beam evaporation. The waveguide pattern is transferred into the  $\text{SiN}_x$  layer through reactive ion etching (RIE – Oxford PlasmaPro80). Cr etch masks are removed in a wet Cr etchant for  $t = 1$  h. Approximately 150 nm PECVD  $\text{SiO}_2$  is then deposited onto the waveguides and the samples are annealed at a temperature of  $T = 700^\circ\text{C}$  under  $\text{N}_2$  atmosphere (Allwin RTA). This leads to the  $\text{SiN}_x$  film compacting to 750 nm in thickness. During compression of the  $\text{SiN}_x$  waveguides, the refractive index increases slightly as seen in Fig. 5.5. Meanwhile,

the extinction coefficient of the films is negligible and cannot be determined via ellipsometry.

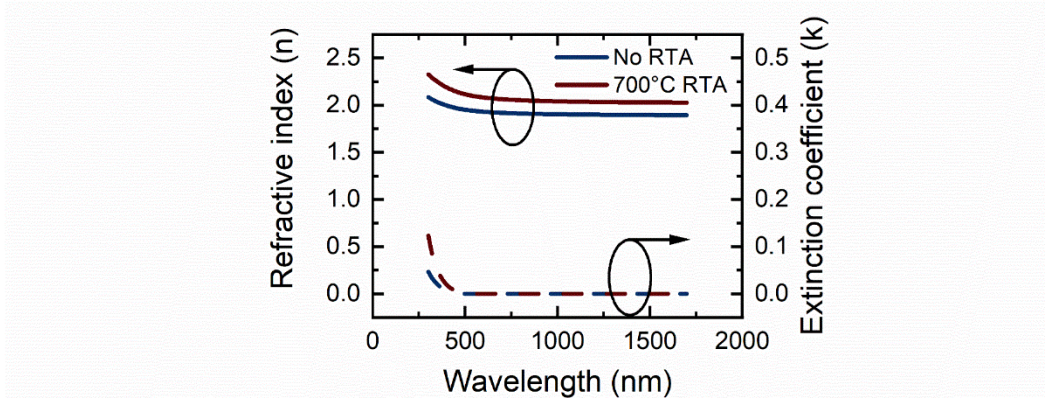


Fig. 5.5: Refractive index and extinction coefficient of PECVD SiN<sub>x</sub> before and after rapid thermal annealing (RTA) at 1100°C for 2 minutes (Repeated 5 times).

Next, electrical contacts are defined using optical lithography and deposited via magnetron sputtering. A 200 nm thick WO<sub>3</sub> optical modulation layer is lithographically patterned and reactively deposited using a W metal target as previously described (Section 3). A lithography step is used to define the waveguide length and etch mask for the underlying SiO<sub>2</sub> layer. Lastly, a deep reactive ion etch (DRIE) (Oxford PlasmaPro - Estrelas) is utilized to divide the wafer into individual dies. While the DRIE step has the same layout as the previous step, all dimensions are increased by  $d = 3 \mu\text{m}$  in  $x$ - and  $y$ - direction, so that a thin layer of photo resist remains to protect the defined SNWG facets. Samples are subjected to a 30-minute oxygen etch prior to experimentation.

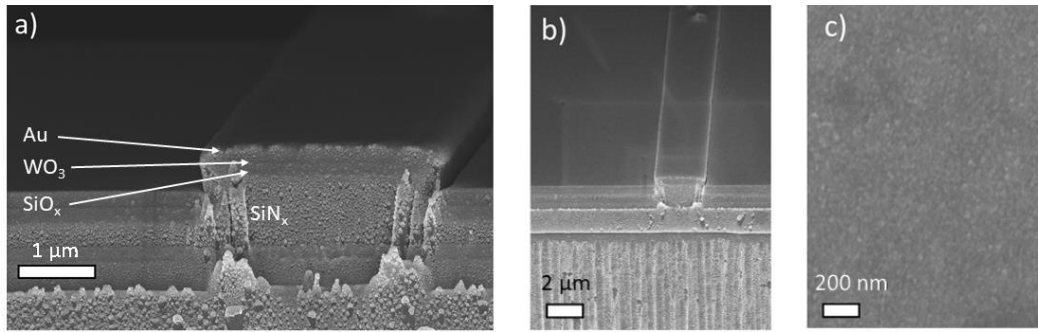


Fig. 5.6: Topological, morphological, and material properties of the EC photonic waveguide. (a) Cross-section SEM image of the  $\text{SiN}_x$  waveguide having a  $\text{SiO}_2$  cladding layer and conductive gold film. (b) Low magnification SEM image of the  $\text{SiN}_x$  waveguide. The image depicts the underlying bright  $\text{SiO}_2$  layer as well as the Si substrate. (c) High resolution image of the  $\text{WO}_3$  surface. The  $\text{WO}_3$  film consists of particulates having sizes ranging between 20 and 80 nm.

Fig. 5.6(a) depicts a SEM image of a rapid thermally annealed (RTA)  $\text{SiN}_x$  waveguide facet having a 150 nm  $\text{SiO}_2$  and a 200 nm  $\text{WO}_3$  thick layer. While the SNWG facet is smooth, it exhibits roughness due to the RIE and the DRIE processing. Such surface roughness leads to a coupling loss of  $\sim 18\%$  of the incident laser beam. Fig. 5.6(b) shows a lower magnification image of the same waveguide showing the 2  $\mu\text{m}$  thick thermal  $\text{SiO}_2$ . As shown in Fig. 5.6(c), the as-deposited  $\text{WO}_3$  thin film exhibits a porous and particulate microstructure ranging in size between roughly 20 nm and 80 nm.

### 5.2.3 Experimental Results

For optimal device operation, 20  $\mu\text{l}$  of  $\text{NaClO}_4$  in PC electrolyte is deposited onto the active  $\text{WO}_3$  layer. To keep the solution in place a layer of photoresist is deposited and developed on top of the waveguide structure to form a reservoir (Fig. 5.2). During CV measurements of the device, a sweeping voltage is applied to the W electrode, leading to the oxidation and reduction of the  $\text{WO}_3$  film through intercalated  $\text{Na}^+$  ions. Meanwhile, the optical transmission of a free space coupled  $P = 10 \text{ mW}$ ,  $\lambda = 1550 \text{ nm}$  wavelength laser is measured through the waveguide. Coupling of the laser is confirmed through a weak second harmonic signal arising from the interfacial stress between  $\text{SiN}_x$  and  $\text{SiO}_2$  cladding.

The optical transmitted power (i.e., 1.12 mW) in the On-state is used to normalize the respective transmittance data. With 11.2% On-state optical transmission and a calculated coupling efficiency of roughly 22%, the SNWG platform offers greatly improved optical transmittance when compared to the PCWG configuration (Section 4.2). Fig. 5.7 displays the effect of coupling losses and linear loss along the SNWG. As seen in Fig 5.7(a), the SNWG having  $d_t = 150 \text{ nm}$   $\text{SiO}_2$  cladding experiences a loss of 6.76 dB/cm, which is slightly higher than reported values for  $\text{Si}_3\text{N}_4$ ,<sup>110,291</sup> but several orders of magnitude lower than the loss in PCWGs. The linear fit of the optical loss in dB indicates that  $\sim 18\%$  or 0.9 dB are lost during coupling (in addition to the coupling efficiency of 22%). Furthermore, the  $\text{WO}_3$  layer in its deintercalated state adds a slightly increased linear loss of 0.67 dB/cm, which is negligible for the investigated EC layer lengths ( $l < 200 \mu\text{m}$ ).

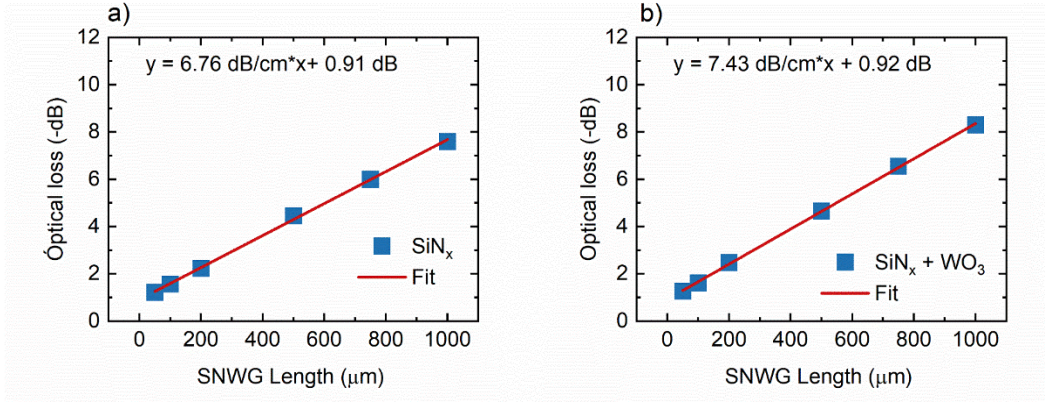


Fig. 5.7: Optical loss experienced in SNWGs of varying length. (a) without WO<sub>3</sub> layer and (b) with WO<sub>3</sub> layer on top of SiO<sub>2</sub> cladding.

The resulting voltage-dependent normalized optical transmission for different Na<sup>+</sup> ion concentrations is presented in Fig. 5.8(a). During the CV measurements with  $v = 50 \text{ mV/s}$  sweep rate, the voltage-dependent optical transmittance curve exhibits a hysteresis, where the optical transmittance depends on the sweep direction. The hysteresis effect is obvious in all of the three investigated samples, with its magnitude changing according to the electrolyte concentration. For an ion concentration of 100 mM, the maximum achievable optical modulation is about  $4 \times 10^5$ , corresponding to an absorption coefficient  $\alpha = 506 \text{ cm}^{-1}$  or an extinction coefficient  $k_{\text{exc}} = 6.2 \times 10^{-3}$  along the waveguide. With decreasing ion concentrations of 10 mM and 1 mM in the electrolyte, the achievable modulation during CV measurements drops to  $9 \times 10^3$  ( $k_{\text{ex}} = 2.9 \times 10^{-3}$ ) and 50 ( $k_{\text{ex}} = 4.2 \times 10^{-4}$ ), respectively, since higher potentials become necessary to intercalate the same amount of charge in the same time frame. Fig. 5.8(b) shows the corresponding current-voltage curve for the same sample in 100 mM Na<sup>+</sup>

electrolyte, exemplifying that the hysteresis effect corresponds to electrochemical processes. The overall shape of the curves in Fig. 5.8(a,b) suggests a strong correlation between intercalated  $\text{Na}^+$  ion concentration and the optical transmission due to the energetic barriers for ion intercalation and deintercalation. During intercalation, a threshold ( $V = 0.5 \text{ V}$ ) needs to be overcome to intercalate ions into  $\text{WO}_3$ . Afterwards, continuous intercalation of up to  $15.5 \text{ mC/cm}^2$  charge leads to negative currents and in turn reduced transmittance of the sample. The maximum transmission modulation is reached with  $\text{Na}^+$  ions reducing  $\text{WO}_3$  close to the  $\text{SiO}_2$  interface. During deintercalation, ions migrate from the  $\text{SiO}_2$  interface towards the  $\text{WO}_3$  – electrolyte interface, explaining the quick on-set of increased transmission. In addition to the overall intercalated charge, the waveguide architecture is dependent on the position of the  $\text{Na}^+$  ions in  $\text{WO}_3$ , with deeper intercalation leading to increased modulation.

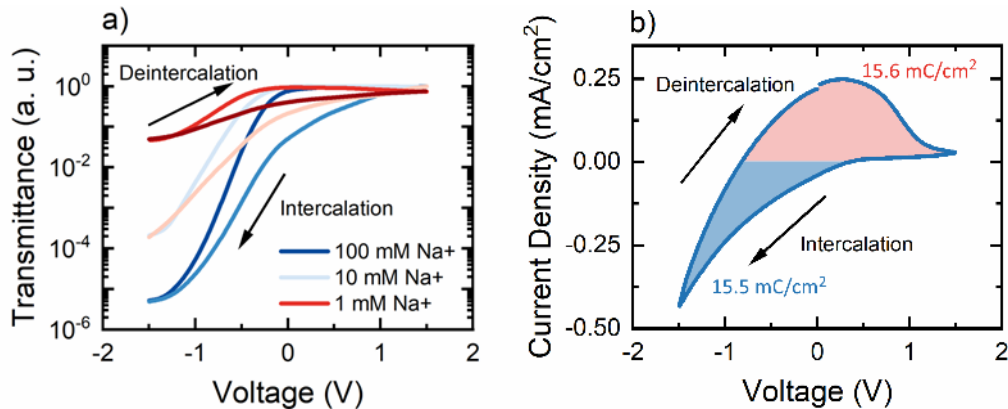


Fig. 5.8: Spectro-electrochemical analysis of  $200 \mu\text{m}$  long SNWG. (a) Optical transmittance for different  $\text{Na}^+$  ion concentrations during CV. The voltage is cycled at  $v = 50 \text{ mV/s}$ . (b) Current-voltage characteristics of SNWG (Same parameter as in (a)).

Fig. 5.9 depicts the long-term effects of CV on device performance. Here, the normalized optical transmission at  $V = -1.5$  V and  $V = +1.5$  V are shown over 2000 switching cycles. After 2000 cycles, the achievable optical transmission in the On-state decreases from 70% to 30%, while the modulation depth decreases by another order of magnitude. Due to the well-known process of irreversible intercalation of  $\text{Na}^+$  ions into the  $\text{WO}_3$  host, the overall performance, especially the optical transmission in the On-state of the device, decreases over time but stabilizes at 30% initial On-state transmission.<sup>7,201</sup> An increase in Off-state optical transmission or maximum achievable optical transmission modulation can be mostly attributed to mechanical degradation of the sputtered  $\text{WO}_3$  film.<sup>233,237</sup> However, the electrochemical degradation of the device is limited and device performance (i.e., optical modulation depth) stabilizes at  $10^5$ .

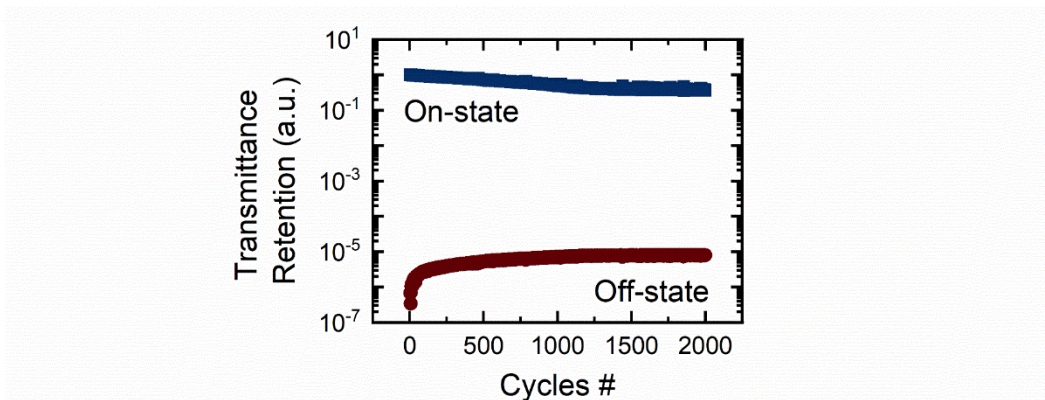


Fig. 5.9: Retention of achievable optical transmission modulation over 2000 On-Off cycles. The applied voltage is alternated between  $V = \pm 1.5$  V, while the optical transmittance is measured accordingly.

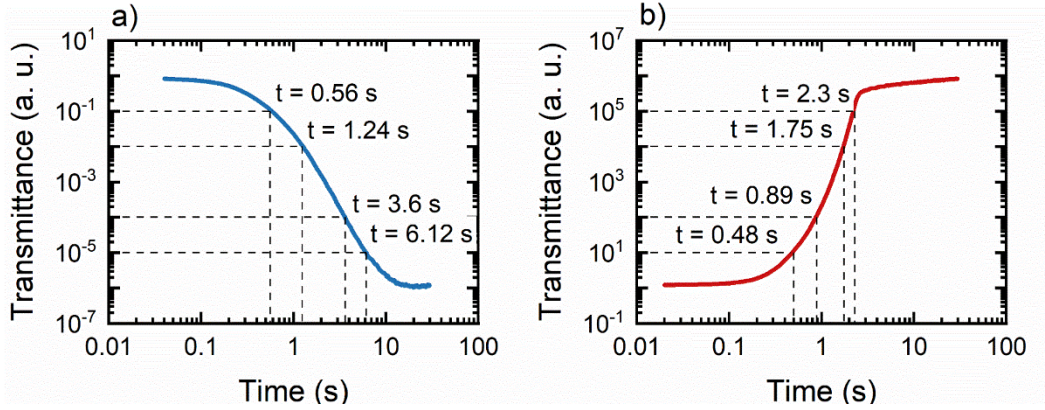


Fig. 5.10: Optical transmittance as a function of time for: (a) intercalation of Na<sup>+</sup> ions at an applied voltage of V = -1.5 V and (b) deintercalation of Na<sup>+</sup> ions at an applied voltage of V = +1.5V. The indicated times correspond to the nearest dashed line's intercepts with the curves.

Due to the EC nature of the modulation process, the optical transmission is directly proportional to the intercalated charge; hence, the diffusion constant governs the switching speed of the device. The charge transfer resistance associated with highly insulating oxidized WO<sub>3</sub> was shown to be negligible in the present samples (Section 3.1.2). Remarkably, the maximum modulation depth of > 10<sup>6</sup> is achieved within only 10 seconds and it can be reset back to the On-state within only 4 seconds (Fig. 5.10). Fig. 5.10 depicts the optical transmittance as a function of time for the intercalation and deintercalation process when a step voltage of ± 1.5 V is applied. For the intercalation (Fig. 5.10(a)), optical modulation of 10% and 1% are achieved within t = 0.56 s and t = 1.24 s respectively, and reaches a value of 10<sup>-5</sup> at t = 6.12 s. However, the recovery of the optical transmission is much faster, reaching 10<sup>5</sup> from the minimum value of 1 in only t = 2.3 s. This indicates that the

deintercalation process is faster than the intercalation process and dependent on ion position within the depth of the  $\text{WO}_3$  thin film. The achieved optical modulation of  $10^6$  is furthermore close to the theoretically predicated value of  $\Delta T \sim 10^7$  for a 200  $\mu\text{m}$  long EC layer.

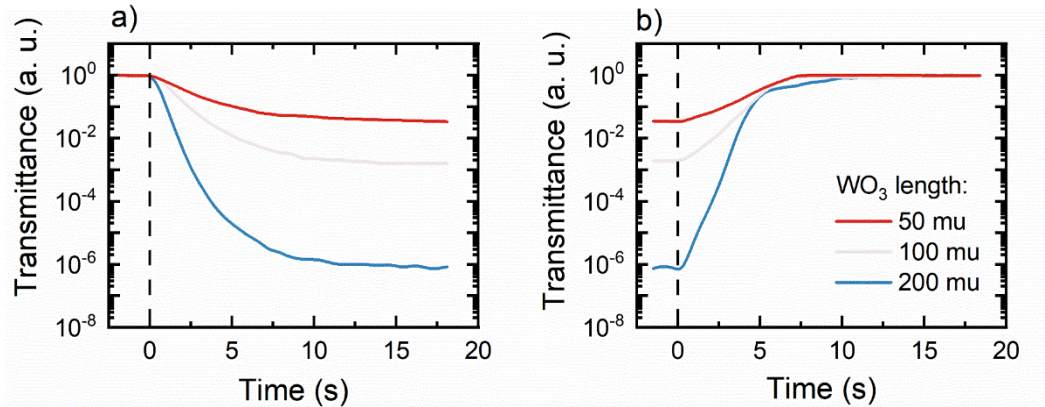


Fig. 5.11: Waveguide length dependent optical transmittance as a function of time. (a) Optical transmission for 50  $\mu\text{m}$ , 100  $\mu\text{m}$  and 200  $\mu\text{m}$  long SNWG over time when a voltage of  $V = +1.5$  V is applied. (b) Optical transmission for 50  $\mu\text{m}$ , 100  $\mu\text{m}$  and 200  $\mu\text{m}$  long EC nanophotonic waveguide over time when a voltage of  $V = -1.5$  V is applied.

Fig. 5.11 further shows the optical transmittance time evolution for SNWGs having different lengths of EC modulation during intercalation (Fig. 5.11(a)) and deintercalation (Fig. 5.11(b)) of  $\text{Na}^+$  ions. Evidently, the length of the EC modulation layer directly determines the achievable modulation depth. As mentioned previously, doubling of the EC modulation layer length approximately doubles the achievable optical modulation depth. Hence, for optical modulation layer lengths of 50  $\mu\text{m}$ , 100  $\mu\text{m}$  and 200  $\mu\text{m}$ , the achieved optical modulation after

$t = 15$  s reaches  $0.03$ ,  $1.5 \times 10^{-3}$  and  $9.6 \times 10^{-7}$ , respectively. Even though the results show optical transmission modulations that are about an order of magnitude lower than predicted through FDTD (Section 5.2.1), the EC waveguide optical transmission modulation is unprecedented when compared to any EC light modulating device. The discrepancy between simulation and experiment can be explained through waveguide morphology and loss due to surface roughness, as well as a lack of  $\text{Na}^+$  ion intercalation all the way to the  $\text{WO}_3\text{-SiO}_2$  interface. Simulations always assume homogeneous intercalation, which as shown in Fig. 5.8 is not achieved in the experiment.

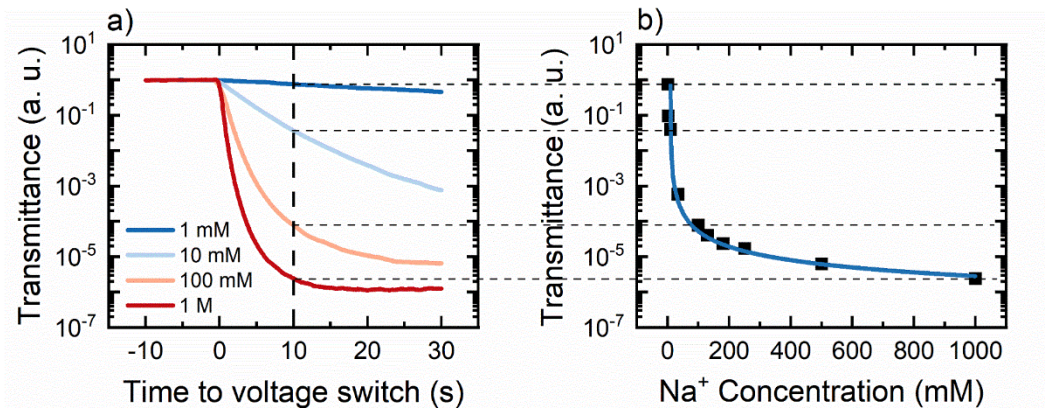


Fig. 5.12:  $\text{Na}^+$  ion sensor operation of SNWG. (a) Dynamic intercalation curve for the investigated EC photonic waveguide ion sensor device for an abrupt voltage onset of  $-1.5$  V. (b) Optical transmission taken 10 s after voltage onset for different electrolyte concentrations. The dashed lines indicate where data points are taken from. The blue curve corresponds to a empirical fit with four independent variables.

Due to its high sensitivity and ultrahigh dynamic range spanning up to five orders of magnitude in ion concentration detectability, the introduced SNWG

platform shows promising features as an ion concentration dependent sensor. Here, the fabricated waveguide's modulation follows the figure of merit,  $\Delta\phi = 1667 \mu\text{m}^{-1}\text{V}^{-1}$ , relating the optical modulation to the applied voltage and waveguide's length. Furthermore,  $\Delta T$  changes over five orders of magnitude when comparing redox cycling in 10 mM or 1 M  $\text{Na}^+$  electrolyte. The high dependency on the ion concentration is utilized to detect predefined concentrations of  $\text{Na}^+$  ions.

The temporal evaluation of the optical transmittance for different  $\text{Na}^+$  ion concentrations is shown in Fig. 5.12. For the four different concentrations (i.e., 1 M, 100 mM, 10 mM and 1 mM) investigated, the optical transmission modulation after 10 s is 0.3 for 1 mM  $\text{Na}^+$  ion concentration and changes to 0.025,  $5 \times 10^{-5}$  and  $1.25 \times 10^{-6}$  for 10 mM, 100 mM and 1 M, respectively. While the curve for the 1 M  $\text{Na}^+$  concentration saturates after 10 seconds, lower  $\text{Na}^+$  ion concentrations lead to saturation after increasingly longer times (30 s for 100 mM, 150 s for 10 mM). To completely intercalate the EC  $\text{WO}_3$  layer, approximately  $N = 10^{14}$   $\text{Na}^+$  ions are required, which is five orders of magnitude lower than the total number (i.e.,  $N = 10^{19}$ ) of the ions in the 1 M electrolyte. Hence, intercalation from the 1 M electrolyte is mainly diffusion limited inside the  $\text{WO}_3$  film, while lower concentration electrolytes suffer from low supply of mobile ions. Fig. 5.12 depicts the optical transmittance for several different electrolyte concentrations at  $t = 10$  s after the application of a  $V = -1.5$  V voltage step. Interestingly, the logarithms of the optical transmittance can be fitted to the empirical equation:

$$\log(T) = -31.96 \times (1 - C^{-0.03}) \quad (5.1)$$

This equation, therefore, provides an inherent calibration curve for inferring the  $\text{Na}^+$  ion concentration in the solution where  $C$  is the ion concentration in mM. To validate the model and evaluate the SNWG platform's suitability as an ion sensor, different electrolyte concentrations are prepared and the normalized optical transmittance is compared to the calibration curve, as shown in Table 9. The measured transmittance values are used to determine the corresponding  $\text{Na}^+$  concentration from the calibration curve. Concentration values derived from the measurement are compared to the prepared concentration and the error is indicated in the third column in the table. The prepared concentrations and measured values differ within the range between 1.8 and 12.1%. For high concentrations ( $> 150\text{mM}$ ), the error between the optically measured and the as-prepared concentrations is  $< 3\%$ . When compared to other ion sensors based on EC materials, the SNWG platform offers a much higher dynamic range for concentration detection.<sup>285</sup> While planar sensors show about 30% modulation over roughly 60 mM ( $\lambda = 5 \text{ M}^{-1}$ ),<sup>285</sup> the SNWG possesses a  $\text{Na}^+$  ion sensitivity of roughly  $\xi = 2 \times 10^7 \text{ M}^{-1}$ .

Table 9: Calculated Na<sup>+</sup> ion concentration based on calibration curve and resulting error.

<b>Prepared Na<sup>+</sup> Concentration (mM)</b>	<b>Calculated Na<sup>+</sup> Concentration from <math>\Delta T</math> (mM)</b>	<b>Error (%)</b>
<b>25</b>	26.9	-7.6
<b>50</b>	48.2	3.6
<b>75</b>	77.9	-3.9
<b>100</b>	87.9	12.1
<b>150</b>	141	6
<b>200</b>	195	2.5
<b>250</b>	257	-2.8
<b>300</b>	297	1
<b>400</b>	414	-3.5
<b>500</b>	491	1.8

## 5.2.4 Discussion

The SNWG platform provides high modulation depths of up to  $10^{-7}$  with sub-second EC switching times. Notably, the degradation of the EC film leads to a declining accuracy of the measurements, which is why devices either need to be seasoned to provide reasonable accuracy or other ways of degradation prevention must be found. Moreover, Na<sup>+</sup> measurement accuracy could be further increased through time averaging, where measurements are taken every second and results are averaged. For implementation in microfluidics, constant measurements could detect a change in the electrolyte concentration nearly instantaneously.

### 5.3 Dynamic Nonlinear Photonic Waveguides

Integrated nanophotonic devices, such as waveguides, resonators, and modulators bear the promise of on-chip optical data processing to increase computation speed and enhance telecommunication devices.<sup>117,158,292–295</sup> Electro- and thermo-optic materials, as well as phase change materials (PCM) are employed in active photonic devices.<sup>82,111,249,296</sup> Their stimuli responsive behavior is used to create a dynamic dielectric environment that results in the manipulation of the effective refractive index an optical mode experiences, or drastically alter the transmission of optical devices.

Nonlinear optical processes in  $\text{Si}_3\text{N}_4$  integrated on CMOS compatible Si platforms have been demonstrated for harmonic generation and frequency mixing.<sup>168,170,278,280,293,297</sup> Phase-matched harmonic generation is achieved either through device design, which ultimately leads to fixed wavelength harmonic generation, or through the photogalvanic effect, which requires sufficient waveguide length to achieve photoinduced self-modulation.<sup>109,276,277</sup> Other ways to create phase-matching are heating of the device or quasi-phase matching through poling of the waveguide material. To allow mainstream integration of nonlinear processes, CMOS compatible sources for harmonic light are necessary. One of the most researched Si-based materials with nonlinear properties is  $\text{Si}_3\text{N}_4$ . Silicon Nitride is readily available through CVD processes and exhibits low optical loss, allowing for efficient waveguiding applications. Nonetheless,  $\chi^2$  values reported for  $\text{SiN}_x$  are low ( $\chi^2 < 1$  pm/V) and, thus, conversion efficiencies for second harmonic generation (SHG) in waveguides is low ( $< 0.05\%/W$  or  $0.003\%/(\text{Wcm}^2)$ ).<sup>110,168</sup>

Section 5.2 introduced a SNWG platform which utilizes the change in the optical extinction coefficient upon  $\text{Na}^+$  ion intercalation into an EC  $\text{WO}_3$  layer on top of a  $\text{SiN}_x$  waveguide. Based on a similar approach, the change in refractive index of the  $\text{WO}_3$  layer can be exploited to for dynamically changing the dielectric properties for nonlinear optical devices.

### 5.3.1 SHWG Device Design and Simulations

Via  $\text{Li}^+$  ion intercalation into  $\text{WO}_3$ , the phase-matching conditions for optical modes in  $\text{SiN}_x$  waveguides can be changed to an extent, which leads to a shift in the generated harmonic wavelength. The introduced second-harmonic waveguide (SHWG) is designed to alter the created SH wavelength over a span of several nanometers. The all-solid-state nonlinear device, fabricated on top of the  $\text{SiN}_x$  waveguide core and cladding, consists of  $\text{WO}_3$  as the modulation layer,  $\text{LiNbO}_3$  as the ion conductor, and  $\text{NiO}$  as an ion storage film. Through device design, namely an adjustable spacer thickness between waveguide core and  $\text{WO}_3$ , the inherent optical extinction introduced by the EC effect can be mitigated. In order to reduce the effect of the thin cladding sidewalls (discussed in Section 5.2), the cladding here is designed to fully incorporate the  $\text{SiN}_x$  waveguide core as shown in Fig. 5.13. Furthermore, the cladding is planarized above the waveguide to mitigate deposition and adhesion of the solid-state ECD onto the cladding. Planarization is conducted using a planarizing coating containing silica beads.

The electrical contacts necessary to drive ions into  $\text{WO}_3$  are positioned  $5\ \mu\text{m}$  to the edge of the waveguide, to prevent coupling of the optical mode to the lossy contacts (Section 5.2). The presence of  $\text{Li}^+$  ions even in as deposited  $\text{WO}_3$  films

leads to a maximum resistivity of  $\rho_{\text{WO}_3} = 12 \text{ m}\Omega\text{cm}$  (minimum  $\rho_{\text{WO}_3} = 98 \mu\Omega\text{cm}$ ), which is about 8 orders of magnitude lower than that of  $\text{LiNbO}_3$  ( $\rho_{\text{LiNbO}_3} > 10^7 \Omega\text{cm}$ ). Hence, the voltage drop over the contact free distance of the  $\text{WO}_3$  layer is on the same order of the voltage drop over the solid ion conductor.

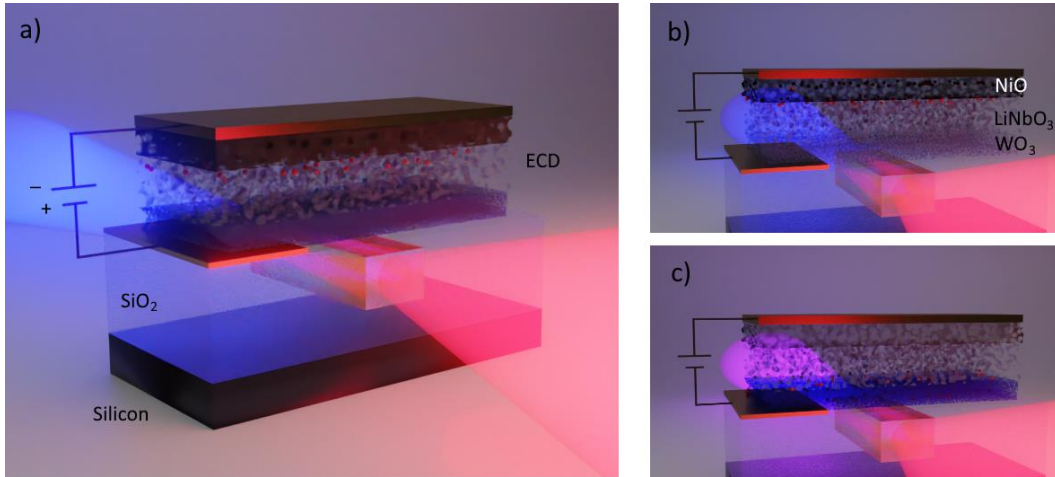


Fig. 5.13: Schematic of the SHWG. (a) An overview of the general device design and functionality. (b) Delithiation of the  $\text{WO}_3$  layer leads to phase-matching at lower wavelengths. (c) Intercalation of  $\text{Li}^+$  ions into  $\text{WO}_3$  change the SH wavelength.

The coupled femtosecond laser pulses lead to SHG along the waveguide and can be measured at the output facet. Waveguide dimensions, surface roughness, and dielectric environment influence the wavelength of the generated harmonic light due to constructive or destructive interference. To optimize the phase-matching criterion needed for HG and enhanced efficiency, the ECD integrated on top of the  $\text{SiN}_x$  waveguide core is used to alter the effective refractive index that the optical mode traversing along the waveguide experiences. Thus, the wavelength of the

SHG in the delithiated state of  $\text{WO}_3$  (Fig. 5.13(b)) is different than that generated in the lithiated state (Fig. 5.13(c)). Alternating the applied voltage, hence, directly influences the SHG wavelength. Such a voltage change is induced via a source meter.

Device behavior in operation can be modelled through FDTD simulations as introduced previously. To estimate optimal device dimension, phase-matching conditions for the overlap of the fundamental (FE)  $\text{TE}_{00}$  mode and the SH  $\text{TE}_{03}$  are assessed through incremental matching of the effective refractive index ( $n_{\text{eff}}$ ) of the modes involved. Higher modes lead to less overlap between the fields of the fundamental (FE) and the SH signals. As such, the SH  $\text{TE}_{03}$  is the dominant mode in the nonlinear optical generation process and, thus, is analyzed accordingly via FDTD simulations.

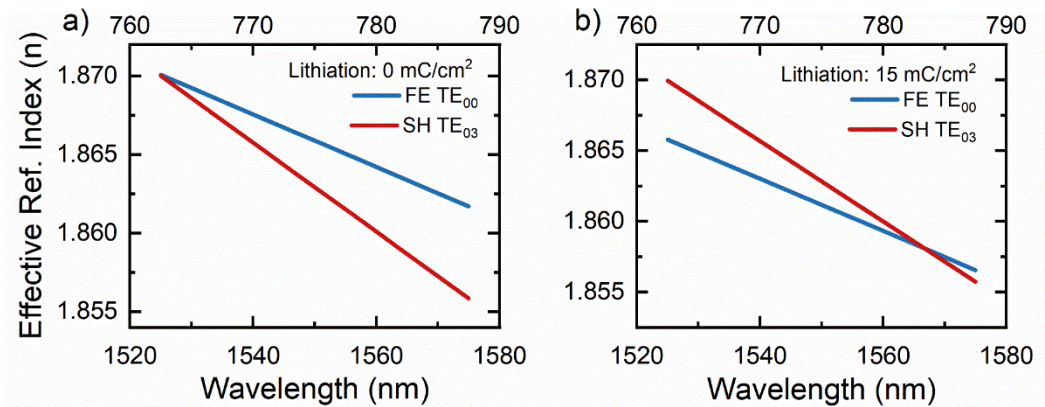


Fig. 5.14: Effective refractive indices for FE  $\text{TE}_{00}$  and SH  $\text{TE}_{03}$  optical modes in a SHWG. (a) At 0 mC/cm<sup>2</sup> lithiation of  $\text{WO}_3$  and a 200 nm thick  $\text{SiO}_2$  layer and (b) at 15 mC/cm<sup>2</sup> lithiation.

The  $n_{\text{eff}}$  is calculated for facet dimensions of  $w = 1.4 \mu\text{m}$  and  $h = 850 \text{ nm}$ , and spacer layer thickness  $d_{\text{SiO}_2} = 200 \text{ nm}$  for optimal phase matching and sufficient spatial overlap between the FE  $\text{TE}_{00}$  and SH  $\text{TE}_{03}$  optical modes in a SHWG. The calculated effective refractive indices over the range of  $\lambda_{\text{FE}} = 1525 \text{ nm}$  to  $\lambda_{\text{FE}} = 1575 \text{ nm}$  fundamental (FE) wavelength and their corresponding SH wavelengths (i.e.,  $\lambda_{\text{SH}} = \lambda_{\text{FE}}/2$ ) are shown in Fig. 5.14. Remarkably, when there is no intercalated charge in the  $\text{WO}_3$  layer, the phase-matching wavelength  $\lambda_{\text{FE}} = 1525 \text{ nm}$  has its SH at  $\lambda_{\text{SH}} = 762.5 \text{ nm}$ , while  $15 \text{ mC/cm}^2$  lithiation of the modulation layer leads to a shift in phase-matching wavelength by nearly  $\Delta\lambda_{\text{FE}} = 42.5 \text{ nm}$  to  $\lambda_{\text{SH}} = 783.6 \text{ nm}$ . For thicker spacer layers, the achievable phase-matching shift reduces to  $\Delta\lambda_{\text{FE}} = 15 \text{ nm}$  for  $d_{\text{SiO}_2} = 350 \text{ nm}$  and  $\Delta\lambda_{\text{FE}} = 3 \text{ nm}$  for  $d_{\text{SiO}_2} = 500 \text{ nm}$ .

The electric field distribution for the FE  $\text{TE}_{00}$  and the resulting SH  $\text{TE}_{03}$  signal are simulated along a  $200 \mu\text{m}$  long waveguide and are captured after  $100 \mu\text{m}$  of propagation. Resulting field distributions of the FE  $\text{TE}_{00}$  and SH  $\text{TE}_{03}$  optical modes are plotted in Fig. 5.15(a) and Fig. 5.15(b), respectively. Evidently, the  $\text{TE}_{00}$  mode at  $\lambda = 1550 \text{ nm}$  wavelength extends out of the waveguide, so that 7% of the magnitude of the electric field interact with the  $\text{WO}_3$  layer (Fig. 5.15(a)). On the other hand, the SH  $\text{TE}_{03}$  at  $\lambda = 782 \text{ nm}$  wavelength is well confined inside the waveguide core with most of the extending field being confined in the  $\text{SiO}_2$  cladding. In fact, only 0.2% of the magnitude of the electric field extends into the EC layer.

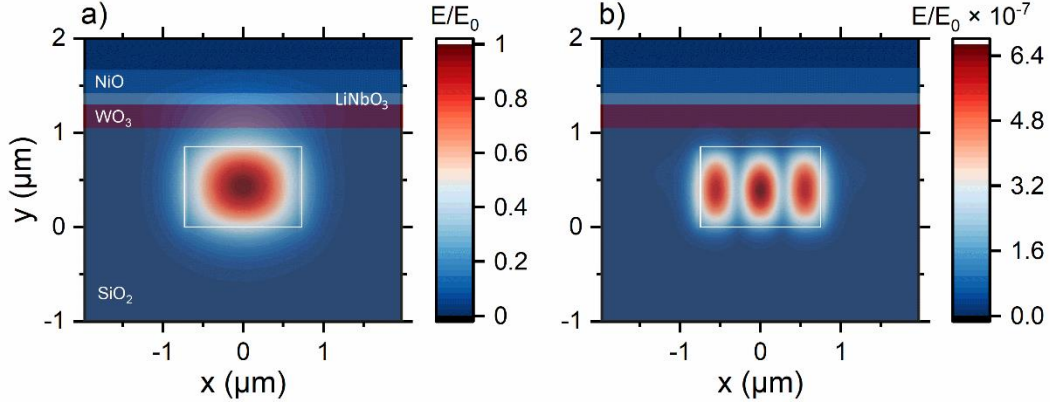


Fig. 5.15: Electric field distribution in SHWG structure with 200 nm thick spacer layer (facet: 850 nm x 1400 nm). (a) FE TE<sub>00</sub> mode showing strong overlap with WO<sub>3</sub> layer. (b) SH TE<sub>03</sub> mode strongly localized to SHWG core.

In addition to the obvious matching of  $n_{\text{eff}}$ , efficient SHG at particular wavelengths is only achieved if the propagation length of the optical pulse is of the order of its coherence length,  $L_{\text{Coh}}$ . Wavelengths that fall within the coherence length window all contribute to the SHG process and hence, spectrally broader SH signals result for shorter waveguides. The coherence lengths resulting from the simulated effective refractive index for  $C = 0 \text{ mC/cm}^2$  and  $C = 15 \text{ mC/cm}^2 \text{ Li}^+$  ion intercalation are calculated via:

$$L_{\text{Coh}} = \frac{\lambda}{4(n_{\text{FE}} - n_{\text{SH}})} \quad (5.2)$$

where  $n_{\text{FE}}$  and  $n_{\text{SH}}$  are the wavelength dependent effective refractive indices of the FE and SH mode.

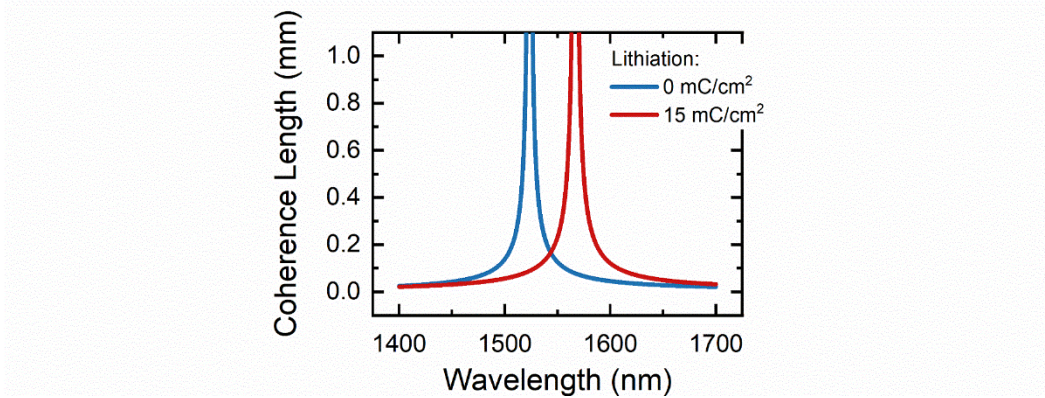


Fig. 5.16: Coherence length of a SHWG device having a delithiated ( $0 \text{ mC/cm}^2$ ) and a fully lithiated ( $15 \text{ mC/cm}^2 \text{ Li}^+$ ) EC  $\text{WO}_3$  modulation layer.

It is evident that waveguide lengths  $L_{\text{Coh}} > 500 \text{ }\mu\text{m}$  are necessary to achieve narrow band SHG and, hence, will introduce a significant shift in the optical SH spectrum via the EC effect (Fig. 5.16). At a propagation length of  $1 \text{ mm}$ , the coherence window spans  $\Delta\lambda_{\text{Coh}} = 7 \text{ nm}$ , indicating that the SH signal interferes constructively within this window and narrow spectral width can be expected. At waveguide lengths of  $l = 500 \text{ }\mu\text{m}$  and  $l = 250 \text{ }\mu\text{m}$ , the window broadens to  $\Delta\lambda_{\text{Coh}} = 13 \text{ nm}$  and  $\Delta\lambda_{\text{Coh}} = 24 \text{ nm}$ , respectively.

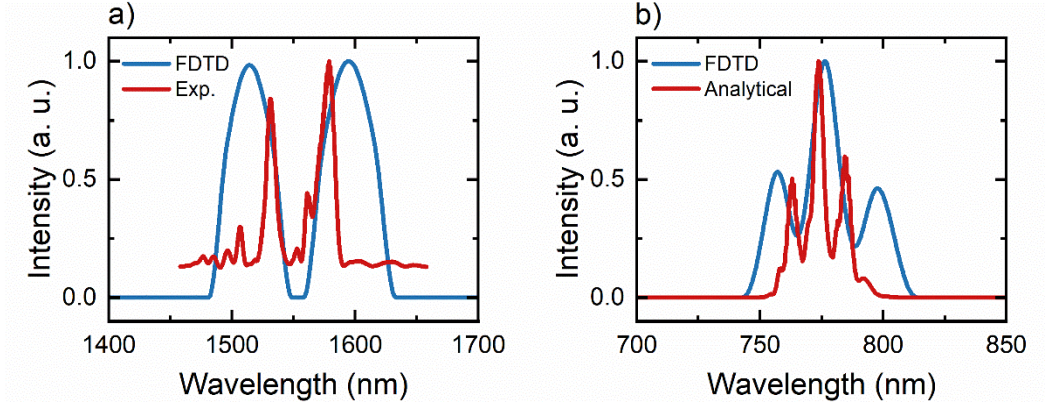


Fig. 5.17: Spectra of source and SH signal for FDTD simulations. (a) FDTD source consisting of two 150 fs pulses and measured NIR spectrum. (b) FDTD simulated SH spectrum and analytical solution from source spectrum.

FDTD simulations are conducted to predict device behavior in operation. Here, a 250  $\mu\text{m}$  long SHWG ( $w = 1400$  nm,  $h = 850$  nm) without ECD modulation layer and  $d = 200$  nm spacer thickness is investigated. With such SHWG dimensions, the device does not exhibit phase-matching for the SH signal when excited at 1550 nm. The  $\text{SiN}_x$  nonlinearity is taken to be  $\chi^2 = 0.3$  pm/V and is assumed to be isotropic<sup>110,168</sup> All, the dielectric properties for  $\text{SiN}_x$ ,  $\text{WO}_3$ ,  $\text{NiO}$  and  $\text{LiNbO}_3$  are determined via ellipsometry. To model the spectrum of the  $\text{Er}^{3+}$  doped fs fiber laser used in the experiments, two sources with a pulse length  $t = 100$  fs are used as shown in Fig. 5.17(a). Two sources; however, make the simulation increasingly complex, leading to long ( $> 100$  h) computation times for a 1 mm long waveguide. Moreover, narrower width for the spectral components of the source spectrum further increases simulation times due to the longer pulse lengths involved. The calculated SH spectrum resulting from the two-source excitation is shown in Fig. 5.17(b) along

with the analytical calculation of the SH signal (i.e., calculated from the spectrum in Fig. 5.17(a) by accounting for mixing between any two frequency components within the fundamental excitation laser pulse spectrum). Such analytically calculated SH signal displays one main peak at  $\lambda_{\text{SH}} = 774.2$  nm due to the mixing of the main spectral components of the FE spectrum. Notably, both the analytical and the FDTD solutions exhibit side peaks. Even though the FDTD simulation does not represent the experiment in all aspects, the two-source setup is very good in serving to characterize the lithiation dependent optical modulation mechanism where the spectral dependency is not important.

To investigate the role of EC effect on phase-matching and tuning of the generated SH spectrum, an ECD (i.e., length of either  $l = 250$   $\mu\text{m}$  or  $l = 1$  mm) is added on top of the SHWG having the dimensions  $d_{\text{WO}_3} = 250$  nm,  $d_{\text{LiNbO}_3} = 120$  nm and  $d_{\text{NiO}} = 270$  nm for  $\text{WO}_3$ ,  $\text{LiNO}_3$  and  $\text{NiO}$ , respectively. For both device lengths, the FDTD simulated SH spectra as a function of lithiation are shown in Fig. 5.18. Fig. 5.18(a) shows the normalized SH spectra for the 250  $\mu\text{m}$  long SHWG without the intercalated charge (i.e., 0 mC) and during redox cycling at 8 mC/cm<sup>2</sup> and 16 mC/cm<sup>2</sup> lithiation. Evidently, even at a high charge intercalation of 16 mC/cm<sup>2</sup>, the initial main SH signal peak position at  $\lambda_{\text{SH}} = 775.1$  nm and a FWHM = 11.7 nm shifts  $\Delta\lambda_{\text{SH}}$  by <1 nm. However, the spectral weight shifts as the lower wavelength shoulder of the main peak decreases in intensity during cycling and the higher wavelength shoulder simultaneously increases in intensity. The results indicate that the generated SH is phase-matched with the FE wavelength; however,

the short waveguide length leads to broad phase-matching due to the coherence length mismatch.

The simulated SH spectra for the 1 mm long SHWG are narrower (i.e., FWHM = 6.8 nm) with less pronounced shoulders. Interestingly, the SH wavelength at peak intensity shifts from  $\lambda_{\text{SH}} = 770.2$  nm to  $\lambda_{\text{SH}} = 777.8$  nm during the lithiation process of 16 mC/cm<sup>2</sup> Li<sup>+</sup> ions. Since the FWHM = 6.8 nm is in good agreement with the SH coherence width (i.e.,  $\Delta\lambda_{\text{Coh}}$ ) and the spectral position shifts accordingly, the FDTD simulations suggest that the SHWG experiences phase matching.

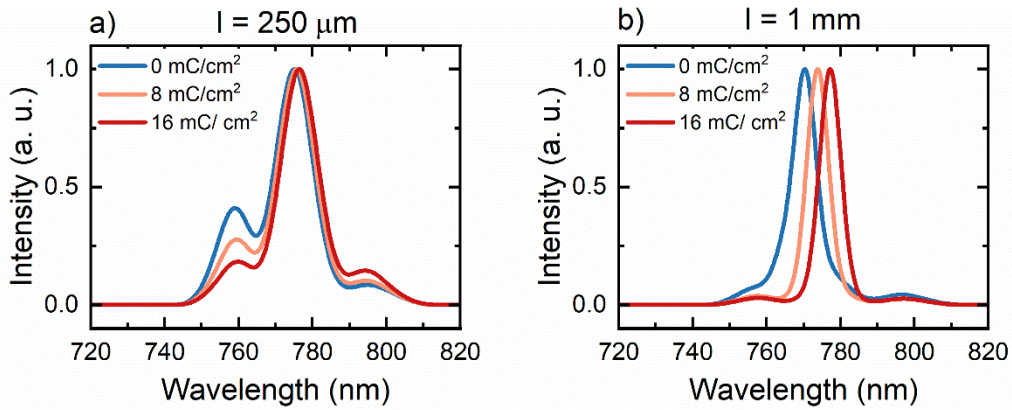


Fig. 5.18: FDTD simulation results for SHWG devices as a function of lithiation.

(a) For a 250 μm long SHWG and (b) for a 1 mm long SHWG.

The FDTD simulations and calculations suggest the achievable spectral shift as a function of Li<sup>+</sup> intercalation density depends on the thickness ( $d_{\text{SiO}_2}$ ) of the SiO<sub>2</sub> spacer used. For a 200 nm thick spacer layer at a maximum achievable intercalation density of  $C = 20$  mC/cm<sup>2</sup>, obeys the relation  $\lambda_{\text{SH}}/\Delta C = 0.45$  nm cm<sup>2</sup>/mC. With increasing spacer thickness to  $d_{\text{SiO}_2} = 350$  nm the achievable wavelength shift

dependence on the intercalation density reduces to  $\lambda_{\text{SH}}/\Delta C = 0.25 \text{ nm cm}^2/\text{mC}$  as shown in Fig. 5.19(a). However, a thicker  $\text{SiO}_2$  spacer layer increases the optical transmittance of the waveguide at the FE wavelength in the lithiated state and, hence, allows for stronger SH signals (Fig. 5.19(b)). Due to the strong localization of the SH mode to the waveguide core, the optical absorption induced through  $\text{Li}^+$  ion intercalation in the  $\text{WO}_3$  layer is negligible. Nonetheless, the decreasing FE signal limits the maximum length of the waveguide needed for such nonlinear optical interaction, since after a certain distance no more SH light signal is generated, while the already generated SH signal propagates through a lossy waveguide core due to the  $\text{WO}_3$  layer.

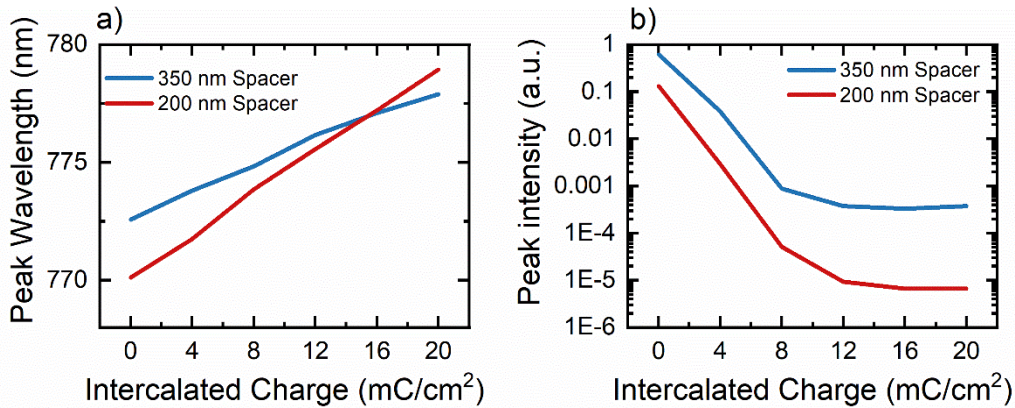


Fig. 5.19: FDTD simulation results for a 1 mm long SHWG as a function the intercalated charge for two spacer thicknesses. (a) SH wavelength at peak intensity during lithiation. (b) Peak intensity of the FE signal during lithiation.

### 5.3.2 SHWG Fabrication

SHWGs are fabricated in a modified SNWG fabrication process described in section 5.2.2. First an 850 nm thick  $\text{SiN}_x$  film is PECVD deposited onto a  $2 \mu\text{m}$

layer of SiO<sub>2</sub> thermal oxide on a 4-inch Si wafer using a Plasmatherm Versaline deposition system (Deposition parameter are outlined in (Appendix B). The Versaline PECVD system is chosen over the PECVD Trion used for SNWGs, since it can accurately deposit the SiN<sub>x</sub> film at inhomogeneities of less than  $\Delta < 0.3\%$  in the center 2 inches of the wafer. Afterwards, the waveguides are defined via a lithography step involving a Cr etch mask and a RIE step (Oxford PlasmaPro 100) (Fig. 5.20 (a)). Consequently, the Cr mask is removed in a Cr wet etch process and the wafer is cleaned in an oxygen plasma. Next, the waveguide samples are annealed at 700°C in N<sub>2</sub> atmosphere. SiO<sub>2</sub> is then deposited onto the samples with thicknesses of 850 nm + d<sub>spacer</sub> + 50 nm, forming a structure of ~ 800 nm in height over the waveguides. The discrepancy in thicknesses of the cladding layer and the structure over the waveguides arises from the isotropic growth of the SiO<sub>2</sub> layer.

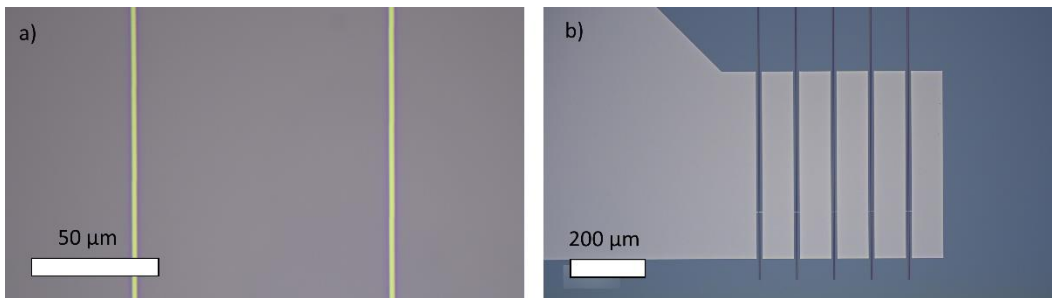


Fig. 5.20: Microscope images taken during fabrication process. (a) 100× magnification image of two patterned waveguide masks. (b) 10× magnification image of the bottom contact before deposition of the ECD.

A planarization step is necessary to create the desired planar spacer. Since no chemical mechanical polishing system is available, a planarization coating is used

to level the sample. A coating (PC43-700 Futurrex Inc.) is spin coated onto the wafers at 3000 rpm and baked to reflow at 200°C for 120 s. After the baking step, a 1150 nm thick PC43-700 coating is formed. To achieve a planarized flat sample surface, a RIE process is adjusted to have the same etching rate for SiO<sub>2</sub> and PC43-700. The modified etch process involves a 50 sccm CF<sub>4</sub> and adjustable amount CHF<sub>3</sub> gas mixture at 100 W plasma power and 125 mTorr pressure. While the etch rate for SiO<sub>2</sub> changes linearly from  $r = 68$  nm/min to  $\sim r = 56$  nm/min when introducing up to 30 sccm CHF<sub>3</sub>, the etch rate for PC43-700 exponentially decreases with the relative amount of CHF<sub>3</sub> (Fig. 5.21). At 2.5 sccm CHF<sub>3</sub> flow (4.7%), both the etch rates are equal  $r = 67$  nm/min. Nonetheless, the etch process is monitored every 180 s, since redeposition of either material can slow the respective etch down. Surface roughness of the coating, as well as the SiO<sub>2</sub> layer after processing is measure to be < 10 nm.

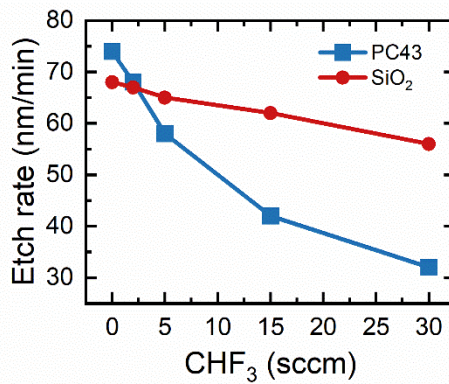


Fig. 5.21: Etch rate of SiO<sub>2</sub> and PC43 as a function of the CHF<sub>3</sub> gas flow.

Following the planarization step, the wafers are annealed rapidly multiple times at 1100°C for 2 min to increase interfacial stress between the SiO<sub>2</sub> and the SiN<sub>x</sub>

layers. Due to the different thermal expansion properties, rapid heating increases the strain between the layers and thus improves the symmetry breaking at the interface. Next, the bottom contact consisting of 20 nm Cr and 80 nm W is defined and deposited as shown in Fig. 5.20(b). The contact pads between the waveguides are contacted via a 1.2  $\mu\text{m}$  wide metal strip.

In the next step, the ECD is patterned via lithography and the oxide films ( $\text{WO}_3$ ,  $\text{LiNbO}_3$  and  $\text{NiO}$ ), as well as the top contact are deposited in the same reactive magnetron sputtering system. EC oxides and  $\text{LiNbO}_3$  are deposited as discussed earlier (Section 3). It is imperative to ignite the plasma over the  $\text{LiNbO}_3$  target at the same time as  $\text{WO}_3$  deposition starts. The shutter to the  $\text{LiNbO}_3$  target remains closed, but nonetheless,  $\text{Li}^+$  ions can diffuse to the sample and intercalate in the EC oxide. The final ECD aligns with the bottom contact as seen in Fig. 5.22(a).

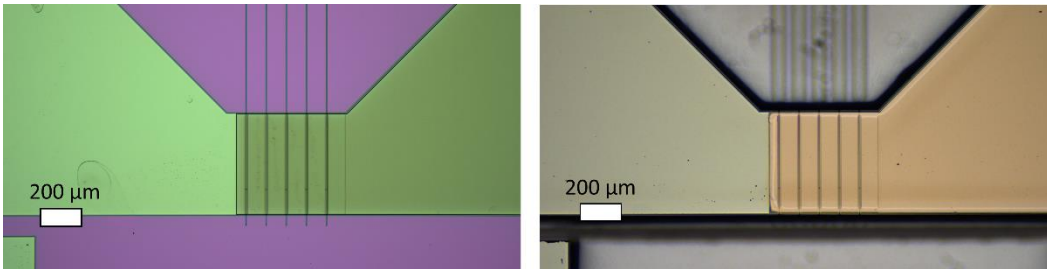


Fig. 5.22: Microscope images taken during fabrication process. (a) 5 $\times$  image after deposition of ECD. (b) 5 $\times$  image of the final device after scoring.

After the ECD deposition, the waveguide length and chip structure are defined. A thick PR is used etch down along the waveguide facets and the insulator layer. The same mask, having an extended dimension in  $y$ -direction to protect waveguide

facets, is then used for etching 300  $\mu\text{m}$  into the Si substrate using a DRIE process (Fig. 5.22(b)). As shown in the microscope images, the waveguide structure is elevated above the substrate, so that the tapered fiber, used for collecting the light from the waveguide output facet, can be inserted from the back. Individual chips are released after scoring the wafer from the top along the DRIE defined trenches. To avoid damage to the facets, the trenches are 100  $\mu\text{m}$  wide to account for the dicing blade 50  $\mu\text{m}$  width. The dicing saw leaves the wafer intact with approximately 80  $\mu\text{m}$  residual thickness left along the trenches. A final oxygen plasma clean is used before the wafer is divided into the patterned waveguide chips.

The finalized SHWG devices are investigated via Field emission scanning electron microscopy (FESEM) imaging and simultaneous EDX elemental analysis. For imaging purposes, the sample is tilted by  $80^\circ$  to visualize the facet. Fig. 5.23(a) shows a FESEM image of the 1.4  $\mu\text{m}$  wide waveguide facet after oxygen plasma cleaning. The waveguide facet appears smooth, but slightly indented due to the RIE process used to etch through  $\text{SiO}_2$ . While the RIE process itself is anisotropic,  $\text{SiN}_x$  etches approximately 10 times faster in the used etch chemistry. Furthermore,  $\sim 100$  nm deep trenches can be seen approximately 800 nm off to the side of the waveguide core. The trenches are artifacts from the PECVD  $\text{SiO}_2$  cladding deposition and the planarization process. Since PECVD is an isotropic deposition process, the  $\text{SiO}_2$  cladding grows in all directions around the waveguide core. The RIE step used to planarize the sample experiences a different local plasma composition where the two materials meet, such that PC43-700 etches faster in an oxygen rich environment. Hence, the oxygen released by etching the waveguide

cladding increases the etch rate of the PC43-700, leading to the trenches formation. Nonetheless, the trenches do not prevent growth of a well-connected ECD on top of the spacer layer.

EDX line scans along the white lines indicated in Fig. 5.23(a) result in the normalized X-ray spectra presented in Fig. 5.23(b,c). The EDX spectra are normalized since the Si signal is much stronger than all other elemental signals. Fig. 5.23(b) shows the elemental signals of Si  $K\alpha$ , O  $K\alpha$  and N  $K\alpha$  captured along the vertical scan line. Evidently, the amount of Si decreases sharply from the bottom to the top of the scan. The higher signal at the bottom of the scan arises from the Si wafer (indicated in dark grey). Then, the signal decreases due to the presence of a 2  $\mu\text{m}$  thick thermal oxide layer (light grey). The local peak of the Si signal between 0.6  $\mu\text{m}$  and - 0.2  $\mu\text{m}$  is attributed to the  $\text{SiN}_x$  waveguide core, since the relative amount of Si is higher in  $\text{SiN}_x$  (blue). The signal decreases again afterwards. The opposite behavior of signal strength is observed for the O  $K\alpha$  line. The presence of the  $\text{SiN}_x$  waveguide core is further confirmed by the presence of the N  $K\alpha$  line which peaks between 0.6  $\mu\text{m}$  and - 0.2  $\mu\text{m}$ . Due to the tilting angle (needed for imaging) and the subsequent change in working distance along the line scan, the signal collected from the top of the cladding layer and the ECD is spatially distorted. The horizontal scan shown in Fig. 5.23(c) confirms the presence of  $\text{SiN}_x$  cladded with  $\text{SiO}_2$ . The relative amount of N along with the Si  $K\alpha$  increases sharply for the center (i.e., 1.4  $\mu\text{m}$ ) of the scan. Meanwhile, the O signal decreases in that window. Nonetheless, the intercept of O and N signals give a good indication of where certain areas begin and end. Finally, Fig. 5.23(d) shows an FESEM overview

of the fabricated waveguide facet in false color. Evidently, the  $\text{SiN}_x$  etches faster than the surrounding  $\text{SiO}_2$  in the RIE step, leading to a roughly  $\sim 2 \mu\text{m}$  deep trench underneath the waveguide core. Furthermore, the results of the off-set DRIE mask become visible where  $\sim 3 \mu\text{m}$  wide step can be seen where the DRIE step through the Si wafer starts. The “scallop” produced by the DRIE process are visible in the lower part of the image. These formations are expected for Bosch-etches and a result of the cycling between etch gases. The electrical contacts buried underneath the ECD are indicated in yellow for better contrast. Additionally, the FESEM image gives a good indication of the planarization.

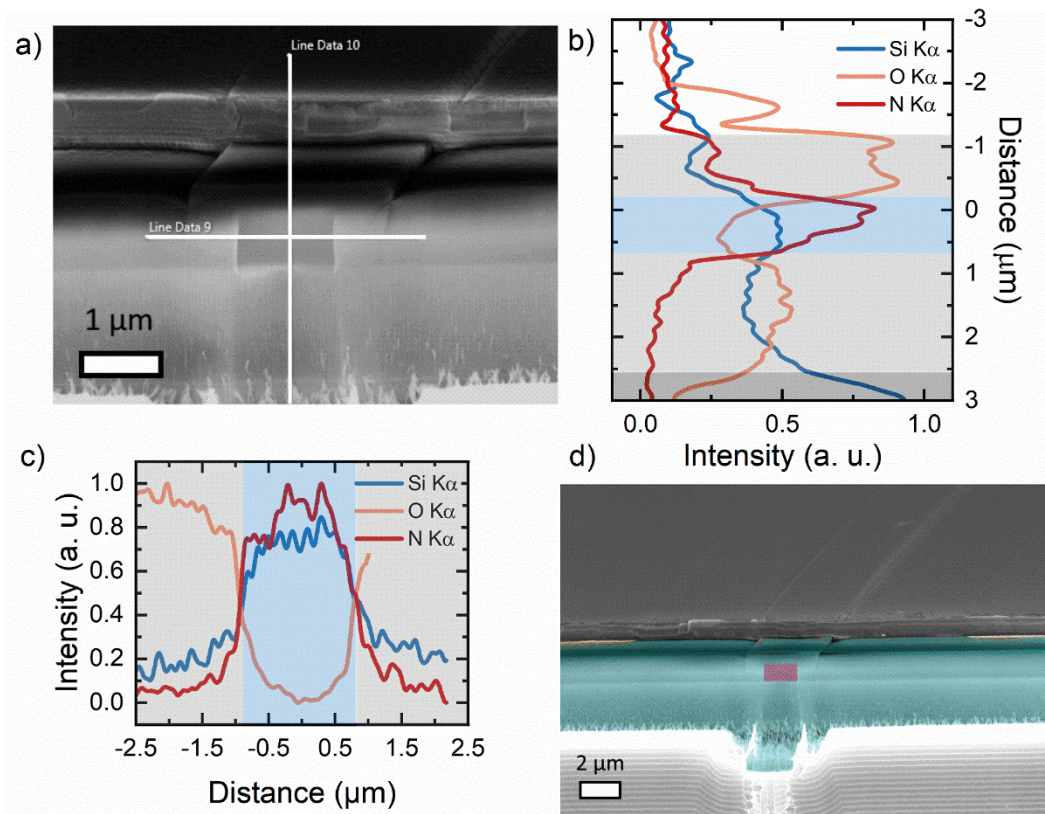


Fig. 5.23: EDX analysis of SHWG after fabrication process. (a) FESEM image with indicated EDX line scan directions. (b) Vertical line scan indicating normalized Si, O, and N signal. (c) Horizontal elemental composition along line scan. Signals are normalized due to the strong Si signal. (d) False color FESEM image of SHWG facet containing the “scallops” produced by the DRIE step.

The ECD and corresponding layer thicknesses are shown in Fig. 5.24. To allow high-resolution facet imaging, the ECD is deposited during the SHWG fabrication process on a pre-scored Si chip. The chip is then cleaved along the score line to create a clean facet. Deposited oxides show distinct contrast to one another, so that approximate thicknesses can be measured with  $d_{\text{WO}_3} = 250 \text{ nm}$ ,  $d_{\text{LiNbO}_3} = 120 \text{ nm}$  and  $d_{\text{NiO}} = 270 \text{ nm}$ . All three films show a nanocrystalline structure. While the  $\text{WO}_3$

film exhibits a rather random nanoparticulate morphology, the  $\text{LiNbO}_3$  and  $\text{NiO}$  films grow at a preferred crystal orientation along the growth direction. The accumulative surface roughness is measured to be  $\pm 11$  nm.

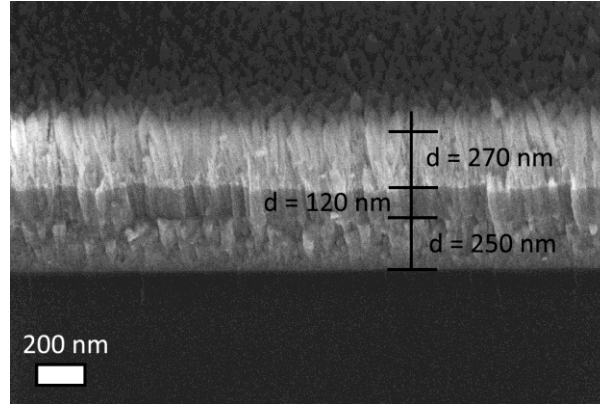


Fig. 5.24: FESEM image of the ECD deposited on Si during the SHWG fabrication process with thicknesses for  $\text{WO}_3$ ,  $\text{LiNbO}_3$  and  $\text{NiO}$  indicated.

### 5.3.3 SHWG Experimental Results

Dynamic SH and transmission modulation experiments of SHWG structures are conducted in the experimental setup introduced in Section 5.1. As seen in Fig. 5.25(a), the NIR fs-pulse is coupled to the nonlinear  $\text{SiN}_x$  waveguide core. The effective refractive index inside the waveguide core can be altered by applying a bias to the ECD consisting of  $\text{WO}_3$ ,  $\text{LiNbO}_3$  and  $\text{NiO}$ . To mitigate losses due to the electrical contacts, Au bottom contacts are off-set by  $5 \mu\text{m}$  to the side of the waveguide core (Fig. 5.25(b)).

Based on the facet dimensions of the SHWG and the measured optical material properties, the calculated optical coupling efficiency of the laser is expected to be

~62%. However, as determined by length dependent optical transmission measurements, the measured optical coupling efficiency is found to be ~50%. As such, the maximum coupled laser pump power is  $P_P = 50$  mW.

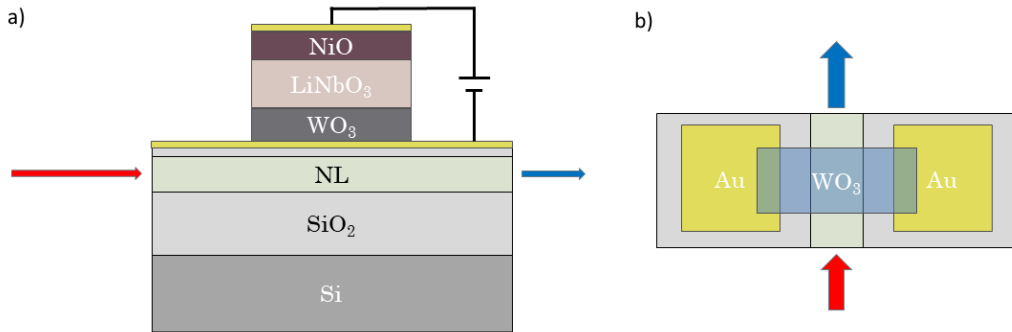


Fig. 5.25: Schematic of the experiment conducted to measure dynamic harmonic generation. a) Side view of the sample with nonlinear SiN<sub>x</sub> core (NL) and electrically driven ECD. b) Top view with off-set contacts. Fundamental NIR mode is indicated as red arrow, SH signal is indicated as blue arrow.

The On-state optical transmission for the 1550 nm excitation wavelength is  $\sim T = 0.05$  even in the case of  $C = 0$  mC/cm<sup>2</sup> intercalated charge, indicating irreversible intercalation of the Li<sup>+</sup> ions into the SHWG during the fabrication process. The On-state optical transmission remains constant even after several minutes of continuous application of a deintercalation voltage. Fig. 5.26 depicts the measured SH signal as a function of the excitation optical power for two different lithiation levels of a SHWG having  $d = 350$  nm spacer layer. When there is no intercalated charge (i.e.,  $C = 0$  mC/cm<sup>2</sup>), the maximum achieved SH signal for a  $l = 1$  mm SHWG length and  $P_P = 50$  mW pump power is  $P_{SH} = 153$  nW. With decreasing SHWG lengths,  $l$

= 0.5 mm, 0.25mm, 0.1 mm, and 0.05 mm, the achievable SH signal decreases to  $P_{SH} = 142.5$  nW,  $P_{SH} = 83.5$  nW,  $P_{SH} = 16.7$  nW and  $P_{SH} = 3.6$  nW, respectively. As expected, the SH power curves exhibit a quadratic dependency on the SHWG's length with fitting coefficients being between  $1.95 < x < 2.04$ . In case of  $C = 16$  mC/cm<sup>2</sup> intercalated charge, the achievable SH power drops to  $P_{SH} = 19.4$  mW for  $l = 1$ mm SHWG length. The factor of eight difference in the achieved SH power is less than the 1% SH power predicted via FDTD simulations (Section 5.3.1). Such discrepancy further supports the hypothesis that the delithiated WO<sub>3</sub> film contains residual Li<sup>+</sup> ions that are permanently intercalated into the WO<sub>3</sub> nanocrystalline structure.

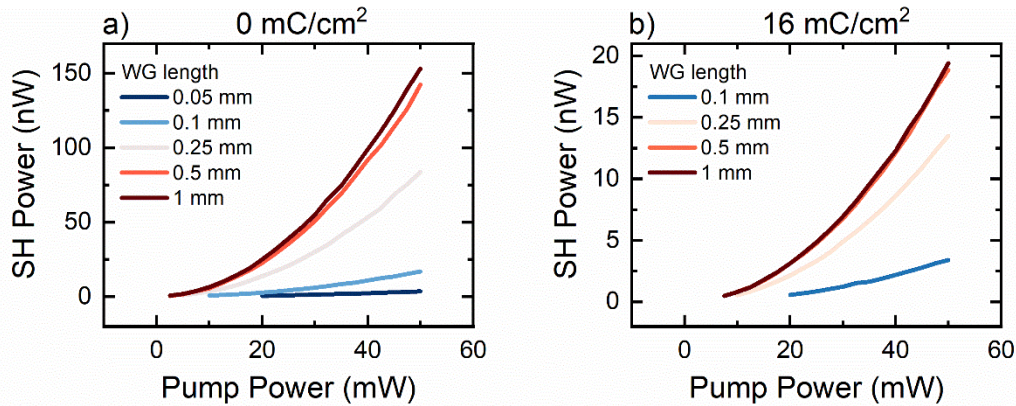


Fig. 5.26: SH power measured as a function of pump laser power ( $P_p$ ) and waveguide length. (a) For  $C = 0$  mC/cm<sup>2</sup> intercalated charge and (b) for  $C = 16$  mC/cm<sup>2</sup> intercalated charge (i.e., lithiation).

The measured SH power as a function of SHWG length indicate that the SHG conversion efficiencies are  $< 6.2 \times 10^{-3}$  %/W, which is less than the reported values for LPCVD Si<sub>3</sub>N<sub>4</sub> waveguides.<sup>108,168</sup> However, the conversion efficiency here is

achieved in shorter waveguides, which is further shown to be several orders of magnitude higher than published ones for PECVD SiN<sub>x</sub>.<sup>110</sup> Fitting of Fig. 5.26(a) with the following equation allows for inferring the amplitude for  $\chi^{(2)}$ :

$$P_{SH} = \left( \frac{2\omega_{SH} \chi^{(2)} P_p l S}{\pi c n_{SH}} \right)^2 \quad (5.3)$$

Here,  $\omega_{SH}$  is the frequency of the generated SH,  $P_p$  is the pump laser power,  $l$  is the SHWG length,  $S$  is the overlap integral between FE and SH optical mode (determined via the Lumerical Mode Solver software), and  $n_{SH}$  is the effective refractive index for the SH radiation. Interestingly, the calculated value of  $\chi^{(2)} = 0.83$  pm/V is on the order of  $\chi^{(2)}$  determined for PECVD SiN<sub>x</sub> films and is three times higher than those reported for quasi phase matched SH waveguides.<sup>108,167,168</sup>

Examining the SHG conversion efficiency, CE, presented in Fig. 5.26(a), reveals that CE saturates for longer SHWGs. This is due to the strong absorption of the FE mode which leads to reduced generation of SH light. In fact, the SH power divided by the SHWG length shows a clear maximum at  $l = 250$   $\mu$ m SHWG length, further supporting that absorption of the IR excitation mode leads to decreased SHG. Notably, the SH power measured for  $d = 200$  nm SiO<sub>2</sub> spacer thickness is only 7% (i.e., 10.6 nW) of that measured for  $d = 350$  nm spacer thickness (i.e., 152 nW) in the delithiated state and at  $P_p = 50$  mW. Hence, SHG power dependency for 200 nm spacer thickness cannot be accurately determined as the  $P_{SH}$  is nearing  $\sim 100$  pW, which is detection limit of our system.

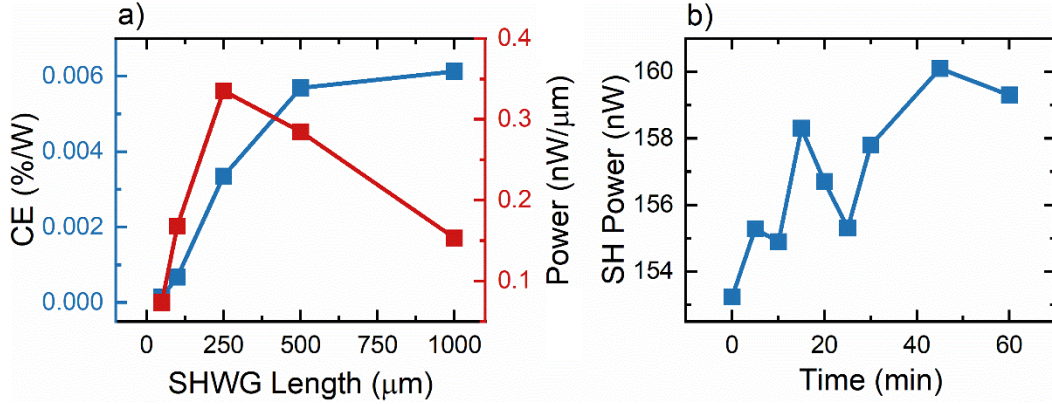


Fig. 5.27: (a) SHG conversion efficiency at  $C = 0 \text{ mC/cm}^2$  intercalated charge as a function of waveguide length. Note that the SH power is divided by the waveguide length to emphasize the maximum achievable conversion efficiency. (b) SH power over time for a  $l = 1 \text{ mm}$  long SHWG.

Several publications have shown that  $\text{Si}_3\text{N}_4$  waveguides exhibit strong quasi phase-matching (QPM) through photoinduced poling of the waveguide.<sup>168,276,298</sup> The photogalvanic effect and the formation of the optical grating have been shown to lead to QPM and, thus, increased SH power over timescales of several minutes. The reported values for SH enhancement through QPM are on the order of 10,<sup>170</sup> over time periods of several minutes to hours. Since the SHWG does not experience a significant increase in SH power over time (Fig. 5.26(b)), it is concluded that the effect of QPM through photoinduced poling of the waveguide is negligible here since dimensions of the SHWG already lead to perfect phase matching between the FE  $\text{TE}_{00}$  and SH  $\text{TE}_{03}$  optical modes. The slight increase in the SH power over time can be attributed to heating of the SHWG through absorption of the excitation laser radiation. Such heating can lead to a change in the effective refractive index the

traversing modes experience. After a reset period of 60 min without coupled laser power, the SH signal drops to  $P_{SH} = 154.2$  nW, indicating that any enhancement effect is temporary and not based on sample annealing.

For a spacer thickness of  $d = 350$  nm and  $l = 1$  mm SHWG length, the measured SH spectra are shown in Fig. 5.28. Evidently, lithiation of the  $WO_3$  layer leads to two distinct effects: (i) a decrease of SH peak intensity and (ii) a shift of the wavelength at peak intensity. The delithiated sample exhibits a maximum of  $P_{SH} = 152$  nW at  $\lambda_{SH} = 773.1$  nm wavelength. During the lithiation process, the intensity decreases to  $P_{SH} = 36$  nW and  $P_{SH} = 12$  nW for  $C = 10$  mC/cm<sup>2</sup> and  $C = 20$  mC/cm<sup>2</sup>, respectively, while the SH generated wavelength at peak intensity shifts to  $\lambda_{SH} = 774.1$  nm and  $\lambda_{SH} = 775.6$  nm. The narrow spectral width of the spectra, ranging between FWHM = 6.9 nm and FWHM = 8.1 nm, indicate perfect phase-matching of the FE and SH mode wavelengths within the coherence length window, since the spectral width fits well with the calculated width for perfect phase-matching.

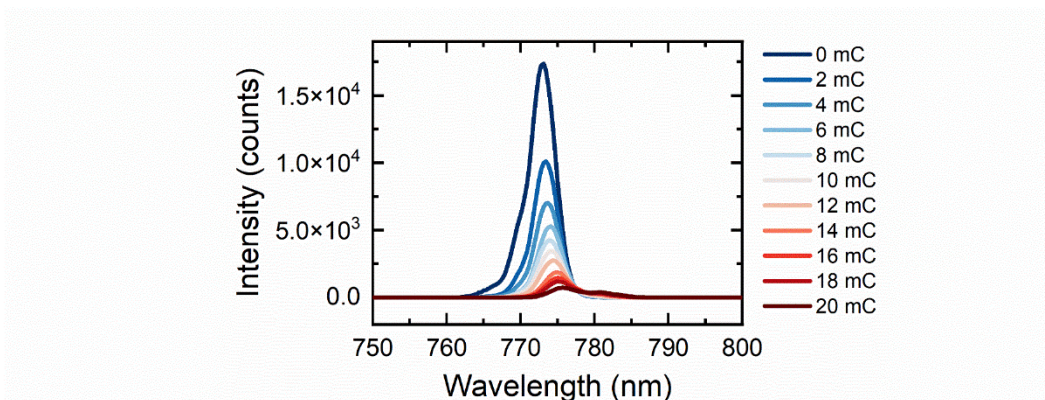


Fig. 5.28: SH spectra measured for SHWG having  $d = 350$  nm spacer thickness and  $l = 1$  mm length as a function of lithiation.

The effect of SHWG and coherence length becomes evident when comparing the normalized spectra for  $l = 0.25$  mm and  $l = 0.5$  mm SHWG length (Fig. 5.29). In the case of a short (i.e.,  $l = 0.25$  mm) SHWG, the SH spectrum does not exhibit a recognizable SH wavelength shift as the intercalated  $\text{Li}^+$  ion charge is increased from  $0 \text{ mC/cm}^2$  to  $16 \text{ mC/cm}^2$ . However, as the lithiation level increases from  $0 \text{ mC/cm}^2$  to  $16 \text{ mC/cm}^2$ , there is a slight change in spectral weight which agrees with the simulated spectra (Section 5.3.1). The coherence length indicates phase-matching in a  $\Delta\lambda_{\text{SH}} = 24$  nm wide spectral window, which is widened by surface roughness and inhomogeneities, so that the full SH signal is equally modulated. When the SHWG length is increased to  $l = 0.5$  mm, there is a noticeable spectral reshaping of the observed SH spectra. Here, the main peak wavelength shifts slightly by  $\Delta\lambda_{\text{SH}} = 1.2$  nm during lithiation, while the spectral weight shifts significantly between the enhanced shoulder at the lower wavelengths (peak  $\Delta\lambda_{\text{SH}} = 762$  nm) side to a pronounced second peak on the higher wavelength (peak  $\Delta\lambda_{\text{SH}} = 785$  nm) side.

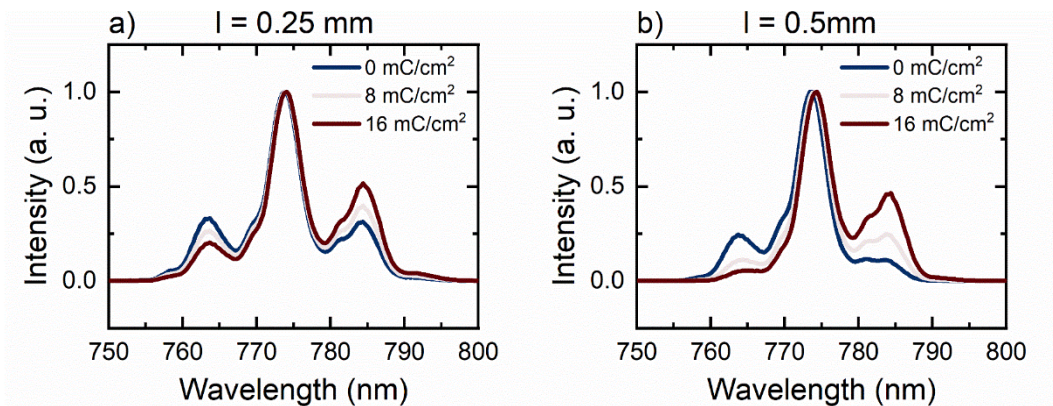


Fig. 5.29: Normalized SH spectra for SHWG as a function of lithiation. (a) For  $l = 0.25$  mm SHWG length and (b) for  $l = 0.5$  mm SHWG length.

To further confirm that the measured SG generated radiation from the SHWG devices experience perfect phase matching, different waveguide structures having a fixed length of  $l = 1$  mm and varying widths are compared and shown in Fig. 5.30. The SH spectrum for a  $w = 1.4$   $\mu\text{m}$  wide SHWG is narrow and exhibits one distinct main peak at  $\lambda_{\text{SH}} = 772.4$  nm. Interestingly, when the SHWG facet is widened by only 200 nm to  $w = 1.6$   $\mu\text{m}$ , the SH spectrum widens and shows all three spectral at 763 nm, 773 nm, and 784 nm. Meanwhile, the main peak shifts about  $\Delta\lambda_{\text{SH}} = 1.8$  nm. This suggest that indicating that perfect phase matching is realized for the  $w = 1.4$   $\mu\text{m}$  wide SHWG at  $\lambda_{\text{SH}} = 773.8$  nm. Fig. 5.30(b) presents the measured SH power as a function of the investigated SHWG widths. The SH power clearly peaks at  $P_{\text{SH}} = 152$  nW for a  $w = 1.4$   $\mu\text{m}$  wide SHWG and decreases sharply for wider and narrower device lengths. Decreasing the SHWG width to  $w = 1.2$   $\mu\text{m}$  nearly halves the generated SH power. Similarly, the SH power drops to  $P_{\text{SH}} = 97$  nW,  $P_{\text{SH}} = 91$  nW and  $P_{\text{SH}} = 62$  nW for wider SHWGs,  $w = 1.6$   $\mu\text{m}$ ,  $w = 2$   $\mu\text{m}$ , respectively.

Since the  $\text{LiNbO}_3$  is used as a source of the intercalated  $\text{Li}^+$  ions, and it is well-known that such a material, even in a form of crystals, exhibits strong optical nonlinearities. As such, it is important to show that the nonlinear second order optical interaction responsible for SHG occurs in the  $\text{SiN}_x$  waveguide core of the device and not in  $\text{LiNbO}_3$  layer. Accordingly, a similar SHWG but without the ion conducting  $\text{LiNbO}_3$  layer is fabricated and investigated for SHG. The generated SH signal power from the  $\text{LiNbO}_3$  free SHWG of  $P_{\text{SH}} = 156.3$  nW (excited at  $P_{\text{P}} = 50$

mW) is comparable to that from a SHWG having LiNbO<sub>3</sub> layer, thus, confirming that the SHG originates from the SiN<sub>x</sub> waveguide core.

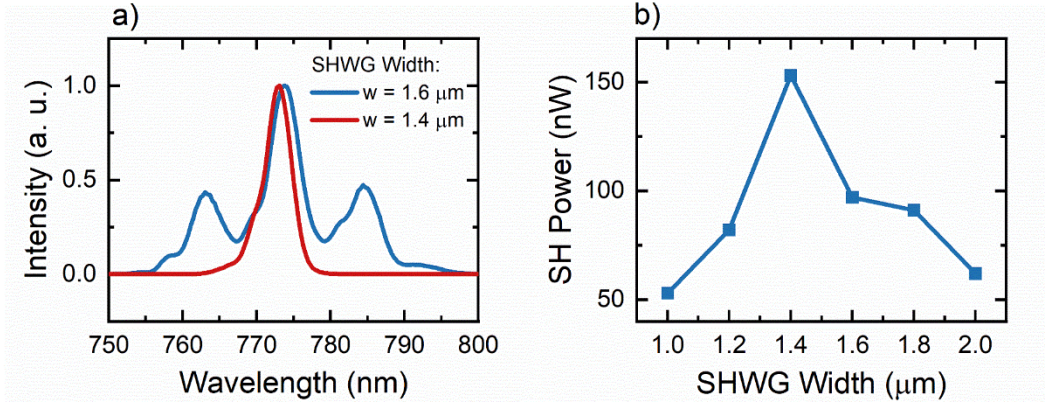


Fig. 5.30: Influence of SHWG width on SH spectrum and power. (a) SH spectra of SHWGs having different widths. (b) SH power as a function of SHWG width.

EC modulation of the generated SH signal is observed in six different SHWG devices exhibiting  $P_{\text{SH}} = 149 \text{ nW} \pm 5.6 \text{ nW}$  at  $C = 0 \text{ mC/cm}^2$  and a wavelength shift of up to  $\Delta\lambda_{\text{SH}} = 3.3 \pm 0.3 \text{ nm}$  during lithiation. The experimentally investigated SHWG having the highest modulation for  $d = 350 \text{ nm}$  spacer layer thickness exhibits a linear wavelength shift of  $\Delta\lambda_{\text{SH}} = 0.179 \text{ nmcm}^2/\text{mC}$  (Fig. 5.31(a)). On the other hand, FDTD simulation results indicate a slightly higher wavelength shift of  $\Delta\lambda_{\text{SH}} = 0.24 \text{ nmcm}^2/\text{mC}$  is expected for such a SHWG. Evidently, several mechanisms can lead to such a reduced wavelength shift dependency on the lithiation level. First, surface roughness and inhomogeneities in the waveguide walls can lead to a widening of the coherence length curve, which in turn leads to reduced  $\Delta\lambda_{\text{SH}}$  as seen for shorter SHWGs. In this case, a wider range of SH is excited, which leads to a smaller shift for the main peak. Next, incomplete Li<sup>+</sup> ion

lithiation reduces the maximum achievable wavelength shift since the maximum refractive index change cannot be achieved. Such a lack of free  $\text{Li}^+$  ions is difficult to overcome in a solid-state device but could be averted by sacrificing switching speed by introducing thicker  $\text{LiNbO}_3$  and  $\text{NiO}$  layers to host more  $\text{Li}^+$  ions in the ECD. Lastly, as experimentally observed for the reduced On-state optical transmission, irreversibly intercalated  $\text{Li}^+$  ions change the refractive index to increase the SH wavelength in the delithiated state permanently and, thereby, decrease the achievable  $\Delta\lambda_{\text{SH}}$ . Hence, the optical transmission modulation in the experiment is between  $T_{\text{ON}} = 0.05$  and  $T_{\text{OFF}} = 7 \times 10^{-4}$  for  $\lambda = 1550$  nm excitation, resulting in  $\Delta T = 71$ , while the simulations suggest On-state optical transmission of  $T_{\text{ON}} = 0.82$  and  $T_{\text{OFF}} = 8.3 \times 10^{-4}$ , leading to  $\Delta T = 10^4$ . Nonetheless, the SH wavelength shift achieved here introduces the first of its kind nonlinear tuning with modulation bandwidths comparable to those devices utilizing thermal effects in  $\text{LiNbO}_3$  ( $\Delta\lambda = 0.84$  nm/K).<sup>111</sup>

To ensure that modulation of the SH signal is achieved through EC modulation rather than heating effects, Fig. 5.31(b) depicts the SH wavelength at peak intensity for a SHWG during lithiation and subsequent delithiation. Clearly, the initial state (i.e., SH generated wavelength at  $\lambda_{\text{SH}} = 773.2$  nm) can be recovered after the redox cycle. Furthermore, both the lithiation and the delithiation curves exhibit the same behavior. At  $C = 12$  mC/cm<sup>2</sup> lithiation, the SH signal shows a wavelength at peak intensity  $\lambda_{\text{SH}}^{\text{L}} = 774.8$  nm during lithiation and  $\lambda_{\text{SH}}^{\text{DL}} = 774.4$  nm during delithiation. Notably, for similar intercalation values, the measured wavelength difference is between  $\lambda_{\text{SH}}^{\text{L}}$  and  $\lambda_{\text{SH}}^{\text{DL}}$  is  $< 0.15$  nm with an outlier at 12 mC/cm<sup>2</sup>

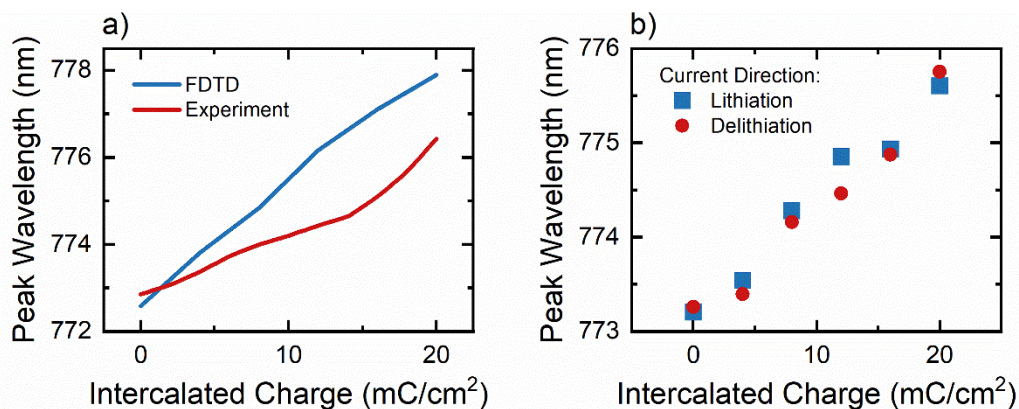


Fig. 5.31: Experimental results for SH wavelength shift as a function of lithiation. (a) Experimentally measured SH wavelength shift in comparison to that from the FDTD simulation. (b) Current flow direction dependence of the induced SH wavelength shift.

$\text{Li}^+$  ion transport, electrical, and the electrochemical properties of the EC active layer within the SHWG are further investigated through spectro-electrochemical CV measurements. The results of redox cycling at  $v = 25$  mV/s voltage sweep rate are shown in Fig. 5.32. Fig. 5.32(a) presents the measured SH wavelength at peak intensity, as well as the transmitted NIR FE intensity during the CV analysis. Evidently, the SH wavelength curve exhibits a hysteretic behavior, which is typical signature for an EC redox cycling mechanism. During lithiation and starting at a voltage of  $V = 1$  V, the generated SH wavelength peak exhibits a weak dependency on the applied voltage as it shifts from  $\lambda_{\text{SH}} = 772.3$  nm at  $V = 1$  V to  $\lambda_{\text{SH}} = 772.5$  nm at  $V = 0$  V. However, this dependency becomes stronger and almost linear for the applied negative potentials reaching a maximum of  $\lambda_{\text{SH}} = 775.4$  nm. During delithiation, the opposite effect is occurring, where excess  $\text{Li}^+$  ions are retained in

WO<sub>3</sub> and accordingly, the SH wavelength shift is small for the applied voltages between  $V = -2$  V and  $V = -0.5$  V before increasing. A similar hysteretic trend is present for the optical transmitted intensity of the NIR FE excitation as a function of the applied voltage. At  $V = 0$ , the maximum transmitted light intensity of  $T = 0.04$  decreases slowly as a function of decreasing voltage before reaching a threshold applied voltage value of  $\sim V = -0.5$  V, after which the transmitted light intensity decreases sharply to  $T = 0$  at  $V = -2$  V and increases back to  $T = 0.04$  as the applied voltage is cycled in reserves. Fig. 5.32(b) depicts the corresponding CV curve shape for a typical WO<sub>3</sub>/NiO layer. Lithiation occurs gradually before a threshold voltage at  $V = -0.5$  V is reached, beyond which, the intercalation current grows rapidly. The CV curve further provides an aerial capacitance  $AC = 2.1$  mF/cm<sup>2</sup> at  $v = 25$  mV/s sweep rate. Here, the lithiation,  $Q_L$ , charge and the delithiation charge,  $Q_{DL}$ , are nearly equal (i.e.,  $\Gamma \approx 0.97$ ), thus, indicating the high electrochemical stability of the SHWG. These results compare well to the ones introduced in section 5.2.3 for the SNWG devices.

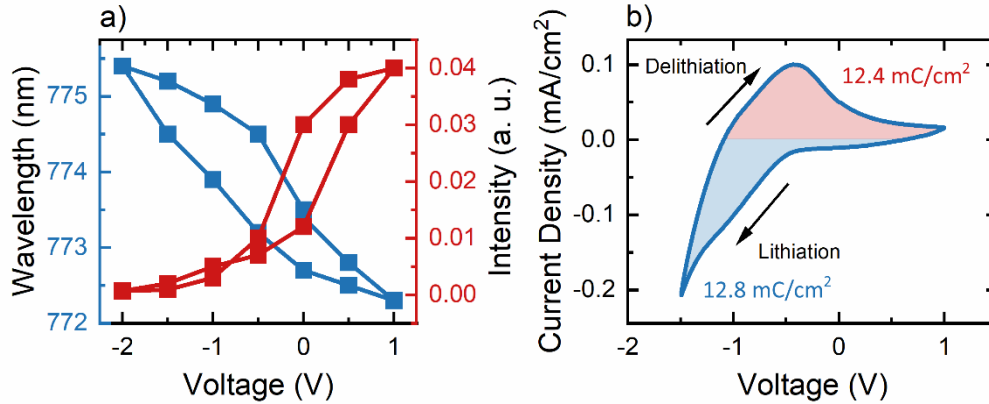


Fig. 5.32: CV analysis of SHWG at  $v = 25$  mV/s sweep rate. (a) SH wavelength at peak intensity, as well as transmitted FE optical intensity as a function of voltage. (b) The corresponding CV curve at a sweep rate of 25 mV/s.

The high electrochemical reversibility is indicative of high retention of the SH wavelength shift modulation over several CV cycles as shown in Fig. 5.33(a). Here, continuous cycling from 0 mC/cm<sup>2</sup> to 20 mC/cm<sup>2</sup> lithiation results in a slight change of the achievable SH wavelength shift modulation, where initially  $\Delta\lambda_{\text{SH}} = 3.7$  nm for the pristine device is slightly reduced to  $\Delta\lambda_{\text{SH}} = 2.4$  nm for the aged device after 1000 CV cycles. Notably though, the SH wavelength at peak intensity for the lithiated state decreases from  $\lambda_{\text{SH}} = 775.9$  nm to  $\lambda_{\text{SH}} = 775.1$  nm within 100 CV cycles. This change is attributed to the Li<sup>+</sup> ions' irreversible intercalation and resulting electrostatic hindrance for the intercalation of Li<sup>+</sup> ions, such that the EC layer does not undergo the full redox cycle. The minimum achievable SH wavelength increases from  $\lambda_{\text{SH}} = 772.1$  nm to  $\lambda_{\text{SH}} = 772.4$  nm over 1000 CV cycles.

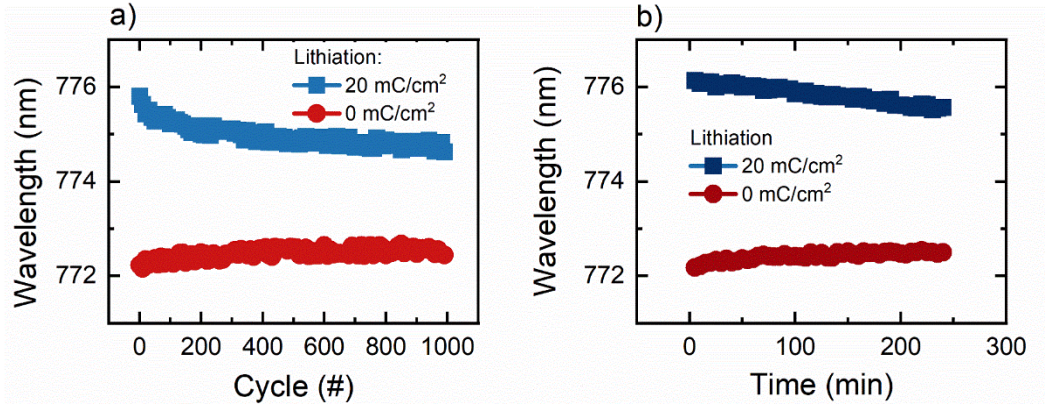


Fig. 5.33: EC behavior of the SHWG over time. (a) SH wavelength at peak intensity depicted as a function of the CV cycles. (b) SH wavelength non-volatile bistability of SHWG after abruptly turning off the applied voltage and measuring the SH signal over time.

The SHWG EC SH wavelength modulation layer is further investigated for its non-volatile bistability. Shown in Fig. 5.33(b) the SH wavelength at peak intensity as SHWG is charged to its maximum (blue) or minimum (red) by applying a potential of  $V = -2$  V and  $V = 1$  V, respectively. The measurement is taken immediately after the applied voltage is turned off. Remarkably, over the course of 4 hrs, the SHWG holds both states extremely well, with the maximum SH wavelength peak in the lithiated state decreasing by only  $\Delta\lambda_{\text{SH}} = 0.35$  nm, while the delithiated SH wavelength peak increases by only  $\Delta\lambda_{\text{SH}} = 0.27$  nm. Both states and the wavelength of the generated SH light change nearly linearly over time, which indicates a continuous deintercalation effect from the respective EC material into LiNbO<sub>3</sub>. Due to its long bistability time, the SHWG offer a novel platform as an

optical memory for nonlinear photonic devices that can be utilized in on-chip computing and telecommunications.

The SHWG switching dynamics are shown in Fig. 5.34. Here, the optical transmittance of the NIR FE excitation beam is modulated by two orders of magnitude, the corresponding wavelength shift of the SH is measured and recorded. The EC switching times for the solid-state SHWG is unprecedented with lithiation and delithiation times being as low as 2.4 s and 0.6 s, respectively, which further affirms that the SH wavelength modulation relates to the intercalation of charges and the EC effect. At the same time, the wavelength at peak intensity for the SH signal can be up and down shifted at the rates of  $R_{SH}^{DL} = -0.32$  nm/s and  $R_{SH}^L = +0.34$  nm/s, respectively. Switching the SH generated wavelength from  $\lambda_{SH} = 776$  nm to  $\lambda_{SH} = 773$  nm is achieved in only 12 s.

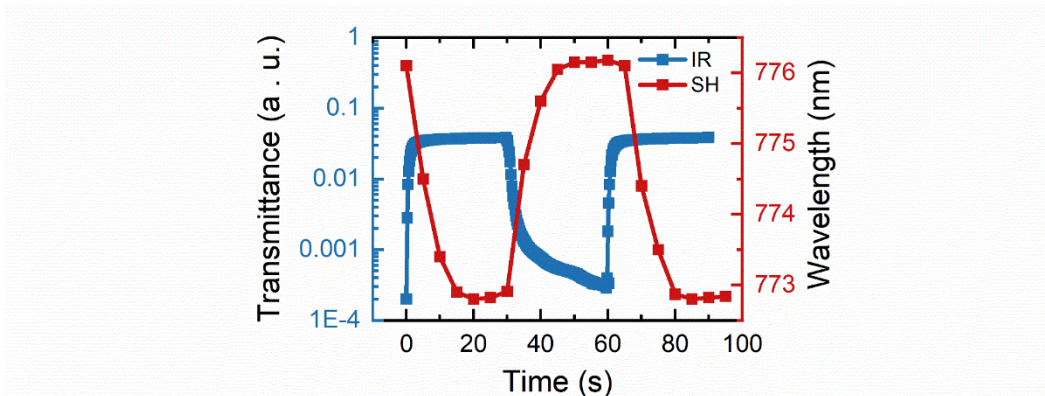


Fig. 5.34: Switching dynamics of the SHWG transmission and SH wavelength. The applied voltage is alternated between  $V = -2$  V and  $V = 1$  V.

To overcome several shortcomings of the all-solid-state SHWG and chart a path towards realizing its full potential in nonlinear optics and photonics, SHWGs without the LiNbO<sub>3</sub> and the NiO layers are investigated. In a similar fashion to the SNWGs presented in Section 5.2, a 1 M LiClO<sub>4</sub> in PC electrolyte is used to investigate and quantify the device's EC modulation behavior. As depicted in Fig. 5.35, when using such a liquid electrolyte, the SH wavelength shift  $\Delta\lambda_{\text{SH}}$  increases at a rate of 0.21 nmcm<sup>2</sup>/mC and reaching  $\Delta\lambda_{\text{SH}} = 4.2$  nm for an intercalated charge of 16 mC/cm<sup>2</sup>. Furthermore, the EC switching of the NIR FE light transmittance increases from  $\Delta T = 70$  for a solid-state device to  $\Delta T = 100$  for the liquid electrolyte. In particular, the higher On-state transmission of  $T = 0.116$  (compared to  $T = 0.05$  for the solid-state device) leads to increased modulation bandwidth of SH wavelength and NIR light transmittance simultaneously. Evidently, the sputtering process of the LiNbO<sub>3</sub> leads to irreversible intercalation that can be eliminated when using liquid electrolytes.

The switching times of the SHWGs without the LiNbO<sub>3</sub> and the NiO layers is shown to be reduced. As measured by NIR FE optical transmission, the time it takes for the sample to reach full lithiation is 1.9 s, where it takes only 0.4 s to reach its delithiation state. Interestingly, by using the liquid electrolyte SHWG, complete penetration of the EC film with Li<sup>+</sup> ions can be achieved. This is evidenced by generating long SH wavelengths up to  $\lambda_{\text{SH}} = 777.1$  nm. However, the liquid electrolyte leads to a faster degradation of the SHWG EC response, with the achievable SH wavelength modulation bandwidth decreasing to  $\Delta\lambda_{\text{SH}} = 2.7$  nm within 30 redox cycles. Such a behavior can be explained by irreversible occupation

of all defect states in the  $\text{WO}_3$  layer that are created during the sputtering process and would have been otherwise occupied when  $\text{LiNbO}_3$  is used as the ion conductor. The degradation of the  $\text{WO}_3$  layer in liquid (i.e.,  $\text{LiClO}_4$  in PC) electrolyte, is evidenced by the measured lower reversibility coefficient of  $\Gamma = 0.91$  in comparison to that for the solid-state  $\text{LiNbO}_3$  electrolyte (i.e.,  $\Gamma = 0.97$ ). Hence, the solid-state SHWG offer better long-term stability, ease of fabrication and easier on-chip integration, but at the cost of slightly lower SH wavelength modulation bandwidth,  $\Delta\lambda_{\text{SH}}$ .

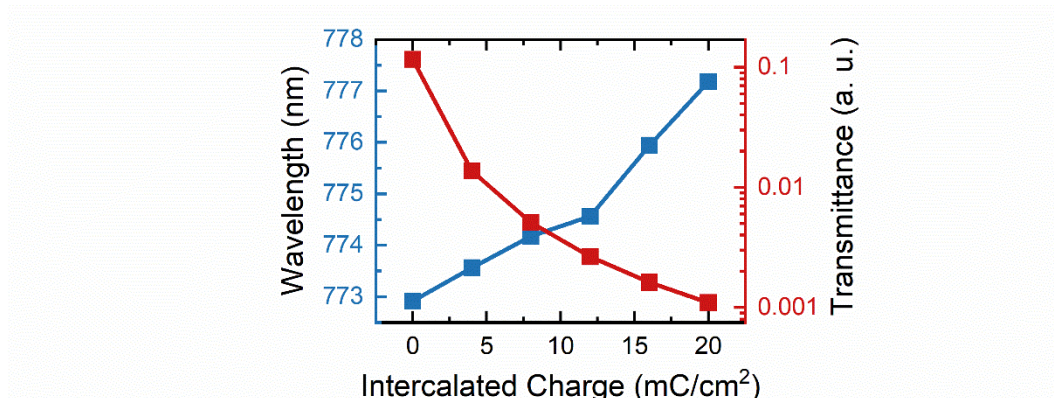


Fig. 5.35: SHWG performance with 1 M  $\text{LiClO}_4$  liquid electrolyte. SH wavelength (blue) and NIR FE transmittance as a function of the intercalated charge.

### 5.3.4 Discussion

The  $\text{LiNbO}_3$  electrolyte SHWG platform offers a multitude of EC modulation features at high optical transmission modulation of  $\Delta T = 10^2$  for the incident NIR light and considerable phase change needed for phase matching nonlinear optical

processes. While there are no direct competitors, one can compare the SHWG platform performance having a theoretical modulation bandwidth of  $\Delta\lambda_{\text{SH}} = 21.25$  nm (i.e., for a  $d = 200$  nm thick spacer) with a similar thermal wavelength modulation waveguide based on  $\text{LiNbO}_3$ , where the wavelength shift bandwidth of  $\Delta\lambda_{\text{SH}} = 17.5$  nm.<sup>111</sup> The experimentally measured SH wavelength shift dependency on the  $\text{Li}^+$  ion intercalation of  $\Delta\lambda_{\text{SH}} = 0.179$  nmcm<sup>2</sup>/mC for 350 nm spacer thickness indicates a strong dependence of SH signal on electrochemical environment. Such a feature can be utilized for sensitive sensing ion applications for creating multiple wavelengths via nonlinear optical mixing for on-chip computation.

The incomplete intercalation of  $\text{Li}^+$  ions, as well as the reduced On-state optical transmission could be explained by the solid-state electrolyte and the finite amount of excess  $\text{Li}^+$  in the device. Clearly, the solid-state  $\text{LiNbO}_3$  electrolyte allows for longevity functionality of the device, making it superior to the liquid electrolyte. Hence, improvements to the solid-state electrolyte are necessary to enhance the optical transmission and the SH wavelength modulation bandwidth.

## 5.4 Summary

In this chapter, the potential of EC modulation in nanophotonic waveguides for sensor and nonlinear optics applications is explored. Utilized in combination with low-loss Silicon Nitride waveguide cores, the introduced device design with off-center electrical contacts and  $\text{SiO}_2$  cladding shows ultra-high modulation depth for NIR optical transmission and offers an unprecedented platform for dynamically modulating the phase-matching criterion for nonlinear optics devices. The

introduced SNWG device for Na<sup>+</sup> ion detection is shown to exhibit the highest optical transmission modulation (i.e.,  $\Delta T = 10^7$ ) and unprecedented sub-second EC switching times in comparison to any EC powered photonic device. Furthermore, the device platform allows detection of Na<sup>+</sup> ion concentrations between 1 mM and 1 M in volumes as low as 20  $\mu$ l. Owing to the high optical modulation bandwidth, real time ion concentration measurements for integrated microfluidics are possible.

In the all-solid-state LiNbO<sub>3</sub> electrolyte SHWG architecture, the modulation depth is  $\Delta T < 10^2$  for the NIR FE excitation; however, the direct influence of the EC layers on the effective refractive index of the propagating modes allows for dynamic modulation of the nonlinear properties of the waveguide. The fabricated SHWGs exhibits up to  $\Delta\lambda_{SH} = 3.6$  nm SH wavelength modulation bandwidth with sensitivities of 0.179 nmcm<sup>2</sup>/mC. Moreover, the employed EC materials within the SHWG reliably hold their oxidation state for more than 4 hrs. Such non-volatile bistability of an optical nonlinear process can be exploited for optical memory applications.

The demonstrated device platform for active control of the nonlinear properties of a SiN<sub>x</sub> waveguide is unprecedented. Nonetheless, improvements in material composition and fabrication process could be made to increase SH wavelength tunability and wavelength modulation speed. We envision that the investigated EC materials to become a staple for integrated photonic devices, especially considering their low operating voltages  $V < \pm 2$  V and potential for non-volatile bistability.

# Chapter 6

## Conclusion & Outlook

The investigations presented in this thesis explore the integration of EC materials, specifically  $\text{WO}_3$ , in nanophotonic and nanoplasmonic devices. To achieve versatile and integrated EC optical modulation functionalities, a variety of device designs are introduced to exploit plasmonic and photonic, resonant effects to enhance the EC effect.

Synthesis and deposition of EC  $\text{WO}_3$  and NiO from wet and dry chemical methods is effectively compared in terms of morphological and electrochemical properties for application in nanophotonic and plasmonic platforms. Furthermore, chemical stability and spectro-electrochemical properties of these oxides are evaluated to infer the optimum material properties. Ionic conductors, such as the all-solid-state  $\text{LiNbO}_3$ , polymeric PMMA and polyacrylamide hydrogels are synthesized and deposited and their interplay with the EC materials is investigated. Such comprehensive studies lay the groundwork for application of the EC  $\text{WO}_3$  in a novel, dual-ion battery architecture with a quasi-solid electrolyte. This smart wearable battery is based on a DMSO-modified hydrogel electrolyte having a remarkably prolonged lifetime. Moreover, a simple, yet highly effective, way to enhance the lifetime of EC materials in otherwise detrimental environments, is introduced by means of self-assembly of a phosphate monolayer.

The fundamental properties of the EC materials and ion conductors are then exploited in resonant and nonresonant plasmochromic devices, utilizing different aspects of the significant change of the dielectric properties of  $\text{WO}_3$  upon redox ion intercalation. In the Kretschmann configuration for surface plasmon polariton coupling, efficient optical modulation of the resonant coupling angle is shown to alter the resonance coupling angle by  $\sim 1.1^\circ$ . Furthermore, the dynamic change in dielectric environment allows for the merger of an optical hysteresis with resistive switching of the employed ECD for potential EC memory-plasmonic platform. In a nonresonant approach, a NIR laser beam is free space coupled to an MIM type plasmonic waveguide having a  $\text{LiNbO}_3$  core that serves as the propagation medium as well as act as an ion conductor. In this arrangement, based on the strong localization of the plasmon mode to the electrode-dielectric interface, an only 50 nm thick  $\text{WO}_3$  film achieves nearly 38 dB optical modulation. The device design further increases EC switching speed by decoupling the light propagation path and ion conduction direction and making them perpendicular to each other. It is shown that FDTD simulations, based on experimentally determined material properties, can accurately predict device behavior. Thus, FDTD simulations are used to predict the optical properties of a resonant nanocavity when combined with a plasmonic nanohole superstructure. Through combination of the cavity reflectance and the LSPR effect of the NHA, highly chromatic colors are produced. The EC optical modulation through ion intercalation allows shifting of the said colors spanning the range of 105 nm from the red to the green color wavelengths, while consuming a power of only  $5.6 \text{ mW/cm}^2$  with high retention.

To utilize the EC optical modulation in waveguiding architectures, two distinct experiments make use of the dynamic extinction and refractive index respectively. Through a novel device architecture, which utilizes the intrinsic conductivity of  $\text{WO}_3$  to place electrical contacts away from the waveguide's core, high On-set optical transmission of up to 50% is achieved. Used in a liquid  $\text{Na}^+$  electrolyte, the Silicon Nitride based waveguiding platform utilizes the dynamic extinction and, thus, exhibits unprecedented ultrahigh optical modulation of  $10^7$  at sub-second switching times. Such a novel device can detect the concentration of  $\text{Na}^+$  ions in the electrolyte between  $C = 1 \text{ mM}$  and  $C = 1 \text{ M}$  at 90% accuracy and, hence, it offers a great potential for applications involving real-time ion sensing. When utilized for the change in refractive index, an all-solid state ECD fabricated on top of the waveguiding core leads to a change in the nonlinear properties of such an arrangement. The change in refractive index in the ECD leads to change in the effective refractive index for the optical mode propagating along the waveguide which, in turn, alters the phase matching conditions for SHG for unprecedented wavelength tunability and enhanced nonlinear second order optical conversion efficiency. While theoretically achieving up to  $\Delta\lambda_{\text{SH}} = 21.25 \text{ nm}$  SH wavelength shift, several conditions have to be met to experience such a large spectral shift. Experimentally, a linear wavelength shift  $\Delta\lambda_{\text{SH}} = 0.179 \text{ nmcm}^2/\text{mC}$  for  $d = 350 \text{ nm}$   $\text{SiO}_2$  spacer thickness between waveguide core and ECD is achieved. Such a shift is extraordinary and exhibits strong bistability for more than 4hs. Hence, the platform developed here is believed to have potential for novel, low operating voltage, dynamic nanophotonic applications. As the first of its kind EC, photonic

device, it is envisioned to pave the way for the development of integrated phase modulation and sensing applications.

## 6.1 Future Directions

Chapter 3 considered the solid-state ion conductor  $\text{LiNbO}_3$  as well as polymeric ion conductors. It was shown that  $\text{LiNbO}_3$  provides the high chemical and mechanical stability necessary for nanofabrication steps, while the other material exhibited better ion dynamics and flexibility. Due to the higher conductivity in PMMA and polyacrylamide-based electrolytes, their integration into nanoplasmonic or nanophotonic ECDs could further increase switching speed and optical transmission modulation for color printing and optical transmission modulation. For such devices to be realized, simple methodologies and processes for their integration into nanofabrication process need to be investigated.

Chapter 4 laid out the results for integration of EC  $\text{WO}_3$  thin films in plasmonic devices. It was shown that the EC effect is an efficacious way for manipulating the plasmonic resonance of SPPs in planar metal films as well LSPRs in nanostructures. However, the high coupling losses combined with the EC optical modulation led to low propagation lengths for SPPs. Devices based on low loss plasmonic films could help to increase the optical modulation depth and the propagation length. To overcome obstacles of full color tunability and device integration of plasmochromic color displays, solid-state approaches need to be further investigated.

Chapter 5 described how EC modulation in nanophotonics can directly influence optical transmittance and phase of propagating optical modes. For

sensing applications,  $\text{WO}_3$  ion sensor waveguides could be easily integrated into microfluidic devices to investigate the potential for real time ion concentration detection. Furthermore, for nonlinear optics applications, the use of highly nonlinear materials, such as  $\text{LiNbO}_3$  single crystals could increase the achievable SHG. Hence, nonlinear waveguides based on  $\text{LiNbO}_3$  and incorporating an EC modulation layer should be investigated. Replacing  $\text{WO}_3$  with polymer EC materials could increase switching speeds but would most definitely lead to shorter lifetime and faster degradation of the EC based device.

## 6.2 Outlook

Through the work conducted and documented in this thesis, the field of nanoscale ECDs has been advanced tremendously. Plasmochromic color devices as well as photochromic waveguides for ion sensing and nonlinear optics explored the EC effect as a tool for dynamic resonance effects and pushed the boundaries for EC device integration. However, further investigation into ionic conductors for high-speed EC switching could provide the means necessary to bring EC modulation to every-day life devices. Hence, the concepts and devices introduced here can be seen as the foundation on which to build a whole class of dynamic ECDs beyond smart windows applications.

Going forward, we expect that plasmochromic color devices can show the lifetimes and switching speeds necessary to replace e-ink readers and electronic paper. Additionally, the integration of such a technology with polymeric and flexible ion conductors promises colorful and dynamic electronic skin and wearable

smart devices. Especially the introduction of other plasmonic materials besides Au could support the development of blue or UV plasmonic resonances. Moreover, the inherent energy storage properties of EC materials inspire colorful and vibrant flexible battery and supercapacitor platforms.

Within this work, this thesis expanded the rudimentary field of EC nanophotonics by providing an avenue for the design of low insertion and propagation loss waveguides based on CMOS compatible Silicon Nitride. The photochromic waveguides exhibit unprecedented optical transmission modulation paired with the potential for dynamic nonlinear devices. We envision such a platform to compete with thermal means of waveguide manipulation and pave a way for on-chip EC optical modulation where low voltage operation and bistability are absolute necessities.

# Thesis Publication List (as January 10<sup>th</sup>, 2023)

This section lists the refereed journals and conference papers published during this thesis work.

## Journal Papers

Publications resulting from this thesis:

- (J1) E. Hopmann, B. Y. Shahriar, and A. Y. Elezzabi, “On-chip high ion sensitivity electrochromic nanophotonic light modulator,” *Nanoscale*, vol. 14, no. 17, pp. 6526–6534, 2022, doi: 10.1039/d2nr00646d.
- (J2) E. Hopmann, B. N. Carnio, C. J. Firby, B. Y. Shahriar, and A. Y. Elezzabi, “Nanoscale All-Solid-State Plasmochromic Waveguide Nonresonant Modulator,” *Nano Letters*, vol. 21, no. 15, pp. 1955–1961, Feb. 2021, doi: 10.1021/acs.nanolett.0c04315.
- (J3) E. Hopmann and A. Y. Elezzabi, “Plasmochromic Nanocavity Dynamic Light Color Switching,” *Nano Letters*, vol. 20, no. 3, pp. 1876–1882, 2020, doi: 10.1021/acs.nanolett.9b05088.
- (J4) E. Hopmann and A. Y. Elezzabi, “Electrochemical Stability Enhancement of Electrochromic Tungsten Oxide by Self-Assembly of a Phosphonate Protection Layer,” *ACS Applied Materials & Interfaces*, vol. 12, pp. 1930–1936, 2020, doi: 10.1021/acsami.9b19961.
- (J5) E. Hopmann, H. Li, and A. Y. Elezzabi, “Rechargeable Zn<sup>2+</sup>/Al<sup>3+</sup> dual-ion electrochromic device with long life time utilizing dimethyl sulfoxide (DMSO)-nanocluster modified hydrogel electrolytes” *RSC Advances*, vol. 9, no. 64, 2019, doi: 10.1039/c9ra90083g.

Publications with relevance to the thesis material:

- (J6) W. Zhang, H. Li, E. Hopmann, and A. Y. Elezzabi, “Nanostructured inorganic electrochromic materials for light applications,” *Nanophotonics*, vol. 10, no. 2, pp. 825–850, 2020, doi: 10.1515/nanoph-2020-0474.

## Conference Papers

- (C1) E. Hopmann *et al.*, “Electrochromic photonic devices for nanoplasmonic transmission modulation,” vol. 12002, no. 5, pp. 14–20, Mar. 2022, doi: 10.1117/12.2606654.
- (C2) E. Hopmann *et al.*, “Plasmonic electrochromic nanodevices for color and transmission modulation,” <https://doi.org/10.1117/12.2576701>, vol. 11684, no. 5, pp. 21–27, Mar. 2021, doi: 10.1117/12.2576701.
- (C3) E. Hopmann, H. Li, A. Elezzabi, A. Y. Elezzabi, H. Eric, and E. Adulhakem, “Dual-ion electrochromic battery with long lifetime based on dimethyl sulfoxide (DMSO)-nanocluster modified hydrogel electrolytes,” <https://doi.org/10.1117/12.2544020>, vol. 11281, no. 5, pp. 142–148, Mar. 2020, doi: 10.1117/12.2544020.

# References

- (1) Granqvist, C. G. Electrochromism and Smart Window Design. *Solid State Ion* **1992**, 53–56 (PART 1), 479–489. [https://doi.org/10.1016/0167-2738\(92\)90418-O](https://doi.org/10.1016/0167-2738(92)90418-O).
- (2) Mortimer, R. J.; Rosseinsky, D. R.; Monk, P. M. S. *Handbook of Stimuli-Responsive Materials*.
- (3) Chua, M. H.; Tang, T.; Ong, K. H.; Neo, W. T.; Xu, J. W. Chapter 1. Introduction to Electrochromism. In *Electrochromism and Electrochromic Devices*; Cambridge University Press: Cambridge, 2019; pp 1–21. <https://doi.org/10.1039/9781788016667-00001>.
- (4) Zhang, W.; Li, H.; Hopmann, E.; Elezzabi, A. Y. Nanostructured Inorganic Electrochromic Materials for Light Applications. *Nanophotonics* **2020**, 10 (2), 825–850. <https://doi.org/10.1515/nanoph-2020-0474>.
- (5) Camurlu, P. Polypyrrole Derivatives for Electrochromic Applications. *RSC Adv* **2014**, 4 (99), 55832–55845. <https://doi.org/10.1039/c4ra11827h>.
- (6) Li, H.; Firby, C. J.; Elezzabi, A. Y. Rechargeable Aqueous Hybrid Zn<sup>2+</sup>/Al<sup>3+</sup> Electrochromic Batteries. *Joule* **2019**, 3 (9), 2268–2278. <https://doi.org/10.1016/j.joule.2019.06.021>.
- (7) Granqvist, C. G.; Arvizu, M. A.; Qu, H.-Y.; Wen, R.-T.; Niklasson, G. A. Advances in Electrochromic Device Technology: Multiple Roads towards Superior Durability. *Surf Coat Technol* **2019**, 357 (April 2018), 619–625. <https://doi.org/10.1016/j.surfcoat.2018.10.048>.
- (8) Li, H.; McRae, L.; Firby, C. J.; Al-Hussein, M.; Elezzabi, A. Y. Nanohybridization of Molybdenum Oxide with Tungsten Molybdenum Oxide Nanowires for Solution-Processed Fully Reversible Switching of Energy Storing Smart Windows. *Nano Energy* **2018**, 47 (March), 130–139. <https://doi.org/10.1016/j.nanoen.2018.02.043>.
- (9) Tarver, J. D.; Sezen-Edmonds, M.; Yoo, J. E.; Loo, Y. L. *Organic Electronic Devices with Water-Dispersible Conducting Polymers*; Elsevier Ltd., 2019; Vol. 1–5. <https://doi.org/10.1016/B978-0-12-803581-8.11235-4>.
- (10) Deb, S. K. Reminiscences on the Discovery of Electrochromic Phenomena in Transition Metal Oxides. *Solar Energy Materials and Solar Cells* **1995**, 39 (2–4), 191–201. [https://doi.org/10.1016/0927-0248\(95\)00055-0](https://doi.org/10.1016/0927-0248(95)00055-0).

- (11) Granqvist, C. G. Electrochromics for Smart Windows: Oxide-Based Thin Films and Devices. *Thin Solid Films* **2014**, *564*, 1–38. <https://doi.org/10.1016/j.tsf.2014.02.002>.
- (12) Yang, C.; Chen, J.-F.; Zeng, X.; Cheng, D.; Cao, D. Design of the Alkali-Metal-Doped WO<sub>3</sub> as a Near-Infrared Shielding Material for Smart Window. *Ind Eng Chem Res* **2014**, *53* (46), 17981–17988. <https://doi.org/10.1021/ie503284x>.
- (13) Runnerstrom, E. L.; Llordés, A.; Lounis, S. D.; Milliron, D. J. Nanostructured Electrochromic Smart Windows: Traditional Materials and NIR-Selective Plasmonic Nanocrystals. *Chem. Commun.* **2014**, *50* (73), 10555–10572. <https://doi.org/10.1039/C4CC03109A>.
- (14) Granqvist, C.-G. Electrochromic Metal Oxides: An Introduction to Materials and Devices. In *Electrochromic Materials and Devices*; Wiley-VCH Verlag GmbH & Co. KGaA: Weinheim, Germany, 2015; pp 1–40. <https://doi.org/10.1002/9783527679850.ch1>.
- (15) Xu, J.; Zhang, Y.; Zhai, T. T.; Kuang, Z.; Li, J.; Wang, Y.; Gao, Z.; Song, Y. Y.; Xia, X. H. Electrochromic-Tuned Plasmonics for Photothermal Sterile Window. *ACS Nano* **2018**, *12* (7), 6895–6903. <https://doi.org/10.1021/acsnano.8b02292>.
- (16) Goldner, R. Thin Film Solid State Ionic Materials for Electrochromic Smart Window™ Glass. *Solid State Ion* **1988**, *28–30* (PART 2), 1715–1721. [https://doi.org/10.1016/0167-2738\(88\)90448-1](https://doi.org/10.1016/0167-2738(88)90448-1).
- (17) Runnerstrom, E. L.; Llordés, A.; Lounis, S. D.; Milliron, D. J. Nanostructured Electrochromic Smart Windows: Traditional Materials and NIR-Selective Plasmonic Nanocrystals. *Chem. Commun.* **2014**, *50* (73), 10555–10572. <https://doi.org/10.1039/C4CC03109A>.
- (18) Fang, H.; Zheng, P.; Ma, R.; Xu, C.; Yang, G.; Wang, Q.; Wang, H. Multifunctional Hydrogel Enables Extremely Simplified Electrochromic Devices for Smart Windows and Ionic Writing Boards. *Mater Horiz* **2018**, *5* (5), 1000–1007. <https://doi.org/10.1039/C8MH00856F>.
- (19) Lee, H. J.; Lee, C.; Song, J.; Yun, Y. J.; Jun, Y.; Ah, C. S. Electrochromic Devices Based on Ultraviolet-Cured Poly(Methyl Methacrylate) Gel Electrolytes and Their Utilisation in Smart Window Applications. *J Mater Chem C Mater* **2020**, *8* (26), 8747–8754. <https://doi.org/10.1039/D0TC00420K>.
- (20) Wang, J.; Zhang, L.; Yu, L.; Jiao, Z.; Xie, H.; Lou, X. W.; Wei Sun, X. A Bi-Functional Device for Self-Powered Electrochromic Window and Self-Rechargeable Transparent Battery Applications. *Nat Commun* **2014**, *5* (1), 4921. <https://doi.org/10.1038/ncomms5921>.

- (21) Zhang, S.; Cao, S.; Zhang, T.; Fisher, A.; Lee, J. Y. Al<sup>3+</sup> Intercalation/de-Intercalation-Enabled Dual-Band Electrochromic Smart Windows with a High Optical Modulation, Quick Response and Long Cycle Life. *Energy Environ Sci* **2018**, *11* (10), 2884–2892. <https://doi.org/10.1039/c8ee01718b>.
- (22) Virbickas, P.; Valiūnienė, A.; Ramanavičius, A. Towards Electrochromic Ammonium Ion Sensors. *Electrochem Commun* **2018**, *94* (June), 41–44. <https://doi.org/10.1016/j.elecom.2018.08.002>.
- (23) de Matteis, V.; Cannavale, A.; Blasi, L.; Quarta, A.; Gigli, G. Chromogenic Device for Cystic Fibrosis Precocious Diagnosis: A “Point of Care” Tool for Sweat Test. *Sens Actuators B Chem* **2016**, *225*, 474–480. <https://doi.org/10.1016/j.snb.2015.11.080>.
- (24) Aller Pellitero, M.; del Campo, F. J. Electrochromic Sensors: Innovative Devices Enabled by Spectroelectrochemical Methods. *Curr Opin Electrochem* **2019**, *15*, 66–72. <https://doi.org/10.1016/j.coelec.2019.03.004>.
- (25) Xu, W.; Fu, K.; Bohn, P. W. Electrochromic Sensor for Multiplex Detection of Metabolites Enabled by Closed Bipolar Electrode Coupling. *ACS Sens* **2017**, *2* (7), 1020–1026. <https://doi.org/10.1021/acssensors.7b00292>.
- (26) Chow, E.; Liana, D. D.; Raguse, B.; Gooding, J. J. A Potentiometric Sensor for PH Monitoring with an Integrated Electrochromic Readout on Paper. *Aust J Chem* **2017**, *70* (9), 979. <https://doi.org/10.1071/CH17191>.
- (27) Park, H.; Kim, D. S.; Hong, S. Y.; Kim, C.; Yun, J. Y.; Oh, S. Y.; Jin, S. W.; Jeong, Y. R.; Kim, G. T.; Ha, J. S. A Skin-Integrated Transparent and Stretchable Strain Sensor with Interactive Color-Changing Electrochromic Displays. *Nanoscale* **2017**, *9* (22). <https://doi.org/10.1039/c7nr02147j>.
- (28) Zhang, F.; Cai, T.; Ma, L.; Zhan, L.; Liu, H. A Paper-Based Electrochromic Array for Visualized Electrochemical Sensing. *Sensors (Switzerland)* **2017**, *17* (2), 1–10. <https://doi.org/10.3390/s17020276>.
- (29) Kim, J. T.; Song, J.; Ah, C. S. Optically Readable Waveguide-Integrated Electrochromic Artificial Synaptic Device for Photonic Neuromorphic Systems. *ACS Appl Electron Mater* **2020**, *2* (7), 2057–2063. <https://doi.org/10.1021/acsaelm.0c00314>.
- (30) Agrawal, A.; Susut, C.; Stafford, G.; Bertocci, U.; McMorran, B.; Lezec, H. J.; Talin, A. A. An Integrated Electrochromic Nanoplasmonic Optical Switch. *Nano Lett* **2011**, *11* (7), 2774–2778. <https://doi.org/10.1021/nl201064x>.
- (31) Kim, J. T.; Song, J.; Ryu, H.; Ah, C. S. Electrochromic Infrared Light Modulation in Optical Waveguides. *Adv Opt Mater* **2020**, *8* (1), 1–8. <https://doi.org/10.1002/adom.201901464>.

- (32) Wang, Z.; Wang, X.; Cong, S.; Chen, J.; Sun, H.; Chen, Z.; Song, G.; Geng, F.; Chen, Q.; Zhao, Z. Towards Full-Colour Tunability of Inorganic Electrochromic Devices Using Ultracompact Fabry-Perot Nanocavities. *Nat Commun* **2020**, *11* (1), 302. <https://doi.org/10.1038/s41467-019-14194-y>.
- (33) Peng, J.; Jeong, H.-H.; Lin, Q.; Cormier, S.; Liang, H.-L.; de Volder, M. F. L.; Vignolini, S.; Baumberg, J. J. Scalable Electrochromic Nanopixels Using Plasmonics. *Sci Adv* **2019**, *5* (5), 1–9. <https://doi.org/10.1126/sciadv.aaw2205>.
- (34) Stec, G. J.; Lauchner, A.; Cui, Y.; Nordlander, P.; Halas, N. J. Multicolor Electrochromic Devices Based on Molecular Plasmonics. *ACS Nano* **2017**, *11* (3), 3254–3261. <https://doi.org/10.1021/acsnano.7b00364>.
- (35) Li, Y.; van de Groep, J.; Talin, A. A.; Brongersma, M. L. Dynamic Tuning of Gap Plasmon Resonances Using a Solid-State Electrochromic Device. *Nano Lett* **2019**, *19* (11), 7988–7995. <https://doi.org/10.1021/acs.nanolett.9b03143>.
- (36) Zhang, S.; Feng, L.; Zhang, H.; Liu, M.; Xu, T. Electrochromic Modulation of Plasmonic Resonance in a PEDOT-Coated Nanodisk Metasurface. *Opt Mater Express* **2020**, *10* (4), 1053. <https://doi.org/10.1364/ome.390052>.
- (37) Li, H.; McRae, L.; Elezzabi, A. Y. Solution-Processed Interfacial PEDOT:PSS Assembly into Porous Tungsten Molybdenum Oxide Nanocomposite Films for Electrochromic Applications. *ACS Appl Mater Interfaces* **2018**, *10* (12), 10520–10527. <https://doi.org/10.1021/acsami.7b18310>.
- (38) Hu, L.; Kim, H. S.; Lee, J.; Peumans, P.; Cui, Y. Scalable Coating and Properties of Transparent, Flexible, Silver Nanowire Electrodes. *ACS Nano* **2010**, *4* (5), 2955–2963. <https://doi.org/10.1021/nn1005232>.
- (39) Shen, L.; Du, L.; Tan, S.; Zang, Z.; Zhao, C.; Mai, W. Flexible Electrochromic Supercapacitor Hybrid Electrodes Based on Tungsten Oxide Films and Silver Nanowires. *Chemical Communications* **2016**, *52* (37), 6296–6299. <https://doi.org/10.1039/C6CC01139J>.
- (40) Neo, W. T.; Chua, M. H.; Xu, J. W. Chapter 2. Fundamentals of Electrochromic Materials and Devices. In *RSC Smart Materials*; 2019; Vol. 2019-Janua, pp 22–50. <https://doi.org/10.1039/9781788016667-00022>.
- (41) Lee, S. H.; Tracy, C. E.; Yan, Y.; Pitts, J. R.; Deb, S. K. Solid-State Nanocomposite Electrochromic Pseudocapacitors. *Electrochemical and Solid-State Letters* **2005**, *8* (4), 188–191. <https://doi.org/10.1149/1.1861050>.
- (42) Chen, Y.; Wang, Y.; Sun, P.; Yang, P.; Du, L.; Mai, W. Nickel Oxide Nanoflake-Based Bifunctional Glass Electrodes with Superior Cyclic

- Stability for Energy Storage and Electrochromic Applications. **2015**.  
<https://doi.org/10.1039/c5ta04011f>.
- (43) Yang, P.; Sun, P.; Chai, Z.; Huang, L.; Cai, X.; Tan, S.; Song, J.; Mai, W. Large-Scale Fabrication of Pseudocapacitive Glass Windows That Combine Electrochromism and Energy Storage. *Angewandte Chemie International Edition* **2014**, *53* (44), 11935–11939. <https://doi.org/10.1002/anie.201407365>.
- (44) Cai, G.; Darmawan, P.; Cui, M.; Wang, J.; Chen, J.; Magdassi, S.; Lee, P. S. Highly Stable Transparent Conductive Silver Grid/PEDOT:PSS Electrodes for Integrated Bifunctional Flexible Electrochromic Supercapacitors. *Adv Energy Mater* **2016**, *6* (4). <https://doi.org/10.1002/AENM.201501882>.
- (45) Chen, J.; Wang, Z.; Chen, Z.; Cong, S.; Zhao, Z. Fabry–Perot Cavity-Type Electrochromic Supercapacitors with Exceptionally Versatile Color Tunability. *Nano Lett* **2020**, *20* (3), 1915–1922. <https://doi.org/10.1021/acs.nanolett.9b05152>.
- (46) Jeong, C. Y.; Kubota, T.; Tajima, K. Flexible Electrochromic Devices Based on Tungsten Oxide and Prussian Blue Nanoparticles for Automobile Applications. *RSC Adv* **2021**, *11* (46), 28614–28620. <https://doi.org/10.1039/D1RA05280B>.
- (47) Wei, D.; Scherer, M. R. J.; Bower, C.; Andrew, P.; Ryhänen, T.; Steiner, U. A Nanostructured Electrochromic Supercapacitor. *Nano Lett* **2012**, *12* (4), 1857–1862. <https://doi.org/10.1021/nl2042112>.
- (48) Li, H.; McRae, L.; Firby, C. J.; Al-Hussein, M.; Elezzabi, A. Y. Nanohybridization of Molybdenum Oxide with Tungsten Molybdenum Oxide Nanowires for Solution-Processed Fully Reversible Switching of Energy Storing Smart Windows. *Nano Energy* **2018**, *47*, 130–139. <https://doi.org/10.1016/J.NANOEN.2018.02.043>.
- (49) Lee, S. H.; Tracy, C. E.; Yan, Y.; Pitts, J. R.; Deb, S. K. Solid-State Nanocomposite Electrochromic Pseudocapacitors. *Electrochemical and Solid-State Letters* **2005**, *8* (4), 188–191. <https://doi.org/10.1149/1.1861050>.
- (50) Li, H.; Firby, C. J.; Elezzabi, A. Y. Rechargeable Aqueous Hybrid Zn<sup>2+</sup>/Al<sup>3+</sup> Electrochromic Batteries. *Joule* **2019**, *3* (9), 2268–2278. <https://doi.org/10.1016/j.joule.2019.06.021>.
- (51) Zhao, J.; Tian, Y.; Wang, Z.; Cong, S.; Zhou, D.; Zhang, Q.; Yang, M.; Zhang, W.; Geng, F.; Zhao, Z. Trace H<sub>2</sub>O<sub>2</sub>-Assisted High-Capacity Tungsten Oxide Electrochromic Batteries with Ultrafast Charging in Seconds. *Angewandte Chemie International Edition* **2016**, *55* (25), 7161–7165. <https://doi.org/10.1002/ANIE.201602657>.

- (52) Miyata, M.; Hatada, H.; Takahara, J. Full-Color Subwavelength Printing with Gap-Plasmonic Optical Antennas. *Nano Lett* **2016**, *16* (5), 3166–3172. <https://doi.org/10.1021/acs.nanolett.6b00500>.
- (53) Gu, Y.; Zhang, L.; Yang, J. K. W.; Yeo, S. P.; Qiu, C. W. Color Generation via Subwavelength Plasmonic Nanostructures. *Nanoscale*. Royal Society of Chemistry 2015, pp 6409–6419. <https://doi.org/10.1039/c5nr00578g>.
- (54) Leroux, Y. R.; Lacroix, J. C.; Chane-Ching, K. I.; Fave, C.; Félidj, N.; Lévi, G.; Aubard, J.; Krenn, J. R.; Hohenau, A. Conducting Polymer Electrochemical Switching as an Easy Means for Designing Active Plasmonic Devices. *J Am Chem Soc* **2005**, *127* (46), 16022–16023. <https://doi.org/10.1021/ja054915v>.
- (55) Leroux, Y.; Lacroix, J. C.; Fave, C.; Trippe, G.; Fé, N.; Aubard, J.; Hohenau, A.; Krenn, J. R. Tunable Electrochemical Switch of the Optical Properties of Metallic Nanoparticles. **2008**. <https://doi.org/10.1021/nn700438a>.
- (56) Stockhausen, V.; Martin, P.; Ghilane, J.; Leroux, Y.; Randriamahazaka, H.; Grand, J.; Felidj, N.; Lacroix, J. C. Giant Plasmon Resonance Shift Using Poly(3,4-Ethylenedioxythiophene) Electrochemical Switching. *J Am Chem Soc* **2010**, *132* (30), 10224–10226. <https://doi.org/10.1021/ja103337d>.
- (57) Wang, Z.; Chumanov, G. WO<sub>3</sub> Sol-Gel Modified Ag Nanoparticle Arrays for Electrochemical Modulation of Surface Plasmon Resonance. *Advanced Materials* **2003**, *15* (15), 1285–1289. <https://doi.org/10.1002/adma.200304989>.
- (58) Jiang, N.; Shao, L.; Wang, J.; Jiang, N. N.; Shao, L.; Wang, J. F. (Gold Nanorod Core)/(Polyaniline Shell) Plasmonic Switches with Large Plasmon Shifts and Modulation Depths. *Advanced Materials* **2014**, *26* (20), 3282–3289. <https://doi.org/10.1002/ADMA.201305905>.
- (59) Yin, A.; He, Q.; Lin, Z.; Luo, L.; Liu, Y.; Yang, S.; Wu, H.; Ding, M.; Huang, Y.; Duan, X. Plasmonic/Nonlinear Optical Material Core/Shell Nanorods as Nanoscale Plasmon Modulators and Optical Voltage Sensors. *Angewandte Chemie - International Edition* **2016**, *55* (2), 583–587. <https://doi.org/10.1002/ANIE.201508586>.
- (60) Jeon, J.-W.; Ledin, P. A.; Geldmeier, J. A.; Ponder, J. F.; Mahmoud, M. A.; El-Sayed, M.; Reynolds, J. R.; Tsukruk, V. v. Electrically Controlled Plasmonic Behavior of Gold Nanocube@Polyaniline Nanostructures: Transparent Plasmonic Aggregates. *Chem. Mater* **2016**, *28*. <https://doi.org/10.1021/acs.chemmater.6b00882>.
- (61) Xu, T.; Walter, E. C.; Agrawal, A.; Bohn, C.; Velmurugan, J.; Zhu, W.; Lezec, H. J.; Talin, A. A. High-Contrast and Fast Electrochromic Switching

Enabled by Plasmonics. *Nat Commun* **2016**, *7*, 10479. <https://doi.org/10.1038/ncomms10479>.

- (62) Lu, W.; Chow, T. H.; Lai, S. N.; Zheng, B.; Wang, J. Electrochemical Switching of Plasmonic Colors Based on Polyaniline-Coated Plasmonic Nanocrystals. *ACS Appl Mater Interfaces* **2020**, *12* (15), 17733–17744. <https://doi.org/10.1021/acsami.0c01562>.
- (63) Kammler, D. R.; Yelton, W. G.; Sweatt, W. C.; Verley, J. C. Use of Electrochromic Materials in Adaptive Optics. In *SPIE Conference Proceedings*; Valley, M. T., Vorontsov, M. A., Eds.; SPIE, 2005; Vol. 5895, p 58950S. <https://doi.org/10.1117/12.621397>.
- (64) Blaich, J. D.; Kammler, D. R.; Ambrosini, A.; Sweatt, W. C.; Verley, J. C.; Heller, E. J.; Yelton, W. G. A Tunable Electrochromic Fabry-Perot Filter for Adaptive Optics Applications. **2006**. <https://doi.org/10.2172/895983>.
- (65) Junesch, J.; Sannomiya, T.; Dahlin, A. B. Optical Properties of Nanohole Arrays in Metal-Dielectric Double Films Prepared by Mask-on-Metal Colloidal Lithography. *ACS Nano* **2012**, *6* (11), 10405–10415. <https://doi.org/10.1021/nm304662e>.
- (66) Debbrecht, B.; McElhiney, M.; Carey, V.; Cullen, C.; Mirotznik, M. S.; DeLacy, B. G. Cavity-Based Aluminum Nanohole Arrays with Tunable Infrared Resonances. *Opt Express* **2017**, *25* (20), 24501. <https://doi.org/10.1364/OE.25.024501>.
- (67) Najiminaini, M.; Vasefi, F.; Kaminska, B.; Carson, J. J. L. Nanohole-Array-Based Device for 2D Snapshot Multispectral Imaging. **2013**. <https://doi.org/10.1038/srep02589>.
- (68) Xiong, K.; Emilsson, G.; Maziz, A.; Yang, X.; Shao, L.; Jager, E. W. H.; Dahlin, A. B. Plasmonic Metasurfaces with Conjugated Polymers for Flexible Electronic Paper in Color. *Advanced Materials* **2016**, *28* (45), 9956–9960. <https://doi.org/10.1002/adma.201603358>.
- (69) Xiong, K.; Tordera, D.; Emilsson, G.; Olsson, O.; Linderhed, U.; Jonsson, M. P.; Dahlin, A. B. Switchable Plasmonic Metasurfaces with High Chromaticity Containing Only Abundant Metals. *Nano Lett* **2017**, *17* (11), 7033–7039. <https://doi.org/10.1021/acs.nanolett.7b03665>.
- (70) Gugole, M.; Olsson, O.; Xiong, K.; Blake, J. C.; Montero Amenedo, J.; Bayrak Pehlivan, I.; Niklasson, G. A.; Dahlin, A. High-Contrast Switching of Plasmonic Structural Colors: Inorganic versus Organic Electrochromism. *ACS Photonics* **2020**, *7* (7), 1762–1772. <https://doi.org/10.1021/acsp Photonics.0c00394>.

- (71) Chen, J.; Wang, Z.; Chen, Z.; Cong, S.; Zhao, Z. Fabry–Perot Cavity-Type Electrochromic Supercapacitors with Exceptionally Versatile Color Tunability. *Nano Lett* **2020**, *20* (3), 1915–1922. <https://doi.org/10.1021/acs.nanolett.9b05152>.
- (72) Chen, J.; Wang, Z.; Liu, C.; Chen, Z.; Tang, X.; Wu, Q.; Zhang, S.; Song, G.; Cong, S.; Chen, Q.; Zhao, Z.; Chen, J.; Wang, Z.; Liu, C. L.; Chen, Z. G.; Tang, X. Q.; Wu, Q.; Zhang, S.; Song, G.; Cong, S.; Zhao, Z. G.; Chen, Q. Mimicking Nature’s Butterflies: Electrochromic Devices with Dual-Sided Differential Colorations. *Advanced Materials* **2021**, *33* (14), 2007314. <https://doi.org/10.1002/ADMA.202007314>.
- (73) Tang, X.; Chen, J.; Wang, Z.; Hu, Z.; Song, G.; Zhang, S.; Chen, Z.; Wu, Q.; Liu, M.; Cong, S.; Zhao, Z. Vibrant Color Palettes of Electrochromic Manganese Oxide Electrodes for Colorful Zn-Ion Battery. *Adv Opt Mater* **2021**, *9* (19). <https://doi.org/10.1002/ADOM.202100637>.
- (74) Wu, Q.; Wang, X.; Sun, P.; Wang, Z.; Chen, J.; Chen, Z.; Song, G.; Liu, C.; Mu, X.; Cong, S.; Zhao, Z. Electrochromic Metamaterials of Metal–Dielectric Stacks for Multicolor Displays with High Color Purity. *Nano Lett* **2021**, *21* (16), 6891–6897. <https://doi.org/10.1021/acs.nanolett.1c02030>.
- (75) Lee, Y.; Yun, J.; Seo, M.; Kim, S.-J.; Oh, J.; Kang, C. M.; Sun, H.-J.; Chung, T. D.; Lee, B. Full-Color-Tunable Nanophotonic Device Using Electrochromic Tungsten Trioxide Thin Film. *Nano Lett* **2020**, *20* (8), 6084–6090. <https://doi.org/10.1021/acs.nanolett.0c02097>.
- (76) Redel, E.; Mlynarski, J.; Moir, J.; Jelle, A.; Huai, C.; Petrov, S.; Helander, M. G.; Peiris, F. C.; von Freymann, G.; Ozin, G. A. Electrochromic Bragg Mirror: ECBM. *Advanced Materials* **2012**, *24* (35), 265–269. <https://doi.org/10.1002/adma.201202484>.
- (77) Chen, J.; Li, Y.; Zhang, T.; Zha, X.; Tang, X.; Mu, X.; Sun, P.; Song, G.; Cong, S.; Chen, Q.; Zhao, Z. Reversible Active Switching of Fano and Fabry–Pérot Resonances by Electrochromic Operation. *Laser Photon Rev* **2022**, 2200303. <https://doi.org/10.1002/LPOR.202200303>.
- (78) Rossi, S.; Jonsson, M. P. Highly Reflective Optical Nanocavities for Structural Coloration by Combining Broadband Absorber and Fabry–Pérot Effects. *Journal of Optics* **2021**, *23* (1), 015001. <https://doi.org/10.1088/2040-8986/abccfe>.
- (79) Gugole, M.; Olsson, O.; Rossi, S.; Jonsson, M. P.; Dahlin, A. Electrochromic Inorganic Nanostructures with High Chromaticity and Superior Brightness. *Nano Lett* **2021**, *21* (10), 4343–4350. <https://doi.org/10.1021/acs.nanolett.1c00904>.

- (80) Flöry, N.; Ma, P.; Salamin, Y.; Emboras, A.; Taniguchi, T.; Watanabe, K.; Leuthold, J.; Novotny, L. Waveguide-Integrated van Der Waals Heterostructure Photodetector at Telecom Wavelengths with High Speed and High Responsivity. *Nature Nanotechnology* **2020**, *15* (2), 118–124. <https://doi.org/10.1038/s41565-019-0602-z>.
- (81) Hopmann, E.; Elezzabi, A. Y. Plasmochromic Nanocavity Dynamic Light Color Switching. *Nano Lett* **2020**, *20* (3), 1876–1882. <https://doi.org/10.1021/acs.nanolett.9b05088>.
- (82) Zhang, H.; Zhou, L.; Rahman, B. M. A.; Wu, X.; Lu, L.; Xu, Y.; Xu, J.; Song, J.; Hu, Z.; Xu, L.; Chen, J. Ultracompact Si-GST Hybrid Waveguides for Nonvolatile Light Wave Manipulation. *IEEE Photonics J* **2018**, *10* (1), 1–10. <https://doi.org/10.1109/JPHOT.2017.2781710>.
- (83) Olivares, I.; Sánchez, L.; Parra, J.; Larrea, R.; Griol, A.; Menghini, M.; Homm, P.; Jang, L.-W.; van Bilzen, B.; Seo, J. W.; Locquet, J.-P.; Sanchis, P. Optical Switching in Hybrid VO<sub>2</sub>/Si Waveguides Thermally Triggered by Lateral Microheaters. *Opt Express* **2018**, *26* (10), 12387. <https://doi.org/10.1364/OE.26.012387>.
- (84) Jung, Y.; Han, H.; Sharma, A.; Jeong, J.; Parkin, S. S. P.; Poon, J. K. S. Integrated Hybrid VO<sub>2</sub>-Silicon Optical Memory. *ACS Photonics* **2022**, *9* (1), 217–223. <https://doi.org/10.1021/acsphotonics.1c01410>.
- (85) Hallman, K. A.; Miller, K. J.; Baydin, A.; Weiss, S. M.; Haglund, R. F.; Hallman, K. A.; Baydin, A.; Miller, K. J.; Weiss, S. M.; Haglund, R. F. Sub-Picosecond Response Time of a Hybrid VO<sub>2</sub>:Silicon Waveguide at 1550 Nm. *Adv Opt Mater* **2021**, *9* (4), 2001721. <https://doi.org/10.1002/ADOM.202001721>.
- (86) Clark, J. K.; Ho, Y. L.; Matsui, H.; Delaunay, J. J. Optically Pumped Hybrid Plasmonic-Photonic Waveguide Modulator Using the VO<sub>2</sub> Metal-Insulator Phase Transition. *IEEE Photonics J* **2018**, *10* (1). <https://doi.org/10.1109/JPHOT.2017.2784429>.
- (87) Ríos, C.; Du, Q.; Zhang, Y.; Popescu, C.-C.; Shalaginov, M. Y.; Miller, P.; Roberts, C.; Kang, M.; Richardson, K. A.; Gu, T.; Vitale, S. A.; Hu, J. Ultra-Compact Nonvolatile Phase Shifter Based on Electrically Reprogrammable Transparent Phase Change Materials. *ArXiv* **2021**.
- (88) Datta, I.; Chae, S. H.; Bhatt, G. R.; Tadayon, M. A.; Li, B.; Yu, Y.; Park, C.; Park, J.; Cao, L.; Basov, D. N.; Hone, J.; Lipson, M. Low-Loss Composite Photonic Platform Based on 2D Semiconductor Monolayers. *Nat Photonics* **2020**, *14* (4), 256–262. <https://doi.org/10.1038/s41566-020-0590-4>.
- (89) Tian, R.; Gan, X.; Li, C.; Chen, X.; Hu, S.; Gu, L.; van Thourhout, D.; Castellanos-Gomez, A.; Sun, Z.; Zhao, J. Chip-Integrated van Der Waals PN

Heterojunction Photodetector with Low Dark Current and High Responsivity. *Light Sci Appl* **2022**, *11* (1), 101. <https://doi.org/10.1038/s41377-022-00784-x>.

- (90) Ma, P.; Flöry, N.; Salamin, Y.; Baeuerle, B.; Emboras, A.; Josten, A.; Taniguchi, T.; Watanabe, K.; Novotny, L.; Leuthold, J. Fast MoTe<sub>2</sub> Waveguide Photodetector with High Sensitivity at Telecommunication Wavelengths. *ACS Photonics* **2018**, *5* (5), 1846–1852. <https://doi.org/10.1021/acsp Photonics.8b00068>.
- (91) Wang, G.; Deng, W.; Chen, X.; Wang, P.; Xiao, Y.; Li, J.; Chu, F.; Liu, B.; Chen, Y.; Lu, Y.; Sui, M.; Liu, Z.; Diao, X.; Yan, H.; Zhang, Y. Transition Metal Dichalcogenides Thyristor Realized by Solid Ionic Conductor Gate Induced Doping. *Appl Phys Lett* **2020**, *117* (5), 053102. <https://doi.org/10.1063/5.0017432>.
- (92) Mehew, J. D.; Unal, S.; Torres Alonso, E.; Jones, G. F.; Fadhil Ramadhan, S.; Craciun, M. F.; Russo, S. Fast and Highly Sensitive Ionic-Polymer-Gated WS<sub>2</sub>-Graphene Photodetectors. *Advanced Materials* **2017**, *29* (23). <https://doi.org/10.1002/ADMA.201700222>.
- (93) Braga, D.; Gutiérrez, I.; Lezama, G.; Berger, H.; Morpurgo, A. F. Quantitative Determination of the Band Gap of WS<sub>2</sub> with Ambipolar Ionic Liquid-Gated Transistors. *Nano Lett* **2012**, *12*, 3. <https://doi.org/10.1021/nl302389d>.
- (94) Cong, C.; Shang, J.; Wang, Y.; Yu, T. Optical Properties of 2D Semiconductor WS<sub>2</sub>. *Adv Opt Mater* **2018**, *6* (1). <https://doi.org/10.1002/ADOM.201700767>.
- (95) Sorianello, V.; Midrio, M.; Contestabile, G.; Asselberghs, I.; van Campenhout, J.; Huyghebaert, C.; Goykhman, I.; Ott, A. K.; Ferrari, A. C.; Romagnoli, M. Graphene-Silicon Phase Modulators with Gigahertz Bandwidth. *Nature Photonics* **2017**, *12* (1), 40–44. <https://doi.org/10.1038/s41566-017-0071-6>.
- (96) Jia, L.; Wu, J.; Zhang, Y.; Qu, Y.; Jia, B.; Chen, Z.; Moss, D. J.; Jia, L.; Wu, J.; Zhang, Y.; Qu, Y.; Moss, D. J.; Jia, B.; Chen, Z. Fabrication Technologies for the On-Chip Integration of 2D Materials. *Small Methods* **2022**, *6* (3), 2101435. <https://doi.org/10.1002/SMTD.202101435>.
- (97) Page, R. H.; Jurich, M. C.; Reck, B.; Sen, A.; Twieg, R. J.; Swalen, J. D.; Bjorklund, G. C.; Willson, C. G. Electrochromic and Optical Waveguide Studies of Corona-Poled Electro-Optic Polymer Films. *Journal of the Optical Society of America B* **1990**, *7* (7), 1239. <https://doi.org/10.1364/JOSAB.7.001239>.

- (98) Piraud, C.; Mwarania, E. K.; Yao, J.; O'Dwyer, K.; Schiffrin, D. J.; Wilkinson, J. S. Optoelectrochemical Transduction on Planar Optical Waveguides. *Journal of Lightwave Technology* **1992**, *10* (5), 693–699. <https://doi.org/10.1109/50.136106>.
- (99) O'Brien, N. A.; Mathew, J. G. H.; Hichwa, B. P. An Electrochromic Variable Optical Attenuator (ECVOA). In *OFC/IOOC . Technical Digest. Optical Fiber Communication Conference, 1999, and the International Conference on Integrated Optics and Optical Fiber Communication*; IEEE, 1999; p PD26/1-PD26/3. <https://doi.org/10.1109/OFC.1999.766059>.
- (100) Cowin, M. A.; Varrazza, R.; Morgan, C.; Penty, R. V.; White, I. H.; McDonagh, A. M.; Bayly, S.; Riley, J.; Ward, M. D.; McCleverty, J. A. Low Power Electrochromic Variable Optical Attenuator with 50dB Attenuation Range. In *OFC 2001. Optical Fiber Communication Conference and Exhibit. Technical Digest Postconference Edition (IEEE Cat. 01CH37171)*; Opt. Soc. America, 2001; Vol. 3, pp WR6-1–3. <https://doi.org/10.1109/OFC.2001.928393>.
- (101) Agrawal, A.; Susut, C.; Stafford, G.; Bertocci, U.; McMorran, B.; Lezec, H. J.; Talin, A. A. An Integrated Electrochromic Nanoplasmonic Optical Switch. *Nano Lett* **2011**, *11* (7), 2774–2778. <https://doi.org/10.1021/nl201064x>.
- (102) Kim, J.; Inamdar, A. I.; Jo, Y.; Woo, H.; Cho, S.; Pawar, S. M.; Kim, H.; Im, H. Effect of Electronegativity on Bipolar Resistive Switching in a WO<sub>3</sub> - Based Asymmetric Capacitor Structure. *ACS Appl Mater Interfaces* **2016**, *8* (14), 9499–9505. <https://doi.org/10.1021/acsami.5b11781>.
- (103) Won, S.; Lee, S. Y.; Park, J.; Seo, H. Forming-Less and Non-Volatile Resistive Switching in WOX by Oxygen Vacancy Control at Interfaces. *Sci Rep* **2017**, *7* (1), 10186. <https://doi.org/10.1038/s41598-017-10851-8>.
- (104) Guo, J.; Zhou, Y.; Yuan, H.; Zhao, D.; Yin, Y.; Hai, K.; Peng, Y.; Zhou, W.; Tang, D. Reconfigurable Resistive Switching Devices Based on Individual Tungsten Trioxide Nanowires. *AIP Adv* **2013**, *3* (4). <https://doi.org/10.1063/1.4804067>.
- (105) Li, Y. T.; Long, S. B.; Lü, H. B.; Liu, Q.; Wang, Q.; Wang, Y.; Zhang, S.; Lian, W. T.; Liu, S.; Liu, M. Investigation of Resistive Switching Behaviours in WO<sub>3</sub>-Based RRAM Devices. *Chinese Physics B* **2011**, *20* (1), 017305. <https://doi.org/10.1088/1674-1056/20/1/017305>.
- (106) Yang, J. T.; Ge, C.; Du, J. Y.; Huang, H. Y.; He, M.; Wang, C.; Lu, H. bin; Yang, G. Z.; Jin, K. J. Artificial Synapses Emulated by an Electrolyte-Gated Tungsten-Oxide Transistor. *Advanced Materials* **2018**, *30* (34). <https://doi.org/10.1002/ADMA.201801548>.

- (107) Xu, J.; Zhang, Y.; Zhai, T. T.; Kuang, Z.; Li, J.; Wang, Y.; Gao, Z.; Song, Y. Y.; Xia, X. H. Electrochromic-Tuned Plasmonics for Photothermal Sterile Window. *ACS Nano* **2018**, *12* (7), 6895–6903. <https://doi.org/10.1021/acsnano.8b02292>.
- (108) Puckett, M. W.; Sharma, R.; Lin, H.-H.; Yang, M.; Vallini, F.; Fainman, Y. Observation of Second-Harmonic Generation in Silicon Nitride Waveguides through Bulk Nonlinearities. *Opt Express* **2016**, *24* (15), 16923. <https://doi.org/10.1364/oe.24.016923>.
- (109) Hickstein, D. D.; Carlson, D. R.; Mundoor, H.; Khurgin, J. B.; Srinivasan, K.; Westly, D.; Kowligy, A.; Smalyukh, I. I.; Diddams, S. A.; Papp, S. B. Self-Organized Nonlinear Gratings for Ultrafast Nanophotonics. *Nat Photonics* **2019**, *13* (7), 494–499. <https://doi.org/10.1038/s41566-019-0449-8>.
- (110) Wang, L.; Xie, W.; van Thourhout, D.; Zhang, Y.; Yu, H.; Wang, S. Nonlinear Silicon Nitride Waveguides Based on PECVD Deposition Platform. *Opt Express* **2018**, *26* (8), 9645. <https://doi.org/10.1364/oe.26.009645>.
- (111) Luo, R.; He, Y.; Liang, H.; Li, M.; Lin, Q. Highly Tunable Efficient Second-Harmonic Generation in a Lithium Niobate Nanophotonic Waveguide. *Optica* **2018**, *5* (8), 1006. <https://doi.org/10.1364/OPTICA.5.001006>.
- (112) Granqvist, C. G. Electrochromics for Smart Windows: Oxide-Based Thin Films and Devices. *Thin Solid Films* **2014**, *564*, 1–38. <https://doi.org/10.1016/j.tsf.2014.02.002>.
- (113) Patel, K. J.; Bhatt, G. G.; Ray, J. R.; Suryavanshi, P.; Panchal, C. J. All-Inorganic Solid-State Electrochromic Devices: A Review. *Journal of Solid State Electrochemistry* **2017**, *21* (2), 337–347. <https://doi.org/10.1007/s10008-016-3408-z>.
- (114) Rai, V.; Singh, R. S.; Blackwood, D. J.; Zhili, D. A Review on Recent Advances in Electrochromic Devices: A Material Approach. *Adv Eng Mater* **2020**, *22* (8), 1–23. <https://doi.org/10.1002/adem.202000082>.
- (115) Jittiarporn, P.; Badilescu, S.; al Sawafta, M. N.; Sikong, L.; Truong, V.-V. Electrochromic Properties of Sol–Gel Prepared Hybrid Transition Metal Oxides – A Short Review. *Journal of Science: Advanced Materials and Devices* **2017**, *2* (3), 286–300. <https://doi.org/10.1016/j.jsamd.2017.08.005>.
- (116) Granqvist, C. G. Electrochromic Materials: Microstructure, Electronic Bands, and Optical Properties. *Applied Physics A Solids and Surfaces* **1993**, *57* (1), 3–12. <https://doi.org/10.1007/BF00331209>.

- (117) Hopmann, E.; Carnio, B. N.; Firby, C. J.; Shahriar, B. Y.; Elezzabi, A. Y. Nanoscale All-Solid-State Plasmonic Waveguide Nonresonant Modulator. *Nano Lett* **2021**, *21* (5), 1955–1961. <https://doi.org/10.1021/acs.nanolett.0c04315>.
- (118) Granqvist, C. Electrochromic Oxides: A Bandstructure Approach. *Solar Energy Materials and Solar Cells* **1994**, *32* (4), 369–382. [https://doi.org/10.1016/0927-0248\(94\)90100-7](https://doi.org/10.1016/0927-0248(94)90100-7).
- (119) Niklasson, G. A.; Granqvist, C. G. Electrochromics for Smart Windows: Thin Films of Tungsten Oxide and Nickel Oxide, and Devices Based on These. *J. Mater. Chem.* **2007**, *17* (2), 127–156. <https://doi.org/10.1039/B612174H>.
- (120) Kido, R.; Ueno, K.; Iwata, K.; Kitazawa, Y.; Imaizumi, S.; Mandai, T.; Dokko, K.; Watanabe, M. Li<sup>+</sup> Ion Transport in Polymer Electrolytes Based on a Glyme-Li Salt Solvate Ionic Liquid. *Electrochim Acta* **2015**, *175*, 5–12. <https://doi.org/10.1016/j.electacta.2015.01.067>.
- (121) Che, X.; Wu, Z.; Dong, G.; Diao, X.; Zhou, Y.; Guo, J.; Dong, D.; Wang, M. Properties of All-Thin-Film Glass/ITO/WO<sub>3</sub>:H/Ta<sub>2</sub>O<sub>5</sub>/NiOx/ITO Electrochromic Devices Prepared by Magnetron Sputtering. *Thin Solid Films* **2018**, *662*, 6–12. <https://doi.org/10.1016/j.tsf.2018.07.005>.
- (122) Reddy, M. R.; Berkowitz, M. Temperature Dependence of Conductance of the Li<sup>+</sup>, Cs<sup>+</sup>, and Cl<sup>-</sup> Ions in Water: Molecular Dynamics Simulation. *J Chem Phys* **1988**, *88* (11), 7104–7110. <https://doi.org/10.1063/1.454360>.
- (123) Atak, G.; Coşkun, Ö. D. LiNbO<sub>3</sub> Thin Films for All-Solid-State Electrochromic Devices. *Opt Mater (Amst)* **2018**, *82* (May), 160–167. <https://doi.org/10.1016/j.optmat.2018.05.062>.
- (124) Yuan, Y. F.; Xia, X. H.; Wu, J. B.; Chen, Y. B.; Yang, J. L.; Guo, S. Y. Enhanced Electrochromic Properties of Ordered Porous Nickel Oxide Thin Film Prepared by Self-Assembled Colloidal Crystal Template-Assisted Electrodeposition. *Electrochim Acta* **2011**, *56* (3), 1208–1212. <https://doi.org/10.1016/j.electacta.2010.10.097>.
- (125) Li, H.; McRae, L.; Firby, C. J.; Elezzabi, A. Y. Rechargeable Aqueous Electrochromic Batteries Utilizing Ti-Substituted Tungsten Molybdenum Oxide Based Zn<sup>2+</sup> Ion Intercalation Cathodes. *Advanced Materials* **2019**, *1807065*, 1807065. <https://doi.org/10.1002/adma.201807065>.
- (126) Wang, D.; Li, H.; Liu, Z.; Tang, Z.; Liang, G.; Mo, F.; Yang, Q.; Ma, L.; Zhi, C. A Nanofibrillated Cellulose/Polyacrylamide Electrolyte-Based Flexible and Sewable High-Performance Zn–MnO<sub>2</sub> Battery with Superior Shear Resistance. *Small* **2018**, *1803978*, 1–10. <https://doi.org/10.1002/smll.201803978>.

- (127) Kim, C.-C.; Lee, H.-H.; Oh, K. H.; Sun, J.-Y. Highly Stretchable, Transparent Ionic Touch Panel. *Science (1979)* **2016**, *353* (6300), 682–687. <https://doi.org/10.1126/science.aaf8810>.
- (128) Bai, Y.; Chen, B.; Xiang, F.; Zhou, J.; Wang, H.; Suo, Z. Transparent Hydrogel with Enhanced Water Retention Capacity by Introducing Highly Hydratable Salt. *Appl Phys Lett* **2014**, *105* (15), 151903 1-5. <https://doi.org/10.1063/1.4898189>.
- (129) Guo, Y.; Zhou, X.; Tang, Q.; Bao, H.; Wang, G.; Saha, P. A Self-Healable and Easily Recyclable Supramolecular Hydrogel Electrolyte for Flexible Supercapacitors. *J Mater Chem A Mater* **2016**, *4* (22), 8769–8776. <https://doi.org/10.1039/c6ta01441k>.
- (130) Virya, A.; Lian, K. Polyacrylamide-Lithium Chloride Polymer Electrolyte and Its Applications in Electrochemical Capacitors. *Electrochem Commun* **2017**, *74*, 33–37. <https://doi.org/10.1016/j.elecom.2016.11.014>.
- (131) Hopmann, E.; Li, H.; Elezzabi, A. Y. Rechargeable Zn<sup>2+</sup>/Al<sup>3+</sup> Dual-Ion Electrochromic Device with Long Life Time Utilizing Dimethyl Sulfoxide (DMSO)-Nanocluster Modified Hydrogel Electrolytes. *RSC Adv* **2019**, *9* (55), 32047–32057. <https://doi.org/10.1039/c9ra06785j>.
- (132) Lim, Y. S.; Jung, H. A.; Hwang, H. Fabrication of PEO-PMMA-LiClO<sub>4</sub>-Based Solid Polymer Electrolytes Containing Silica Aerogel Particles for All-Solid-State Lithium Batteries. *Energies (Basel)* **2018**, *11* (10). <https://doi.org/10.3390/en11102559>.
- (133) Wang, J. Y.; Wang, M. C.; Jan, D. J. Synthesis of Poly(Methyl Methacrylate)-Succinonitrile Composite Polymer Electrolyte and Its Application for Flexible Electrochromic Devices. *Solar Energy Materials and Solar Cells* **2017**, *160* (October 2016), 476–483. <https://doi.org/10.1016/j.solmat.2016.11.009>.
- (134) Zhang, J.; Zhao, N.; Zhang, M.; Li, Y.; Chu, P. K.; Guo, X.; Di, Z.; Wang, X.; Li, H. Flexible and Ion-Conducting Membrane Electrolytes for Solid-State Lithium Batteries: Dispersion of Garnet Nanoparticles in Insulating Polyethylene Oxide. *Nano Energy* **2016**, *28*, 447–454. <https://doi.org/10.1016/j.nanoen.2016.09.002>.
- (135) Yap, Y. L.; You, A. H.; Teo, L. L.; Hanapei, H. Inorganic Filler Sizes Effect on Ionic Conductivity in Polyethylene Oxide (PEO) Composite Polymer Electrolyte. *Int J Electrochem Sci* **2013**, *8* (2), 2154–2163.
- (136) Hu, X. L.; Hou, G. M.; Zhang, M. Q.; Rong, M. Z.; Ruan, W. H.; Giannelis, E. P. A New Nanocomposite Polymer Electrolyte Based on Poly(Vinyl Alcohol) Incorporating Hypergrafted Nano-Silica. *J Mater Chem* **2012**, *22* (36), 18961–18967. <https://doi.org/10.1039/c2jm33156j>.

- (137) Heitjans, P.; Tobschall, E.; Wilkening, M. Ion Transport and Diffusion in Nanocrystalline and Glassy Ceramics. *European Physical Journal: Special Topics* **2008**, *161* (1), 97–108. <https://doi.org/10.1140/epjst/e2008-00753-4>.
- (138) Karuppasamy, A.; Subrahmanyam, A. Studies on Electrochromic Smart Windows Based on Titanium Doped WO<sub>3</sub> Thin Films. *Thin Solid Films* **2007**, *516* (2–4), 175–178. <https://doi.org/10.1016/j.tsf.2007.07.163>.
- (139) Deb, S. K. A Novel Electrophotographic System. *Appl Opt* **1969**, *8* (101), 192–195. <https://doi.org/10.1364/AO.8.S1.000192>.
- (140) Shimizu, I.; Shizukuishi, M.; Inoue, E. Solid-State Electrochromic Device Consisting of Amorphous WO<sub>3</sub> and Cr<sub>2</sub>O<sub>3</sub>. *J Appl Phys* **1979**, *50*, 4027. <https://doi.org/10.1063/1.326483>.
- (141) Ol, J. L.; Gordon, J.; Mathew, H.; Sapers, S. P.; Cumbo, M. J.; O'brien, N. A.; Sargent, R. B.; Raksha, V. P.; Lahaderne, R. B.; Hichwa, B. P. Large Area Electrochromics for Architectural Applications. *J Non Cryst Solids* **1997**, *218*, 342–346.
- (142) Nagai, J.; McMeeking, G. D.; Saitoh, Y. Durability of Electrochromic Glazing. *Solar Energy Materials and Solar Cells* **1999**, *56* (3–4), 309–319. [https://doi.org/10.1016/S0927-0248\(98\)00140-8](https://doi.org/10.1016/S0927-0248(98)00140-8).
- (143) Tajima, K.; Yamada, Y.; Bao, S.; Okada, M.; Yoshimura, K. Near Colorless All-Solid-State Switchable Mirror Based on Magnesium-Titanium Thin Film. *J Appl Phys* **2008**, *103* (1), 013512. <https://doi.org/10.1063/1.2829816>.
- (144) Niwa, T.; Takai, O. Optical and Electrochemical Properties of All-Solid-State Transmittance-Type Electrochromic Devices. *Thin Solid Films* **2010**, *518* (6), 1722–1727. <https://doi.org/10.1016/J.TSF.2009.11.062>.
- (145) Wang, R.; Pan, L.; Han, Q.; Zhu, H.; Wan, M.; Mai, Y. Reactively Sputtered Ta<sub>2</sub>O<sub>5</sub> Solid Electrolyte Layers in All Thin Film Electrochromic Devices. *J Alloys Compd* **2021**, *865*, 158931. <https://doi.org/10.1016/J.JALLCOM.2021.158931>.
- (146) Goldner, R. Thin Film Solid State Ionic Materials for Electrochromic Smart Window™ Glass. *Solid State Ion* **1988**, *28–30* (PART 2), 1715–1721. [https://doi.org/10.1016/0167-2738\(88\)90448-1](https://doi.org/10.1016/0167-2738(88)90448-1).
- (147) Goldner, R. B.; Arntz, F. O.; Berera, G.; Haas, T. E.; Wei, G.; Wong, K. K.; Yu, P. C. A Monolithic Thin-Film Electrochromic Window. *Solid State Ion* **1992**, *53–56* (PART 1), 617–627. [https://doi.org/10.1016/0167-2738\(92\)90438-U](https://doi.org/10.1016/0167-2738(92)90438-U).

- (148) Ashrit, P. v; Benaissa, I. L.; Bader, G.; Girouard, F. E.; Truong, V.-V. Lithiation Studies on Some Transition Metal Oxides for an All-Solid Thin Film Electrochromic System. *Solid State Ion* **1993**, *59*, 47–57.
- (149) Daneo, A.; Macrelli, G.; Polato, P.; Poli, E. Photometric Characterization of an All Solid State Inorganic Electrochromic Large Area Device. *Solar Energy Materials and Solar Cells* **1999**, *56* (3–4), 237–248. [https://doi.org/10.1016/S0927-0248\(98\)00134-2](https://doi.org/10.1016/S0927-0248(98)00134-2).
- (150) Liu, Q.; Dong, G.; Xiao, Y.; Gao, F.; Wang, M.; Wang, Q.; Wang, S.; Zuo, H.; Diao, X. An All-Thin-Film Inorganic Electrochromic Device Monolithically Fabricated on Flexible PET/ITO Substrate by Magnetron Sputtering. *Mater Lett* **2015**, *142*, 232–234. <https://doi.org/10.1016/J.MATLET.2014.11.151>.
- (151) Zhu, Y.; Xie, L.; Chang, T.; Bell, J.; Huang, A.; Jin, P.; Bao, S. High Performance All-Solid-State Electrochromic Device Based on  $\text{Li}_x\text{NiO}_y$  Layer with Gradient Li Distribution. *Electrochim Acta* **2019**, *317*, 10–16. <https://doi.org/10.1016/J.ELECTACTA.2019.05.125>.
- (152) Atak, G.; Duyar Coşkun, Ö.  $\text{LiNbO}_3$  Thin Films for All-Solid-State Electrochromic Devices. **2018**.
- (153) Boyd, R. W. *Wave-Equation Description of Nonlinear Optical Interactions*; 2020. <https://doi.org/10.1016/b978-0-12-811002-7.00011-4>.
- (154) Maier, S. A. *Fundamentals and Applications of Plasmonics*; 2006.
- (155) Maier, S. A. *Plasmonics : Fundamentals and Applications*; Springer, 2007.
- (156) Pandey, P. S.; Raghuvanshi, S. K.; Kumar, S. Recent Advances in Two-Dimensional Materials-Based Kretschmann Configuration for SPR Sensors: A Review. *IEEE Sens J* **2022**, *22* (2), 1069–1080. <https://doi.org/10.1109/JSEN.2021.3133007>.
- (157) Verhagen, E.; Polman, A.; Kuipers, L. (Kobus). Nanofocusing in Laterally Tapered Plasmonic Waveguides. *Opt Express* **2008**, *16* (1), 45. <https://doi.org/10.1364/oe.16.000045>.
- (158) Oulton, R. F.; Sorger, V. J.; Genov, D. A.; Pile, D. F. P.; Zhang, X. A Hybrid Plasmonic Waveguide for Subwavelength Confinement and Long-Range Propagation. *Nat Photonics* **2008**, *2* (8), 496–500. <https://doi.org/10.1038/nphoton.2008.131>.
- (159) Carnio, B. N.; Elezzabi, A. Y. Second Harmonic Generation in Metal-LiNbO<sub>3</sub> -Metal and LiNbO<sub>3</sub> Hybrid-Plasmonic Waveguides . *Opt Express* **2018**, *26* (20), 26283. <https://doi.org/10.1364/oe.26.026283>.

- (160) Zhang, J.; Cassan, E.; Gao, D.; Zhang, X. Highly Efficient Phase-Matched Second Harmonic Generation Using an Asymmetric Plasmonic Slot Waveguide Configuration in Hybrid Polymer-Silicon Photonics. *Opt Express* **2013**, *21* (12), 14876. <https://doi.org/10.1364/oe.21.014876>.
- (161) Otte, M. A.; Sepúlveda, B.; Ni, W.; Juste, J. P.; Liz-Marzán, L. M.; Lechuga, L. M. Identification of the Optimal Spectral Region for Plasmonic and Nanoplasmonic Sensing. *ACS Nano* **2010**, *4* (1), 349–357. <https://doi.org/10.1021/nn901024e>.
- (162) Khurgin, J. B. How to Deal with the Loss in Plasmonics and Metamaterials. *Nature Nanotechnology* *2015* *10:1* **2015**, *10* (1), 2–6. <https://doi.org/10.1038/nnano.2014.310>.
- (163) Franken, P. A.; Hill, A. E.; Peters, C. W.; Weinreich, G. Generation of Optical Harmonics. *Phys Rev Lett* **1961**, *7* (4), 118–119. <https://doi.org/10.1103/PhysRevLett.7.118>.
- (164) Castellán, C.; Trenti, A.; Vecchi, C.; Marchesini, A.; Mancinelli, M.; Ghulinyan, M.; Pucker, G.; Pavesi, L. On the Origin of Second Harmonic Generation in Silicon Waveguides with Silicon Nitride Cladding. *Sci Rep* **2019**, *9* (1), 1088. <https://doi.org/10.1038/s41598-018-37660-x>.
- (165) Lettieri, S.; Finizio, S. di; Maddalena, P.; Ballarini, V.; Giorgis, F. Second-Harmonic Generation in Amorphous Silicon Nitride Microcavities. *Appl Phys Lett* **2002**, *81* (25), 4706–4708. <https://doi.org/10.1063/1.1526171>.
- (166) Levy, J. S.; Foster, M. A.; Gaeta, A. L.; Lipson, M. Harmonic Generation in Silicon Nitride Ring Resonators. *Opt Express* **2011**, *19* (12), 11415. <https://doi.org/10.1364/OE.19.011415>.
- (167) Ning, T.; Pietarinen, H.; Hyvärinen, O.; Simonen, J.; Genty, G.; Kauranen, M. Strong Second-Harmonic Generation in Silicon Nitride Films. *Appl Phys Lett* **2012**, *100* (16). <https://doi.org/10.1063/1.4704159>.
- (168) Billat, A.; Grassani, D.; Pfeiffer, M. H. P.; Kharitonov, S.; Kippenberg, T. J.; Brès, C. S. Large Second Harmonic Generation Enhancement in Si<sub>3</sub>N<sub>4</sub> Waveguides by All-Optically Induced Quasi-Phase-Matching. *Nat Commun* **2017**, *8* (1), 1–7. <https://doi.org/10.1038/s41467-017-01110-5>.
- (169) Minissale, S.; Yerci, S.; Dal Negro, L. Nonlinear Optical Properties of Low Temperature Annealed Silicon-Rich Oxide and Silicon-Rich Nitride Materials for Silicon Photonics. *Appl Phys Lett* **2012**, *100* (2), 021109. <https://doi.org/10.1063/1.3675882>.
- (170) Nitiss, E.; Liu, T.; Grassani, D.; Pfeiffer, M.; Kippenberg, T. J.; Brès, C. S. Formation Rules and Dynamics of Photoinduced  $\chi(2)$  Gratings in Silicon

- Nitride Waveguides. *ACS Photonics* **2020**, *7* (1), 147–153. <https://doi.org/10.1021/acsp Photonics.9b01301>.
- (171) Hajibabaei, H.; Hamann, T. W. Selective Electrodeposition of Tantalum(V) Oxide Electrodes. *Langmuir* **2017**, *33* (41), 10800–10806. <https://doi.org/10.1021/acs.langmuir.7b02414>.
- (172) Lee, J. K.; Kim, G. P.; Song, I. K.; Baeck, S. H. Electrodeposition of Mesoporous V<sub>2</sub>O<sub>5</sub> with Enhanced Lithium-Ion Intercalation Property. *Electrochem Commun* **2009**, *11* (8), 1571–1574. <https://doi.org/10.1016/j.elecom.2009.05.053>.
- (173) Kondalkar, V. v.; Patil, P. B.; Mane, R. M.; Patil, P. S.; Choudhury, S.; Bhosal, P. N. Electrochromic Performance of Nickel Oxide Thin Film: Synthesis via Electrodeposition Technique. *Macromol Symp* **2016**, *361* (1), 47–50. <https://doi.org/10.1002/masy.201400253>.
- (174) Vijayakumar, E.; Yun, Y.; Quy, V. H. V.; Lee, Y.-H.; Kang, S.; Ahn, K.; Lee, S. W. Development of Tungsten Trioxide Using Pulse and Continuous Electrodeposition and Its Properties in Electrochromic Devices. *J Electrochem Soc* **2019**, *166* (4), D86–D92. <https://doi.org/10.1149/2.0271904jes>.
- (175) Krings, L. H. M.; Talen, W. Wet Chemical Preparation and Characterization of Electrochromic WO<sub>3</sub>. *Solar Energy Materials and Solar Cells* **1998**, *54* (1–4), 27–37. [https://doi.org/10.1016/S0927-0248\(97\)00220-1](https://doi.org/10.1016/S0927-0248(97)00220-1).
- (176) Pellitero, M. A.; Guimerà, A.; Kitsara, M.; Villa, R.; Rubio, C.; Lakard, B.; Doche, M. L.; Hihn, J. Y.; del Campo, F. J. Quantitative Self-Powered Electrochromic Biosensors. *Chem Sci* **2017**, *8* (3), 1995–2002. <https://doi.org/10.1039/c6sc04469g>.
- (177) Tajima, K.; Yamada, Y.; Bao, S.; Okada, M.; Yoshimura, K. Proton Conductive Tantalum Oxide Thin Film Deposited by Reactive DC Magnetron Sputtering for All-Solid-State Switchable Mirror. *J Phys Conf Ser* **2008**, *100* (8), 082017. <https://doi.org/10.1088/1742-6596/100/8/082017>.
- (178) Xin, Y.; Zhou, H.; Ni, X.; Pan, Y.; Zhang, X.; Zheng, J. Y.; Bao, S.; Jin, P. The Optical Properties of Low Infrared Transmittance WO<sub>3-x</sub> Nanocrystal Thin Films Prepared by DC Magnetron Sputtering under Different Oxygen Ratios. *RSC Adv* **2015**, *5* (71), 57757–57763. <https://doi.org/10.1039/c5ra09518b>.
- (179) Alsawafta, M.; Golestani, Y. M.; Phonemac, T.; Badilescu, S.; Stancovski, V.; Truong, V.-V. Electrochromic Properties of Sol-Gel Synthesized Macroporous Tungsten Oxide Films Doped with Gold Nanoparticles. *J*

*Electrochem Soc* **2014**, *161* (5), H276–H283.  
<https://doi.org/10.1149/2.012405jes>.

- (180) Epifani, M.; Zamani, R.; Arbiol, J.; Fabrega, C.; Andreu, T.; Pace, G. B.; Siciliano, P.; Morante, J. R. Soft Chemistry Routes to Transparent Metal Oxide Thin Films. the Case of Sol-Gel Synthesis and Structural Characterization of Ta<sub>2</sub>O<sub>5</sub> Thin Films from Tantalum Chloromethoxide. *Thin Solid Films* **2014**, *555*, 39–41. <https://doi.org/10.1016/j.tsf.2013.05.139>.
- (181) Xuping, Z.; Haokang, Z.; Qing, L.; Hongli, L. All-Solid-State Inorganic Electrochromic Display of WO<sub>3</sub> and NiO Films with LiNbO<sub>3</sub> Ion Conductor. *IEEE Electron Device Letters* **2000**, *21* (5), 215–217. <https://doi.org/10.1109/55.841300>.
- (182) Hopmann, E.; Elezzabi, A. Y. Electrochemical Stability Enhancement of Electrochromic Tungsten Oxide by Self-Assembly of a Phosphonate Protection Layer. *ACS Appl. Mater. Interfaces* **2019**. <https://doi.org/10.1021/acsami.9b19961>.
- (183) Wang, Q.; Puntambekar, A.; Chakrapani, V. Vacancy-Induced Semiconductor-Insulator-Metal Transitions in Nonstoichiometric Nickel and Tungsten Oxides. *Nano Lett* **2016**, *16* (11), 7067–7077. <https://doi.org/10.1021/acs.nanolett.6b03311>.
- (184) Ohta, H.; Hirono, M.; Onozato, T.; Katase, T.; Mizuno, T. A Transparent Electrochromic Metal-Insulator Switching Device with Three-Terminal Transistor Geometry. *Sci Rep* **2016**, *6* (1), 1–9. <https://doi.org/10.1038/srep25819>.
- (185) Nishihaya, S.; Uchida, M.; Kozuka, Y.; Iwasa, Y.; Kawasaki, M.; Nishihaya, S.; Uchida, M.; Kozuka, Y.; Iwasa, Y.; Kawasaki, M.; Iwasa, Y.; Kawasaki, M. Evolution of Insulator-Metal Phase Transitions in Epitaxial Tungsten Oxide Films during Electrolyte-Gating. *ACS Appl Mater Interfaces* **2016**, *8* (34), 22330–22336. <https://doi.org/10.1021/acsami.6b06593>.
- (186) Yang, M.; Zhang, X.; Grosjean, A.; Soroka, I.; Jonsson, M. Kinetics and Mechanism of the Reaction between H<sub>2</sub>O<sub>2</sub> and Tungsten Powder in Water. *The Journal of Physical Chemistry C* **2015**, *119* (39), 22560–22569. <https://doi.org/10.1021/acs.jpcc.5b07012>.
- (187) Leftheriotis, G.; Papaefthimiou, S.; Yianoulis, P. Dependence of the Estimated Diffusion Coefficient of Li<sub>x</sub>WO<sub>3</sub> Films on the Scan Rate of Cyclic Voltammetry Experiments. *Solid State Ion* **2007**, *178* (3–4), 259–263. <https://doi.org/10.1016/j.ssi.2006.12.019>.
- (188) Zhou, M.; Bao, J.; Xu, Y.; Zhang, J.; Xie, J.; Guan, M.; Wang, C.; Wen, L.; Lei, Y.; Xie, Y. Photoelectrodes Based upon Mo:BiVO<sub>4</sub> Inverse Opals for

Photoelectrochemical Water Splitting. *ACS Nano* **2014**, *8* (7), 7088–7098. [https://doi.org/10.1021/NN501996A/SUPPL\\_FILE/NN501996A\\_SI\\_001.PDF](https://doi.org/10.1021/NN501996A/SUPPL_FILE/NN501996A_SI_001.PDF).

- (189) Kröger, M.; Hamwi, S.; Meyer, J.; Riedl, T.; Kowalsky, W.; Kahn, A. Role of the Deep-Lying Electronic States of MoO<sub>3</sub> in the Enhancement of Hole-Injection in Organic Thin Films. *Appl Phys Lett* **2009**, *95* (12), 123301. <https://doi.org/10.1063/1.3231928>.
- (190) Bringans, R. D.; Höchst, H.; Shanks, H. R. Defect States in W  $\langle \text{math} \text{Display}=\text{"inline"} \rangle \langle \text{mrow} \rangle \langle \text{msub} \rangle \langle \text{mrow} \rangle \langle \text{mi} \text{Mathvariant}=\text{"normal"} \rangle \text{O} \langle \text{/Mi} \rangle \langle \text{/Mrow} \rangle \langle \text{mrow} \rangle \langle \text{mn} \rangle 3 \langle \text{/Mn} \rangle \langle \text{/Mrow} \rangle \langle \text{/Msub} \rangle \langle \text{/Mrow} \rangle \langle \text{/Math} \rangle$  Studied with Photoelectron Spectroscopy. *Phys Rev B* **1981**, *24* (6), 3481–3489. <https://doi.org/10.1103/PhysRevB.24.3481>.
- (191) Lee, T.; Lee, Y.; Jang, W.; Soon, A. Understanding the Advantage of Hexagonal WO<sub>3</sub> as an Efficient Photoanode for Solar Water Splitting: A First-Principles Perspective. *J Mater Chem A Mater* **2016**, *4* (29), 11498–11506. <https://doi.org/10.1039/C6TA03659G>.
- (192) Xie, S.; Bi, Z.; Chen, Y.; He, X.; Guo, X.; Gao, X.; Li, X. Electrodeposited Mo-Doped WO<sub>3</sub> Film with Large Optical Modulation and High Areal Capacitance toward Electrochromic Energy-Storage Applications. *Appl Surf Sci* **2018**, *459*, 774–781. <https://doi.org/10.1016/j.apsusc.2018.08.045>.
- (193) Tu, J.; Lei, H.; Yu, Z.; Jiao, S. Ordered WO<sub>3</sub>-Xnanorods: Facile Synthesis and Their Electrochemical Properties for Aluminum-Ion Batteries. *Chemical Communications* **2018**, *54* (11), 1343–1346. <https://doi.org/10.1039/c7cc09376d>.
- (194) Eren, E.; Alver, C.; Yurdabak Karaca, G.; Uygun, E.; Uygun Oksuz, A. Enhanced Electrochromic Performance of WO<sub>3</sub>hybrids Using Polymer Plasma Hybridization Process. *Synth Met* **2018**, *235* (October 2017), 115–124. <https://doi.org/10.1016/j.synthmet.2017.12.003>.
- (195) Liu, Y.; Jiao, Y.; Zhou, H.; Yu, X.; Qu, F.; Wu, X. Rational Design of WO<sub>3</sub>nanstructures as the Anode Materials for Lithium-Ion Batteries with Enhanced Electrochemical Performance. *Nanomicro Lett* **2014**, *7* (1), 12–16. <https://doi.org/10.1007/s40820-014-0013-5>.
- (196) Pan, L.; Han, Q.; Dong, Z.; Wan, M.; Zhu, H.; Li, Y.; Mai, Y. Reactively Sputtered WO<sub>3</sub> Thin Films for the Application in All Thin Film Electrochromic Devices. *Electrochim Acta* **2019**, *328*. <https://doi.org/10.1016/j.electacta.2019.135107>.
- (197) Lee, H. J.; Lee, C.; Song, J.; Yun, Y. J.; Jun, Y.; Ah, C. S. Electrochromic Devices Based on Ultraviolet-Cured Poly(Methyl Methacrylate) Gel

Electrolytes and Their Utilisation in Smart Window Applications. *J Mater Chem C Mater* **2020**, *8* (26), 8747–8754. <https://doi.org/10.1039/D0TC00420K>.

- (198) Vakulov, Z.; Zamburg, E.; Khakhulin, D.; Geldash, A.; Golosov, D. A.; Zavadski, S. M.; Miakonkikh, A. v.; Rudenko, K. v.; Dostanko, A. P.; He, Z.; Ageev, O. A. Oxygen Pressure Influence on Properties of Nanocrystalline LiNbO<sub>3</sub> Films Grown by Laser Ablation. *Nanomaterials* **2020**, *Vol. 10*, *Page 1371* **2020**, *10* (7), 1371. <https://doi.org/10.3390/NANO10071371>.
- (199) Meek, P. R.; Holland, L.; Townsend, P. D. Sputter Deposition of LiNbO<sub>3</sub> Films. *Thin Solid Films* **1986**, *141* (2), 251–259. [https://doi.org/10.1016/0040-6090\(86\)90353-6](https://doi.org/10.1016/0040-6090(86)90353-6).
- (200) Judenstein, P.; Morineau, R.; Livage, J. Electrochemical Degradation of WO<sub>3</sub>·nH<sub>2</sub>O Thin Films. *Solid State Ion* **1992**, *51* (3–4), 239–247. [https://doi.org/10.1016/0167-2738\(92\)90206-5](https://doi.org/10.1016/0167-2738(92)90206-5).
- (201) Wen, R. T.; Granqvist, C. G.; Niklasson, G. A. Eliminating Degradation and Uncovering Ion-Trapping Dynamics in Electrochromic WO<sub>3</sub> Thin Films. *Nat Mater* **2015**, *14* (10), 996–1001. <https://doi.org/10.1038/nmat4368>.
- (202) Wen, R.; Malmgren, S.; Granqvist, C. G.; Niklasson, G. A. Degradation Dynamics for Electrochromic WO<sub>3</sub> Films under Extended Charge Insertion and Extraction: Unveiling Physicochemical Mechanisms. *ACS Appl Mater Interfaces* **2017**, *9* (14), 12872–12877. <https://doi.org/10.1021/acsami.7b01324>.
- (203) Tajima, K.; Yamada, Y.; Bao, S.; Okada, M.; Yoshimura, K. Electrochemical Evaluation of Ta<sub>2</sub>O<sub>5</sub> Thin Film for All-Solid-State Switchable Mirror Glass. *Solid State Ion* **2009**, *180* (6–8), 654–658. <https://doi.org/10.1016/j.ssi.2008.12.034>.
- (204) Lee, H. J.; Lee, C.; Song, J.; Yun, Y. J.; Jun, Y.; Ah, C. S. Electrochromic Devices Based on Ultraviolet-Cured Poly(Methyl Methacrylate) Gel Electrolytes and Their Utilisation in Smart Window Applications. *J Mater Chem C Mater* **2020**, *8* (26), 8747–8754. <https://doi.org/10.1039/D0TC00420K>.
- (205) Rakibuddin, M.; Shinde, M. A.; Kim, H. Sol-Gel Fabrication of NiO and NiO/WO<sub>3</sub> Based Electrochromic Device on ITO and Flexible Substrate. *Ceram Int* **2020**, *46* (7), 8631–8639. <https://doi.org/10.1016/J.CERAMINT.2019.12.096>.
- (206) Cai, G.; Darmawan, P.; Cui, M.; Chen, J.; Wang, X.; Eh, A. L. S.; Magdassi, S.; Lee, P. S. Inkjet-Printed All Solid-State Electrochromic Devices Based

- on NiO/WO<sub>3</sub> Nanoparticle Complementary Electrodes. *Nanoscale* **2015**, *8* (1), 348–357. <https://doi.org/10.1039/C5NR06995E>.
- (207) Chen, P. W.; Chang, C. te; Ko, T. F.; Hsu, S. C.; Li, K. D.; Wu, J. Y. Fast Response of Complementary Electrochromic Device Based on WO<sub>3</sub>/NiO Electrodes. *Sci Rep* **2020**, *10* (1). <https://doi.org/10.1038/s41598-020-65191-x>.
- (208) Kirchner, B.; Reiher, M. The Secret of Dimethyl Sulfoxide-Water Mixtures. A Quantum Chemical Study of 1DMSO-Nwater Clusters. *J Am Chem Soc* **2002**, *124* (21), 6206–6215. <https://doi.org/10.1021/ja017703g>.
- (209) Lebel, R. G.; Goring, D. A. I. Density, Viscosity, Refractive Index, and Hygroscopicity of Mixtures of Water and Dimethyl Sulfoxide. *J Chem Eng Data* **1962**, *7* (1), 100–101. <https://doi.org/10.1021/je60012a032>.
- (210) Liu, Y.; Li, H.; Wang, X.; Lv, T.; Dong, K.; Chen, Z.; Yang, Y.; Cao, S.; Chen, T. Flexible Supercapacitors with High Capacitance Retention at Temperatures from –20 to 100 °C Based on DMSO-Doped Polymer Hydrogel Electrolytes. *J Mater Chem A Mater* **2021**, *9* (20), 12051–12059. <https://doi.org/10.1039/D1TA02397G>.
- (211) Jiang, D.; Wang, H.; Wu, S.; Sun, X.; Li, J.; Jiang, D.; Wang, H.; Wu, S.; Sun, X.; Li, J. Flexible Zinc–Air Battery with High Energy Efficiency and Freezing Tolerance Enabled by DMSO-Based Organohydrogel Electrolyte. *Small Methods* **2022**, *6* (1), 2101043. <https://doi.org/10.1002/SMTD.202101043>.
- (212) Li, M.; Chen, D.; Sun, X.; Xu, Z.; Yang, Y.; Song, Y.; Jiang, F. An Environmentally Tolerant, Highly Stable, Cellulose Nanofiber-Reinforced, Conductive Hydrogel Multifunctional Sensor. *Carbohydr Polym* **2022**, *284*, 119199. <https://doi.org/10.1016/J.CARBPOL.2022.119199>.
- (213) Li, H.; Lv, T.; Li, N.; Yao, Y.; Liu, K.; Chen, T. Ultraflexible and Tailorable All-Solid-State Supercapacitors Using Polyacrylamide-Based Hydrogel Electrolyte with High Ionic Conductivity. *Nanoscale* **2017**, *9* (46), 18474–18481. <https://doi.org/10.1039/c7nr07424g>.
- (214) Murat Ozmen, M.; Okay, O. Formation of Macroporous Poly(Acrylamide) Hydrogels in DMSO/Water Mixture: Transition from Cryogelation to Phase Separation Copolymerization. *React Funct Polym* **2008**, *68* (10), 1467–1475. <https://doi.org/10.1016/j.reactfunctpolym.2008.07.005>.
- (215) Mahajan, P. S.; Tanpure, S. D.; More, N. A.; Gajbhiye, J. M.; Mhaske, S. B. Ammonium Persulfate Activated DMSO as a One-Carbon Synthon for the Synthesis of Methylenebisamides and Other Applications. *RSC Adv* **2015**, *5* (123), 101641–101646. <https://doi.org/10.1039/c5ra21801b>.

- (216) Parimaladevi, P.; Srinivasan, K. Understanding the Crystallization Behavior of  $\alpha$ -Lactose Monohydrate ( $\alpha$ -LM) through Molecular Interaction in Selected Solvents and Solvent Mixtures under Different Growth Conditions. *CrystEngComm* **2016**, *18* (13), 2312–2318. <https://doi.org/10.1039/c5ce02548f>.
- (217) Mahajan, P. S.; Tanpure, S. D.; More, N. A.; Gajbhiye, J. M.; Mhaske, S. B. Ammonium Persulfate Activated DMSO as a One-Carbon Synthone for the Synthesis of Methylenebisamides and Other Applications. *RSC Adv* **2015**, *5* (123), 101641–101646. <https://doi.org/10.1039/c5ra21801b>.
- (218) Wallace, V. M.; Dhumal, N. R.; Zehentbauer, F. M.; Kim, H. J.; Kiefer, J. Revisiting the Aqueous Solutions of Dimethyl Sulfoxide by Spectroscopy in the Mid- and Near-Infrared: Experiments and Car-Parrinello Simulations. *Journal of Physical Chemistry B* **2015**, *119* (46), 14780–14789. <https://doi.org/10.1021/acs.jpcc.5b09196>.
- (219) Tenhu, H.; Sundholm, F.; Bjorksten, J. Studies of Crosslinked Poly(N-Vinyl-2-Pyrrolidone) by Calorimetry and by NMR. *Makromol. Chem.* **1984**, *2019* (1984), 2011–2019.
- (220) Li, H.; Liu, Z.; Liang, G.; Huang, Y.; Huang, Y.; Zhu, M.; Pei, Z.; Xue, Q.; Tang, Z.; Wang, Y.; Li, B.; Zhi, C. Waterproof and Tailorable Elastic Rechargeable Yarn Zinc Ion Batteries by a Cross-Linked Polyacrylamide Electrolyte. *ACS Nano* **2018**, *12* (4), 3140–3148. <https://doi.org/10.1021/acsnano.7b09003>.
- (221) Fu, J.; Zhang, J.; Song, X.; Zarrin, H.; Tian, X.; Qiao, J.; Rasen, L.; Li, K.; Chen, Z. Environmental Science Integration of Rechargeable Zinc – Air Batteries †. *Energy Environ Sci* **2016**, *9*, 663–670. <https://doi.org/10.1039/C5EE03404C>.
- (222) Chae, M. S.; Heo, J. W.; Kwak, H. H.; Lee, H.; Hong, S.-T. Organic Electrolyte-Based Rechargeable Zinc-Ion Batteries Using Potassium Nickel Hexacyanoferrate as a Cathode Material. *J Power Sources* **2017**, *337*, 204–211. <https://doi.org/10.1016/j.jpowsour.2016.10.083>.
- (223) Wang, Z.; Ruan, Z.; Liu, Z.; Wang, Y.; Tang, Z.; Li, H.; Zhu, M.; Hung, T. F.; Liu, J.; Shi, Z.; Zhi, C. A Flexible Rechargeable Zinc-Ion Wire-Shaped Battery with Shape Memory Function. *J Mater Chem A Mater* **2018**, *6* (18), 8549–8557. <https://doi.org/10.1039/c8ta01172a>.
- (224) Lahan, H.; Das, S. K. An Approach to Improve the Al<sup>3+</sup> Ion Intercalation in Anatase TiO<sub>2</sub> Nanoparticle for Aqueous Aluminum-Ion Battery. *Ionics (Kiel)* **2018**, *24* (6), 1855–1860. <https://doi.org/10.1007/s11581-018-2530-6>.
- (225) Cong, S.; Tian, Y.; Zhang, W.; Zhao, Z.; Geng, F.; Zheng, Y. Unconventional Aluminum Ion Intercalation/Deintercalation for Fast

- Switching and Highly Stable Electrochromism. *Adv Funct Mater* **2015**, *25* (36), 5833–5839. <https://doi.org/10.1002/adfm.201502638>.
- (226) Liu, J.; Xu, C.; Chen, Z.; Ni, S.; Shen, Z. X. Progress in Aqueous Rechargeable Batteries. *Green Energy & Environment* **2018**, *3* (1), 20–41. <https://doi.org/10.1016/j.gee.2017.10.001>.
- (227) Gu, S.; Wang, H.; Wu, C.; Bai, Y.; Li, H.; Wu, F. Confirming Reversible Al<sup>3+</sup> storage Mechanism through Intercalation of Al<sup>3+</sup> into V<sub>2</sub>O<sub>5</sub> nanowires in a Rechargeable Aluminum Battery. *Energy Storage Mater* **2017**, *6*, 9–17. <https://doi.org/10.1016/j.ensm.2016.09.001>.
- (228) Wang, Y.; Meng, Z.; Chen, H.; Li, T.; Zheng, D.; Xu, Q.; Wang, H.; Liu, X. Y.; Guo, W. Pulsed Electrochemical Deposition of Porous WO<sub>3</sub> on Silver Networks for Highly Flexible Electrochromic Devices. *J Mater Chem C Mater* **2019**, *7* (7), 1966–1973. <https://doi.org/10.1039/C8TC05698F>.
- (229) Yan, C.; Kang, W.; Wang, J.; Cui, M.; Wang, X.; Foo, C. Y.; Chee, K. J.; Lee, P. S. Stretchable and Wearable Electrochromic Devices. *ACS Nano* **2014**, *8* (1), 316–322. <https://doi.org/10.1021/nn404061g>.
- (230) Li, J.; Li, H.; Li, J.; Wu, G.; Shao, Y.; Li, Y.; Zhang, Q.; Wang, H. A Single-Walled Carbon Nanotubes/Poly(3,4-Ethylenedioxythiophene)-Poly(Styrenesulfonate)/Copper Hexacyanoferrate Hybrid Film for High-Volumetric Performance Flexible Supercapacitors. *J Power Sources* **2018**, *386* (September 2017), 96–105. <https://doi.org/10.1016/j.jpowsour.2018.03.046>.
- (231) Cao, S.; Zhang, S.; Zhang, T.; Yao, Q.; Lee, J. Y. A Visible Light-Near-Infrared Dual-Band Smart Window with Internal Energy Storage. *Joule* **2019**, *3* (4), 1152–1162. <https://doi.org/10.1016/j.joule.2018.12.010>.
- (232) Guo, J.; Wang, M.; Diao, X.; Zhang, Z.; Dong, G.; Yu, H.; Liu, F.; Wang, H.; Liu, J. Prominent Electrochromism Achieved Using Aluminum Ion Insertion/Extraction in Amorphous WO<sub>3</sub> Films. *Journal of Physical Chemistry C* **2018**, *122* (33), 19037–19043. <https://doi.org/10.1021/acs.jpcc.8b05692>.
- (233) Hopmann, E.; Elezzabi, A. Y. Electrochemical Stability Enhancement of Electrochromic Tungsten Oxide by Self-Assembly of a Phosphonate Protection Layer. *ACS Appl Mater Interfaces* **2020**, *12*, 1930–1936. <https://doi.org/10.1021/acsami.9b19961>.
- (234) Yue, Y.; Li, H.; Li, K.; Wang, J.; Wang, H.; Zhang, Q.; Li, Y.; Chen, P. High-Performance Complementary Electrochromic Device Based on WO<sub>3</sub>·0.33H<sub>2</sub>O/PEDOT and Prussian Blue Electrodes. *Journal of Physics and Chemistry of Solids* **2017**, *110* (January), 284–289. <https://doi.org/10.1016/j.jpics.2017.06.022>.

- (235) Mancinelli, R.; Botti, A.; Bruni, F.; Ricci, M. A.; Soper, A. K. Hydration of Sodium, Potassium, and Chloride Ions in Solution and the Concept of Structure Maker/Breaker. *Journal of Physical Chemistry B* **2007**, *111* (48), 13570–13577. <https://doi.org/10.1021/jp075913v>.
- (236) Judeinstein, P.; Livage, J. Role of the Water Content on the Electrochromic Properties of WO<sub>3</sub>nH<sub>2</sub>O Thin Films. *Materials Science and Engineering B* **1989**, *3* (1–2), 129–132. [https://doi.org/10.1016/0921-5107\(89\)90191-8](https://doi.org/10.1016/0921-5107(89)90191-8).
- (237) Li, C.-P.; Tenent, R. C.; Dillon, A. C.; Morrish, R. M.; Wolden, C. A. Improved Durability of WO<sub>3</sub> Nanocomposite Films Using Atomic Layer and Vapor Deposited Coatings. *ECS Electrochemistry Letters* **2012**, *1* (5), H24–H27. <https://doi.org/10.1149/2.002206eel>.
- (238) Hanson, E. L.; Schwartz, J.; Nickel, B.; Koch, N.; Danisman, M. F. Bonding Self-Assembled, Compact Organophosphonate Monolayers to the Native Oxide Surface of Silicon. *J Am Chem Soc* **2003**, *125* (51), 16074–16080. <https://doi.org/10.1021/ja035956z>.
- (239) Xiong, K.; Tordera, D.; Emilsson, G.; Olsson, O.; Linderhed, U.; Jonsson, M. P.; Dahlin, A. B. Switchable Plasmonic Metasurfaces with High Chromaticity Containing Only Abundant Metals. *Nano Lett* **2017**, *17* (11), 7033–7039. <https://doi.org/10.1021/acs.nanolett.7b03665>.
- (240) Yanase, Y.; Hiragun, T.; Ishii, K.; Kawaguchi, T.; Yanase, T.; Kawai, M.; Sakamoto, K.; Hide, M. Surface Plasmon Resonance for Cell-Based Clinical Diagnosis. *Sensors 2014, Vol. 14, Pages 4948-4959* **2014**, *14* (3), 4948–4959. <https://doi.org/10.3390/S140304948>.
- (241) Karabchevsky, A.; Tsapovsky, L.; Marks, R. S.; Abdulhalim, I. Study of Immobilization Procedure on Silver Nanolayers and Detection of Estrone with Diverged Beam Surface Plasmon Resonance (SPR) Imaging. *Biosensors 2013, Vol. 3, Pages 157-170* **2013**, *3* (1), 157–170. <https://doi.org/10.3390/BIOS3010157>.
- (242) Kim, S.; Brady, J.; Al-Badani, F.; Yu, S.; Hart, J.; Jung, S.; Tran, T. T.; Myung, N. v. Nanoengineering Approaches Toward Artificial Nose. *Front Chem* **2021**, *9*, 11. <https://doi.org/10.3389/FCHEM.2021.629329/BIBTEX>.
- (243) Luo, W.; Wang, R.; Li, H.; Kou, J.; Zeng, X.; Huang, H. E.; Hu, X.; Huang, W. Simultaneous Measurement of Refractive Index and Temperature for Prism-Based Surface Plasmon Resonance Sensors. *Optics Express, Vol. 27, Issue 2, pp. 576-589* **2019**, *27* (2), 576–589. <https://doi.org/10.1364/OE.27.000576>.
- (244) Liu, Q.; Dong, G.; Chen, Q.; Guo, J.; Xiao, Y.; Delplancke-Ogletree, M. P.; Reniers, F.; Diao, X. Charge-Transfer Kinetics and Cyclic Properties of Inorganic All-Solid-State Electrochromic Device with Remarkably

- Improved Optical Memory. *Solar Energy Materials and Solar Cells* **2018**, *174* (April 2017), 545–553. <https://doi.org/10.1016/j.solmat.2017.09.012>.
- (245) Coşkun, Ö. D.; Atak, G. The Effects of Lithiation Process on the Performance of All-Solid-State Electrochromic Devices. *Thin Solid Films* **2018**, *662*, 13–20. <https://doi.org/10.1016/J.TSF.2018.07.019>.
- (246) Fang, Y.; Sun, M. Nanoplasmonic Waveguides: Towards Applications in Integrated Nanophotonic Circuits. *Light Sci Appl* **2015**, *4* (December 2014), 1–11. <https://doi.org/10.1038/lsa.2015.67>.
- (247) Berweger, S.; Atkin, J. M.; Xu, X. G.; Olmon, R. L.; Raschke, M. B. Femtosecond Nanofocusing with Full Optical Waveform Control. *Nano Lett* **2011**, *11* (10), 4309–4313. <https://doi.org/10.1021/nl2023299>.
- (248) Jeyaselvan, V.; Pal, A.; Anil Kumar, P. S.; Selvaraja, S. K. Thermally-Induced Optical Modulation in a Vanadium Dioxide-on-Silicon Waveguide. *OSA Contin* **2020**, *3* (1), 132. <https://doi.org/10.1364/osac.382861>.
- (249) Gosciniak, J.; Bozhevolnyi, S. I. Performance of Thermo-Optic Components Based on Dielectric-Loaded Surface Plasmon Polariton Waveguides. *Sci Rep* **2013**, *3*, 3–10. <https://doi.org/10.1038/srep01803>.
- (250) Niklasson, G. A.; Granqvist, C. G. Electrochromics for Smart Windows: Thin Films of Tungsten Oxide and Nickel Oxide, and Devices Based on These. **2006**. <https://doi.org/10.1039/b612174h>.
- (251) Nam, Y. J.; Oh, D. Y.; Jung, S. H.; Jung, Y. S. Toward Practical All-Solid-State Lithium-Ion Batteries with High Energy Density and Safety: Comparative Study for Electrodes Fabricated by Dry- and Slurry-Mixing Processes. *J Power Sources* **2018**, *375* (November 2017), 93–101. <https://doi.org/10.1016/j.jpowsour.2017.11.031>.
- (252) Beydaghyan, G.; Bader, G.; Ashrit, P. v. Electrochromic and Morphological Investigation of Dry-Lithiated Nanostructured Tungsten Trioxide Thin Films. **2007**. <https://doi.org/10.1016/j.tsf.2007.05.006>.
- (253) Li, Z.; Butun, S.; Aydin, K. Large-Area, Lithography-Free Super Absorbers and Color Filters at Visible Frequencies Using Ultrathin Metallic Films. *ACS Photonics* **2015**, *2* (2), 183–188. <https://doi.org/10.1021/ph500410u>.
- (254) Kumar, K.; Duan, H.; Hegde, R. S.; Koh, S. C. W.; Wei, J. N.; Yang, J. K. W. Printing Colour at the Optical Diffraction Limit. *Nat Nanotechnol* **2012**, *7* (9), 557–561. <https://doi.org/10.1038/nnano.2012.128>.
- (255) Franklin, D.; Chen, Y.; Vazquez-Guardado, A.; Modak, S.; Boroumand, J.; Xu, D.; Wu, S. T.; Chanda, D. Polarization-Independent Actively Tunable

- Colour Generation on Imprinted Plasmonic Surfaces. *Nat Commun* **2015**, *6*, 1–8. <https://doi.org/10.1038/ncomms8337>.
- (256) Kaplan, A. F.; Xu, T.; Jay Guo, L. High Efficiency Resonance-Based Spectrum Filters with Tunable Transmission Bandwidth Fabricated Using Nanoimprint Lithography. *Appl Phys Lett* **2011**, *99* (14), 28–31. <https://doi.org/10.1063/1.3647633>.
- (257) Gwo, S.; Wang, C. Y.; Chen, H. Y.; Lin, M. H.; Sun, L.; Li, X.; Chen, W. L.; Chang, Y. M.; Ahn, H. Plasmonic Metasurfaces for Nonlinear Optics and Quantitative SERS. *ACS Photonics* **2016**, *3* (8), 1371–1384. <https://doi.org/10.1021/acsp Photonics.6b00104>.
- (258) Wang, Z.; Ai, B.; Möhwald, H.; Zhang, G. Colloidal Lithography Meets Plasmonic Nanochemistry. *Adv Opt Mater* **2018**, *6* (18), 1–18. <https://doi.org/10.1002/adom.201800402>.
- (259) Colson, P.; Henrist, C.; Cloots, R. Nanosphere Lithography: A Powerful Method for the Controlled Manufacturing of Nanomaterials. *J Nanomater* **2013**, *2013*. <https://doi.org/10.1155/2013/948510>.
- (260) Duan, X.; Kamin, S.; Liu, N. Dynamic Plasmonic Colour Display. *Nat Commun* **2017**, *8*, 1–9. <https://doi.org/10.1038/ncomms14606>.
- (261) Duan, X.; Liu, N. Scanning Plasmonic Color Display. *ACS Nano*. American Chemical Society 2018, pp 8817–8823. <https://doi.org/10.1021/acsnano.8b05467>.
- (262) Ming, F.; Liang, H.; Lei, Y.; Kandambeth, S.; Eddaoudi, M.; Alshareef, H. N. Layered Mg XV<sub>2</sub>O<sub>5</sub>·NH<sub>2</sub>O as Cathode Material for High-Performance Aqueous Zinc Ion Batteries. *ACS Energy Lett* **2018**, *3* (10), 2602–2609. <https://doi.org/10.1021/acsenenergylett.8b01423>.
- (263) Wang, F.; Liu, Z.; Wang, X.; Yuan, X.; Wu, X.; Zhu, Y.; Fu, L.; Wu, Y. A Conductive Polymer Coated MoO<sub>3</sub> Anode Enables an Al-Ion Capacitor with High Performance. *J Mater Chem A Mater* **2016**, *4* (14), 5115–5123. <https://doi.org/10.1039/c6ta01398h>.
- (264) Li, Y.; van de Groep, J.; Talin, A. A.; Brongersma, M. L. Dynamic Tuning of Gap Plasmon Resonances Using a Solid-State Electrochromic Device. *Nano Lett* **2019**, *19* (11), 7988–7995. <https://doi.org/10.1021/acs.nanolett.9b03143>.
- (265) Miller, M. M.; Lazarides, A. A. Sensitivity of Metal Nanoparticle Surface Plasmon Resonance to the Dielectric Environment. *Journal of Physical Chemistry B* **2005**, *109* (46), 21556–21565. <https://doi.org/10.1021/jp054227y>.

- (266) Dahlin, A. B.; Zahn, R.; Vörös, J. Nanoplasmonic Sensing of Metal-Halide Complex Formation and the Electric Double Layer Capacitor. *Nanoscale* **2012**, *4* (7), 2339–2351. <https://doi.org/10.1039/c2nr11950a>.
- (267) Dahlin, A. B.; Sannomiya, T.; Zahn, R.; Sotiriou, G. A.; Vörös, J. Electrochemical Crystallization of Plasmonic Nanostructures. *Nano Lett* **2011**, *11* (3), 1337–1343. <https://doi.org/10.1021/nl104424q>.
- (268) Sannomiya, T.; Scholder, O.; Jefimovs, K.; Hafner, C.; Dahlin, A. B. Investigation of Plasmon Resonances in Metal Films with Nanohole Arrays for Biosensing Applications. *Small* **2011**, *7* (12), 1653–1663. <https://doi.org/10.1002/sml.201002228>.
- (269) Fredriksson, H.; Alaverdyan, Y.; Dmitriev, A.; Langhammer, C.; Sutherland, D. S.; Zäch, M.; Kasemo, B. Hole-Mask Colloidal Lithography. *Advanced Materials* **2007**, *19* (23), 4297–4302. <https://doi.org/10.1002/adma.200700680>.
- (270) Chiappini, A.; Armellini, C.; Chiasera, A.; Ferrari, M.; Fortes, L.; Gonçalves, M. C.; Guider, R.; Jestin, Y.; Retoux, R.; Conti, G. N.; Pelli, S.; Almeida, R. M.; Righini, G. C. An Alternative Method to Obtain Direct Opal Photonic Crystal Structures. *J Non Cryst Solids* **2009**, *355* (18–21), 1167–1170. <https://doi.org/10.1016/j.jnoncrsol.2009.01.054>.
- (271) Chokprasombat, K.; Sirisathitkul, C.; Ratphonsan, P. Liquid–Air Interface Self-Assembly: A Facile Method to Fabricate Long-Range Nanoparticle Monolayers. *Surf Sci* **2014**, *621*, 162–167. <https://doi.org/10.1016/J.SUSC.2013.11.014>.
- (272) Song, S.; Liu, Y.; Liu, X.; Ge, J.; Ge, D.; Yang, L. Color Brightness Modulation of a Responsive Photonic Liquid for Multicolored Electrochromic Displays. *J Mater Chem C Mater* **2022**, *10* (8), 3114–3120. <https://doi.org/10.1039/D1TC05516J>.
- (273) García-García, F. J.; Mosa, J.; González-Elipe, A. R.; Aparicio, M. Sodium Ion Storage Performance of Magnetron Sputtered WO<sub>3</sub> Thin Films. *Electrochim Acta* **2019**, *321*. <https://doi.org/10.1016/j.electacta.2019.134669>.
- (274) Wen, R.; Malmgren, S.; Granqvist, C. G.; Niklasson, G. A. Degradation Dynamics for Electrochromic WO<sub>3</sub> Films under Extended Charge Insertion and Extraction: Unveiling Physicochemical Mechanisms. *ACS Appl Mater Interfaces* **2017**, *9* (14), 12872–12877. <https://doi.org/10.1021/acsami.7b01324>.
- (275) Sannomiya, T.; Scholder, O.; Jefimovs, K.; Hafner, C.; Dahlin, A. B. Investigation of Plasmon Resonances in Metal Films with Nanohole Arrays

- for Biosensing Applications. *Small* **2011**, *7* (12), 1653–1663. <https://doi.org/10.1002/SMLL.201002228>.
- (276) Tan, D. T. H.; Ikeda, K.; Sun, P. C.; Fainman, Y. Group Velocity Dispersion and Self Phase Modulation in Silicon Nitride Waveguides. *Appl Phys Lett* **2010**, *96* (6), 1–4. <https://doi.org/10.1063/1.3299008>.
- (277) Lu, X.; Moille, G.; Rao, A.; Westly, D. A.; Srinivasan, K. Efficient Photoinduced Second-Harmonic Generation in Silicon Nitride Photonics. *Nat Photonics* **2021**, *15* (2), 131–136. <https://doi.org/10.1038/s41566-020-00708-4>.
- (278) Levy, J. S.; Foster, M. A.; Gaeta, A. L.; Lipson, M. Harmonic Generation in Silicon Nitride Ring Resonators. *Opt Express* **2011**, *19* (12), 11415. <https://doi.org/10.1364/OE.19.011415>.
- (279) Ikeda, K.; Saperstein, R. E.; Alic, N.; Fainman, Y. Thermal and Kerr Nonlinear Properties of Plasma-Deposited Silicon Nitride/ Silicon Dioxide Waveguides. *Opt Express* **2008**, *16* (17), 12987. <https://doi.org/10.1364/oe.16.012987>.
- (280) Krüchel, C. J.; Fülöp, A.; Klintberg, T.; Bengtsson, J.; Andrekson, P. A.; Torres-Company, V. Linear and Nonlinear Characterization of Low-Stress High-Confinement Silicon-Rich Nitride Waveguides. *Opt Express* **2015**, *23* (20), 25827. <https://doi.org/10.1364/oe.23.025827>.
- (281) Hopmann, E.; Shahriar, B. Y.; Elezzabi, A. Y. On-Chip High Ion Sensitivity Electrochromic Nanophotonic Light Modulator. *Nanoscale* **2022**, *14* (17), 6526–6534. <https://doi.org/10.1039/D2NR00646D>.
- (282) Pellitero, M. A.; Guimerà, A.; Kitsara, M.; Villa, R.; Rubio, C.; Lakard, B.; Doche, M. L.; Hihn, J. Y.; del Campo, F. J. Quantitative Self-Powered Electrochromic Biosensors. *Chem Sci* **2017**, *8* (3), 1995–2002. <https://doi.org/10.1039/c6sc04469g>.
- (283) Santos, L.; Neto, J. P.; Crespo, A.; Nunes, D.; Costa, N.; Fonseca, I. M.; Barquinha, P.; Pereira, L.; Silva, J.; Martins, R.; Fortunato, E. WO<sub>3</sub> Nanoparticle-Based Conformable PH Sensor. *ACS Appl Mater Interfaces* **2014**, *6* (15), 12226–12234. <https://doi.org/10.1021/am501724h>.
- (284) Wang, X.; Miura, N.; Yamazoe, N. Study of WO<sub>3</sub>-Based Sensing Materials for NH<sub>3</sub> and NO Detection. *Sens Actuators B Chem* **2000**, *66* (1), 74–76. [https://doi.org/10.1016/S0925-4005\(99\)00410-4](https://doi.org/10.1016/S0925-4005(99)00410-4).
- (285) de Matteis, V.; Cannavale, A.; Blasi, L.; Quarta, A.; Gigli, G. Chromogenic Device for Cystic Fibrosis Precocious Diagnosis: A “Point of Care” Tool for Sweat Test. *Sens Actuators B Chem* **2016**, *225*, 474–480. <https://doi.org/10.1016/j.snb.2015.11.080>.

- (286) Santos, L.; Neto, J. P.; Crespo, A.; Nunes, D.; Costa, N.; Fonseca, I. M.; Barquinha, P.; Pereira, L.; Silva, J.; Martins, R.; Fortunato, E. WO<sub>3</sub> Nanoparticle-Based Conformable PH Sensor. *ACS Appl Mater Interfaces* **2014**, *6* (15), 12226–12234. <https://doi.org/10.1021/am501724h>.
- (287) Wang, X.; Miura, N.; Yamazoe, N. Study of WO<sub>3</sub>-Based Sensing Materials for NH<sub>3</sub> and NO Detection. *Sens Actuators B Chem* **2000**, *66* (1), 74–76. [https://doi.org/10.1016/S0925-4005\(99\)00410-4](https://doi.org/10.1016/S0925-4005(99)00410-4).
- (288) Bessière, A. Structural and Electrochemical Study of Li<sup>+</sup> Insertion in the Infrared Reflectance Modulating Compound Li<sub>x</sub>WO<sub>3</sub>·H<sub>2</sub>O. *Solid State Ion* **2003**, *165* (1–4), 23–33. <https://doi.org/10.1016/j.ssi.2003.08.011>.
- (289) Cai, G.; Wang, J.; Lee, P. S. Next-Generation Multifunctional Electrochromic Devices. *Acc Chem Res* **2016**, *49* (8), 1469–1476. <https://doi.org/10.1021/acs.accounts.6b00183>.
- (290) Kuratani, K.; Uemura, N.; Senoh, H.; Takeshita, H. T.; Kiyobayashi, T. Conductivity, Viscosity and Density of MClO<sub>4</sub> (M = Li and Na) Dissolved in Propylene Carbonate and  $\gamma$ -Butyrolactone at High Concentrations. *J Power Sources* **2013**, *223*, 175–182. <https://doi.org/10.1016/j.jpowsour.2012.09.039>.
- (291) Yoon, D. H.; Yoon, S. G.; Kim, Y. T. Refractive Index and Etched Structure of Silicon Nitride Waveguides Fabricated by PECVD. *Thin Solid Films* **2007**, *515* (12), 5004–5007. <https://doi.org/10.1016/j.tsf.2006.10.059>.
- (292) Haffner, C.; Chelladurai, D.; Fedoryshyn, Y.; Josten, A.; Baeuerle, B.; Heni, W.; Watanabe, T.; Cui, T.; Cheng, B.; Saha, S.; Elder, D. L.; Dalton, L. R.; Boltasseva, A.; Shalaev, V. M.; Kinsey, N.; Leuthold, J. Low-Loss Plasmon-Assisted Electro-Optic Modulator. *Nature* **2018**, *556* (7702), 483–486. <https://doi.org/10.1038/s41586-018-0031-4>.
- (293) de Oliveira, R. E. P.; de Matos, C. J. S. Quasi-Phase-Matched Second Harmonic Generation in Silicon Nitride Ring Resonators Controlled by Static Electric Field. *Opt Express* **2013**, *21* (26), 32690. <https://doi.org/10.1364/oe.21.032690>.
- (294) Firby, C. J.; Chang, P.; Helmy, A. S.; Elezzabi, A. Y. Magnetoplasmonic Faraday Rotators: Enabling Gigahertz Active Polarization Control for Integrated Plasmonics. *ACS Photonics* **2016**, *3* (12), 2344–2352. <https://doi.org/10.1021/acsp Photonics.6b00523>.
- (295) Firby, C. J.; Elezzabi, A. Y. High-Speed Nonreciprocal Magnetoplasmonic Waveguide Phase Shifter. *Optica* **2015**, *2* (7), 598. <https://doi.org/10.1364/optica.2.000598>.

- (296) Zhang, H.; Zhou, L.; Xu, J.; Wang, N.; Hu, H.; Lu, L.; Rahman, B. M. A.; Chen, J. Nonvolatile Waveguide Transmission Tuning with Electrically-Driven Ultra-Small GST Phase-Change Material. *Sci Bull (Beijing)* **2019**, *64* (11), 782–789. <https://doi.org/10.1016/j.scib.2019.04.035>.
- (297) Wang, L.; Xie, W.; van Thourhout, D.; Zhang, Y.; Yu, H.; Wang, S. Nonlinear Silicon Nitride Waveguides Based on PECVD Deposition Platform. *Opt Express* **2018**, *26* (8), 9645. <https://doi.org/10.1364/oe.26.009645>.
- (298) Lu, X.; Moille, G.; Rao, A.; Westly, D. A.; Srinivasan, K. Efficient Photoinduced Second-Harmonic Generation in Silicon Nitride Photonics. *Nat Photonics* **2021**, *15* (2), 131–136. <https://doi.org/10.1038/s41566-020-00708-4>.

# Appendix A: Process Parameter

This appendix is comprised of several tables listing all the rate investigations used for sputtering and etching of the various materials reported in this thesis.

Table A1: Process parameter for reactive magnetron sputtering of  $\text{WO}_3$  from a 2" diameter metallic W target.

<b>Pressure (mTorr)</b>	<b>Plasma power (W)</b>	<b>Ratio Ar/O2</b>	<b>Deposition rate (nm/s)</b>
5	125	20/5	0.06
10	125	20/5	0.075
20	125	20/5	0.1
20	200	20/5	0.223
30	125	20/5	0.141
30	200	20/5	0.23

Table A2: Process parameter for reactive magnetron sputtering of  $\text{LiNbO}_3$  from a 2" ceramic  $\text{LiNbO}_3$  target (purity > 99.95% - Angstrom Engineering)

<b>Pressure (mTorr)</b>	<b>Plasma power (W)</b>	<b>Ratio Ar/O2</b>	<b>Deposition rate (nm/min)</b>
5	88	20/0	1.2
5	88	20/0.5	0.65
5	88	20/1	0.5

Table A3: Process parameter for reactive magnetron sputtering of NiO from a 2” metallic Ni target.

<b>Pressure (mTorr)</b>	<b>Plasma power (W)</b>	<b>Ratio Ar/O<sub>2</sub></b>	<b>Deposition rate (nm/s)</b>
20	125	20/1	0.16
20	200	20/1	0.24
30	125	20/1	0.12
30	200	20/1	0.2

# Appendix B: Fabrication Process for Silicon Nitride EC Waveguides

In this appendix, a detailed description of the fabrication process for SHWGs and SNWGs is given with explanations for every single step.

## 1<sup>st</sup> mask: Waveguide width definition through RIE of Silicon Nitride

- 1) Silicon wafers with 2  $\mu\text{m}$  thermal oxide are cleaned in Piranha solution, rinsed with DI water and spin dried.
  - a) Thermal oxide with thicknesses  $d > 1 \mu\text{m}$  is necessary to prevent coupling of the laser beam to the Silicon substrate.
  - b) Processing within 24h of Piranha clean.
- 2) PECVD of  $d = 850 \text{ nm}$  Silicon Nitride (Plasmatherm Versaline)
  - a) Deposition of stoichiometric  $\text{SiN}_x$  with 10 sccm  $\text{SiH}_4$ , 7.5 sccm  $\text{NH}_3$ , 1030 sccm He as a carrier gas and 550 sccm  $\text{N}_2$ .
  - b)  $P = 65 \text{ W}$  and  $p = 1000 \text{ mTorr}$ .
  - c)  $R = 0.39 \text{ nm/s}$  and  $\pm 0.3\%$  thickness homogeneity.
  - d) Cleaning of the wafers in oxygen plasma
- 3) Photolithography step (Heidelberg MLA150)
  - a) Deposit HMDS monolayer for resist adhesion.
  - b) Spin coating of LOR5B lift-off resist at 3500 rpm for  $t = 60 \text{ s}$ , followed by baking at  $T = 150^\circ\text{C}$  for  $t = 5 \text{ min}$ . Parameter result in  $d = 420 \text{ nm}$  thickness.
  - c) Rest wafers for  $t = 10 \text{ min}$  to allow wafers to cool down.

- d) Spin coating of AZ1512 photoresist at 5000 rpm for  $t = 50$  s, followed by baking at  $T = 100^\circ\text{C}$  for  $t = 1$  min. Parameter result in  $d = 1.1 \mu\text{m}$  thickness.
  - e) Exposure in Heidelberg MLA150 with  $J = 110 \text{ mJ}/\text{cm}^2$  dose.
  - f) Develop in AZ1:1 developer for  $t = 90$  s, rinse with water and dry with  $\text{N}_2$ , then develop in MIF319 1:1 for  $t = 60$  s. Rinse and dry.
- 4) Deposit  $d = 80 \text{ nm}$  Cr through electron beam evaporation (Gomez). Deposition rate held constant  $r < 0.2 \text{ nm}/\text{s}$ . Base pressure  $p = 2 \times 10^{-7} \text{ mTorr}$  and deposition current  $I = 10 \text{ mA}$ .
- a) Lift-off in Remover PG under strong sonication
- 5) RIE of  $\text{SiN}_x$  (Oxford PlasmaPro 100 – Cobra).
- a) Etch gas: 30 sccm  $\text{CHF}_3$ , 10 sccm  $\text{SF}_6$  and 4 sccm  $\text{O}_2$
  - b) Power:  $P_{\text{ICP}} = 300 \text{ W}$ ,  $P_{\text{DC}} = 20 \text{ W}$
  - c) Pressure: 5 mTorr
- 6) Wet etch of Cr etch mask for  $t = 60$  min to remove any residual Cr or  $\text{CrO}$ .
- a) Wafers are cleaned in oxygen plasma afterwards
- 7) Rapid thermal annealing (Allwin RTA) at  $T = 700^\circ\text{C}$  under  $\text{N}_2$  atmosphere with five times  $t = 2$  min heating and  $t = 3$  min cooling period. Ramping time is  $t = 10$  s. Annealing step is used to drive out residual H.
- 8) PECVD of  $\text{SiO}_2$  cladding.
- a) Thickness of cladding determined by spacer thickness ( $d_{\text{SiO}_2} = d_{\text{SiN}_x} + d_{\text{Spacer}} + 50 \text{ nm}$ ).
  - b)  $\text{SiO}_2$  deposition with  $0.39 \text{ nm}/\text{s}$  and  $\pm 0.3\%$  thickness homogeneity.

- c) Cladding grows isotropically resulting in  $d = 800$  nm bumps over the waveguides
- 9) Rapid thermal annealing (Allwin RTA) at  $T = 1100^{\circ}\text{C}$  under  $\text{N}_2$  atmosphere with three times  $t = 2$  min heating and  $t = 3$  min cooling period. Ramping time is  $t = 10$  s. Annealing step is used to drive out residual H.
- 10) Planarizing of the cladding layer
- a) Spin coating of PC43-700 planarizing coating at 3000 rpm for 60 s.
  - b) Reflow bake at  $T = 200^{\circ}\text{C}$  for  $t = 2$  min
  - c) Thickness  $d = 1160$  nm
  - d) Etching of  $\text{SiO}_2$  cladding and PC43 simultaneously in 5 sccm  $\text{CHF}_3$  and 50 sccm  $\text{CF}_4$  at  $P = 125$  W and  $p = 100$  mTorr.
  - e) Monitor the etch rate every  $t = 180$  s with profilometry. Etch rates roughly  $r = 64$  nm/min for both materials.
  - f) Bumps of less than  $d = 50$  nm over waveguide.
- 11) Samples are cleaned in Piranha solution, rinsed with DI water and spin dried.

2<sup>nd</sup> mask: Bottom contact definition

- 12) Photolithography step (Heidelberg MLA150)
- a) Deposit HMDS monolayer for resist adhesion.
  - b) Spin coating of AZ1529 photo resist at 3000 rpm for  $t = 60$  s, followed by baking at  $T = 100^{\circ}\text{C}$  for  $t = 3$  min. Parameter result in  $d = 2900$  nm thickness.
  - c) Rest wafers for  $t = 10$  min to allow wafers to cool down.

- d) Exposure in Heidelberg MLA150 with  $J = 230 \text{ mJ/cm}^2$  dose.
- e) Develop in AZ4:1 400k developer for  $t = 120 \text{ s}$ , rinse with water and dry with  $\text{N}_2$ .

- 13) Deposition of  $d = 50 \text{ nm}$  Cr through sputtering (Floyd). Deposition rate held constant  $r = 14.2 \text{ nm/min}$ . Base pressure  $p < 5 \times 10^{-7} \text{ mTorr}$ . Deposition of  $d = 50 \text{ nm}$  W through sputtering (Floyd). Deposition rate held constant  $r = 7.8 \text{ nm/min}$ . Base pressure  $p < 5 \times 10^{-7} \text{ mTorr}$
- a) Lift-off in Remover PG under strong sonication.

3<sup>rd</sup> mask: ECD layer definition:

- 14) Photolithography step (Heidelberg MLA150)
- a) Deposit HMDS monolayer for resist adhesion.
  - b) Spin coating of AZ1529 photo resist at 3000 rpm for  $t = 60 \text{ s}$ , followed by baking at  $T = 100^\circ\text{C}$  for  $t = 3 \text{ min}$ . Parameter result in  $d = 2900 \text{ nm}$  thickness.
  - c) Rest wafers for  $t = 10 \text{ min}$  to allow wafers to cool down.
  - d) Exposure in Heidelberg MLA150 with  $J = 230 \text{ mJ/cm}^2$  dose.
  - e) Develop in AZ4:1 400k developer for  $t = 120 \text{ s}$ , rinse with water and dry with  $\text{N}_2$ .
- 15) Deposition of  $d = 250 \text{ nm}$   $\text{WO}_3$  through reactive DC magnetron sputtering (Moe). Base pressure  $p < 5 \times 10^{-7} \text{ mTorr}$ . Deposition parameter: 20/5 sccm  $\text{Ar/O}_2$ ,  $p = 20 \text{ mTorr}$ ,  $P = 125 \text{ W}$ . Deposition of  $d = 120 \text{ nm}$   $\text{LiNbO}_3$  through reactive RF magnetron sputtering (Moe). Base pressure  $p < 5 \times 10^{-7} \text{ mTorr}$ . Deposition parameter: 20/1 sccm  $\text{Ar/O}_2$ ,  $p = 5 \text{ mTorr}$ ,  $P = 88 \text{ W}$ . Deposition of

d = 270 nm NiO through reactive DC magnetron sputtering (Moe). Base pressure  $p < 5 \times 10^{-7}$  mTorr. Deposition parameter: 20/1 sccm Ar/O<sub>2</sub>,  $p = 20$  mTorr,  $P = 200$  W. Deposition of d = 100 nm W through magnetron sputtering (Moe). Base pressure  $p < 5 \times 10^{-7}$  mTorr. Deposition parameter: 20/0 sccm Ar/O<sub>2</sub>,  $p = 20$  mTorr,  $P = 200$  W.

a) Lift-off in Remover PG under strong sonication.

4<sup>th</sup> mask: SiN<sub>x</sub> waveguide length and beam definition:

16) Photolithography step (Heidelberg MLA150)

- a) Deposit HMDS monolayer for resist adhesion.
- b) Spin coating of AZ4330P photo resist at 2500 rpm for  $t = 60$  s, followed by baking at  $T = 100^\circ\text{C}$  for  $t = 10$  min. Parameter result in  $d = 4250$  nm thickness.
- c) Rest wafers for  $t = 10$  min to allow wafers to cool down.
- d) Exposure in Heidelberg MLA150 with  $J = 260$  mJ/cm<sup>2</sup> dose.
- e) Develop in AZ 4:1 400k developer for  $t = 120$  s, rinse with water and dry with N<sub>2</sub>.

17) RIE of SiO<sub>2</sub> cladding and thermal oxide layer, as well as SiN<sub>x</sub> waveguide structure.

18) Oxygen plasma clean

5<sup>th</sup> mask: DRIE mask definition:

19) Photolithography step (Heidelberg MLA150) with same mask as 4<sup>th</sup> but offset in all directions by  $l = 3 \mu\text{m}$ .

- a) Deposit HMDS monolayer for resist adhesion.
- b) Spin coating of AZ4330P photo resist at 2500 rpm for  $t = 60 \text{ s}$ , followed by baking at  $T = 100^\circ\text{C}$  for  $t = 10 \text{ min}$ . Parameter result in  $d = 4250 \text{ nm}$  thickness.
- c) Rest wafers for  $t = 10 \text{ min}$  to allow wafers to cool down.
- d) Exposure in Heidelberg MLA150 with  $J = 260 \text{ mJ/cm}^2$  dose.
- e) Develop in AZ 4:1 400k developer for  $t = 120 \text{ s}$ , rinse with water and dry with  $\text{N}_2$ .

20) DRIE step with high aspect ratio with five times 170 cycles

- a) Selectivity of 120:1 Si/PR and  $60 \mu\text{m}/170$  cycles etch rate.
- b) Cool down between repetitions  $t = 2 \text{ min}$ .

21) Dicing of the etched trenches with  $80 \mu\text{m}$  blade height

- a) PR still on for protection. Dicing at  $10 \text{ mm/s}$  with  $d = 50 \mu\text{m}$  blade.

22) Oxygen plasma clean of intact wafer for  $t = 15 \text{ min}$ .

- a) Breaking of wafer into individual dies.